DESIGN, MODELLING AND BIOFABRICATION OF SCAFFOLDS FOR OSTEOCHONDRAL REPAIR

by

Cristina Ferro Barbosa, MSc (Res),

Thesis submitted to the University of Nottingham in fulfilment of the requirements for the degree of Doctor of Philosophy.

Faculty of Engineering

Department of Mechanical, Materials and Manufacturing Engineering

Advanced Manufacturing Technology Group

January 2024

This page is intentionally blank.

Acknowledgements

I am profoundly grateful for the amazing experience that my PhD journey has been, a roller coaster of emotions marked by both challenges and opportunities, each playing a pivotal role in shaping the person I am today. The decision to move abroad to the UK immersed me in the fascinating world of biofabrication, coupled with the unexpected trials brought forth by a global pandemic, underscored the resilience required to navigate such endeavours, especially when separated from loved ones. Amidst these, I found unwavering support in my marriage to an exceptionally intelligent, dedicated, and loyal partner.

Firstly, I am sincerely grateful to my PhD supervisor, **Professor Joel Segal**, not only for the opportunity to undertake this PhD but also for his dedication and unconditional support throughout my PhD journey. His invaluable insight, positivity, and guidance were vital in sustaining my confidence in my abilities on the project, particularly during the challenging times posed by the pandemic. In addition, I would like to express my gratitude to my co-supervisor, **Professor Felicity Rose**, not only for all your support throughout this journey but also for providing me with critical-thinking skills and encouraging me to conduct impactful research. Also, I would like to thank **Dr Laura Ruiz-Cantu**, who was part of this research for half of this journey. She was always there to guide me, show me her wizardry skills, and encourage me always to give my best.

I want to thank the National Council of Humanities, Science and Technology (CONAHCYT) in Mexico for the scholarship granted to pursue this PhD. As well, I would like to express my gratitude to the University of Nottingham, particularly the Institute for Advanced Manufacturing (IfAM), Centre for Additive Manufacturing (CfAM), Biodiscovery Institute (BDI), and School of Life Sciences Imaging (SLIM). I am deeply appreciative of the supportive individuals who are part of these groups, as they have generously extended their assistance, dedicating their time and energy throughout this journey.

I would like to express my profound gratitude to the technicians and staff who have made this journey significantly smoother with their expertise and support. Mark East, Adam Whitbread, and Mark Hardy, your assistance within the CfAM laboratories has been invaluable. Likewise, thanks to Teresa Marshal and Ann Williams for providing various lab equipment training and unwavering support at the Biofabrication Laboratory in BDI 1. Additionally, Ian Ward, I am grateful for your valuable assistance with the confocal microscope in the SLIM facilities. I would also like to acknowledge the following individuals who provided me with valuable training

during my PhD research. Dr Robert Owen and Dr Jason Hutchinson, I appreciate your scientific expertise and training in the cell culture world. A heartfelt thanks goes to Kerri Lindley, who has been an indispensable asset in the AMB. Kerri, your kindness and always happy face have made a significant impact. Thank you for being the person who knows everyone in the building and is always willing to help.

The PhD journey becomes significantly smoother when you walk alongside friends who share the same goals. To all those who have been integral to this collective experience, whether old friends back in Mexico or those here in the UK, thank you for your unwavering support. You have contributed to maintaining a harmonious work-life balance. In this moment of acknowledgement, I want to express my gratitude to each one of you. While the list of names may be extensive, the immeasurable impact of your collective presence deserves recognition.

To all my family, I would like to express my deepest gratitude for their unconditional love and support. My father, **Rubén**, serves as an inspiring example of responsibility and diligence, both personally and professionally, emphasizing that dedication can achieve anything. His enduring commitment and unlimited love have been a constant inspiration. To my mother, **Socorro**, who inspired in me the essential virtues of humility, empathy, values, education, and diverse knowledge. Her guidance has been crucial in overcoming obstacles, demonstrating the significance of resilience in adversity. Thanks for your constant support and trust. To my brother, **Rubén**, a phenomenal sibling and unwavering friend, your daily lessons motivate me to strive for continuous improvement. I appreciate your role in providing a different perspective on life. Lastly, to my grandparents, whose honour I constantly think of, this milestone holds special meaning for them.

Above all, I want to extend my heartfelt admiration to my extraordinary husband, **Jorge**. I am truly fortunate to have you by my side. Your unwavering support and encouragement have been my pillars throughout this challenging journey, discussing my research and being patient with me during my stressful time. As a partner, you have been my rock; as a colleague, my confidant; as a friend, my solace; and as a lover, my joy and happiness. Your belief in me has propelled me forward, and many of my achievements are a testament to your influence. Your love has made me a better person, and I am endlessly thankful for the strength and happiness you bring into my life. Your encouragement echoes in my heart, and I look forward to sharing the next chapter with you. Together, we have created a beautiful PhD journey, and I wholeheartedly agree that the best is yet to come.

"solo mírame con esos ojitos lindos, que con eso yo estoy bien"

Abstract

Osteochondral (OC) defect refers to a focal area of injury that involves both the cartilage and a piece of underlying bone, occurring often as a result of traumas or degenerative illnesses such as osteoarthritis (OA). Currently, numerous orthopaedic procedures are used for repairing the damage of the OC lesions, but none of these treatments have been able to accomplish a full repair of an OC defect. Over the past two decades, the field of tissue engineering has provided a prospective alternative strategy using biomaterials and cells in a scaffold. Extrusion- based three-dimension printing (3D) technology has achieved advancements in bone and cartilage reconstruction, providing a new strategy for restoring joint function. The aim of this research was to design and manufacture a multi-material graded OC scaffold that mimics the cartilage and bone interface with the specific graded mechanical properties. A novel approach involves addressing the complexity of an OC scaffold by aiming to mimic the four zones of the cartilage and the subchondral zone. Following Kabir et al., discovery regarding the mechanical properties of the cartilage within OC tissue, the research strategy proposed designing a scaffold with no bounding, this focus on achieving the desired mechanical characteristics of an OC scaffold. Kabir et al., study reported a compressive modulus of 10.60 ± 3.62 MPa for cartilage within OC tissue under unconfined compression, which served as a foundational reference. To implement this into the strategy, the materials chosen were polycaprolactone (PCL) to provide structural support and gelatin methacrylate (GelMA) to act as a cell carrier. These materials possess properties that make them well-suited to processing through the extrusion technique, utilising the 3D Discovery RegenHu machine, allowing the co-printing of these two materials. Three geometries, square, sinusoidal, and spiral, were investigated to vary the mechanical properties in the OC scaffold. The results demonstrate intriguing trends in Young's modulus across various scaffold geometries. Integration of these geometries into a unified OC scaffold yielded a Young's modulus of 50.68 ± 3.38MPa after 14 days of cell culture, surpassing the mechanical properties of individual designs. Moreover, viability assessment studies were performed on the PCL/GelMA scaffolds. The findings indicate that the scaffold designs support cell proliferation, as shown in DNA quantification. The findings in this thesis therefore support the feasibility of using extrusion-based 3D printed scaffolds for repair of OC defects.

Declaration of figures & Data Authorship

Cristina Ferro-Barbosa is the sole author of all graphics, diagrams, figures, tables and other associated data used in this thesis or in presentations during the course of doctoral study. Any graphics, diagrams, figures, tables, or associated data not authored by Cristina Ferro-Barbosa have been appropriately acknowledged.

Cristina Ferro Barbosa

January 2024

COVID-19 Impact Statement

The COVID-19 pandemic has had a significant impact on my research in Manufacturing Engineering, specifically in tissue engineering, focusing on the designing, modelling, and biofabrication of an Osteochondral Scaffold. As the pandemic emerged in early 2020, I was in the early stages of my PhD, conducting a literature review and planning laboratory inductions. However, the subsequent lockdown and closure of non-essential buildings disrupted my plans, delaying my access to the laboratories and equipment.

Furthermore, the initial lockdown in March 2020 had a detrimental effect on my training schedule, which was intended to take place at the beginning of March. With school closures and uncertainty surrounding the pandemic, I had to do the lockdown away from my family, where working from home proved to be challenging. The inability to plan each day's work effectively, coupled with uncertainty about when I could return to the university, hindered my ability to conduct experimental work during this crucial period.

The phased return to the university in August provided restricted access to the laboratories, primarily prioritizing post-doctoral staff and senior PhD students. It was not until September 2020, six months after the initial lockdown, that I could resume training and experimental work. The rearrangement of trainings during this period also proved challenging due to increased demand from students and the constraints imposed by university protocols aligned with government requirements.

However, access to facilities in different buildings with varying protocols and operating hours presented further complications, as it was preferable not to be between buildings. The limited laboratory time affected my project's progression and hindered the depth and breadth of the work that could have been explored. Additionally, other laboratory users faced similar issues, resulting in competition for resources and further delays. Consequently, I was unable to perform the necessary experiments to keep my project on schedule, resulting in a setback and falling behind in terms of the intended timescale. The development and completion of my research heavily rely on the preparation and execution of experiments in the laboratory, and this interruption significantly impacted the progress of my work.

Subsequent lockdowns in November 2020 and from January to March 2021 presented additional challenges and uncertainties, making it difficult to foresee the development of my project within the diminishing timeframe. The limitation on moving between buildings

further exacerbated the situation. To manage these difficulties, I had to scale back and prioritize my proposed ideas, which compromised the extent of the investigation and reduced the level of understanding that could be attained. Specifically, the loss of time in developing skills in cell culture necessitated scaling back the scope of the cell culture elements, limiting the study to cytocompatibility alone and excluding the intended focus on cell differentiation using chondrocytes.

In light of the significant disruptions caused by the COVID-19 pandemic, I kindly request that this impact statement be taken into consideration during the assessment of my thesis. The unforeseen circumstances and the resultant delays have had a substantial impact on the progression and outcomes of my research, which were beyond my control.

Table of Contents

Acknowledgements i

Abstract iii

Declaration of figures & Data Authorship iv

COVID-19 Impact Statement v

Table of Contents vii

List of Figures xii

List of Tables xxiv

List of Abbreviations xxvi

Chapter 1. Introduction. 1

1.1. Background. 1

1.2. Aim and Hypothesis. 3

1.3. Paper. 5

1.4. Attended Conferences. 5

1.5. Outline of Thesis. 6

Chapter 2. Literature Review. 8

2.1. OC Tissue. 8

2.2. OC Defect. 11

2.3. Tissue Engineering Approaches. 14

2.3.1. Tissue Engineering Approaches for the OC Defect Repair. 14

2.4. 3D printing in Tissue Engineering. 15

2.4.1. Additive Manufacturing Techniques. 15

2.5. Biomaterials for 3D Printing OC Scaffolds. 25

2.6. Design of the OC Scaffold. 34

2.7. Finite Element Modelling. 36

2.8. Mechanical Properties of the OC Tissue. 37

2.9. OC Scaffolds. 44
2.10. Knowledge Gaps. 49
Chapter 3. Methodology 51
3.1. Introduction. 51
3.2. Materials. 54
3.3. Methods of Materials Synthesis and Characterisation. 54
3.3.1. Gelatin Methacrylate. 54
3.3.1.1. Procedure for Synthesis of GelMA 54
3.3.1.2. Characterisation of GelMA. 56
3.3.1.3. GelMA Hydrogel Preparation. 56
3.3.1.4. Rheological Test. 56
3.3.1.5. Swelling Analysis. 57
3.3.1.6. Degradation Analysis. 57
3.3.2. Polycaprolactone. 58
3.3.2.1. Rheological Measurements. 58
3.4. Scaffold Design, Fabrication and Analysis. 58
3.4.1. Scaffold Design. 60
3.4.2. Extrusion-based 3D printing. 61
3.4.3. Surface Morphology. 63
3.4.4. Mechanical Properties. 63
3.4.5. Porosity. 64
3.4.6. Finite Element Software – Abaqus. 64
3.5. Mammalian Cell Culture and Viability Analysis. 66
3.5.1. Cell Culture. 66
3.5.2. Scaffold Sterilisation. 66
3.5.3. Scaffold Seeding and Culture. 66

3.5.4. Assessment of Cell Viability and Proliferation. 67
3.5.4.1. Metabolic Activity. 67
3.5.4.2. Toluidine Blue O. 67
3.5.4.3. Cell Viability. 68
3.5.4.4. DNA Content as a Measure of Cell Number/Proliferation. 68
3.6. Data Analysis and Statistical Analysis. 69
Chapter 4. Characterisation of Polycaprolactone and GelMA for 3D co-printing. 70
4.1. Introduction. 70
4.2. Characterisation of 3D Printing Polycaprolactone. 71
4.2.1. Rheological Properties. 71
4.3. Characterisation of 3D Printing GelMA. 73
4.3.1. Degree of Methacrylation – GelMA. 73
4.3.2. Rheological Properties. 75
4.3.3. Swelling Analysis 82
4.3.4. Degradation Analysis 86
4.4. Conclusion 88
Chapter 5. 3D Bioprinting: characterisation of GelMA/PCL for 3D printing of multi-material for osteochondral defect. 90
5.1. Introduction. 90
5.2. RegenHU Bioprinting Configuration. 91
5.3. Optimisation of Polycaprolactone Printing Process. 94
5.3.1. Feeding Rate and Building Speed Optimisation. 95
5.3.2. Optimisation of Space Between Strand's Layer Thickness. 97
5.3.3. Effects of the Heating System on PCL during 3D Printing Process. 100
5.4. Optimisation of Gelatin Methacrylate Printing Process. 102
5.4.1. Effects of the Cooling System on GelMA during 3D Printing Process. 105

5.4.2. Pressure and Speed Optimisation. 105
5.5. 3D printing of PCL/GelMA scaffolds. 108
5.5.1. Design of PCL/GelMA Scaffolds. 108
5.5.2. BioCAD Design. 112
5.5.3. Co-printing. 117
5.5.3.1. Effects of Co-printing a Hydrogel with a Polymer. 117
5.5.4. Surface Morphology and Porosity Characterisation 118
5.5.5. Swelling and Degradation. 121
5.5.5.1. Swelling. 121
5.5.5.2. Degradation. 123
5.6. Mechanical Testing. 126
5.6.1. Polycaprolactone. 126
5.6.2. Gelatin Methacrylate 130
5.6.3. PCL/GelMA Scaffolds 131
5.6.4. PCL/GelMA/Cells Scaffolds 134
5.7. Conclusions. 138
Chapter 6. FE Modelling of the designs for osteochondral scaffolds. 140
6.1. Introduction. 140
6.2. CAD Geometries. 141
6.2.1. Development of CAD scaffolds. 141
6.3. Finite Element Analysis. 144
6.4. Simulations Conditions. 145
6.4.1. Mesh. 145
6.4.2. Compression Properties. 147
6.5. Conclusions. 149
Chapter 7. Characterisation of cell viability on the OC scaffold. 152

7.1. Introduction. 152
7.2. Viability Studies of 3T3 Cells for PCL/GelMA Scaffolds. 154
7.2.1. Effect of Scaffold Sterilisation. 154
7.2.2. Cells Seeding with Static method. 156
7.3. Cell Distribution, Proliferation, and Viability Analysis. 156
7.3.1. Cell Distribution. 159
7.3.2. Metabolic Activity. 162
7.3.3. Cell Viability. 167
7.3.4. Cell Proliferation. 177
7.4. Conclusions. 179
Chapter 8. Summary and future directions. 181
8.1. Future Work. 184
8.2. Concluding Statement of Research Purpose and Novelty. 185
REFERENCES 187
Appendix A. Cell Culture Solutions 232
Appendix B. Standard Curves 233

List of Figures

Figure 2.1 OC tissue representation (re-drawn from Imhof *et al.*.(Imhof et al., 1999)).....9

Figure 2.2 Representative image of the stages of an OC defect: Stage I – Chondral defect with partial thickness, Stage II – Chondral defect with full thickness, and Stage III–OC defect with cartilage and bone affected (re-drawn from Nukavarapu et al. (Nukavarapu & Dorcemus, 2013b)).....11

Figure 2.3 Clinical methods for the OC defects treatments (re-draw from Deng et al. 2019 Deng et al., 2019).....12

Figure 2.4 Schematics of representative 3D printing techniques: A) Freeze Dryer, B) , thermal-induced phase separation (TIPS), C) Stereolithography (SLA), D) Selective laser sintering (SLS), E) Inkjet, F) Digital light procession (DLP), G) Electrospinning, H) Fused Deposition Modelling (FDM) and I)Extrusion. (re-drawn from (Hussain et al., 2022; Isaac et al., 2021; S. Park et al., 2022; W. S. Park et al., 1998; Sekmen et al., 2022; Taskin, 2020; Zeinali et al., 2021).....16

Figure 3.1 Link between aim - objectives and specific methods and parameters. (Abbreviation as follows: OC- Osteochondral, FE- Finite Element, CAD- Computer-Aided Design NMR- Nuclear Magnetic Resonance).....51

Figure 3.2. Flowchart of the key steps in the development of scaffolds.....52

Figure 3.3 Schematic illustration of the methodology for developing the 3D OC scaffold.53

Figure 3.4 Visual summary of GelMA synthesis workflow. The precipitation protocol to produce GelMA was used to eliminate the unreacted MA; the precipitation was repeated three times, as stated in steps 2 to 4. Samples were in the vacuum oven at room temperature (RT) for a day to remove any remaining liquid and then added to the -80°C freezer overnight. Finally, samples were lyophilised for three to four days, and the final product was blended and stored in a -80°C freezer.....55

Figure 3.5 Schematic of the OC tissue indicating physical property changes across the different zones. From top to bottom, chondrocyte size, fibre diameter and stiffness increase gradually between each zone, whereas water absorption, collagen II and chondrocyte number increase from the bottom to the top -(image re-drawn from Imhof et al.(Imhof et al., 1999) (Bartnikowski et al., 2015; Boschetti et al., 2004; Jurvelin et al., 2003; Korhonen et al., 2002).....59

Figure 3.6 3D Bioprinter RegenHU setup. Schematic showing the complete process to manufacture a dual material scaffold using two printheads, one with GelMA and the other with PCL and UV light (365nm wavelength). 62

Figure 3.7 Unconfined compression setup. Conducting the unconfined test, A) the sample is placed between B) the two stainless steel platens and compressed. 63

Figure 3.8 Overview of workflow for FE modelling in ABAQUS. A) Cast and printed scaffolds of each material were performed for B) experimental analysis of PCL and GelMA mechanical behaviour under unconfined compression to access materials properties and validate numerical predictions. C) BioCAD software was used to create the designs, and the geometries that were copied to D) Solidworks CAD designs and then imported to ABAQUS to do the FEA model. 65

Figure 3.9 Schematic of the DNA quantification using QuantiT dsDNA kit. (1) media was removed, and samples were transferred to the Eppendorf tubes. (2) Samples were sliced and mashed, and (3) 1000ul of Lysis freezing solution was added to each sample. (4) Samples were frozen and defrosted 3X at -80˚C (5) 20ul of the sample aliquot and 180ul of Quant-iT reagent were transferred to a 96 well plate. (6) fluorescence was measured at a: 502/523 nm (7) and analysed. 69

Figure 4.1 Shear viscosity of the PCL. A) PURASORB PC12 B) PCL45, C)PCL 80. Results denote mean± SD (n=3, N=3). 72

Figure 4.2 Effect of temperature on the PCL. A) PCL45, B)PCL 80. Results denote mean± SD (n=3, N=3). 73

Figure 4.3 1H-NMR spectra of gelatin and GELMA batches. Signals have been highlighted, in red for the phenylalanine signal, the green for the methacrylic groups signal and in blue for the lysine methylene signal. 75

Figure 4.4 Shear rate vs. viscosity for GELMA concentration A) 5%, B) 10%, C) 15% and C) 20%. Results denote mean± SD (n=3, N=3). 76

Figure 4.5 Temperature vs. viscosity for GELMA concentration A) 5%, B) 10%, C) 15% and C) 20%. Results denote mean± SD (n=3, N=3). 78

Figure 4.6 Pressure difference in time for the 5% (w/v), 10% (w/v), 15% (w/v) and 20% (w/v). Results denote mean ± SD (n=3, N=3). 80

Figure 4.7 10% (w/v) GelMA with and without dye, A) Temperature vs viscosity of 0% and 2% of dye. B) Shear rate vs. viscosity of 0% and 2% of dye. Results denote mean± SD (n=3, N=3). 81

Figure 4.8 Swelling behaviour analysis of GelMA-cast cubes at various concentrations (5% (w/v), 10% (w/v), 15% (w/v), and 20% (w/v)) with 2% (w/v) dye. A) Cube weight variation over the initial 5-week period, investigated at 37°C. B) Percentage swelling ratio at weeks 1, 2, 3, and 4. The graphs provide valuable insights into the swelling characteristics of the GelMA composite across different concentrations and temperature conditions. Results denote mean ± SD (n = 3). 83

Figure 4.9 Swelling behaviour of 10% (w/v) GelMA + 2% (w/v) dye cubes. A) dehydration of cast cubes over a 24-hour period, and B) hydration of cast cubes within 24-hour timeframe. Rapid response of the material changes in moisture conditions, providing insight into its swelling behaviour. Results denote mean ± SD (n = 3). 85

Figure 4.10 Biodegradation analysis of GelMA-cast cubes at varying concentrations (5% (w/v), 10% (w/v), 15% (w/v), and 20% (w/v)) with 2% (w/v) dye. (A) Evolution of cube weight observed over a 25-week period at 37°C. (B) Percentage biodegradation ratio at weeks 5, 10, 15, and 20. Results denote mean ± SD (n = 3). 86

Figure 4.11 Stages of 10% (w/v) GelMA degradation, A) as cast, B) swelling in PBS at 37°C after five weeks, C) signs of degradation at week 15 and D) week 20, E) finally, full degradation at week 25. F) 10% (w/v) GelMA graph during the period of swelling and degradation. Results denote mean ± SD (n = 3). 88

Figure 5.1 3D Biodiscovery RegenHU System Configurations and Equipment. Overview of the configurations and equipment associated with the 3D Biodiscovery RegenHU system, offering an understanding of the technological setup employed. 92

Figure 5.2 3D Biodiscovery RegenHU system tools and variable parameters for PCL and GelMA Printing enable the precise printing of both materials, depending on the printhead. 93

Figure 5.3 Needles optimisation used for the Thermo-Polymer (HM-300H) Printhead. A1-B1) Filaments while printing G32 and G30, showcasing the material flow characteristics. A2i - B2i) Needle dimensions are illustrated in millimetres (mm), providing precise

measurements for reference. A2ii-B2ii) Scaled representation of the filament, with a 2mm scale bar. 95

Figure 5.4 3D printing PCL samples at varied feeding rates. A) At 5 rpm, B) 10 rpm, C) 15rpm, and D) 17.5 rpm. The scale bar represents 4mm..... 96

Figure 5.5 3D printing PCL samples at different nozzle speeds. A) At 10mm/s, B) 15mm/s, C) 18mm/s, and D) 20mm/s. The scale bar represents 4mm..... 97

Figure 5.6 Scaffolds with a layer thickness of 200µm and varied space ratios. A) Full scaffold view, providing an overview of the structure (scale bar is 4mm). B) Vertical layers, showcasing the printed filaments within a single layer, allowing for detailed examination. C) Vertical and horizontal filaments are in a single layer, highlighting the complex architecture of the scaffold. A scale bar of 500µm is included in B and C to aid dimensional assessment. 98

Figure 5.7 Scaffold thickness variation for machine setting parameters. A) layer thickness of 0.25mm, B) scaffold with a thickness of 1.25mm and C) scaffold with a layer thickness of 3.25mm. 1) represents the top view, and 2)the isometric view. Scale bars = 4mm. 99

Figure 5.8 3D printing PCL sample with delamination. The scale bar represents 4mm... 100

Figure 5.9 3D printing PCL samples using different printhead temperatures. A) Printhead temperature set at 80°C, B) Printhead temperature set at 90°C, and C) Printhead temperature set at 100°C. Scale bar = 4mm. 101

Figure 5.10 PCL Scaffold characteristics and microscope closeup. PCL scaffold with specific dimensions, featuring a thickness of 4.6mm and a diameter of 8mm. Additionally, a microscope closeup view allows for an in-depth exploration of the scaffold's layers at a scale of 500µm..... 102

Figure 5.11 Needles optimisation used for the Time-Pressure dispensing DD-135N printhead. A1-B1-C1) Filaments during the printing of G32, G30 and G27 showcasing the material flow characteristics and the influence of needle optimisation on the printing process. A2i-B2i-C2i) Needle dimensions are illustrated in millimetres (mm), providing precise measurements for reference. A2ii-B2ii- C2ii) Scaled representation of the filament, with a 2mm scale bar. D) UV light distance of 4mm for the photocuring of the hydrogel..... 104

Figure 5.12 3D printing GelMA samples at varied nozzle speeds. A) 1mm/s, B) 2mm/s, and 3 mm/s. The scale bar represents 4mm..... 106

Figure 5.13 Scaffolds with a layer thickness of 200μm and varied space ratios. A) Full scaffold view at a scale of 4mm, providing an overview of the structure with a scale bar of 4mm. B) Vertical layers, showcasing the printed filaments within a single layer, allowing for detailed examination. Scale bar of 500μm. 107

Figure 5.14 GelMA Scaffold characteristics and microscope closeup. GelMA scaffold with specific dimensions, featuring a thickness of 4mm and a diameter of 8mm with a feed rate of 3.5 mm/s. A microscope closeup view for an in-depth exploration of the scaffold's layers at a scale of 500μm. 108

Figure 5.15 Design and fabrication of PCL scaffolds for an OC repair. A,B,C,D) Representative images of single-layer design with a diameter of 8 mm. A) Triangle, B) Hexagon, C) Caracol, D) Sinusoidal, and E) Square, D) Spiral. A, B, C) Highlighting points of intersection and excessive toolpath start and stop points in red circles. D, E,F) 3D-printed PCL scaffolds of sinusoidal, square, and spiral, respectively. 109

Figure 5.16 Schematic Representations of Multi-Material Bioprinting Designs for PCL/GelMA Composite Scaffolds. A)Frontal view provides a frontal perspective of the scaffold, with a diameter of 8 mm. C) Top view of a single layer D) Cross-section view highlighting the spacing between two PCL strands, varying between 1mm and 2mm depending on the design. C) Cross-section view highlighting the gap between PCL and GelMA strands, ranging from 0.22mm to 0.72mm, depending upon the specific design. 111

Figure 5.17 Square BioCAD design layer-by-layer provided a comprehensive visual insight into its intricate construction. This design is distinguished by the selective use of two distinct materials. Blue filaments- correspond to PCL serve as the structural framework of the design, providing stability and support. Magenta filaments- represent GelMA layers, which are strategically placed between the layers of PCL, as indicated by the black arrows. These GelMA layers facilitate specific functionalities and biological interactions within the construct. 113

Figure 5.18 Sinusoidal BioCAD design layer-by-layer provided a comprehensive visual insight into its intricate construction. This design is distinguished by the selective use of two distinct materials. Blue filaments- correspond to PCL serve as the structural framework of the design, providing stability and support. Magenta filaments- represent GelMA layers, which are strategically placed between the layers of PCL, as indicated by the black arrows.

These GelMA layers facilitate specific functionalities and biological interactions within the construct. 114

Figure 5.19 Spiral BioCAD design layer-by-layer provided a comprehensive visual insight into its intricate construction. This design is distinguished by the selective use of two distinct materials. Blue filaments- correspond to PCL serve as the structural framework of the design, providing stability and support. Magenta filaments- represent GelMA layers, which are strategically placed between the layers of PCL, as indicated by the black arrows. These GelMA layers facilitate specific functionalities and biological interactions within the construct. 115

Figure 5.20 OC BioCAD design layer-by-layer represented to emulate the structure of the OC tissue. This design is characterised by the selective use of two distinct materials. Blue filaments- correspond to PCL serve as the structural framework of the design, providing stability and support. Magenta filaments- represent GelMA layers, which are strategically placed between the layers of PCL, as indicated by the black arrows. These GelMA layers facilitate specific functionalities and biological interactions within the construct..... 116

Figure 5.21 Samples 3D co-printed PCL/GelMA. The scale bar top row represents 4mm and the bottom row 4mm. 118

Figure 5.22 Characterisation of PCL/GelMA scaffolds with different geometries, including square, sinusoidal, spiral and OC. Each design A) Square, B) Sinusoidal, , C) Spiral , and D) OC, represents a fundamental aspect of the scaffold's structural and functional attributes. A-D) Scanning Electron Microscopy (SEM) images of section of the PCL/GelMA scaffolds. The scale bar in these images is set at 500μm. A1-D1) GelMA pores within the scaffold. The scale for these images is set at 200μm, providing a closer look at the GelMA component. A2-D2) PCL pores within the scaffold. Similar to A1-D1, the scale is set at 200μm for a detailed examination of the PCL component. 120

Figure 5.23 Swelling behaviour analysis of PCL/GelMA-scaffolds. PCL/GelMA-scaffolds weight variation over the initial 5-week period, investigated at 37°C. Providing valuable insights into the swelling characteristics of the designs of PCL/GelMA scaffolds and temperature conditions. Results denote mean± S.D. (n=6,N=3). 122

Figure 5.24 Biodegradation analysis of PCL/GelMA scaffolds. (A) Evolution of cube weight observed over ten weeks at 37°C. (B) Percentage biodegradation ratio at weeks 4, 6, and 8. Comprehensive insights are presented into the biodegradation behaviour of the GelMA

composite under different conditions and concentration levels. Results denote mean± S.D. (n=6, N=3). Statistical analysis and significance levels are indicated as *** $p < 0.01$ and **** $p < 0.0001$. 124

Figure 5.25 Mechanical testing of PCL structures comprising cast cubes and cylindrical printed scaffolds. A-B) PCL cast cubes (10mmx10mmx10mm). C) Illustrates the unconfined compression testing of the PCL cube under axial load. D) Cylindrical scaffolds with varying designs (1.2 mm, 3.6 mm, and 4.2 mm) offer a comparative analysis of their size-dependent mechanical properties. E) Unconfined compression testing of the cylindrical scaffolds.. 127

Figure 5.26 Mechanical properties of PCL 3D printed scaffolds and a PCL casted cube. A) Representative stress/strain curves illustrating deformation, the elastic (proportionality) limit, and the plastic region. B) Youngs modulus represents printed samples' compressive stress/strain curves. Results denote mean± S.D. (n=6,N=3). Statistical analysis and significance levels are indicated as ** $p < 0.024$ and **** $p < 0.0001$. 128

Figure 5.27 Mechanical testing of GelMA casted cubes comprising. A-B) GelMA casted cubes (1mmx1mmx1mm). C) Illustrates the unconfined compression testing of the GelMA cube under axial load. 130

Figure 5.28 Mechanical properties of 10% w/v GelMA casted cube. A) Representative stress/strain curves illustrating deformation, the elastic (proportionality) limit, and the plastic region. B) Youngs modulus representing compressive stress/strain curves of 10% w/v GelMA casted cube. Results denote mean± S.D. (n=6,N=3). 131

Figure 5.29 Mechanical properties of PCL/GelMA 3D printed scaffolds. A) Representative stress/strain curves illustrating deformation, the elastic (proportionality) limit, and the plastic region. B) Youngs modulus represents printed samples' compressive stress/strain curves. Results denote mean± S.D. (n=6,N=3). Statistical analysis and significance levels are indicated as * $p < 0.0162$, * $p < 0.0014$ and ** $p < 0.001$..... 133

Figure 5.30 Mechanical properties of PCL/GelMA with cells 3D printed scaffolds. A) Representative stress/strain curves illustrating deformation, the elastic (proportionality) limit, and the plastic region. B) Youngs modulus represents printed samples' compressive stress/strain curves. Results denote mean± S.D. (n=6,N=3). Statistical analysis and significance levels are indicated as ** $p < 0.0140$, *** $p < 0.0020$ and **** $p < 0.0001$. 135

Figure 5.31 Comparative analysis of Youngs modulus representing compressive stress/strain curves of 3D printed scaffolds of PCL, PCL/GelMA, and PCL/GelMA with cells. Results are expressed as mean ± SD (n=6, N=3). Statistical analysis and significance levels are denoted as **** $p < 0.0001$. 137

Figure 6.1 Square PCL/GelMA Scaffold. A) Side view, B) top view, and C) geometry scaffold encapsulated between two rigid planar shells. 145

Figure 6.2 Tetrahedral mesh (0.05mm element size) of the Square Scaffold with 200μm Contact Width. 146

Figure 6.3 Experimental results vs. model Youngs modulus comparison of PCL scaffolds. Experimental results are expressed as mean ± SD (n=6, N=3). 147

Figure 6.4 Experimental results vs. model Youngs modulus comparison of PCL/GelMA scaffolds. Experimental results are expressed as mean ± SD (n=6, N=3). 148

Figure 6.5 Youngs modulus of scaffold geometries, A) PCL OC scaffold representation, B) PCL/GelMA scaffolds representation, C) representation of the stress distribution of the OC scaffold and D) Graph showing the data of PCL and PC/GelMA of the model. 149

Figure 7.1 Comparative illustration of distinct sterilisation approaches employed for the scaffolds. A) Scaffolds underwent a treatment involving submersion in dH_2O followed by UV disinfection. B) Direct UV disinfection of scaffolds after allowing them to dry without prior immersion in dH_2O. C) Scaffolds were dried and subsequently disinfected with AB/AM. D) Scaffolds were dried and disinfection protocol involved submerging them into AB/AM and PBS prior to UV disinfection. Cloudy media with green bacteria at the top was considered contaminated, clear media was considered not infected. 155

Figure 7.2 Schematic showing the methodology for static cell seeding in the scaffolds. (1) Mammalian cells 3T3-E291 were extracted. (2) Scaffolds were top-seeded by pipetting the cells. (3) Samples were incubated for 3hr at 37˚C (4). 1000 µl f media was added aliquots added to the scaffolds in the well plates. 156

Figure 7.3 Schematic overview of the experimental setup to assess the ability of PCL/GelMa scaffold to support cell culture. 157

Figure 7.4 Representative images of the cell distribution on the top of the scaffold at day 7. A) Printed PCL/GelMA scaffold image representing the designs B) Full scaffold structure is depicted, and the imaging was conducted utilising the Leica TCS LSI 0306809 Laser

Scanning Confocal Microscope. Scale bar representing 1000 µm. C) A specific section is highlighted, providing enhanced visibility of the cells. The imaging was conducted utilising the Zeiss LSM T-PMT 880 Confocal Fluorescence Microscopy with a 40x objective, with the scale bar representing 50 µm. 158

Figure 7.5 Schematic describing the visualisation of mammalian cells on the scaffolds using Toluidine Blue O. The protocol followed consists of (1) removing the media from the samples. (2) Fixing the samples using PFA for one hour at room temperature (3) removal of the PFA from the sample. (4) Samples were submerged into the toluidine blue O solution for two hours (5) Samples were washed 3X with PBS. (6). Samples were visualised with a microscope. 159

Figure 7.6 Cell proliferation is examined alongside the OC scaffold across square, sinusoidal, and spiral scaffold designs. Representative images of 3T cells stained with toluidine blue after seven days illustrate cell attachment and distribution throughout the scaffold. Both, front and middle views are presented for each design on days 1, 3 and 7 in scaffolds seeded at the top. Scale bars: 4 mm. 161

Figure 7.7 Schematic showing the methodology for the metabolic activity using Presto Blue® protocol. (1) Media was removed from the samples. (2) Presto Blue Working Reagent was made and 1 mL was added to the scaffold. (3)Samples were incubated for 30 min in a dark environment at 37˚C (4). 100 µl aliquots were taken and added to the 96 well plates in triplicates. (5) Plate reader was used to(6) measure fluorescence, providing a quantitative measure of viability and proliferation of cells. 163

Figure 7.8 3T3 cell metabolic activity to determine seeding efficiency using the Presto Blue assay following one day after seeding for each design, square, sinusoidal, spiral, and OC untreated plate well. Results denote mean± S.D. (n=3, N=3). Statistical analysis and significance levels are indicated as ** $p < 0.0041$, *** $p = 0.0004$ and **** $p < 0.0001$ 164

Figure 7.9 Metabolic activity across scaffold designs at different time points: day 1, day 3, and day 7. Results denote mean± S.D. (n=3,N=3). Statistical analysis and significance levels are indicated as **** $p \leq 0.01$, **** $p \leq 0.001$ and **** $p \leq 0.0001$. 165

Figure 7.10 Schematic showing the Live/Dead™ protocol for cell viability. (1) media was removed from the scaffolds. (2) Live/Dead™ working solution was added to the well containing the scaffolds, (3) and incubated at room temperature in the dark for 30 min. (4) Live/Dead™ stain was removed, and PFA was added and incubated for an hour. (5) Samples

were visualised using confocal microscopy, where green are the live cells and red are dead. 167

Figure 7.11 Representative fluorescence images of 3T3 cells adherent on the square scaffold at day 1, day 3, and day 7. Live and dead cells were discriminated using the LIVE/DEAD™ Viability/Cytotoxicity Kit for mammalian cells, employing green fluorescent calcein-AM for live cell identification based on intracellular esterase activity and red-fluorescent ethidium homodimer-1 to discern compromised plasma membrane integrity in dead cells. Cellular imaging was conducted utilising the Leica TCS LSI 0306809 Laser Scanning Confocal Microscope, with the scale bar representing 1000 µm for accurate assessment of live/dead staining. 169

Figure 7.12 Visual representation of full sinusoidal scaffold for adhesion and viability assessment of 3T3 cells at day 1, day 3, and day 7. Live and dead cells were discriminated using the LIVE/DEAD™ Viability/Cytotoxicity Kit for mammalian cells, employing green fluorescent calcein-AM for live cell identification based on intracellular esterase activity and red-fluorescent ethidium homodimer-1 to discern compromised plasma membrane integrity in dead cells. Cellular imaging was conducted utilising the Leica TCS LSI 0306809 Laser Scanning Confocal Microscope, with the scale bar representing 1000 µm for accurate assessment of live/dead staining. 170

Figure 7.13 Visual representation of full spiral scaffold for adhesion and viability assessment of 3T3 cells at day 1, day 3, and day 7. Live and dead cells were discriminated using the LIVE/DEAD™ Viability/Cytotoxicity Kit for mammalian cells, employing green fluorescent calcein-AM for live cell identification based on intracellular esterase activity and red-fluorescent ethidium homodimer-1 to discern compromised plasma membrane integrity in dead cells. Cellular imaging was conducted utilising the Leica TCS LSI 0306809 Laser Scanning Confocal Microscope, with the scale bar representing 1000 µm for accurate assessment of live/dead staining. 171

Figure 7.14 Adhesion and viability assessment of 3T3 cells on square scaffolds on day 1, day 3, and day 7. Live and dead cells were discriminated using the LIVE/DEAD™ Viability/Cytotoxicity Kit for mammalian cells, employing green-fluorescent calcein-AM for live cell identification based on intracellular esterase activity and red-fluorescent ethidium homodimer-1 to discern compromised plasma membrane integrity in dead cells. Notably, the micrographs vividly illustrate the robust adhesion and extensive spreading of

3T3 cells across all scaffold variations. Cellular imaging was conducted utilising the Zeiss LSM T-PMT 880 Confocal Fluorescence Microscopy equipped with a 40x objective, with the scale bar representing 50 µm for accurate assessment of live/dead staining..... 173

Figure 7.15 Adhesion and viability assessment of 3T3 cells on sinusoidal scaffolds at day 1, day 3, and day 7. Live and dead cells were discriminated using the LIVE/DEAD™ Viability/Cytotoxicity Kit for mammalian cells, employing green-fluorescent calcein-AM for live cell identification based on intracellular esterase activity and red-fluorescent ethidium homodimer-1 to discern compromised plasma membrane integrity in dead cells. Notably, the micrographs vividly illustrate the robust adhesion and extensive spreading of 3T3 cells across all scaffold variations. Cellular imaging was conducted utilising the Zeiss LSM T-PMT 880 Confocal Fluorescence Microscopy equipped with a 40x objective, with the scale bar representing 50 µm for accurate assessment of live/dead staining..... 174

Figure 7.16 Adhesion and viability assessment of 3T3 cells on spiral scaffolds at day 1, day 3, and day 7. Live and dead cells were discriminated using the LIVE/DEAD™ Viability/Cytotoxicity Kit for mammalian cells, employing green-fluorescent calcein-AM for live cell identification based on intracellular esterase activity and red-fluorescent ethidium homodimer-1 to discern compromised plasma membrane integrity in dead cells. Notably, the micrographs vividly illustrate the robust adhesion and extensive spreading of 3T3 cells across all scaffold variations. Cellular imaging was conducted utilising the Zeiss LSM T-PMT 880 Confocal Fluorescence Microscopy equipped with a 40x objective, with the scale bar representing 50 µm for accurate assessment of live/dead staining..... 175

Figure 7.17 Adhesion and viability assessment of 3T3 cells on OC scaffolds at day 1, day 3, and day 7. Live and dead cells were discriminated using the LIVE/DEAD™ Viability/Cytotoxicity Kit for mammalian cells, employing green-fluorescent calcein-AM for live cell identification based on intracellular esterase activity and red-fluorescent ethidium homodimer-1 to discern compromised plasma membrane integrity in dead cells. Notably, the micrographs vividly illustrate the robust adhesion and extensive spreading of 3T3 cells across all scaffold variations. Cellular imaging was conducted utilising the Zeiss LSM T-PMT 880 Confocal Fluorescence Microscopy equipped with a 40x objective, with the scale bar representing 50 µm for accurate assessment of live/dead staining..... 176

Figure 7.18 Cell viability assessment employing the live/dead cell assay conducted on day 1, day 3, and day 7 for the different geometries and the OC scaffold. The quantification

analysis was carried out utilising ImageJ/Fiji software. T. Results denote mean± SD (n=3, N=3). 177

Figure 7.19 Cell Proliferation as assessed by dsDNA content at day 1, day 3, and day 7. A) Cell Proliferation using dsDNA assay comparing square, sinusoidal, spiral and OC scaffolds at day 1, day 3, and day 7. B) Square scaffolds. C) Sinusoidal scaffolds. D) Spiral scaffolds. E) OC scaffolds. Results denote mean± S.D. (n=3,N=3). Statistical analysis and significance levels are indicated as $p < 0.01$,** $p < 0.001$. 178

List of Tables

Table 2.1 Surgical methods for OC repair based on defect dimensions (Howell et al.., 2021; Logli et al.., 2019; K. C. Wang et al.., 2016). 13

Table 2.2 Summary of different 3D printing technologies for tissue engineering repair and their bio-inks. 20

Table 2.3 Characteristics of biomaterials used for the fabrication of OC scaffolds and their advantages and disadvantages 27

Table 2.4 Properties of PCL. 32

Table 2.5 Summary of studies representing Youngs modulus of an OC tissue for each region depending on the type and age of tissue and the mechanical test carried out. 39

Table 2.6 Summary of studies representing Youngs modulus of an OC scaffold depending on the tissue target using a specific manufacturing technique and the specific compression mechanical test. 46

Table 3.1**:** Multiple designs using various geometries: square, sinusoidal, and spiral. 60

Table 3.2. RegenHU parameters for the extrusion-based 3D printing of PCL/GelMA. 62

Table 4.1 Viscosity at different shear rates of the four different concentrations of GelMA. Results denote mean± SD (n=3, N=3). 77

Table 4.2 Viscosity at different temperatures of the four different concentrations of GelMA. Results denote mean± SD (n=3, N=3). 79

Table 4.3 Superficial tension, viscosity, and density of GelMA concentrations. Results denote mean ± SD (n=3, N=3). 80

Table 4.4 Mass swelling data collected from casted cubes of different concentrations of GelMA, 5%, 10%, 15%, and 20% (w/v). Raw data valuesvat 37°C for each concentration, mass (g), were used to calculate swelling ratio results. Swelling ratio is calculated using Equation (3. Results denote mean ± SD (n = 3). 84

Table 4.5 Mass degradation data collected from cast cubes of different concentrations of GelMA, 5%, 10%, 15%, and 20% (w/v), with 2%(w/v) dye until week 20. Raw data values at 37°C for each concentration, mass (g) used to calculate swelling ratio results. Results denote mean ± SD (n = 3). 87

Table 5.3 Mass degradation data collected of PCL/GelMA scaffolds, square, sinusoidal, spiral, and OC until week 8. Raw data values at 37°C for each scaffold, mass (g) used to calculate swelling ratio results. Results denote mean ± SD (n = 6, N=3). 125

Table 5.1 Comparative analysis of Youngs modulus for diverse structures, including cast PCL cubes and 3D-printed scaffolds with square, sinusoidal, and spiral designs. Likewise, including OC scaffolds with multiple designs extends the investigation, showcasing the mechanical implications of different geometries. Results denote mean± S.D. (n=6,N=3). 129

Table 5.2 Comparative analysis of Youngs modulus for diverse structures, including casted GelMA cubes, showcasing the mechanical implications of the material. Results denote mean± S.D. (n=6, N=3). 131

Table 5.4 Comparative analysis of Youngs modulus for diverse structures, including PCL/GelMA, with different square, sinusoidal, and spiral designs. Likewise, including OC scaffolds with multiple designs extends the investigation, showcasing the mechanical implications of different geometries. Results denote mean± S.D. (n=6,N=3). 134

Table 5.5 Comparative analysis of Youngs modulus for diverse structures, including PCL/GelMA with cells with different square, sinusoidal, and spiral designs. Likewise, including the OC scaffolds with multiple designs extends the investigation, showcasing the mechanical implications of different geometries. Results denote mean± S.D. (n=6,N=3). 136

Table 6.1 Samples designs of the three different geometries using BioCAD and SolidWorks based on the sketch design..... 143

List of Abbreviations

3D	Three-Dimensional
ACECM	Articular cartilage extracellular matrix
ACI	Autologous Chondrocyte Implantation
AM	Additive Manufacturing
BMSCs	Bone marrow Mesenchymal Stem Cells
CAD	Computer Aided Design
CC	Calcified Cartilage
Col-HA	Collagen-hydroxyapatite
dH_2O	Distilled Water
DLP	Digital light Procession
DM	Degree of Methacrylation
DMEM	Dulbecco's Modified Eagle's medium
DMSO	Dimethyl Sulfoxide
DNA	Deoxyribonucleic Acid
DT	Doubling Time
E	Youngs Modulus
ECM	Extra Cellular Matrix
EDTA	Ethylenediaminetetraacetic Acid
FDM	Fused Deposition Modelling
GelMA	Gelatin Methacrylate
HA	Hydroxyapatite
HyA	Hyaluronic Acid
ID	Internal Diameter
MA	Methacrylate Anhydride
MACI	Matrix-induced Autologous Chondrocyte Implantation
MSCs	Mesenchymal Stem Cells
Mn	Average Molecular Weight
MPa	Mega Pascals
MW	Molecular Weight
NCC	Non-Calcified Cartilage
OA	Osteoarthritis
OC	Osteochondral

OD	Outer diameter
Pa-s	Pascals per Second
PBS	Phosphate Buffer Saline
PCL	Polycaprolactone
PD	Population Doublings
PDLLA	Poly-d, l-lactide
PED	Precision Extrusion Deposition
PEG	Polyethylene Glycol
PFA	Paraformaldehyde
PLA	Poly(lactic acid)
PLGA	Poly(lactic-co-glycolic acid
PLLA	poly-l-lactide
RT	Room Temperature
SEM	Scanning Electron Microscopy
SLA	Stereolithography
SLS	Selective laser Sintering
TCP	β-tricalcium phosphate
TE	Tissue Engineering
TIPS	Thermal-Induced Phase Separation
T_m	Melting Temperature
TPU	Polyurethane
w/v	Weight/volume

Chapter 1. Introduction.

1.1. Background.

Osteochondral (OC) defects affect the articular cartilage and subchondral bone (Nooeaid et al., 2012a; Seo et al., 2014a; Sun et al., 2016; Tamaddon et al., 2018; Xiao et al., 2019). The most common cause is chronic osteoarthritis (OA); however, other causes are associated with an injury in the knee or ankle (Brandt et al., 2006; Seo et al., 2014b). Currently, numerous techniques such as microfractures, fixation, mosaicplasty, autologous chondrocyte implantation, and matrix-induced autologous chondrocyte implantation are used to repair the damage of the OC lesion. Although none of these treatments has been able to accomplish a full repair of OC defect, the field of tissue engineering provides a prospective alternative strategy using biomaterials and cells in a scaffold (Huang et al., 2017; Levingstone et al., 2016; Nooeaid et al., 2012b; Zhou et al., 2020).

Several studies have explored different approaches based on a combination of synthetic and natural polymers in order to fulfil the physical and biological properties of scaffolds (Archer et al., 2021; Azimi et al., 2014; Wei & Dai, 2021; Woodruff & Hutmacher, 2010). A widely explored biomaterial is polycaprolactone (PCL), which is used for bone tissue engineering applications due to its notable biodegradability, biocompatibility, non-toxicity, and high mechanical strength (Azimi et al., 2014). Additionally, the low melting point and chemical properties of PCL allow it to be processed by different manufacturing techniques such as extrusion (Beatrice et al., 2021; Viidik et al., 2021), inkjet, electrospinning (Ghasemi-Mobarakeh et al., 2008; Serra, 2014; Tillman et al., 2009), freezing drying (Fereshteh et al., 2016; Gerçek et al., 2008; Li et al., 2020), phase separation (Borsøe et al., 2012.; Munir & Callanan, 2018; Zeinali et al., 2021), among others (Archer et al., 2021; Azimi et al., 2014). A more recent method, solvent-cast 3D printing with peptide-polymer, has been employed to fabricate spatially structured scaffolds for OC tissue engineering. This method can be used to manipulate the spatial presentation of peptides known to promote cartilage and bone growth on PCL materials (Camacho et al., 2019, 2021).

Gelatin Methacyloyl (GelMA) is one of the most common hydrogels used for cartilage tissue engineering. Biocompatibility, cell adhesion, and fast photocuring are beneficial properties providing an advantage of using GelMA compared with most other hydrogels. The mechanical properties of GelMA can be adjusted by using different concentrations and photo-crosslinking time (Pepelanova et al., 2018; Ruiz-Cantu et al., 2020).

Billiet *et al.*. used a novel photoinitiator (VA-086) to study 3D bioprinting of GelMA cell-laden scaffolds. However, some variables that affect extrusion include hydrogel concentration, printing pressure, printing speed, and printing temperature. The printing speed was reported as the key factor that affected the shape and quality of the final scaffold. The printing pressure and needle shape impacted the cell viability (Billiet et al., 2014). Hehong Li *et al.*. investigated the differences between two types of scaffolds, GelMA/PCL and GelMA/PCL/USPIO (Ultrasmall Super Paramagnetic Iron Oxide). Comparing GelMA/PCL with GelMA/PCL/USPIO scaffolds, the GelMA/PCL/USPIO confirmed the biocompatibility and appropriate mechanical properties of 5.03 kPa, which met the requirements before implantation (Li et al., 2020).

Over the last decades, the OC scaffolds for tissue engineering has seen a progression in scaffold design from monophasic to biphasic, triphasic, and multiphasic scaffolds (Jeon et al., 2014). Graded scaffolds have also been developed to create a more sophisticated imitation of the native OC tissue and increase the bond at the bone-cartilage interface(Tamaddon et al., 2016). The interface between the calcified cartilage zone and the subchondral zone is characterised by a change from a hydrogel (cartilage) to a hard tissue (bone). (Loy et al., 2018). The literature has highlighted an issue in the construction of multi-layered scaffolds, likely leading to layer delamination, known as poor interfacial strength (Boushell, 2016; Boushell et al., 2017; Dellaquila et al., 2020; Nukavarapu & Dorcemus, 2013).

The manufacturing process used is critical for the structural strength at the interface (Schek et al., 2004). Liu et al. described a successful approach of producing multi-layered scaffolds by using extrusion-based multi-nozzle 3D printing technology. Different concentrations of bio-ink but using the same materials, 15% GelMA, 20%/3% GelMA/nHA and 30%/3% GelMA/nHA, were reported to improve the integration at the interface(J. Liu et al., 2019a).

Most of the manufacturing methods investigated have limitations including poor reproducibility, irregular shapes, manufacturing difficulties and cost. In contrast, 3D printing stands out as an exception to these limitations due to its ability to enhance reproducibility and facilitate the fabrication of complex shapes. Notably, a scaffold created by 3D printing may be used to create a replica of tissue engineering, in this case, an OC scaffold.

The research presented in this thesis outlines the steps undertaken to design and fabricate an OC scaffold, with a focus on minimising the interface between its components (i.e., the cartilage and bone zones). A 3D Discovery RegenHU extrusion printer was employed for the fabrication of the OC scaffold. Mechanical tests were conducted to ensure that the mechanical properties of the OC scaffold closely matched those of native tissue as determined from the literature. The data collected from these tests help to create a FE modelling of the scaffold, enabling to understand the behaviour and enabling to refined the design. Additionally, cells (fibroblasts) were seeded onto the scaffold to assess their viability and interaction with the scaffold.

1.2. Aim and Hypothesis.

The aim of this thesis was to design and manufacture a multiphasic graded OC scaffold that mimics the bone-cartilage interface with integrated, graded mechanical properties for these two tissues. The core hypothesis was that by fabricating a graded interface using the same materials throughout the scaffold, delamination will be minimised, and the mechanical properties will match those of native tissue. This approach was designed to improve scaffold durability and reliability and support cell integration within the scaffold structure.

The hypotheses of this work were:

1. The use of specific materials and optimized printing parameters will result in a single manufacturing technique of the different OC tissue zones within a single scaffold.

2. Achieving the desired mechanical properties, such as a compressive Youngs modulus similar to a native OC tissue, will be possible through scaffold design and materials choice which will be influenced by the scaffold fabrication technique.

3. Key parameters and assumptions for the construction of an accurate Finite Element Analysis (FEA) model aims to predict the mechanical behaviour of the OC scaffold.

4. Design parameters of different configurations PCL/GelMA scaffolds will promote enhanced cell adhesion and proliferation, fostering a conducive environment for cellular growth within the OC scaffold.

To fulfil the hypotheses the following research question will be addressed:

1. What materials and printing parameters are most suitable for achieving a unified integration between the different OC tissue zones within a single scaffold?

2. What are the specific mechanical properties (e.g., compressive Youngs modulus) required to mimic the native OC tissue, and how can these be achieved in the scaffold?

3. What are the key parameters and assumptions needed to construct an accurate Finite Element Analysis (FEA) model for assessing the mechanical behaviour of the OC scaffold?

4. How do the scaffold designs support cell adhesion and proliferation within the OC scaffold?

These research questions are addressed by investigating the likely contribution of various factors to the successful fabrication of 3D-printed OC scaffolds. The study investigates the optimisation of 3D printing technology, with a priority on incorporating all OC tissue zones while eliminating interfaces between them. Material selection, along with precise printing parameters, is examined to achieve this goal. Additionally, the research scrutinises the manufacturing process to produce the OC scaffolds with mechanical properties that closely resemble those of a native OC tissue, ensuring their ability to withstand relevant mechanical forces. The FEA model is developed to validate the 3D-printed OC scaffold. Furthermore, the OC scaffold needs to encourage cell adhesion and proliferation, thereby creating an environment conducive to tissue regeneration.

The thesis has four objectives:

- Manufacture an OC scaffold utilising 3D printing technology, enabling the simultaneous construction of all OC tissue zones (cartilage: superficial, intermediate, deep, calcified, and bone: subchondral) while eliminating interfaces between them.

- Manufacture an OC scaffold that meets the mechanical properties required for the native OC tissue.

- Develop an FEA model to rigorously assess and validate the mechanical properties of the 3D-printed OC scaffold, providing a computational framework for predictive analysis.

- Design an OC scaffold with properties conducive to cell adhesion and proliferation, fostering an environment where cells can seamlessly integrate and grow within the scaffold, promoting tissue regeneration.

1.3. Paper.

- Ferro-Barbosa, C., Segal, J., Rose, F. “Design, modelling and biofabrication of scaffolds for osteochondral repair”. *Pending Review, 2024*

1.4. Attended Conferences.

- 3rd edition of the Bioengineering and Applied Mechanics Week 2022, by the University of Guanajuato through the Division of Engineering Campus Irapuato-Salamanca and in collaboration with the student chapter BMAS-SOMIB UG DICIS. Online, oral presentation Ferro-Barbosa, C., Segal, J., Rose, F. "Biofabrication of scaffolds for Osteochondral Defect" 23rd November 2022, Salamanca Guanajuato, México.

- Tissue Engineering and Regenerative Medicine International Society (TERMIS) European Chapter Conference 2022. In-person poster presentation Ferro-Barbosa, C., Segal, J., Rose, F. "Design, Modelling & Biofabrication of Osteochondral Defect Repair". Krakow, Poland, 28th June to 1st July 2022.

- Future Investigators of Regenerative Medicine (FIRM) Symposium 2022. In-person oral & poster presentation Ferro-Barbosa, C., Segal, J., Rose, F. "Design, Modelling & Biofabrication of Osteochondral Defect Repair" Middleton Lodge, North Yorkshire, UK. 23rd – 24th May 2022.

- XVIII Symposium of Mexican Studiers and Students in the UK 2021. Online oral presentation Ferro-Barbosa, C., Segal, J., Rose, F. "Design, Modelling, and biofabrication of Osteochondral Scaffolds", Nottingham UK. 1 – 2 July 2021.

- 2nd edition of the Bioengineering and Applied Mechanics Week 2021, by the University of Guanajuato through the Division of Engineering Campus Irapuato-

Salamanca and in collaboration with the student chapter BMAS-SOMIB UG DICIS. Online, oral presentation Ferro-Barbosa, C., Segal, J., Rose, F. "Engineering as an essential part of the health sector" 12th November 2021, Salamanca Guanajuato, México.

- 10th Symposium of CONACyT Scholars in Europe 2021 by MUFRAMEX. Online oral presentation Ferro-Barbosa, C., Segal, J., Rose, F. "Biofabrication of Osteochondral Defect Repair". 7^{th}-9^{th} December 2021.

- Women in Engineering 2020 is an annual event by the University of Guanajuato through the Division of Engineering Campus Irapuato-Salamanca and in collaboration with the student chapter ASME-SOMIM UG DICIS. Online, oral presentation Ferro-Barbosa, C., Segal, J., Rose, F. "Engineering as an essential part of the health sector" 27th November 2020, Salamanca Guanajuato, México.

1.5. Outline of Thesis.

This thesis consists of 8 chapters related to addressing the above research questions. **Chapter 1** serves as an introduction to the overarching themes of this thesis. It begins by providing an overview of the general topic and research context. The aims, objectives, and central research questions of this study are clearly articulated, setting the stage for the subsequent chapters' detailed exploration. **Chapter 2** is a comprehensive review of the relevant literature that informs this research. It encompasses an examination of the OC tissue, various manufacturing techniques employed in the field, existing OC scaffold designs, and the critical mechanical properties associated with these scaffolds. This chapter offers a vital foundation upon which the subsequent chapters build**. Chapter 3** describes the materials and methodologies employed throughout this research are detailed. It provides an in-depth exploration of the techniques used for material characterisation, 3D printing via extrusion-based methods for OC scaffold fabrication, the mechanical testing procedures applied to assess scaffold properties, and the methodologies used for cell viability assessments—a crucial aspect of tissue engineering. **Chapter 4** is dedicated to the thorough characterisation of the materials at the core of this research: PCL and GelMA. By comprehensively examining the properties and behaviours of these materials, the groundwork is laid for the subsequent phases of the study involving 3D co-printing of the OC scaffolds. **Chapter 5** describes the 3D co-printing of OC scaffolds and the subsequent evaluation of their

mechanical properties. It offers insights into the intricacies of the 3D printing process, including the characterisation of mechanical properties across various scaffold designs. Moreover, this chapter studies the design elements that contribute to interlayer mechanical properties, a key factor in optimising the OC scaffold performance. **Chapter 6** introduces the FEA approach employed to validate the structural designs of the OC scaffolds. This modelling technique was employed to inform the required structural integrity and mechanical properties of the scaffold. It serves as a critical step in the development of the OC scaffolds that closely mimic native tissue mechanical properties. **Chapter 7** focuses on the assessment of cell viability within the OC scaffolds. It explores the scaffold's ability to support cell adherence and proliferation, crucial factors in successful tissue engineering endeavours. This chapter provides insights into the potential for these scaffolds to serve as platforms for cellular growth and tissue regeneration. **Chapter 8** discusses a comprehensive summary of the key findings and their implications. It highlights the main conclusions derived from the study, emphasising the contributions made to the field. Additionally, this chapter acknowledges any limitations encountered during the research, providing valuable insights for future work in this area.

Chapter 2. Literature Review.

2.1. OC Tissue.

OC defects occur in articulating joint disease frequently presenting in the knee and ankle (*Osteochondritis Dissecans - OrthoInfo - AAOS*, n.d.). OC defects involve damage to both the articular cartilage as well as the underlying subchondral bone. The cause is often related to a trauma correlated by an injury or a long-term chronic disease such as osteoarthritis (OA) (Brandt et al., 2006; Seo et al., 2014b).

Worldwide, OA is one of the most common chronic diseases, affecting 15% of the global population over the age of 30 (The Lancet, 2023.). The Global RA network suggests that more than 350 million people are currently suffering from OA, and it is expected that this number will increase due to the rise in life expectancy and the escalating levels of obesity (Csaki et al., 2008; Global RA Network» About Arthritis and RA, n.d.; M. Y. Hu & Nukavarapu, 2019; Kingsbury et al., 2014.; Y. Zhang & Jordan, 2010). In some cases, if the OA is left untreated, it can damage not only the articular cartilage tissue but also the subchondral bone, ligaments, periarticular muscles and sometimes the meniscus (Brandt et al., 2006).

Figure 2.1 shows the structure of the OC tissue, which consists of four distinct cartilage zones (superficial, intermediate, deep and calcified) and the subchondral zone. All the zones have a different composition of cells and extracellular matrix (ECM) (Yousefi et al., 2015a).

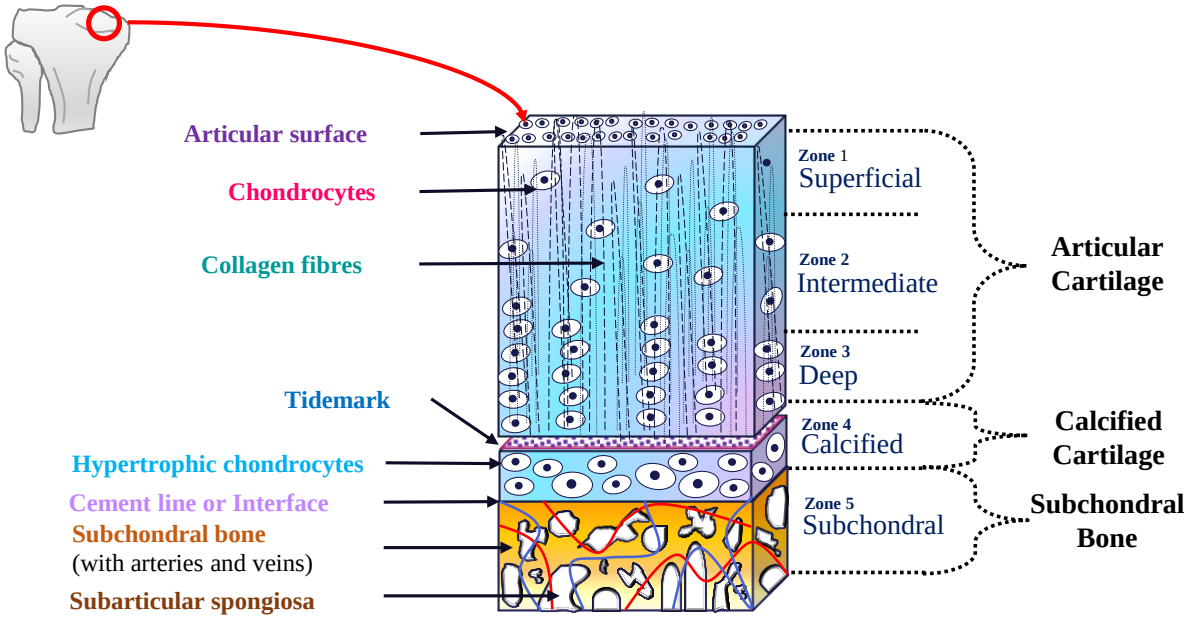


Figure 2.1 OC tissue representation (re-drawn from Imhof *et al.*.(Imhof et al., 1999)).

The superficial zone is characterised by non-calcified (hyaline) cartilage, comprising 10%-20% of the articular cartilage. This zone's composition is established by the parallel orientation of the collagen fibres to the articular surface and the presence of small and flattened chondrocytes. Another feature is a lower proteoglycan concentration compared with other zones, with higher fibronectin and water concentrations. In this zone, the cellular density of articular cartilage is the highest and slowly diminishes through to the following articular zones, in contrast with proteoglycan and cell volume, which increase from the superficial to the deep zone. All these characteristics contribute to the development of properties such as high tensile stiffness and strength, aiding in resistance to forces generated on the surface (Daly et al., 2017a; M.-Y. Hu & Nukavarapu, 2019; W. D. Lee et al., 2015).

The intermediate zone is situated between the two articular cartilage zones, providing an anatomic and functional bridge between them. This is the thickest zone, with the total cartilage volume comprising 40% to 60%. In this section, the collagen fibres are thick, less organised and are typically oblique to the articular surface. In contrast to the superficial zone, chondrocyte morphology is more rounded, with higher proteoglycan content and a lower concentration of water and collagen. One of the properties of this tissue is high compressibility, serving the primary purpose of a cushioning effect for impacts (Daly et al., 2017a; M.-Y. Hu & Nukavarapu, 2019; W. D. Lee et al., 2015).

The deep zone represents approximately 30% of the articular cartilage volume, characterised by the collagen fibres and chondrocytes oriented in vertical columns perpendicular to the articular cartilage surface. This zone contains the highest concentration of proteoglycan and the lowest concentration of water and collagen. Moreover, in this area, approximately a third of cellular density is established compared to the superficial zone. The properties of this tissue zone are related to greater stiffness and compressive strength, in contrast with the calcified cartilage (Daly et al., 2017a; M.-Y. Hu & Nukavarapu, 2019; W. D. Lee et al., 2015).

The calcified zone, as the name implies, is composed of calcified cartilage, and the structure of this zone begins with the collagen fibres transversing into the tidemark, representing a transition from the deep zone to the calcified cartilage zone. Additionally, a smaller layer contains radially oriented collagen fibres embedded in a calcified matrix. Moreover, chondrocytes in this calcified zone typically express hypertrophic phenotype similar to the growth plate, providing a buffer with intermediate mechanical properties between those of the non-calcified cartilage and the underlying subchondral bone. With age, the number of tidemarks in this zone increases (Kauppinen et al., 2019; Kosik-Kozioł et al., 2019; W. D. Lee et al., 2015).

The interface is one of the most essential components in the OC tissue structure between the cartilage and subchondral zone, representing the connection between them. The first interface in the OC defect goes from the deep zone, where the collagen fibres are oriented vertically, to a calcified zone across a curvy tidemark. This description signifies a band between mineralised and no mineralised cartilage, although these fibres do not penetrate the subchondral zone (Lyons et al., 2005). The function of these fibres is to absorb and distribute the pressure carried by the weight-bearing subchondral zone (Tamaddon et al., 2018b). Another interface in this tissue is the cement line, acting as a barrier between the calcified zone and the subchondral zone, with the thickness of the line varying depending on the joint (Bayrak & Ozcan, 2016; Di Luca et al., 2015; Dormer et al., 2012).

The subchondral zone is stiffer and has a higher compressive strength due to its composition and structure compared to the cartilage zones. The cartilage transmits loads into the underlying subchondral bone, making it more compressible. The structure is composed of two parts: the subchondral plate separating the articular cartilage and the marrow cavity, and the subarticular spongia supporting the trabecula and the bone components, characterised by numerous holes

with blood vessels supplying nutrients and oxygen(Duncan et al., 1987; Imhof et al., 1999; Madry et al., 2010a).

2.2. OC Defect.

Currently, there are numerous treatments available for an OC defect, which depend on factors such as the depth, size, and extent of damage to the OC tissue. The OC defect can be categorised into three stages: partial-thickness defect, full-thickness defect, and OC defect, depending on the depth of the damaged tissue (refer to **Figure 2.2**). Given their restricted ability to self-repair, the majority of profound OC lesions lead to the manifestation of severe pain, joint deformity, and impaired joint mobility (Ai et al., 2021; Niu et al., 2023; Schaefer et al., 2002; W. Wei & Dai, 2021b).

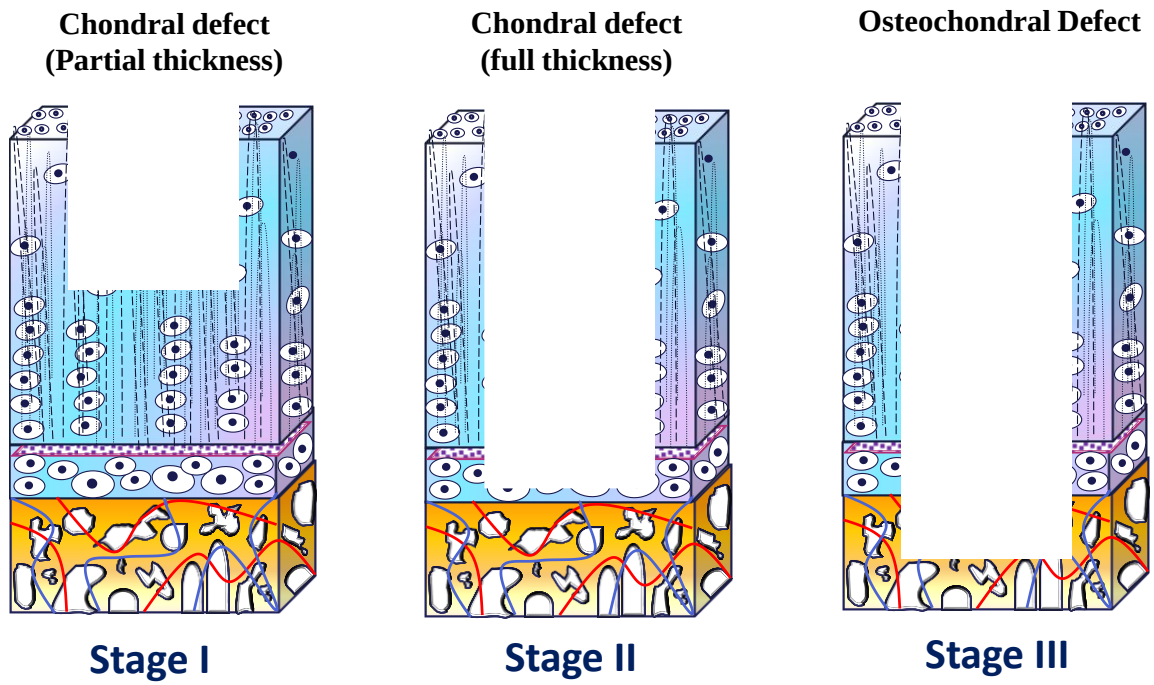


Figure 2.2 Representative image of the stages of an OC defect: Stage I – Chondral defect with partial thickness, Stage II – Chondral defect with full thickness, and Stage III–OC defect with cartilage and bone affected (re-drawn from Nukavarapu et al. (Nukavarapu & Dorcemus, 2013b)).

In the treatment of the OC defects, the approach varies depending on the stage of the condition. In stage one, the common treatment involves nonoperative methods, including chondroprotective pharmacotherapy, nonsteroidal anti-inflammatory medication, and physiotherapy. This type of treatment is preventive and may help reduce further damage.

However, when the defect progresses to stages two and three, it is recommended that a surgical approach be considered, which may include procedures such as microfractures, fixation, mosaicplasty, autologous chondrocyte implantation, and matrix-induced autologous chondrocyte implantation. The choice of the appropriate treatment method depends on the size and depth of the lesion. Nevertheless, despite these interventions, none of the treatments are able to achieve a full repair of an OC defect with hyaline cartilage similar to the native tissue.

Clinical treatment methods can be categorised based on the level of repair they provide to the OC defect site, as represented in **Figure 2.3**. Palliative treatment methods generally do not replace the defective cartilage and bone, while reparative treatment methods aim to replace the defect area with biological material. Nevertheless, due to the unique nature of cartilage, bone, and the cartilage-bone interface, the ideal repair method is a restorative treatment that helps reconstruct the natural tissue(Brittberg et al., 1994; Cong et al., 2023; Leng et al., 2012; Madry et al., 2010b; Richter et al., 2016; Sarin et al., 2018; J. Sun et al., 2016b; Toom et al., 2023; Upmeier et al., 2007).

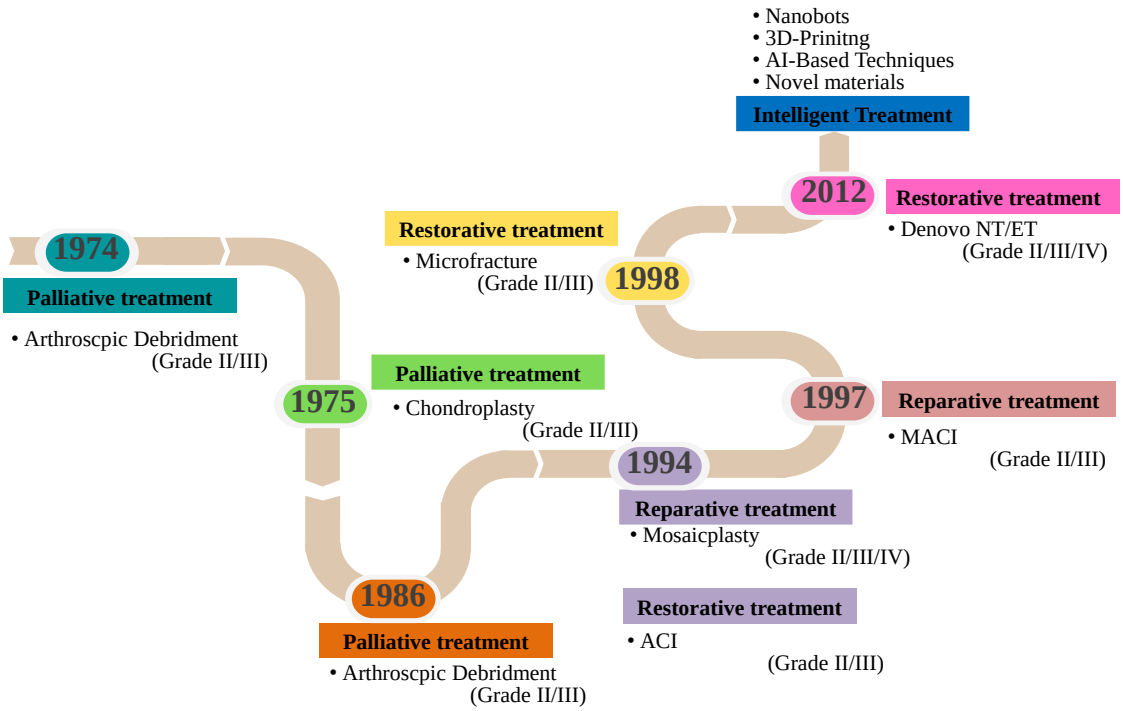


Figure 2.3 Clinical methods for the OC defects treatments (re-draw from Deng et al. 2019 Deng et al., 2019).

Therefore, there is a significant need for suitable surgical treatments and advancements in technology, such as grafting and tissue engineering. Presently, the typical methods for addressing the OC injuries predominantly involve surgical procedures, which vary based on the size of the defect, as outlined in **Table 2.1.**

Table 2.1 Surgical methods for OC repair based on defect dimensions (Howell et al.., 2021; Logli et al.., 2019; K. C. Wang et al.., 2016).

Surgical Methods	Description	Issue	Defect dimension
Microfracture	The arthroscopic technique stimulates the bone marrow through a bone perforation.	• Although short-term results appear promising, over time tend to deteriorate.	Smaller than 2 cm^2
Mosaicplasty Autologous Chondrocyte Implantation (ACI)	One or many OC cylinders are removed from a non-weight bearing area to the OC defect area	• Two stages of surgery • Limited by the amount of donor tissue. • The viability of the chondrocytes from a non-weight bearing is transferred to a weight area.	Between 2 cm^2 and 4 cm^2
Matrix-induced Autologous Chondrocyte Implantation (MACI)	A matrix is used to cultivate the chondrocytes.	• Two stages of surgery • High Cost • Hypertrophy	Larger than 2 cm^2 and smaller than 12 cm^2

All the clinical methods mentioned in **Table 2.1**. are not suitable for long-term effectiveness. Microfracture, ACI, and MACI often result in the formation of fibrocartilage instead of healthy articular cartilage, which can adversely affect the patient's joint function (Makris et al., 2015). Instead, today, numerous alternative strategies established in advancements in regenerative medicine and tissue engineering have been suggested and put into practice for repairing and regenerating the OC defects.

2.3. Tissue Engineering Approaches.

2.3.1. Tissue Engineering Approaches for the OC Defect Repair.

Tissue engineering OC scaffolds are reported in the literature as a promising new method to regenerate damaged tissue utilising scaffolds and cells (Nooeaid et al., 2012b). These scaffolds aim to mimic the physiological properties and structure of both tissues, cartilage and bone. Literature shows different approaches to manufacturing the OC scaffolds, which are usually classified as monophasic, bi-phasic, tri-phasic or multiphasic scaffolds (Castro, Patel et al., 2015; Deng et al., 2018a; M. Liu et al., 2013; Shimomura et al., 2014; Yousefi et al., 2015b; P. Yu et al., 2017). Due to the complexity of the OC tissue, monophasic scaffolds cannot mimic the native structure of OC tissue. For this reason, more than one material or layer with different properties is required for the scaffold to be manufactured (Brittberg et al., 2016; Gille et al., 2013). Several authors show that the benefits of using bi-phasic, tri-phasic and multiphasic approaches help to mimic cartilage and bone tissue. This is done by separately optimising the different components of a scaffold with the addition of osteogenic and chondrogenic growth factors before in vivo implantation (Re'Em et al., 2012; Woodfield et al., 2002).

OC scaffolds feature a distinctive gradient structure that incorporates essential attributes, including porosity, biodegradability, biocompatibility, mechanical characteristics, and the ability to accommodate various growth factors or cells (Ai et al., 2021). One of the initial methods for manufacturing an OC scaffold was the monophasic approach, where the scaffold is produced using a uniform material throughout its graded structure, this can entail the use of a single material or a combination of several materials merged into a unified composite. Numerous studies have utilised common materials such as poly(lactic-co-glycolic acid) and PCL (Im & Lee, 2010; Y. Cao et al., 2021a; Fares et al., 2018; H.-W. Kim et al., 2006; Kumai et al., 2019; Suo et al., 2021). These materials enable the scaffold to support the attachment and proliferation of chondrocytes and bone cells. Nevertheless, their mechanical properties are insufficient for effectively replacing damaged OC tissue.

Another technique employed is the biphasic scaffold, inspired by the mosaicplasty technique, which seeks to replicate both the cartilage and bone zones within a single scaffold, encompassing gradient compositions and mechanical characteristics(Lopa & Madry, 2014). Several authors have demonstrated success in preclinical animal studies using these types of scaffolds. However, biphasic scaffolds do not fully emulate all the gradients present in the

natural OC tissue (Bernhardt et al., 2018; Getgood et al., 2012; X. Li et al., 2015; X. Lin et al., 2018; Pérez-Silos et al., 2019; H. Zhou et al., 2020b).

Triphasic and multiphasic scaffolds incorporate the articular cartilage, calcified cartilage, and subchondral bone, offering superior mechanical properties and improved in vivo regeneration outcomes compared to biphasic and monophasic counterparts(Nooeaid et al., 2012c, 2014; B. Zhang, Huang, & Narayan, 2020). However, the individual manufacture and subsequent combination of triphasic and multiphasic components through techniques such as suturing, glueing, and press-fitting have given rise to challenges associated with layer delamination during mechanical testing (Nooeaid et al., 2012c, 2014; B. Zhang, Huang, & Narayan, 2020).

2.4. 3D printing in Tissue Engineering.

2.4.1. Additive Manufacturing Techniques.

Manufacturing the OC scaffolds have been produced using many techniques, as illustrated in **Figure 2.4,** depicting commonly utilised methods such as freeze dryer, thermal-induced phase separation (TIPS), Stereolithography (SLA), Selective laser sintering (SLS), Inkjet, Digital Light Procession (DLP), Electrospinning, Fused Deposition Modelling (FDM) and Extrusion. Numerous authors have extensively discussed these techniques. (Daly et al., 2017.; X. Du, 2018; Tappa & Jammalamadaka, 2018; Vijayavenkataraman, Yan, et al., 2018; B. Zhang et al., 2019). The authors highlighted the precision of the methods and emphasised the capabilities for reproducing the scaffold. Each method exhibits varying levels of versatility, offering different opportunities to create either more or less complex structures.(Deng et al., 2018b; Kilian et al., 2020; Kosik-Kozioł et al., 2020a; Vijayavenkataraman, Zhang, et al., 2018)**. Table 2.2,** illustrates a comprehensive analysis by various authors, highlighting the benefits and drawbacks associated with different 3D printing techniques employed in scaffold development.

These techniques encompass key factors such as pressure, temperature, and speed, all of which significantly impact the internal and external geometry of the scaffold. Despite reported advancements in the OC scaffolds within the literature, the successful integration of the cartilage and bone phases remains elusive. (Haaparanta, 2016; Levingstone et al., 2014a; Levingstone, Thompson, et al., 2016b; Marras-Marquez et al., 2014; Re'Em et al., 2012; Zhai et al., 2018).

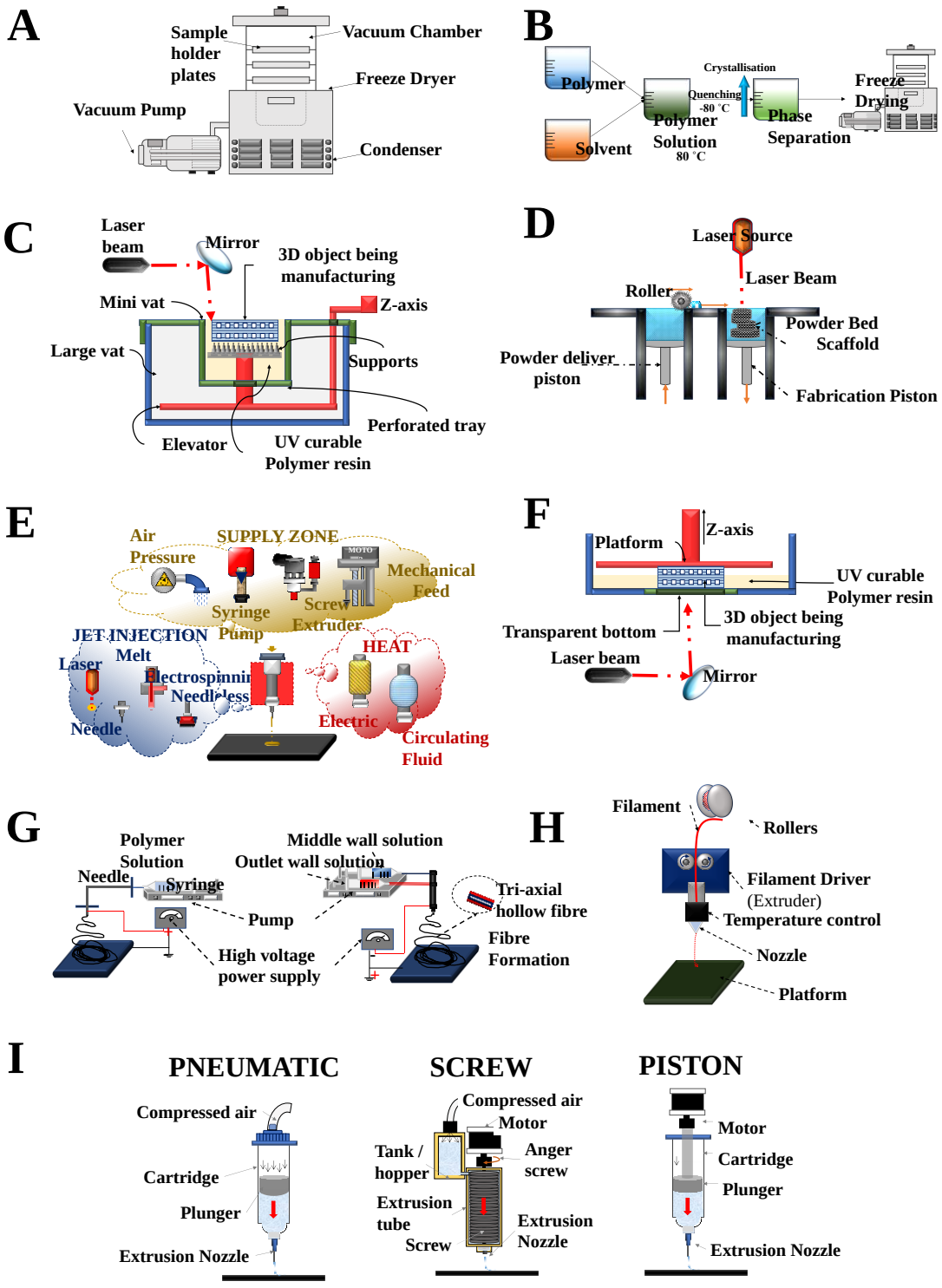


Figure 2.4 Schematics of representative 3D printing techniques: A) Freeze Dryer, B) , thermal-induced phase separation (TIPS), C) Stereolithography (SLA), D) Selective laser sintering (SLS), E) Inkjet, F) Digital light procession (DLP), G) Electrospinning, H) Fused Deposition Modelling (FDM) and I)Extrusion. (re-drawn from (Hussain et al., 2022; Isaac et al., 2021; S. Park et al., 2022; W. S. Park et al., 1998; Sekmen et al., 2022; Taskin, 2020; Zeinali et al., 2021)

SLA stands as a versatile 3D printing technique for designing structures. Recent advancements in more cell-friendly blue light and materials, alongside enhanced resolution and geometric capabilities, make SLA a valuable tool in tissue engineering, including when cells are to be included in the printing process (H. Lin et al., 2013; K. Zhang et al., 2015).

Different approaches employing SLA in the OC scaffold manufacturing have been explored. Castro et al. developed a nHA/PEG-Da biomimetic nanocomposite scaffold, demonstrating improved mesenchymal stem cell adhesion, proliferation, and OC differentiation (Castro, O'Brien, et al., 2015). Similarly, Zhou et al. focused on designing a GelMA-PEGDA-nHA TPNPs (TGFβ1 encapsulated in PLGA NPs, nanoparticles) biphasic structure using 3D SLA printing, promoting osteogenic and chondrogenic differentiation of human bone marrow mesenchymal stem cells, along with enhanced gene expression associated with both osteogenesis and chondrogenesis after 2 weeks in culture (X. Zhou et al., 2019).

DLP, another technique used for tissue engineering, closely resembles SLA, with the distinction of using a DLP projector instead of UV light to project the entire cross-sectional layer of the 3D structure (Pan et al., 2012). Schoonraad et al. demonstrated scaffold control over modulus and well-integrated multilayered structures through the use of a single hydrogel-based resin despite facing issues such as pillar buckling under strain. The arrangement of vertical pillar structures fulfilled important criteria in terms of achieving high porosity and regulating modulus. Although the design had deficiencies that caused the pillars to buckle when subjected to strain, it did not result in complete structural failure. (Schoonraad et al., 2021).

Studies conducted by Lin et al., Skoog et al.,Valentinčič et al.,and K. Zhang et al. have highlighted the general advantages and disadvantages of the DLP system, mirroring those of the SLA method. Notably, the main advantages of DLP over SLA in scaffold fabrication include lower system costs due to the absence of a laser and higher build speeds resulting from the exposure of one layer at a time (H. Lin et al., 2013; Skoog et al., 2014; Valentinčič et al., 2017; K. Zhang et al., 2015). However, Yantan Tang et al. observed that printed parts are susceptible to deformation due to inhomogeneous curing with projection-based SLA (DLP) with lower light intensity, resulting in less polymerisation(Tang et al., 2005).

Another manufacturing technique for the OC scaffolds is SLS, a laser-assisted printing technology that selectively sinters powder particles with a high-intensity laser, producing 3D

objects layer by layer (Fina et al., 2018). Successfully fabricated a simple integrated OC scaffold using PCL microspheres (PCL50 and PCL150) without loading cells and growth factors, obtaining excellent mechanical properties with the SLS technique (X. Gu et al., 2022a). Likewise, Yingying Du et al. demonstrated that multilayer scaffolds with highly interconnected porosity and desirable mechanical properties could induce articular cartilage formation by accelerating early subchondral bone regeneration (Y. Du et al., 2017). One of the notable drawbacks of both SLS and SLA equipment is their high cost (Eltom et al., 2019; Valentinčič et al., 2017).

Electrospinning utilises various principles such as electrospray, multi-jet, uni-axial, co-axial, tri-axial, emulsion, melt, blending, and surface immobilisation. Electrospun materials are appealing for the OC scaffold development due to their biomimetic properties, including various fibre diameters, high porosity, variable pore sizes, and adaptability into different shapes and sizes. However, the literature suggests that this technique lacks the precision of some other methods, leading to challenges in accurately reproducing the same scaffold in addition to a lack in mechanical properties of the resultant materials (X. Liu et al., 2014; Serra, 2014; Subramanian et al., 2005; S. Zhang et al., 2009; Y. Z. Zhang et al., 2008).

FDM is employed for manufacturing porous scaffolds for tissue engineering. Several authors have highlighted a key advantage of this process in terms of mechanical properties, as the resulting scaffolds exhibit notable strength within the range of articular cartilage and calcified cartilage (Cano-Vicent et al., 2021; Ceretti et al., 2017; Esposito Corcione et al., 2019; Winarso et al., 2022; Zein et al., 2002)

However, the high processing temperatures associated with FDM prevent the incorporation of cells during the printing process, which limits its application in bioprinting. Despite this, when scaffolds produced using FDM were seeded with cells and cultured, the central sections of the scaffold exhibited various lay-down patterns, altering the angles of the lines used to process PEG-PCL-P(DL)LA scaffolds. This resulted in greater cell viability compared to control samples. This difference has been attributed to the more effective diffusion of nutrients and oxygen within the oriented pores of the FDM scaffold (Swieszkowski et al., 2007a). Additionally, Bruyas et al. fabricated an OC scaffold using FDM, with one phase consisting of PCL/β-TCP for the bone region and the other featuring PCL-fibrin for the cartilage region (Bruyas et al., 2018). Gong et al. developed a bi-layer scaffold, the upper layer consists of an interleukin-4 (IL-4)-loaded radially oriented GelMA scaffold, printed with DLP. Meanwhile,

the lower layer features a porous PCL-HA scaffold, printed using FDM., which suggests that scaffold structures printed with DLP enable higher infiltration and migration of surrounding cells to the hydrogel compared to the FDM technique (Gong et al., 2020).

The inkjet technique is another method used to manufacture OC scaffolds, involving the precise deposition of specific liquid volumes at exact locations on a substrate, achieved through thermal or acoustic methods ejecting liquid droplets (Cui et al., 2014; Roth et al., 2004; Xu et al., 2009, 2012). Inzana et al. have designed solid elliptical cylinders (1.2 x 2 x 3 mm) calcium phosphate-collagen scaffolds with notable mechanical strength and cell viability benefits. However, a decrease in the scaffold's strength has been attributed to the material's degradability (Inzana et al., 2014).

Extrusion-based manufacturing has been most widely reported for constructing OC scaffolds. This method operates by depositing bioink through a continuous nozzle via physical force and pneumatic pressure, effectively emulating OC structures to enhance tissue (S. Chen et al., 2023; F. Wang et al., 2022; Xu et al., 2013). It not only facilitates the development of highly personalised 3D scaffolds but also ensures precision in the manufacturing process. Studies have emphasised the ability of extrusion-based printing to closely replicate the mechanical and biological properties of subchondral bone, underscoring its potential in the OC tissue engineering. Nonetheless, it is imperative to acknowledge the limitations posed by the size of the nozzle and the printing speed, as they can restrict the resolution achievable through this method (S. Chen et al., 2023; Geng et al., 2019; P. Wang et al., 2023)

Liu et al. have demonstrated the regeneration of neo-tissue in the defect with an abundant of collagen type II in vivo using pneumatic extrusion with three different bio-inks, resulting in a tri-layered scaffold for the OC defect (J. Liu et al., 2019b). In another study, a scaffold produced using the extrusion technique with cell-laden GelMA hydrogels, exhibiting cell proliferation and cartilage ECM secretion (Ruiz-Cantu et al., 2020b). Similarly, Susan Critchley et al. have created an orthogonal biphasic scaffold (12 mm diameter and 6mm height, with a spacing of 2mm) through extrusion, using PCL and PLA, with PCL serving as a reinforcing network for both the osseous and endochondral structures, were evaluated in vitro and in vivo, even was found the regeneration of hyaline, implants failure in vivo and improvements in the designs are required (Critchley et al., 2020).

Table 2.2 Summary of different 3D printing technologies for tissue engineering repair and their bio-inks.

3D printing technique	Advantages	Disadvantages	Bioink requirements	Bioink examples	References
Stereolithography (SLA)	High resolution and precision. Smooth surface finish. Suitable for creating complex geometries with distinct regions.	Limited choice of biocompatible resins. Additional post-processing steps for complete curing.	Photopolymerisable resins that are biocompatible. Bioinks should be suitable for UV curing.	PEGDA (polyethylene glycol diacrylate) PCL GelMA	(Castro, O'Brien, et al., 2015; K. W. Lee et al., 2007; H. Lin et al., 2013; Skoog et al., 2014; Tang et al., 2005; K. Zhang et al., 2015)
Selective Laser Sintering (SLS)	High precision and complex structure capabilities. Can use a variety of biocompatible materials. Suitable for creating porous structures	Limited resolution for small features. Higher cost compared to some other techniques.	A laser can sinter powdered biocompatible materials, such as ceramics or polymers.	Hydroxyapatite (HA) Poly(lactic-co-glycolic acid) (PLGA)	(Y. Du et al., 2017; F. Liu et al., 2018)

Inkjet 3D Printing	Precise placement of cells and materials. Ability to create complex, multi-material structures. Potential for creating functional tissues with living cells.	Limited in terms of material choices. Challenges with maintaining cell viability during the printing process.	Biocompatible hydrogels or bio-inks that support cell viability and maintain the desired structural integrity.	Alginate GelMA	(Cui et al., 2014; Roth et al., 2004; Xu et al., 2009)
Digital Light Processing (DLP):	High-speed printing due to simultaneous curing of entire layers. Excellent resolution and surface finish. High resolution Mild condition for cells (85-95%) Fast printing speed Suitable for creating detailed	Limited material options compared to other techniques. Post-processing may be required to remove unreacted resin. Force in the platform and a separate for the printed Need of a cytotoxicity of photoinitiator surface	Photopolymer resins that are biocompatible and can be cured by a digital light source.	GelMA PEGDA Silk-fibrin	(Schoonraad et al., 2021; Valentinčič et al., 2017, H. Lin et al., 2013; Skoog et al., 2014; Valentinčič et al., 2017; K. Zhang et al., 2015, Tang et al., 2005)

	and intricate structures				
Electrospinning	High surface area-to-volume ratio, mimicking natural extracellular matrix. Suitable for creating nanofiber scaffolds with fine control over fibre diameter. Versatile in terms of materials, including biocompatible polymers and natural materials.	Typically produces 2D or randomly oriented fibres, which may not be suitable for all applications. Additional processing to create 3D structures. While electrospinning does not use traditional bio-inks, as seen in extrusion-based or inkjet-based bioprinting, it is a valuable technique for creating nanofiber scaffolds that can support cell adhesion and	Electrospinning does not involve the use of traditional bioinks. Instead, it uses polymer solutions or melts that are electrospuned into nanofibers. These solutions can include biocompatible polymers or blends.	PCL Poly(lactic-co-glycolic acid) (PLGA) Collagen	(Buzgo et al., 2018; H.-W. Kim et al., 2006; Reneker DH, Yarin AL, Fong H, 2000)

		tissue regeneration. It is often used in combination with other 3D printing or scaffold fabrication methods to create hybrid scaffolds with both nanofiber and macroscopic structures.			
FDM (Fused Deposition Modelling)	Relatively low cost and widely accessible. Suitable for a range of thermoplastic materials. Highly porous scaffolds. Suitable for continuous filament deposition.	Limited in achieving high-resolution features compared to some other techniques. Post-printing processing to achieve desired scaffold properties.	Thermoplastic materials are for the bone region, and biocompatible hydrogels or polymers are for the cartilage region. Bioinks should be extrudable at the printing temperature. Filaments or strands made from biocompatible materials that can be deposited layer by layer.	PCL GelMA HyA-based Polyurethane (TPU)	(Cano-Vicent et al., 2021; Winarso et al., 2022; Zein et al., 2002)

	Variety of materials, including biocompatible polymers and ceramics.				
Extrusion-Based 3D Printing	Versatile and suitable for a wide range of materials, including bioinks. Affordable and accessible technology. Can create multi-material and multi-cellular scaffolds. Improved shape fidelity Support cell-laden bio-inks Moderate-resolution	Limitations in achieving high-resolution structures. Prolonged printing times for complex scaffolds. Cell viability of 40-80% Expensive cost Slow printing speed Challenges with maintaining cell viability during extended printing.	Bio-inks are specifically formulated for extrusion-based printing, typically hydrogels or polymer-based materials that are shear-thinning to facilitate extrusion while maintaining structural integrity post-printing. These bioinks should also support cell encapsulation and promote tissue-specific differentiation.	GelMA Alginate Hyaluronic (HyA). Collagen	(Askari et al., 2021; Bittner et al., 2019a; W. Liu et al., 2017, 2018a; Pepelanova et al., 2018b; Yan et al., 2022)

2.5. Biomaterials for 3D Printing OC Scaffolds.

The biomaterials used in tissue engineering scaffolds can be classified as natural and synthetic polymers, as represented on **Table 2.3** (Yousefi et al., 2015c). Synthetic polymers are the most used due to their low cost of processing and better functionality than natural polymers. However, they have some disadvantages, such as the potential for causing an immune response (G. Chen et al., 2006; Grigore, 2017a). Studies have suggested that a combination of synthetic and natural polymers is a good strategy for biomimicking the complex OC tissue (Daly et al., 2017a; Raeisdasteh Hokmabad et al., 2017; X. Wang et al., 2004).

Bi-phasic OC scaffolds have been developed by Shen *et al.*. using a combination of natural and synthetic materials; human fibrinogen, bovine thrombin and PCL microspheres were used to prepare the fibrin scaffold, for the wollastonite scaffold 8% MgSiO3 (CS-Mg8) were used. The study showed that after 18 weeks of implantation, neo-cartilage was found, good integrity with the surrounding tissue, and a tidemark was identified when bone marrow mesenchymal stem cells (BMSCs) were preloaded (Shen et al., 2018a).

Levingston *et al.* developed a tri-phasic OC scaffold, suggesting that the material used in developing the scaffold has shown considerable regeneration and repair of the tissue. The first phase (cartilage section) was made with collagen I, collagen II and hyaluronic acid (HyA). For the second phase (intermediate zone), the materials used were collagen I, collagen II and Hydroxyapatite (HA). Finally, the third phase (subchondral zone) was fabricated using collagen I and HA. This iterative layering technique enabled the fabrication of scaffolds with independent characteristics of porosity, pore size and mechanical properties in each layer of the scaffold while manufacturing. These characteristics permitted cellular infiltration and flow of nutrients and stimulated the OC tissue regeneration (Levingstone et al., 2014a).

The interface between the chondral and subchondral bone represents functionality in the long term because of their essential integration. Wang *et al.*. study compared three biodegradable scaffolds; the first one was made with poly-l-lactide (PLLA]), the second one used poly-d, l-lactide (PDLLA) and the last one utilised collagen-hydroxyapatite (Col-HA). The scaffolds were cultured for 15 weeks before analysing them. A similar structure of the three types was shown in a macroscopic view. Although deformations and reductions of cell in-growth were

observed in PLLA scaffolds, in PDLL and Col-HA scaffolds, an increase in cell infiltration and the formation of a group of cells was seen. However, both types of scaffolds revealed a collapse at week 11, and at week 15. Half of the PDLLA scaffolds were pore collapsed with deformations in the structure, and the Col-HA construct shows cell clusters more distributed than the PDLLA scaffolds (X. Wang et al., 2004). Likewise, several studies have shown that the interface at different sections of the OC scaffolds is extremely complex and important in transitioning mechanical load between unrelated tissues.(Dormer et al., 2012; Jia et al., 2018a; Lausch et al., 2018a; Sahoo et al., 2011)

Table 2.3 Characteristics of biomaterials used for the fabrication of OC scaffolds and their advantages and disadvantages (Low, ** Medium, ***High).*

Materials	Bio-compatibility	Mechanical properties	Highlight		Ref
			Advantage	Disadvantage	
Alginate	**	*	Good water retention. Ease of gelation Versatility in applications	Limited mechanical strength Potential for ion release	(Carla et al., 2011; Kolambkar et al., 2011; Kosik-Kozioł et al., 2017; K. Y. Lee & Mooney, 2012; Reyes et al., 2012)
Chitosan	***	**	Good mechanical strength Biodegradable Mucoadhesive properties.	Limited control over degradation rate. Cytotoxicity if not properly purified.	(Dutta, 2015; Felfel et al., 2019; Korpayev et al., 2020; Pitrolino et al., 2022; Varoni et al., 2018)
Collagen	*******	*	Excellent biocompatibility. Promotes cell adhesion and tissue regeneration. Widely used in tissue engineering.	Weak mechanical properties. Rapid degradation, Potential for immunogenic responses.	(Lausch et al., 2018b; Levingstone, Ramesh, et al., 2016; O'Brien et

Collagen-Based	***	*	Collagen is a major component of natural bone, making collagen-based scaffolds biocompatible. These scaffolds can support cell attachment and bone matrix formation.	Collagen scaffolds may have weaker mechanical properties and faster degradation rates, necessitating reinforcement with other materials.	al., 2008; Parisi et al., 2020; H. Zhou et al., 2020b)
GelMA	***	*	Precise control over gel properties. Suitable for cell encapsulation and tissue engineering. Controlling mechanical properties.	Batch-to-batch variability in properties and photoinitiator used in the polymerisation process can potentially be cytotoxic.	(Ghorbani et al., 2020a; J. Liu et al., 2019b)
Hyaluronic Acid (HyA)	***	*	Excellent biocompatibility, ability to retain water, and can be easily modified for drug delivery and tissue engineering.	Limited mechanical strength and rapid degradation in vivo.	(Fischer et al., 2012; Kogan et al., 2007; Matsiko et al., 2012)
Hydroxyapatite (HA)	**	***	Hydroxyapatite is a biocompatible ceramic often combined with polymers to improve bone scaffold biocompatibility. HA-based composites can mimic the mineral component of natural bone.	HA alone is fragile, so combining it with polymers is necessary to improve scaffold flexibility and toughness.	(Khanarian et al., 2012; Pitrolino et al., 2022; Suo et al., 2021a)

Polycaprolactone (PCL)	*	***	PCL is a biocompatible polymer with good mechanical properties. It has been used in cartilage scaffolds due to its slow degradation rate, providing long-term support for cartilage tissue regeneration. PCL's slow degradation rate and mechanical strength make it suitable for bone scaffolds. It provides long-term structural support during bone regeneration.	PCL is relatively stiff and may not precisely mimic the mechanical properties of native cartilage. PCL alone lacks the compatibility properties required for cartilage regeneration, so combinations with other materials are needed.	(Nowicki et al., 2020; H. Sun et al., 2006; F. Wang et al., 2022; P. Wei et al., 2021)
Poly(lactic acid) (PLA)	*	**	PLA is biocompatible and biodegradable. It can be used to create porous scaffolds for cartilage tissue engineering. PLA is biocompatible and can be used in bone scaffold fabrication. It is biodegradable and provides initial structural support during bone regeneration.	PLA can be brittle, and its degradation rate may not align with cartilage regeneration timelines without modification. Similar to PCL, PLA may not possess inherent biocompatibility properties and may require additives or surface treatments.	(Badami et al., 2006; H.-W. W. Kim et al., 2008; Naghieh et al., 2017)
Poly(lactic-co-glycolic acid) (PLGA)	**	***	PLGA is a copolymer of lactic and glycolic acids and offers good biocompatibility and controllable degradation rates. It	Pure PLGA may lack the mechanical strength needed for load-bearing bone applications and may require reinforcement	(Liang et al., 2018a; Reyes et al., 2012; P. Wei et al., 2021)

			can be loaded with bioactive agents to enhance bone regeneration.	or blending with other polymers.	
Polyethylene Glycol (PEG)	***	*	PEG is a hydrophilic polymer with good biocompatibility. It can be modified to create hydrogels that support cell encapsulation and cartilage matrix deposition. Highly control of properties, resistance to protein adsorption, and minimal immunogenicity.	PEG hydrogels can be mechanically weak and may require reinforcement or blending with other polymers. Limited cell adhesion properties without modification, potential for rapid clearance in vivo.	(C. Fan & Wang, 2015; Han et al., 2022; Riewruja et al., 2022; Y. Yang et al., 2020)
Silk Fibroin	*	***	Good mechanical strength, biodegradable, and biocompatible.	Limited control over degradation rate potential allergenic responses in some individuals.	(Panjapheree et al., 2018; Pérez-Silos et al., 2019; Xiao, huang, et al., 2019)

One of the materials frequently utilised by various authors in the field of tissue engineering, especially for OC scaffolds is PCL. (Cipitria et al., 2011; Doyle et al., 2014a; Fereshteh et al., 2016b; Gerçek et al., 2008b; H. Li et al., 2020b; Nowicki et al., 2020; Patrício et al., 2014; W. Wang et al., 2016; P. Wei et al., 2021). The properties of PCL, including its physical, thermal, and mechanical attributes, can exhibit variation based on factors such as its molecular weight and degree of crystallinity. **Table 2.4** presents a range of physical and mechanical properties of the PCL, reported in the literature. Similarly, the biodegradability of PCL can span from a few months to several years, depending on its molecular weight, crystallinity, and the rate of polymer degradation.

PCL has been used in a broad range of applications, driven by its material properties, including hydrophobic, slow-degradability, compatibility with other polymers, biocompatibility, and the potential to be synthesised from monomers derived from renewable sources (Cao et al., 2021; Labet & Thielemans, 2009; Patrício et al., 2014; Prasad & Pramanik, 2022), as a hydrophobic polymer due to its chemical composition. This characteristic reduces it less level to hydrolysis compared to hydrophilic polymers. The rate of hydrolysis in polymers is intricately linked to the type of chemical bonds present within their molecular structure. As a slow-degrading, biocompatible synthetic thermoplastic polymer, PCL's degradation mechanism primarily joints on the nature of these bonds (Bartnikowski et al., 2019; Göpferich, 1996a, 1996b). Given its utility, PCL is considered a highly advantageous polymer, provided that its properties can be effectively controlled, and it can be manufactured cost-effectively (Ikada & Tsuji, 2000).

Table 2.4 Properties of PCL.

Properties	Range	References
Density ($\rho/g\ cm^{-3}$)	1.070 – 1.200	Gross & Kalra, 2002; Labet & Thielemans, 2009; Van De Velde & Kiekens, 2002a
Glass Transition temperature ($T_g/°C$)	-66 - -60	Pillai & Sharma, 2010; Sinha et al., 2004; Van De Velde & Kiekens, 2002b)
Melting Point ($T_m/°C$)	56 - 65	Pillai & Sharma, 2010; Sinha et al., 2004; Van De Velde & Kiekens, Gross & Kalra, 2002; Labet & Thielemans, 2009
Youngs modulus (E/GPa)	0.20 – 0.44	Azimi et al., 2014.; Pillai & Sharma, 2010; Van De Velde & Kiekens, 2002b
Elongation at break ($\varepsilon/\%$)	20 - 1000	Gross & Kalra, 2002; Labet & Thielemans, 2009; Van De Velde & Kiekens, 2002a, Azimi et al., 2014.; Pillai & Sharma, 2010; Van De Velde & Kiekens, 2002b

PCL is characterised by its low cost, good stability, and mechanical strength; however, it has poor hydrophilicity and slow biodegradation (Cipitria et al., 2011; J. Gao et al., 2019; Hiep & Lee, 2010; H. Sun et al., 2006). Combining PCL with other biomaterials has been used as a strategy to increase the biocompatibility and modulate the degradation rate, but these composites often exhibit inferior mechanical properties. Święszkowsk et al. demonstrated the potential efficacy of porous PCL and PCL-TCP scaffolds in stimulating bone regeneration. However, significant challenges persist in the domain of cartilage repair and replacement. Despite advancements, joint replacements have yet to fully replicate natural cartilage, leaving room for complications and underscoring the imperative for further research in scaffold development.(Swieszkowski et al., 2007b).

PCL/PLGA scaffolds were made with different proportions (1:90, 50:50, 70:30, 90:10), showing successful characteristics for chondral tissue reported by several authors, (González-González et al., 2023; Peng et al., 2018; Sánchez-Pech et al., 2020). All studies reported the combination of these materials could provide scaffolds with the desired degradation properties, surface characteristics, and biocompatibilities, demonstrating potential in tissue engineering as they are non-toxic. Gonzalez-Gonzalez et al. focuses on the combination of PCL/PLGA (80:20) scaffolds, manufactured by electrospinning for

chondral defect repair, a drop of a high level of F-actin was presented after 28 days of culture.(González-González et al., 2023).

GelMA has emerged as a prevalent material for promoting cartilage tissue formation within the OC scaffolds through the incorporation of chondrocytes and mesenchymal stem cells (MSCs), as noted in the research conducted by M. Costantini et al. (Costantini et al., 2016) While Costantini's work revealed the capability of GelMA in facilitating cartilage tissue formation, it also highlighted the tendency of this bioink to foster the development of a fibrocartilaginous tissue variant, characterised by elevated levels of collagen type I production. Daly's study further accentuated GelMA's potential, emphasising that the supplementation of GelMA with hyaluronic acid and chondroitin sulphate significantly enhances chondrogenesis (Daly et al., 2016). This supplementation not only improves the chondrogenic potential but also augments the bio-ink viscosity, thereby enhancing its printability, as supported by Schuurman and Levett's research. Consequently, the incorporation of additional components in GelMA-based bioinks offers a promising avenue for steering cartilage tissue formation towards a more desirable outcome while concurrently enhancing the printability of the bioink (Daly et al., 2016; Levett et al., 2014).

The results from Shien et al. demonstrate the capability to control both the mechanical and swelling attributes of the material. Additionally, the observed high cell viability, coupled with the growth of cartilaginous tissue, positions GelMA as a promising candidate for applications in cartilage tissue engineering. By integrating viscosity-enhancing additives like hyaluronic acid (HA) and a reinforcing framework such as PCL, and GelMA can be structured into layered formations (Shie et al., 2020).

De Ruijter et al. and Ruiz-Cantu et al. took a similar approach fabricating a bioprinted scaffold by extrusion composed of GelMA and reinforced with PCL fibres. The authors showed that the inclusion of these techniques had no negative effects on cell viability and proliferation for cartilage. In fact, cells maintained the ability to produce GAGs and collagen even after the bioprinting process, as cells were deposited into the GELMA bioink.

Therefore, the inclusion of PCL with this technique may be a good option to increase the mechanical properties of scaffolds for cartilage regeneration (de Ruijter et al., 2019; Ruiz-Cantu et al., 2020b). Yanyan Cao et al. findings further establish the efficacy of a PCL/GelMA biphasic scaffold with a co-culture of BMSCs and chondrocytes in mitigating

mechanical pain associated with the implantation in cartilage defects observed in the gait analysis, underlining its potential for cartilage regeneration. These comprehensive studies emphasise the multifaceted role of PCL and GelMA in cartilage tissue formation. (Y. Cao et al., 2021)

These studies underscore the multifaceted role of PCL and GelMA in cartilage and bone tissue formation, shedding light on the intricate relationship between its composition, the resulting tissue type, and the feasibility of its application in bioprinting technology. While GelMA alone might tend to support fibrocartilaginous tissue development, the incorporation of specific components such as hyaluronic acid and chondroitin sulphate serves as a promising approach to steer the tissue formation towards a more desirable articular chondrogenic outcome.

2.6. Design of the OC Scaffold.

Manufacturing an OC scaffold is dependent on the fundamental design of the scaffold. The design in turn must support the growth, adhesion, migration and differentiation of cells to support the generation of the OC tissue. To fulfil the requirements for an OC scaffold, the design has to consider the biocompatible and degradable materials, the mechanical properties, the pore structure, and the interface integration between phases (Seo et al., 2014c)

The design of a scaffold has been done by combining the manufacturing process with a computer design (CAD) and imaging software, which allows for the production of the same scaffold. These tools have been very useful in accurately developing the shape of the scaffold internally and externally. At the same time, the prototype can be developed exactly as the previous one, creating an easy methodology to manufacture scaffolds.

Significant attention has been directed towards the criticality of achieving a balance in stiffness for scaffolds, as highlighted by Heuijerjans et al. The critical nature of stiffness matching lies in preventing the emergence of high shear stresses at the interfaces of the implant and the surrounding tissue, thus averting potential instances of implant failure. Additionally, differences in stiffness or errors in surgical implementation can contribute to irregular displacement, subsequently leading to complications, including the uneven wear of articular cartilage surfaces that would otherwise remain healthy. This underscores the necessity of meticulous considerations in scaffold design and implementation to ensure a harmonious interaction between the implant and the host tissue.(Heuijerjans et al., 2018)

A combination of rapid prototyping manufacturing techniques with computer-aided systems for tissue scaffolds (CASTS) has been used by Naning *et al.*. The CASTS software demonstrated an advantage of CAD and medical imaging techniques together using a rapid prototype technique. Pore size, porosity, surface area and interconnectivity within the scaffold are some of the characteristics that have been controlled by the author (Naing et al., 2005)

In 2020, Margaret Nowicki et al. demonstrated that manipulation of both mechanical properties and cell performance can be achieved through the utilisation of bio-ink and 3D printing process. This approach enhances mechanical properties and improves human mesenchymal stem cell (hMSC) adhesion, growth, and differentiation (Nowicki et al., 2020).

In the pursuit of advanced OC scaffold design, Xiang Gu's research uncovered an integrated scaffold characterised by an inconsecutive channel structure and vascularised modulation. The study emphasised the pivotal role of the channel pattern not only in determining mechanical strength but also in influencing the infiltration of bone marrow, consequently facilitating a synergistic repair process for the OC defects (X. Gu et al., 2022b). In a parallel vein, Yuqing Gu's work showcased the successful application of digital light processing (DLP) for the one-step 3D printing of a bilayered scaffold. By competently manipulating the pore sizes, the mechanical properties of the scaffold could be fine-tuned, thus showcasing the potential of this technique for facilitating the OC regeneration (Yuqing Gu et al., 2023)

Concurrently, the literature highlighted the potential of combining cells, novel small-molecule drugs, and various gradient synthesis materials for the development of gradient scaffolds. Notably, the study advocated for the adoption of a continuous gradient scaffold over a discrete gradient scaffold, attributing its superior ability to mimic the native tissue structure without abrupt layer changes for the fabrication of an OC tissue(L. Chen et al., 2023).

Collectively, these studies contribute significantly to the evolving landscape of scaffold design, each providing valuable insights into the optimisation of mechanical properties, replication of native tissue structure, and integration of novel materials to advance the realm of an OC regeneration.

2.7. Finite Element Modelling.

Mathematical modelling has emerged as a pivotal tool for assessing the mechanical properties of scaffolds to validate these biomimetic scaffold designs (Gibson, Ashby, & Harley, 2010). The choice of modelling approach is inherently tied to the specific structure and materials utilised in the scaffold, a parameter that offers considerable variability (Fu et al., 2020; Wasyłeczko et al., 2020). These materials encompass both synthetic and natural options, including thermoplastics, hydrogels, and decellularised tissue (Hutmacher *et al.*., 2001; Ren *et al.*., 2016). For modelling hydrogels and decellularised tissue, poroelastic models prove effective(Isobe et al., 2018; Vidal-Lesso et al., 2012) while numerous polymer scaffolds designed with porous foam structures can have their mechanical properties approximated via cellular solids modelling approaches (Cano-Vicent et al., 2021; Doyle et al., 2014b; Marcelino et al., 2023; Nowicki et al., 2020).

Vijayavenkataraman *et al.* describe a design method established by parametric optimisation approaches which consider requirements such as porosity, Youngs modulus, and pore size. The study focuses on three distinct designs such as primitive, gyroid and diamond geometry, these in a cubic form, by three applications tissue-specific scaffolds, scaffolds for stem cell differentiation, and functionally graded scaffolds with biomimetic functional gradients. The results revealed by the commercial software Abaqus/Standard was a high mechanical stiffness for the straight Youngs modulus of all designs. However, decreasing Youngs modulus is related to the rise of porosity, and the high permeability has been achieved by a bigger pore, such as a primitive cubic form. The diamond scaffold presented the best surface area and a higher Youngs modulus than primitive and gyroid cube scaffolds, so this would expand the porosity and diminish the weight. Utilising the results of the geometry models, a functional gradient design could be achieved for the OC defects (Vijayavenkataraman, Zhang, et al., 2018). On the other hand, Shipani *et al.*. used fused deposition modelling as the manufacturing process and the PCL as the material. Even though FE modelling was made to approach the key aspects of geometry and material behaviour, a modelling strategy was developed. The pre and post manufacture shown critical inconsistencies in the geometric and mechanical behaviour of 3D printed scaffolds (Schipani, Nolan, et al., 2020a).

Hairui Suo et al. conducted FE simulations demonstrating a biomimetic strengthened structure with a deformable cartilage layer, signifying advancements in the design and manufacture of biopolymer-based OC biomimetic scaffolds. This work underscores the

importance of integrating computational modelling techniques to not only understand the structural mechanics of these complex scaffolds but also to drive their innovative design. The deformable cartilage layer offers a promising avenue for more realistic biomechanical simulations, thereby aiding in the optimisation of scaffolds for improved tissue.

Lastly, the estimation of effective and shear modulus of scaffolds, underlining the significance of considering microstructural features such as surface roughness and microporosity in determining scaffold properties using CAD models in ABAQUS software. The outcomes of their research shed light on the intricate relationship between the microarchitecture of scaffolds and their mechanical behaviours, emphasising the importance of thorough material characterisation and microstructural analysis in the design and evaluation of scaffolds for tissue engineering applications (Cahill et al., 2009).

2.8. Mechanical Properties of the OC Tissue.

Extensive research efforts have been directed towards the reconstruction of the cartilage and bone regions in the OC tissue, underscoring the importance of comprehending their changing mechanical characteristics throughout the tissue structure (Ansari et al., 2019). When considering the changing mechanical properties of the OC tissue, it is essential to consider factors such as the tissue source, including human, bovine, porcine, equine, and others, alongside the tissue's age and specific conditions during measurement. It has become increasingly apparent that these variables can significantly impact the measurements obtained, thereby rendering the ideal mechanical properties requisite for the OC tissue transplantation somewhat uncertain, as reported by different authors as presented in **Table 2.5.** As a result, the establishment of a comprehensive understanding of the dynamic mechanical profile of the OC tissue remains a critical requirement for advancing the efficacy and precision of tissue engineering and regenerative medicine interventions for the OC defect repair.

In the investigation of articular cartilage, both Korhonen et al., and Jurvelin et al., employed unconfined compression testing methodologies, yielding similar compression modulus of 0.80 ± 0.33 MPa and 0.85 ± 0.35 MPa, respectively. One study utilised a bovine humeral head, while the other employed a human femoral condyle, showcasing the consistency of results across species (Korhonen et al., 2002, Jurvelin et al., 2003). In contrast, Bartnikowski et al., reported a notably higher compression modulus of 1.72 ± 0.27 MPa in 5 samples of human cartilage. The disparity between the findings of Bartnikowski and Jurvelin may be

attributed to variations in the age of the specimens or the specific conditions under which the tissue was obtained for the experiment, emphasising the critical influence of these factors on mechanical testing outcomes (Bartnikowski et al., 2015).

The study conducted by Kabir et al., presented a comprehensive investigation into the mechanical behaviour of the cartilage in the OC tissue, demonstrating distinct compressive Youngs modulus of 1.03 ± 0.48 MPa for indentation testing and 10.60 ± 3.62 MPa for unconfined compression. The study specified the tissue being measured as the OC cartilage, obtained from donors, with the subchondral bone manually removed from the collected the OC tissue samples. However, the manual removal technique introduces an element of uncertainty, potentially leading to errors, as certain fragments of the subchondral tissue may remain, or a portion of the cartilage tissue could accidentally be removed during the process, potentially impacting the accuracy of the measurements (Kabir et al., 2021).

Table 2.5 Summary of studies representing Youngs modulus of an OC tissue for each region depending on the type and age of tissue and the mechanical test carried out.

OC Region	Type of tissue	Tissue Age	Mechanical Test	Youngs Modulus	References
Articular Cartilage	Ankle (Human)	33-80y	Indentation	10.6 ± 5.6 MPa - 15.6 ± 7.6 MPa	Shepherd & Seedhom, 1999
	Knee (Human)	33-80y	Indentation	6 ± 3.1 MPa - 11.8 ±4.8 MPa	
	Knee (Human)	33-80y	Indentation	4.5 ± 1.2 MPa - 10.2 ± 2.5MPa	
	Femoral patellar (Human)	33-80y	Indentation	3.1 ± 0.4 MPa - 10.0 ± 2.6 MPa	
	Femoral condyles (Human)	33-80y	Indentation	4.3 ± 1.4 MPa - 13.0 ±4.2 MPa	
	Humeral head (Bovine)	NM	Unconfined Compression	0.80 ± 0.33 MPa	Korhonen et al., 2002)
	Humeral head (Bovine)	NM	Confined Compression	0.81 ± 0.34 MPa	
	Humeral head (Bovine)	NM	Indentation	1.15 ± 0.33 MPa	
	Patella (Bovine)	NM	Unconfined Compression	0.57 ± 0.17 MPa	

Patella (Bovine)	NM	Confined Compression	0.62 ± 0.19 MPa	
Patella (Bovine)	NM	Indentation	0.83 ± 0.17 MPa	
Femoral condyle (Bovine)	NM	Unconfined Compression	0.31 ± 0.18 MPa	
Femoral condyle (Bovine)	NM	Confined Compression	0.34 ± 0.17 MPa	
Femoral condyle (Bovine)	NM	Indentation	0.55 ± 0.18 MPa	
Femoral condyles (Human)	23-50y	Unconfined compression	0.85 ± 0.35 MPa	Jurvelin et al., 2003
Femoral condyles (Human)	23-50y	Confined Compression	1.237±0.486 Mpa	
Femoral Head (Human)	73-81y	Confined Compression	~0.26MPa	Boschetti et al., 2004
Tibial (Rabbit)	6mo	Micro-indentation	~2MPa	Cao et al., 2006

	Femoral Head (Human)	73-81y	Unconfined	~0.25MPa	Boschetti et al., 2004
	Patella (Human)	55-73y	Indentation	0.64 ± 0.30 MPa	Kiviranta et al., 2008
	Femoral Head (Human)	NM	Indentation	4.89 ± 0.76 MPa	Taylor et al., 2012
	Femoral Head (Porcine)	NM	Indentation	1.18 ± 0.17 MPa	
	Femoral Head (Bovine)	NM	Indentation	1.86 ± 0.44 MPa	
	Femoral Head (Ovine)	NM	Indentation	3.94 ± 2.52 MPa	
	Femoral Head (Rabbit)	6mo	Indentation	5.7±1 GPa	Campbell et al., 2012
	Femoral condyles (Human)	NM	Unconfined compression	1.70-2.75 MPa	Bartnikowski et al., 2015
	(Human)	71y	Unconfined compression	1.63 ± 0.26 MPa	Bas et al., 2017
Calcified Cartilage	Patella and femur (Bovine)	NM	Three-point bending	0.32±0.25 GPa	Mente & Lewis, 1994

	Femoral head (Human)	55-89 y	Indentation	19.01±0.29 GPa	Ferguson et al., 2003
	Patella (Human)	39-54y	Indentation	13 GPa	Gupta et al., 2005
	Femoral Head (Human)	73-81y	Confined Compression	~0.39MPa	Boschetti et al., 2004
	Femoral Head (Human)	73-81y	Unconfined	~0.36MPa	
	Distal condyle (Equine)	12-18mo	Indentation	12.9±1.66 GPa	Doube et al., 2010
Articular / Calcified Cartilage	Femoral condyles (Human)	71-77y	Indentation	1.03 ± 0.48 MPa	Kabir et al., 2021
	Femoral condyles (Human)	71-77y	Unconfined Compression	10.60 ± 3.62 MPa	
Subchondral Bone	Femoral Head (Human)	73-81y	Confined Compression	~0.50GPa	Boschetti et al., 2004
	Femoral Head (Human)	73-81y	Unconfined	~0.49GPa	

	Subchondral / tibia (Human)	NM	Three-point bending	1.15 ± 0.8 GPa	Choi 1990
	Patella and femur (Bovine)	NM	Three-point bending	5.7±1.9 GPa	Mente & Lewis, 1994
	Femoral head (Human)	55-89 years	Indentation	19.05±0.39 GPa	Ferguson et al., 2003
	Patella (Human)	39-54y	Indentation	25 GPa	Gupta et al., 2005
	Distal condyle (Equine)	12-18mo	Indentation	14.57±1.76 GPa	Doube et al., 2010
	Femoral Head (Rabbit)	6mo	Indentation	22.8±1.8 GPa	Campbell et al., 2012
Cartilage/Subchondral	Patella (Bovine)	NM	Three Point bending	9.96±4.99 GPa	
	Patella (Bovine)	NM	Indentation	1.47±0.13 GPa	Hargrave-Thomas et al., 2015
	Patella (Bovine)	NM	Nanoindentation	1.91±0.36 GPa	

2.9. OC Scaffolds.

The OC tissue represents a complex integration of cartilage and bone layers, with a significant portion of its composition attributed to water content (cartilage). Several studies have demonstrated that engineered scaffolds can closely emulate the intricate structure of an OC tissue. Considering the fundamental role of water in both tissues, cartilage and bone, of the OC tissue, the utilisation of diverse polymers with varying water absorption capabilities emerges as a promising strategy for the effective replication and regeneration of this complex tissue. Particularly for cartilage tissue engineering, the development of hydrogels exhibiting high water swelling properties has garnered attention. These hydrogels are similar to the native cartilage tissue, characterised by the presence of polymer chains of glycosaminoglycans and collagens immersed within a substantial water content, accounting for approximately 60–80% of the cartilage tissue. Conversely, for bone tissue, which typically comprises a mere 10% water, scaffold fabrication necessitates the use of polymers possessing low water swelling properties or tailored hydrogels engineered to exhibit heightened mechanical strength(Neill, 2016; Patel et al., 2019; Schoonraad et al., 2021)

Various studies have reported differing Youngs modulus for their OC scaffolds. Levingstone et al. constructed a scaffold using Type I collagen/HA for the first part, Type I & II collagen/HA for the second part, and Type I & II collagen/HyA for the bone layer, leading to a compressive modulus of 0.51 ± 0.03 kPa, indicating an enhanced modulus due to the presence of HA (Levingstone et al., 2014b). Similarly, J. Liu et al. adopted a comparable approach but utilised 30/3% GelMA/nHa for subchondral zone, 20/3% GelMA/nHa for interface zone, and 15% GelMA solely for cartilage zone, resulting in a higher Youngs modulus of 550 ± 74.70 kPa, attributed to the variation in materials and their proportions within the combination (J. Liu et al., 2019b). Conversely, Gao et al. developed PLGA-based scaffolds with suboptimal mechanical properties, which were significantly improved with the combination of PLGA-g-PC-PEG, leading to a notable increment in the mechanical properties of the scaffold, acquiring a value of 220 ± 30 MPa. Additionally, Cometa et al. (2021) produced a PCL/HA/CD scaffold demonstrating a compressive Youngs modulus of 106 ± 11 MPa, highlighting the provision of more suitable mechanical properties for the bone tissue(J. Gao et al., 2021).

Kosik-Kozioł et al. emphasise the mechanical properties of a triphasic OC scaffold, delineating each zone. The scaffold is composed of 2.5% Alginate, 2% PLA for the non-calcified cartilage, 4% Alginate, 6% GelMA, 0.5% β-TCP for the calcified cartilage, and polycaprolactone for the

subchondral bone. In terms of mechanical properties, the study reveals a compression modulus of 33.39±7.76 kPa, 3.69±0.88 kPa, and 22,935.10±1888.45 kPa, respectively, for each zone (non-calcified cartilage, calcified cartilage, and subchondral scaffolds). Conversely, the triphasic scaffold exhibits a compression modulus of 16.02±3.52 kPa, indicating relatively poorer mechanical properties in the intermediate zone (Kosik-Kozioł et al., 2020b).

The literature indicates that several structures have been investigated and carried out to solve the OC defect, as shown in **Table 2.6**. The manufacturing processes and materials used vary; nonetheless, all authors, according to the calculations and designs, try to model an OC scaffold with the main characteristics of the OC tissue. The porosity and the size of the pore can vary, but a core issue to address in this type of scaffold is the interconnectivity. The OC tissue structure is complex since it has four cartilage zones plus the subchondral zone. Each author tries to develop these areas using bi-phasic, tri-phasic, or multiphasic scaffolds.

Table 2.6 Summary of studies representing Youngs modulus of an OC scaffold depending on the tissue target using a specific manufacturing technique and the specific compression mechanical test.

Scaffolds	Fabrication Technique	Target Tissue	Compression test	Youngs Modulus	Application	Remarks	References
Type I collagen/HA – Type I & I collagen/HA- Type I & IIcollagen/HyA	Freeze-drying	OC Tissue	NS	0.51 ± 0.03 kPa	OC Defect	The presence of HA in the bone layer led to an increase in the compressive modulus. The bone layer was found to have the highest compressive modulus of approximately 0.95 kPa	Levingstone et al., 2014b
Multilayered scaffold Cartilage matrix & Chitosan-core-sheath PLGA/TCP	Thermal-induced phase separation	Cartilage Layer	NS	951±112.64 kPa	OC Defect	The compressive modulus of the core-sheath PLGA/TCP scaffolds was higher than that of pure PLGA scaffolds, but lower than that of PLGA/TCP scaffolds	T. Zhang et al., 2017
	Low-temperature deposition	Bone Layer	NS	805.7± 17.47 kPa			

Cartilage PLGA scaffold	Fabricated by room-temperature compression-Moulding/porogen-leaching	OC tissue	NS	0.4±0.1 MPa	PLGA was used for the cartilage layer scaffold and PLGA/HA subchondral layer scaffold. Scaffolds were prepared separately and then glued by dichloromethane (CH2Cl2) to obtain a bilayer scaffold.	Liang et al., 2018
Subchondral PLGA scaffold			NS	5.6±0.3 MPa		
Subchondral PLGA/HA scaffold			NS	12.4±1.0 MPa		
Bilayer scaffold PLGA-PLGA/Hap			NS	2.8±1.7 MPa (dry) 20.3±0.7 MPa (wet)		
Multilayered Scaffold ACECM-PLGA/TCP	Thermal-induced phase separation	OC Tissue	NS	0.773 ± 0.068 MPa	OC Defect	The compressive modulus of the multilayered scaffolds showed remarkable enhancement of the mechanical properties supporting well-organised OC repair.	Jia et al., 2018b

Tri-layered scaffold GelMA/nHa-GelMA/nHa-GelMA	3D multi-nozzle pneumatic printing	OC Tissue	Unconfined compression	550 ± 74.70 Kpa	OC Defect	which is similar to or exceeding that of native human articular cartilage	J. Liu et al., 2019
PCL Scaffolds	BioCell printing	OC tissue	NS	106 ± 11 MPa	Osteoporotic Bone	The PCL/HA/CD scaffolds produced via BioCell Printing displayed adequate mechanical properties for the regeneration of cancellous bone tissue.	Cometa et al., 2021
PCL/HA Scaffolds			NS	108 ± 10 MPa			
PCL/CD Scaffolds			NS	220 ± 30 MPa			
PCL/HA/CD Scaffolds			NS	228 ± 27 MPa			
Bilayered Porous Scaffold GelMA-GelMA/HA scaffolds	3D printer (Extrusion)	OC Tissue	NS	152.015 ± 34.297 Kpa	OC Defect	The addition of HA enhanced the mechanical properties of the scaffold	Gao et al., 2021

2.10. Knowledge Gaps.

In the field of osteochondral scaffold manufacturing, several knowledge gaps were found for an articular cartilage in the OC gradient scaffold fulfilling the mechanical properties of the OC tissue. Firstly, insufficient strength at the bounding has frequently been cited as an issue in the construction of multilayered scaffolds, potentially resulting in the separation or delamination of these layers (Cui et al., 2012; Holmes et al., 2014; Jia et al., 2018c; Levingstone et al., 2014b; Shen et al., 2018b; W. Wang et al., 2018; T. Zhang et al., 2017b). Kosik-Kosik et al. manufactured a hybrid triphasic OC scaffold by producing each of the zones separately with different materials in each zone (non-calcified cartilage, calcified cartilage, and subchondral bone). These zones were integrated using fibrin glue to manufacture the hybrid triphasic scaffold. The design of these scaffolds maintained the perpendicular alignment of successive zones. However, the compressive modulus in the triphasic scaffold shows poor mechanical properties, particularly in the intermediate zone (Kosik-Kozioł et al., 2020). A lack of comprehensive understanding concerning the mechanical interactions and potential failure points between different zones within these scaffolds remains. Various authors have utilised fibrin glue, and they have reported similar issues with its mechanical properties, attributing these challenges to the rapid degradation of fibrin glue. (M. Lee & Wu, 2012; Swieszkowski et al., 2007c).

Methodologies for creating interface-free gradients in osteochondral scaffolds have been targeted using different techniques. One of the techniques, as demonstrated by Schoonraad et al., was to showcase the capability of a hydrogel-based resin to print two distinct phases utilising the same soft hydrogel. They modified the formulation slightly to create both cartilage-mimetic and bone-mimetic hydrogel scaffolds and to bind them, the scaffolds were filled with the same soft hydrogel. This approach allowed for the control of modulus and the creation of well-integrated multilayered structures within a scaffold. However, exhibited pillar buckling during strain (Schoonraad et al., 2021). On the other hand, with a similar approach from Liu et al. which fabricate a tri-layered scaffold using the same GelMA/nHA hydrogel but with different GelMA/nHA ratios and photo-crosslinked after printing by UV light irradiation. The graded scaffold shows integrity and interfacial bonding strength; however, a fracture strength is reported when at 20KPa of interfacial strength (J. Liu et al., 2019c).

PCL and GelMA are widely used in osteochondral scaffolds because of their properties. PCL is a biocompatible synthetic polymer with slow degradation, excellent mechanical strength, and 3D printing compatibility, used for osteochondral scaffolds for the support and intricate structures (Doyle et al., 2014a; Patrício et al., 2014; H. Sun et al., 2006; F. Wang et al., 2022). GelMA is a natural polymer that combines degradation, hydrophilicity, and 3D printing capabilities, mimicking the extracellular matrix and promoting cell adhesion. The use of these materials has been employed as materials for scaffolds for tissue engineering, (Elomaa et al., 2020; M. Fan et al., 2023; Ghorbani et al., 2020b; Jiang et al., 2021; H. Li et al., 2020c; J. Liu et al., 2019c). However, the use of these two materials together in extrusion-based 3D printing for an OC has been limited, some authors have integrated an additional material, such as Pluronic, used by Daly & Kelly, with an equilibrium modulus of approximately 3000KPa using unconfined compression testing (Daly & Kelly, 2019). Moreover, current designs predominantly feature rectangular scaffolds with angle variation for extrusion 3D printing. Some designs with staggered configurations show decreased mechanical properties when compared with aligned scaffolds (Ahmadi Soufivand et al., 2023; Bittner et al., 2019b; H. Chen et al., 2023; Daly et al., 2017b; Qin et al., 2021; Suo et al., 2021b; X. Yang et al., 2023). However, the use of double layer configuration increased both scaffold compressive modulus and yield stress.

This research project focus on developing a multiphasic graded OC scaffold, which is distinct from previous studies on graded structures. The project aims to replicate the bone-cartilage interface with integrated, graded mechanical properties, addressing challenges in achieving comparable mechanical properties to native articular cartilage in OC tissue. Unlike traditional manufacturing methods, which often face limitations such as poor reproducibility and irregular shapes, 3D printing offers an efficient solution by enhancing reproducibility and fabricating complex shapes. The thesis details a meticulous process of designing and fabricating the OC scaffold, with particular attention to minimising interfaces between its components and ensuring that the mechanical properties closely match those of native tissue. To achieve these goals, the project focuses on material selection, optimised printing parameters, achieving desired mechanical properties, and supporting cell adhesion and proliferation within the scaffold structure. A key strategy involves incorporating diverse geometries within the scaffold, utilising the same materials throughout, to create a more complex representation of the desired mechanical characteristics in articular OC tissue, with varying properties across different zones of the articular cartilage.

Chapter 3. Methodology.

3.1. Introduction.

This chapter presents a comprehensive description of the methodology employed throughout the research. The methodology involves material characterisation, 3D extrusion, scaffold design, printing parameters, compression testing, finite element analysis (FE), and cell culture. The methods relevant to each research objective are presented in **Figure 3.1**, together with the inputs to and outputs from each method.

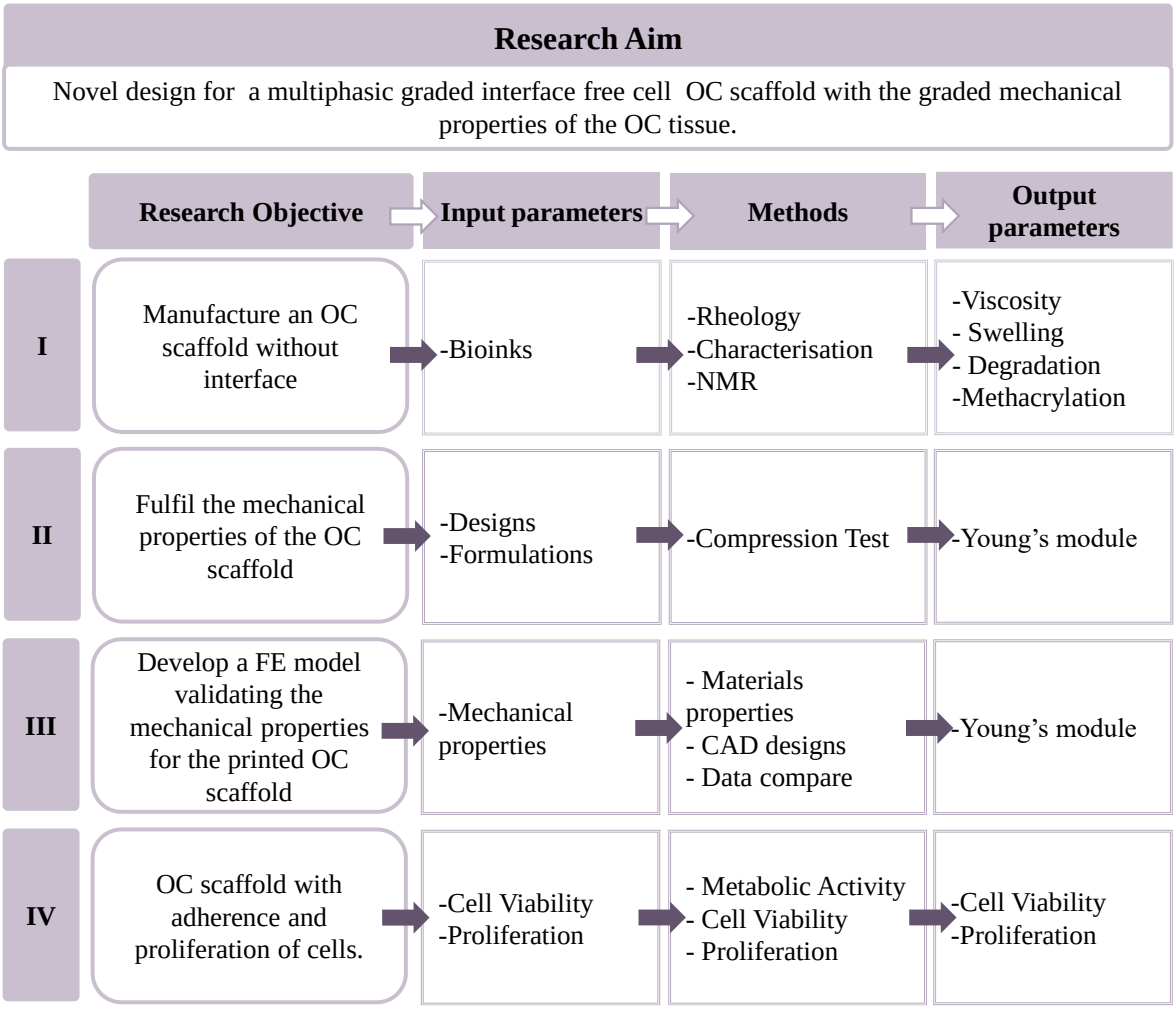


Figure 3.1 Link between aim - objectives and specific methods and parameters. (Abbreviation as follows: OC- Osteochondral, FE- Finite Element, CAD- Computer-Aided Design NMR- Nuclear Magnetic Resonance)

These methods specify the range of the related parameters which allow an extruded 3D bioprinted OC scaffold to achieve the mechanical properties required by the tissue. These

methods contribute to increasing the capability and matching the requirements of novel applications in tissue engineering. **Figure 3.2** shows the experimental design employed throughout the thesis.

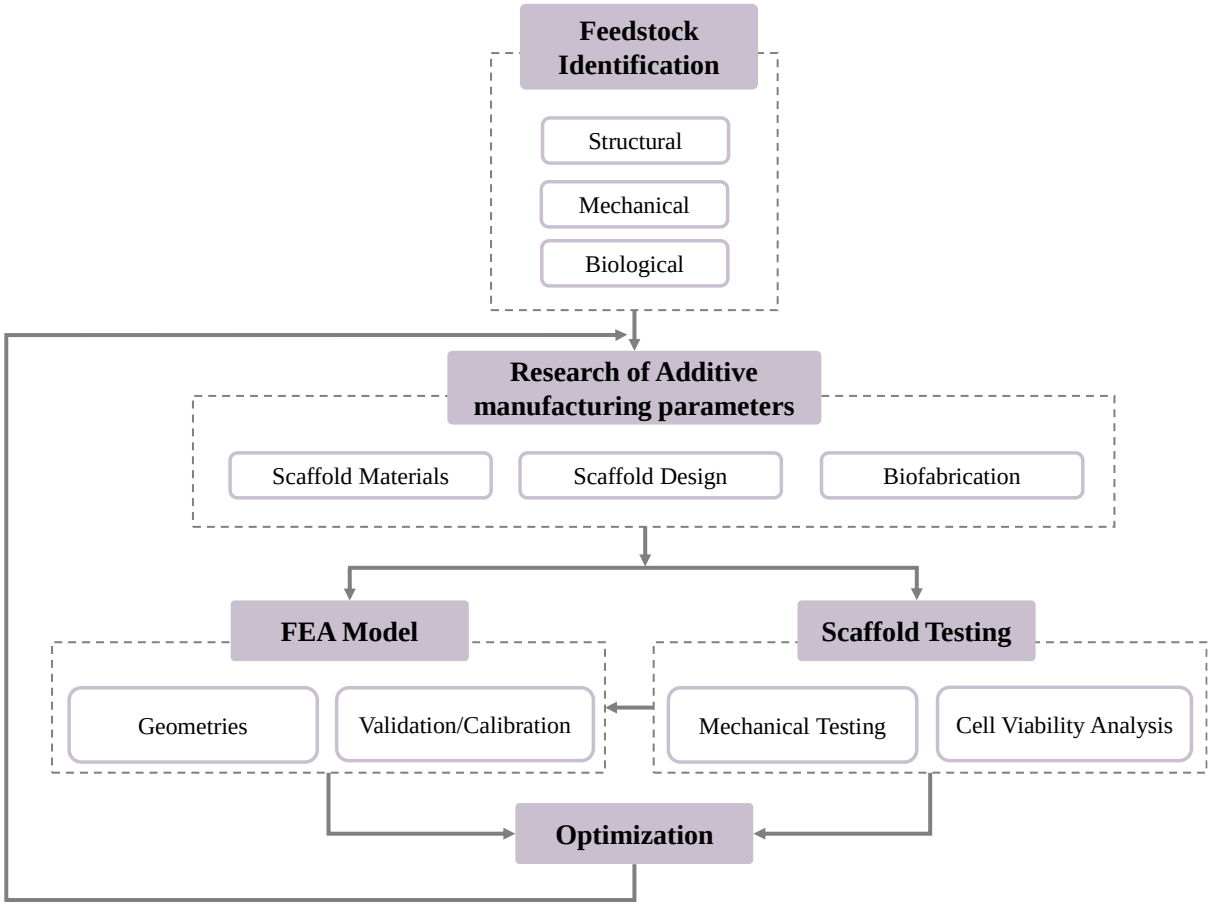


Figure 3.2. Flowchart of the key steps in the development of scaffolds.

A detailed outline of steps in the methodology of manufacturing an OC scaffold is presented in **Figure 3.3**. Materials were selected for their mechanical and biological properties to create an OC scaffold. First, a characterisation of the bio-ink was made to evaluate the properties and printability of the materials to be extruded on the RegenHu 3D Discovery^{TM} G5 bio-printer (RegenHu, Villaz-St-Pierre, Switzerland) using the pneumatic and screw extrusion printheads. The characterisation to ensure printability of the materials was carried out. For the PCL material, rheology analysis was performed to analyse the viscosity and shear thinning behaviour. For GelMA, both rheology and H-NMR tests were conducted. H-NMR tests assisted in adjusting the degree of methacryloylation, resulting in a hydrogel with tailored solution viscosity, equilibrium degree of swelling, and mechanical strength. Compression tests were then performed to

compare and modify the designs to achieve the desired mechanical properties of the scaffold. The scaffolds were seeded with cells, tested, and analysed to verify the cell viability in the scaffolds. Finally, all the data collected regarding the materials were added to the FE ABAQUS model to create a validation of the scaffold. The procedural methods are explained in more detail in the following sections.

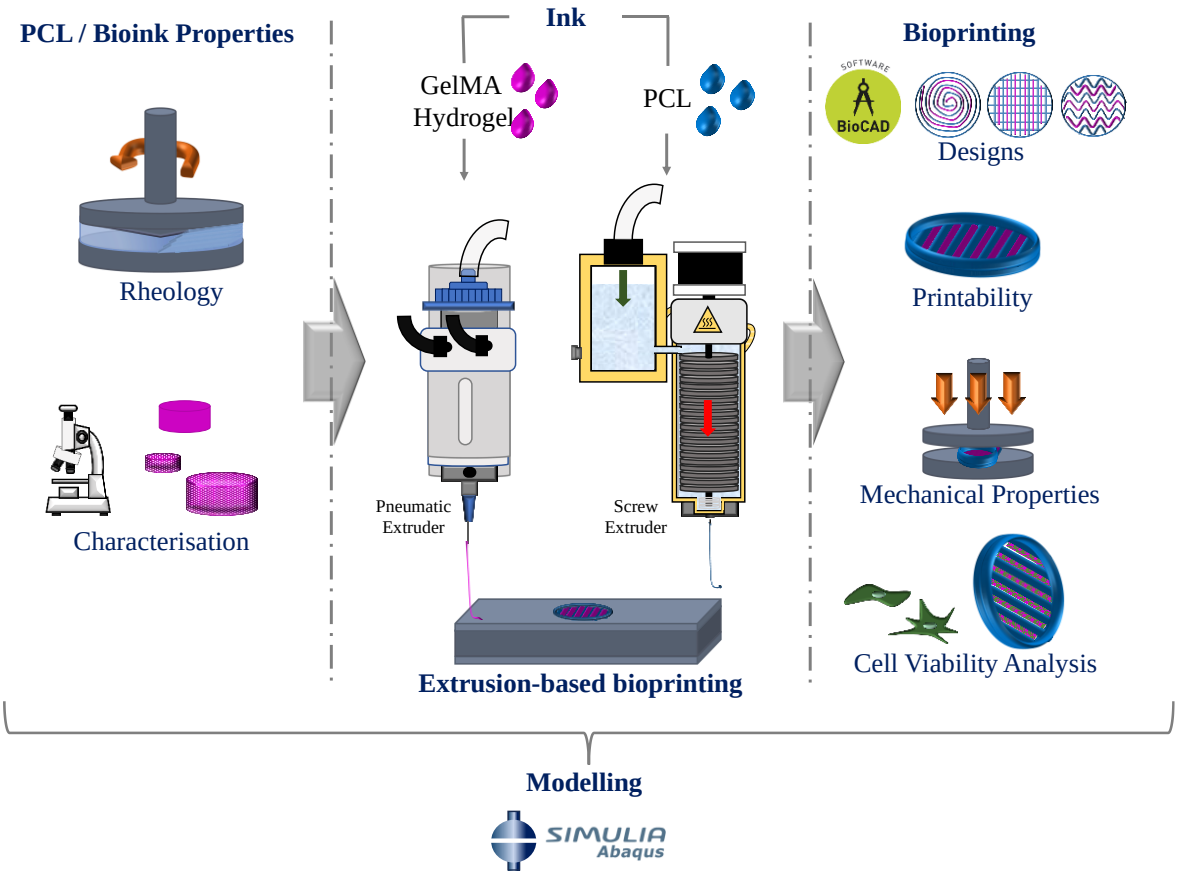


Figure 3.3 Schematic illustration of the methodology for developing the 3D OC scaffold.

This chapter provides an overview of the thesis methodology and the importance of the materials and processes involved, such as the material characterisation for the 3D extrusion base printing parameters. It describes the methodology used to create the designs to meet the mechanical properties, as well as the cell viability in the scaffold. In addition, the finite element (FE) of the scaffold is a tool to validate subsequent scaffolds using the same techniques. This extensive methodology contributes to the advancement of knowledge in scaffold fabrication, mechanical behaviour, and cell interaction, specifically within the field of OC tissue engineering and regenerative medicine.

3.2. Materials.

The materials were provided by different suppliers. Skin porcine gelatin (~175g Bloom, type A, G2625), Methacrylic anhydride (MA) (94%, 276685), Sodium Carbonate (222321), Sodium hydrogen carbonate (1.06329.0500), Polycaprolactone (PCL) pellets (Mn 45,000, 704105) and Toluidine Blue O (T3260-G5) were purchased from Sigma-Aldrich. Methylated Spirit Industrial (IMS) (74 OP.) M/4550/17 was acquired from Fisher. Irgacure ® 2959, 2-Hydroxy-4′-(2-hydroxyethoxy)-2-methylpropiophenone by BASF. Quant-iT™ dsDNA Assay Kits, high sensitivity (HS) (2561635), Live/Dead™ Viability/Cytotoxicity Kit for mammalian cells (2261453) and Presto Blue™ Cell viability Reagent (2413466) were purchased from ThermoFisher Scientific.

3.3. Methods of Materials Synthesis and Characterisation.

This section presents the characterisation of the materials, specifically PCL and GelMA. Their physical and chemical properties were determined through a series of tests, including rheological analysis and assessment of the degree of methacrylation. This characterisation phase laid the foundation for subsequent stages of the project.

3.3.1. Gelatin Methacrylate.

3.3.1.1. Procedure for Synthesis of GelMA

GelMA was synthesised in-house via a precipitation method following Jopeth Ramis protocol with some modifications (RAMIS, 2021). Briefly, 10% (w/v) gelatin solution (porcine skin gelatin ~175g Bloom, type A, G2625, Sigma-Aldrich) was prepared in 0.25M carbonate-bicarbonate buffer prepared with sodium carbonate, sodium hydrogen carbonate and distilled water (sodium carbonate, 222321, Sigma-Aldrich) (sodium hydrogen carbonate,1.06329.0500, Sigma-Aldrich). After one hour, methacrylic anhydride (276685 Sigma-Aldrich) was added dropwise at a speed of 0.5 ml/min to the gelatin solution and allowed to react for two hours at 60 °C. To stop the reaction, precipitation of the solution was carried out dropwise into Methylated Spirit Industrial (IMS) (74 OP); the volume of the IMS was 10x the volume of the reaction. The precipitated GelMA was filtered by compressing it with filter paper to remove as much liquid as possible. In order to remove any unreacted methacrylic anhydride (MA), the mixture was dialysed against distilled water 1/5 of the first volume reaction, and the precipitation was repeated 3x more times to ensure the removal of any unreacted methacrylic anhydride. To ensure all the IMS had been

removed, GelMA was introduced to the vacuum oven at room temperature(RT) for one day and then dissolved again with distilled water and storage in the -80°C freezer overnight. Finally, the solution was freeze-dried for four days, blended, and stored in a −80 °C freezer. **Figure 3.4** summarises the methodology followed for GelMA synthesis.

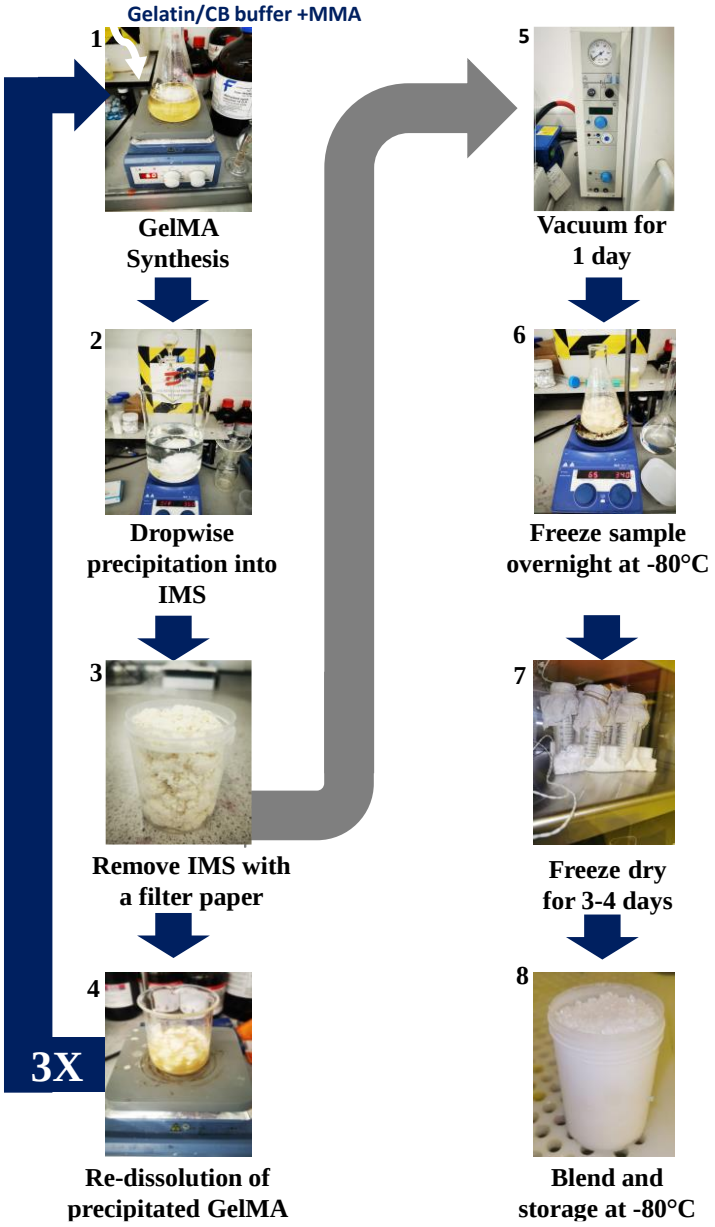


Figure 3.4 Visual summary of GelMA synthesis workflow. The precipitation protocol to produce GelMA was used to eliminate the unreacted MA; the precipitation was repeated three times, as stated in steps 2 to 4. Samples were in the vacuum oven at room temperature (RT) for a day to remove any remaining liquid and then added to the -80°C

freezer overnight. Finally, samples were lyophilised for three to four days, and the final product was blended and stored in a -80°C freezer.

3.3.1.2. Characterisation of GelMA.

Nuclear Magnetic Resonance (H-NMR) is a powerful analytical method used to investigate the structure and composition of organic molecules. H-NMR runs by detecting the magnetic properties of hydrogen nuclei protons in the sample. The resonance of the proton's magnetic moments in an applied magnetic field and the proton's absorption of energy when exposed to radiofrequency radiation are the underlying principles of H-NMR spectroscopy.

H-NMR was used to determine the quantity of methacryloyl groups in the different batches of GelMA. Before being analysed by the Bruker Avance AVIII HD 400MHz NMR spectrometer, a mixture of 15-25mg of porcine gelatin and GELMA powder was dissolved on 700ul of warm deuterated- dimethyl sulphoxide (DMSO). This concentration was used on the in order to determine the degree of methacrylation of each batch and analysed using Mestre-Nova software. The degree of methacrylation (DM) was defined as the percentage of ε-amino groups of gelatin (lysine, hydroxylysine) that are modified in the GelMA molecule. For the quantification of the DM by 1H-NMR, the spectra were normalised to the phenylalanine signal (6.5–7.0 ppm), representing the gelatin concentration. The lysine methylene signals (2.8–3.15 ppm) of gelatin spectra and GelMA spectra were integrated to obtain the areas [A (lysine methylene of unmodified gelatin)] and [A (lysine methylene of GelMA)]. Following the method published by Li et al, 2016, Equation (1) was used to calculate the DMs of the GelMA batches.

$$\boldsymbol{DM}[\%] = \left(\mathbf{1} - \frac{\left(\boldsymbol{A}(\boldsymbol{lysine\ methylene\ of\ GelMA})\right)}{\boldsymbol{A}(\boldsymbol{Lysine\ mehtylene\ of\ unmodified\ gelatin})}\right)\boldsymbol{X}\ \mathbf{100} \qquad (1)$$

3.3.1.3. GelMA Hydrogel Preparation.

Different concentrations of GelMA hydrogels (5, 10, 15 and 20% w/v) were prepared by dissolving the required amount of GelMA powder in distilled water. The photoinitiator Irgacure ® 2959 was added to the different GelMA solutions at a concentration of 0.5% w/v at 60 ˚C with 0.5% w/v of food colouring for 20 min.

3.3.1.4. Rheological Test.

Rheological evaluation of the GelMA hydrogels (5, 10, 15 and 20% w/v) was performed on a Hamilton Microlab Star Let (Automated Liquid handling workstation) with two different batches to evaluate the viscosity and the surface tension. Each concentration was added 1ml to the machine to determine the viscosity of different concentrations of GelMA. The test was carried out using 200 µl; surface tension was used at 100 µl. Viscosity and surface tension measurements were carried out using a 3X droplet for each concentration.

The Malvern Kinexus Pro Rheometer was used to measure the viscosity of the GelMA hydrogels (5, 10, 15 and 20% w/v) with and without dye. To evaluate the viscosity, different concentrations of GelMA with and without dye were tested under a 25 mm diameter parallel plate with a gap of 0.5 mm. The viscosity was measured at each temperature while the gels were subjected to a temperature ramp decrease in the range of 37–15 °C with a decrease rate of 5 °C/min at a constant shear rate of $100s^{-1}$. All measurements were conducted in triplicates.

3.3.1.5. Swelling Analysis.

Water absorption capacity is an essential metric for hydrogel-based materials . GelMA cubes (10 x 10 x 10 mm) were cast and photo-crosslinked using the Firefly 25x10AC365-1.5W for 3min. PCL/GelMA scaffolds photo-crosslinked samples were manufactured as stated in **section 3.4**. The swelling behaviour of the samples was evaluated at 37°C. The initial weight of the crosslinked hydrogels was measured (W_i) and soaked in distilled water solution for 24 hours. After removing the surface water using tissue paper, the final swelling weight (W_s) was measured, and the degree of hydration was estimated using Equation (2). The volume change after rehydration was further calculated using Equation (3), where Vi and Vs are the initial volumes of the printed scaffolds and the hydrated hydrogels after swelling.

$$\boldsymbol{Swelling\ Ratio\ or\ Degree\ of Swelling} = \frac{\boldsymbol{Ws - Wi}}{\boldsymbol{Wi}} \boldsymbol{X100} \qquad (2)$$

$$\boldsymbol{Volume\ Swelling\ ratio} = \frac{\boldsymbol{Vs}}{\boldsymbol{Vi}} \qquad (3)$$

3.3.1.6. Degradation Analysis.

In the same manner as described above, the GelMA hydrogel cubes (10 x 10 x 10 mm) for a degradation study to quantify the rate of hydrogel degradation. The hydrogels were

incubated in distilled water at 37˚C. Gross images and mass loss were measured in order to calculate the degradation regarding the initial weight of the hydrogel (W_i) and the degraded weight (W_d) using Equation (4).

$$\boldsymbol{Biodegradation = \frac{Wi - Wd}{Wi} X\ 100} \quad (4)$$

3.3.2. Polycaprolactone.

PCL used in this thesis was purchased from Sigma-Aldrich (Queenstown, Singapore). The granular PCL had a weight average molecular weight (M_W) of 69,000, an average molecular weight (M_N) of 45,000 g mol^{-1} with a melting point of approximately 60°C.

3.3.2.1. Rheological Measurements.

Thermoplastic polycaprolactone pellet samples of different molecular weights (M_w) (45 000 80 000, and 120,000) were subjected to rheological testing using the Kinexus Pro Rheometer(Malvern, Worcestershire, UK). The viscosity of PCL was measured in response to temperature changes by increasing temperature from 60°C to 160°C at a constant shear rate of 100 s^{-1}. A stainless steel 65 mm flat plate with a CP4/40 cone plate (40mm diameter with a 4° angle) was used with a measuring gap of 1 mm. To study the rheological properties under shear force, shear rate was increased from 0.01 to 1000 s^{-1} at a constant temperature of 160°C.

3.4. Scaffold Design, Fabrication and Analysis.

This section is focused on the mechanical properties of each zone within the tissue engineering scaffold, the design, fabrication, and analysis process aimed to create a construct that mimics the mechanical behaviour of the native tissue, as represented in Schematic of the OC tissue indicating physical property changes across the different zones. From top to bottom, chondrocyte size, fibre diameter and stiffness increase gradually between each zone, whereas water absorption, collagen II and chondrocyte number, as presented in **Figure 3.5.** This approach was followed to ensure that the scaffold could adequately support compressive load bearing and provide an environment conducive to cellular activities, ultimately enhancing the potential for successful tissue regeneration and functional tissue engineering outcomes.

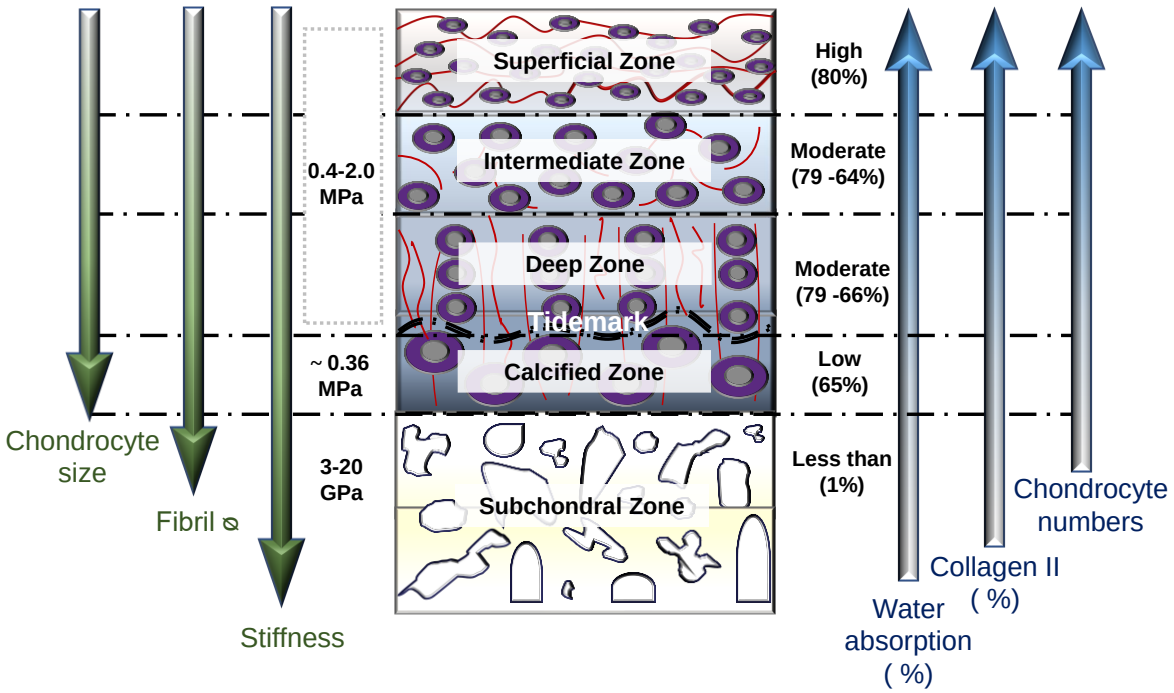


Figure 3.5 Schematic of the OC tissue indicating physical property changes across the different zones. From top to bottom, chondrocyte size, fibre diameter and stiffness increase gradually between each zone, whereas water absorption, collagen II and chondrocyte number increase from the bottom to the top -(image re-drawn from Imhof et al.(Imhof et al., 1999) (Bartnikowski et al., 2015; Boschetti et al., 2004; Jurvelin et al., 2003; Korhonen et al., 2002).

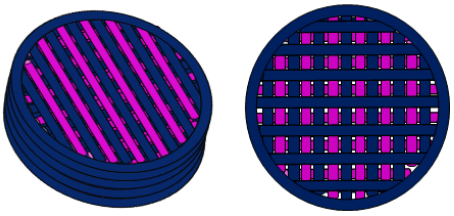
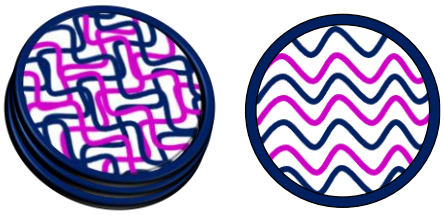
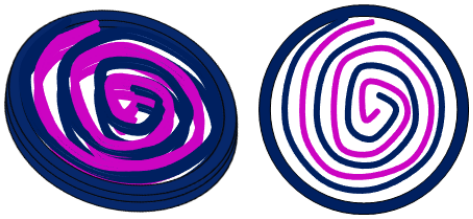
OC PCL-GelMA scaffold was designed on the BioCAD software (RegenHU, Switzerland) and manufactured with the RegenHU 3D Discovery™ G5 (Villaz-St-Pierre, Switzerland) detailed in **section 3.4.1 and 3.4.2**. The 3D extrusion printing method was used to create intricate scaffold architectures with precise control over structural features and material composition. By tailoring the design parameters, including pore size, porosity, and fibre alignment, it was possible to manufacture the scaffolds and modify the mechanical properties of specific zones by the analysing the Youngs modulus of the designs.

In the printing setup, PCL pellets were employed along with 10% w/v GelMA. The dimensions of the OC scaffold were standardised at 8mm in diameter and 4.6mm in thickness. Nonetheless, each zone's design was individually evaluated, with dimensions measuring approximately 8mm in diameter and 1.2mm in thickness.

3.4.1. Scaffold Design.

Scaffolds were designed using the BioCAD (RegenHU) software, which allows the designing of different shapes and customises diverse parameters such as layer thickness, spacing between strands and alignment of each print head. A unique G-code is generated by the BioCAD software for the printing patterns of the design. Cylindrical PCL/GelMA scaffolds were created using the BioCAD software. Multiple designs were created as shown in **Table 3.1** with different strand spacing, and their corresponding G-codes were generated. The dimension of the printed scaffolds was separated into two groups. The first group had a dimension of approximately 8mm in diameter and 1.2 mm in thickness, and this group was divided into three subgroups depending on the design (square, sinusoid, and spiral). The second group was designed with a combination of the previous designs for the OC scaffold with a dimension of 8mm in diameter and 4.6 mm in thickness.

*Table 3.1**:** Multiple designs using various geometries: square, sinusoidal, and spiral.*

Sample Design Code	**Sample Design**
Geometry A – Square	
Geometry B – Sinusoidal	
Geometry C - Spiral	

3.4.2. Extrusion-based 3D printing.

The RegenHU printer system was used for extruding thermoplastic polymers and hydrogels with a precision extrusion deposition, using two printheads. The BioCAD software creates a G-Code model to manufacture the scaffolds using different tools on the machine, such as screw extrusion, pneumatic extrusion, and UV light. Screw extrusion was used to print the PCL component; 3gr of PCL pellets were added to the heating chamber, the PCL material was heated and liquefied, and compressed air used to push the material through the printhead. On the printhead, the material is pushed through the nozzle by controlling the movement of the screw to deposit the material on the build plate. Pneumatic extrusion was used to print GelMA; a 10 ml syringe containing the GelMA hydrogel and a needle were loaded into the cartridge cooler, and then inserted into the cartridge holder on the left-hand side of the RegenHU machine. The cartridge cooler is connected to the cooling unit, which is a tank of temperature-controlled liquid used to cool down the material. Photocuring is achieved by UV light incorporated within the RegenHU system emitting a wavelength of 365nm with a maximal optical output power of 500mW.

Each material required different parameters to set up the RegenHu machine, such as needle gauges, pressures, temperatures, and the material used for depositing the material on the platform. All of these parameters help to generate the filament, which creates the structure of the scaffold. The temperature of the material is one of the most important parameters, as each material has its viscosity parameter. **Figure 3.6** represents the 3D bioprinting setup of the RegenHU; as mentioned before, the PCL pellets were added to the heated chamber set at 100°C, and the printing temperature was set at 80°C, where the screw printhead moved the material to the G32 nozzle and a first layer of PCL. Then, the pneumatic extrusion of 10% w/v of GelMA hydrogel was performed by introducing the material to a 10 ml syringe with a 32G needle. The syringe was inserted into the cartridge cooler for 30 min before starting the printer to stabilise the material at 18°C. The GelMA filament was printed on the same layer as the PCL and then exposed to the UV light to crosslink the GelMA, with an exposure time of around 4 min per layer of GelMA. The procedure was repeated for each layer until the OC scaffold was manufactured. The parameters for manufacturing a PCL/GelMA scaffold are presented in **Table 3.2**; to identify these parameter values, multiple experiments were undertaken, altering each parameter.

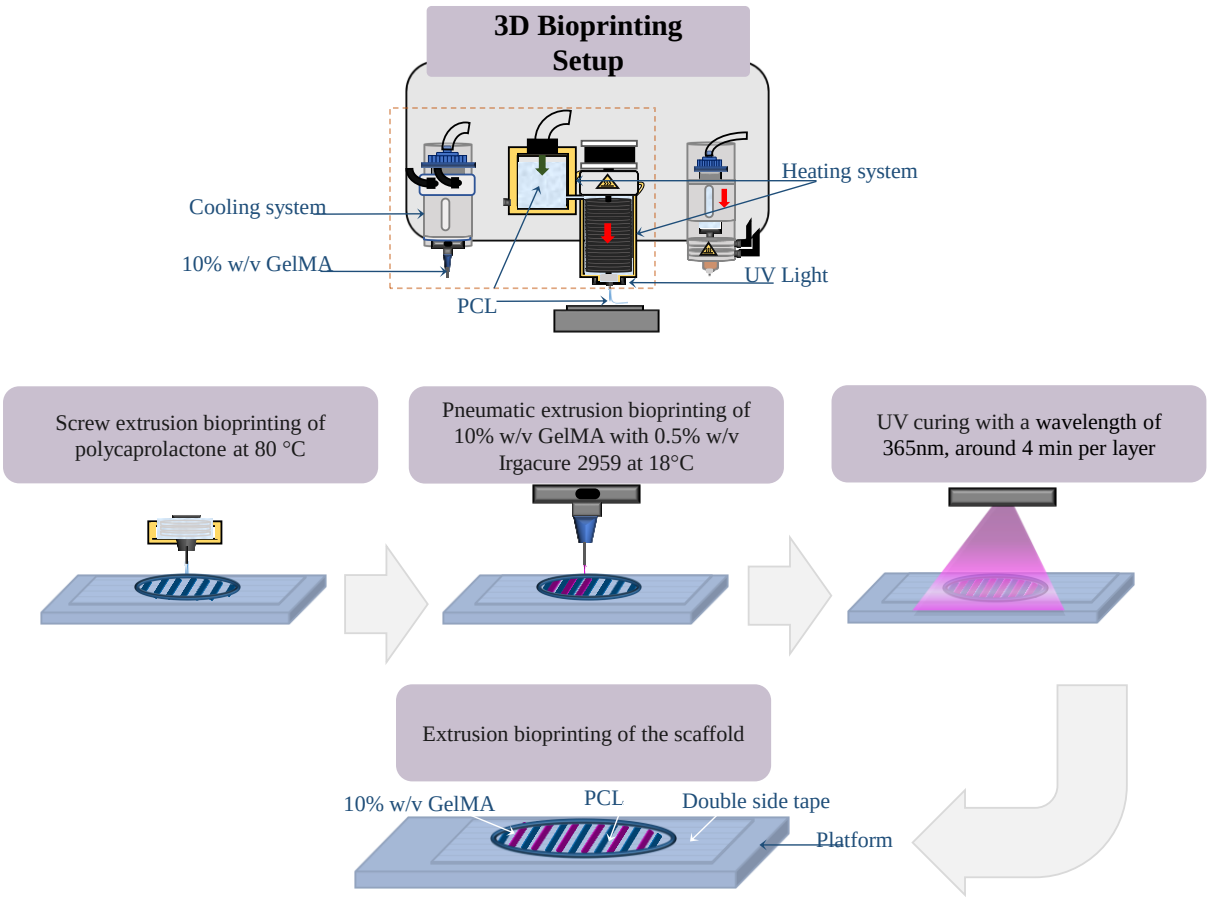


Figure 3.6 3D Bioprinter RegenHU setup. Schematic showing the complete process to manufacture a dual material scaffold using two printheads, one with GelMA and the other with PCL and UV light (365nm wavelength).

Table 3.2. RegenHU parameters for the extrusion-based 3D printing of PCL/GelMA.

Material	**Needle**			**Machine Condition**		**Temperature**	**Printhead Conditions**		**Tape**
	Gauge	Inner Diameter	Length	Feed rate	Manual Pressure		Pressure	Extrude Feed	
PCL	32	0.1 mm	4.75mm	17.5	No pressure	Heater printhead = 80.0˚C Heater tank =100.0˚C	No pressure	35.0 rev/m	Double-sided tape
GelMA	32	0.1 mm	6.35mm	3.5	0.516MPa	Cooling System= 18 ˚C	Pressure	NA	Double-sided tape

3.4.3. Surface Morphology.

Scanning Electron Microscopy (SEM) was used to determine the morphology of the materials fabricated. This type of microscopy employs electron energies ranging from 10-40 kV to create a beam of high-energy electrons interacting with the sample's atoms. This interaction results in the emission of secondary electrons and radiation in the form of X-rays. Detectors collect the emitted secondary electrons and provide information on the topography of the sample's surface; backscattered electron detectors use scattered electrons to produce an image of the sample's composition.

An SEM tabletop microscope TM3030 Plus Hitachi (Hitachi, Tokyo, Japan) was employed in this research to study the properties and surface morphology of the materials. Samples were fixed onto sticky carbon tabs to the SEM specimen stub and coated with gold (Au) for secondary electron mode viewing using an Agar sputter coater A7260 B7340 240V/50Hz instrument. High-magnification images of 500x were captured for each material and analysed on ImageJ.

3.4.4. Mechanical Properties.

Compression testing was conducted using an Instron C 5966 Universal Testing Machine (Instron Ltd.) with a 10KN load cell and a 0.1 mm/min displacement rate. Unconfined compression tests were performed on three different types of scaffolds such as PCL without GelMA, PCL with GelMA and PCL/GelMA with cells. Samples (n=6), OC scaffolds of 8mm in diameter with 4.6mm in thickness and square, sinusoidal and spiral scaffolds of 8mm in diameter and 1.2mm in thickness, were placed between the platens, as in

Figure 3.7 and carried out with the compression test for each design and the OC scaffold. Tested under compression makes an approximation of the biomechanical behaviour of osteochondral tissue, as it could maintain structural integrity under compressive stresses.

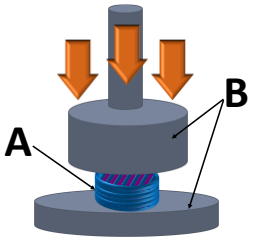


Figure 3.7 Unconfined compression setup. Conducting the unconfined test, A) the sample is placed between B) the two stainless steel platens and compressed.

The PCL/GelMA scaffolds were kept in PBS, and the PCL/GelMA/Cells were kept in media at 37°C for one week to ensure that the GelMA and cells were fully hydrated. The influence of GelMA and cell conditions on the Youngs modulus in an unconfined compression were compared using PCL, PCL/GelMA, and PCL/GelMA/Cells scaffold groups. Mechanical tests were performed at a constant compression rate of 0.05 mm/s to a maximum strain of 35%. All tests were carried out for each design and the OC scaffolds.

3.4.5. Porosity.

The morphologies of 3D-printed PCL/GelMA scaffolds were observed under the microscope. Then microscope images of three scaffolds of each geometry were processed using the ImageJ software (version 1.53t, National Institutes of Health, USA) to calculate the scaffold's printed porosity (PP.) using the Equation 5.

$$\boldsymbol{Porosity = \frac{Area\ of\ pores}{Total\ area} X\ 100\%} \qquad (5)$$

3.4.6. Finite Element Software – Abaqus.

The Finite Element Analysis (FEA) software package ABAQUS/CAE 2019 (Abaqus Standard; Dassault Systèmes SIMULIA Corp.) was used to create a model to predict deformation to predict the deformation behaviour of the OC scaffold under unconfined compression. **Figure 3.8** represents the steps to create and run the model on ABAQUS. Briefly, the scaffold design model was developed using SolidWorks modelling software based on the BioCAD RegenHU designs. Scaffold design geometries were imported and modelled using ABAQUS/CAE 2019. The geometries assembly were set up to simulate the unconfined compression enclosed between two platens. Compression was performed for PCL and PCL/GelMA scaffolds, with a dimensions of 8mm in diameter and 1.2 mm in thickness and 8mm in diameter and 4.6 mm (n=6), as explain previously in Section 3.4.4. In addition, with the analysis of the PCL and GelMA cube-cast compression tests, this information was added to a customised library of the material, such as linear stiffness, elastic modulus, and elastic modulus.

The centroid of the top compression plate was locked in place for all directions, but the vertical and the centroid of the bottom compression plate were constrained. For a compressive load of magnitude, 5KN and 10KN were simulated on the top plate to create the deformations of the material. To prevent sliding, the model was subjected to universal contact conditions with a 0.1 coefficient of friction.

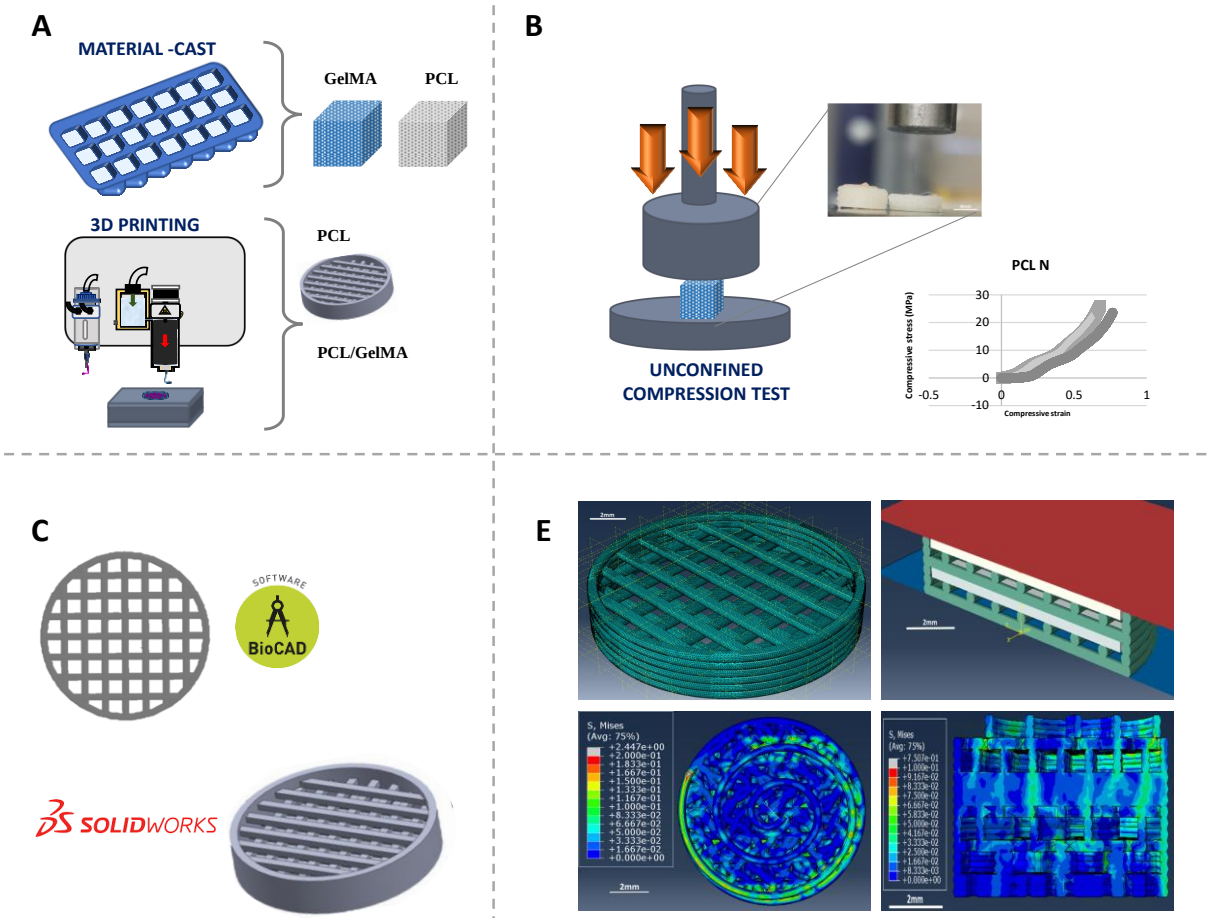


Figure 3.8 Overview of workflow for FE modelling in ABAQUS. A) Cast and printed scaffolds of each material were performed for B) experimental analysis of PCL and GelMA mechanical behaviour under unconfined compression to access materials properties and validate numerical predictions. C) BioCAD software was used to create the designs, and the geometries that were copied to D) Solidworks CAD designs and then imported to ABAQUS to do the FEA model.

3.5. Mammalian Cell Culture and Viability Analysis.

3.5.1. Cell Culture.

Mouse embryonic fibroblast cells 3T3-E291 (originally obtained from the European Collection of Authenticated Cell Cultures ECACC) were cultured in tissue culture treated flasks using DMEM (1X) Dulbecco's Modified Eagle Medium with 10 % Fetal bovine serum (FBS), 1% Antibiotic/Antimycotic (solution contained 10,000 units penicillin, 10 mg streptomycin and 25 µg amphotericin B per mL, BioReagent from Merck Life Science UK Ltd), L-glutamine (LG) at 37°C, 5% CO_2 in air. The media was replaced every three days, and the cells were extracted when required for experiments or when 80% confluent (for expansion) from the flasks using 3ml of trypsin-EDTA solution. A haemocytometer was used to count the cells using the Trypan Blue to evaluate the viability of the cells. 3T3 cells were chosen for their cost-effectiveness and availability, serving as a preliminary step to assess scaffold viability.

3.5.2. Scaffold Sterilisation.

Scaffolds were cured during fabrication with the UV light (365nm) of the RegenHU, as explained in **section 3.4.2,** based on the infection detected in the scaffolds the methodology applied was immersed in dH_2O the scaffold right after printing to keep the GelMA hydrated. Afterwards, the scaffolds were removed from the dH_2O and placed into the 24-plate well for final sterilisation. The scaffolds were exposed to UV light for 40 minutes to sterilise them with a wavelength of 254nm using the UV Clave Ultraviolet Disinfection Chamber (B1450 (-E)) Benchmark Scientific, which includes six 4W UV-C bulbs, three on the top and three on the bottom of the chamber allowing >90% UV-C light transmission and highly reflective chamber walls, resulting in 360° exposure with no blind spots.

3.5.3. Scaffold Seeding and Culture.

Scaffolds were assessed for the ability to support cellular attachment, cellular colonisation, and matrix deposition using fibroblast cells. Each scaffold, after sterilisation, was top-seeded by pipetting the cells onto the scaffolds, depending on the surface dimension area. For the 4.6mm high scaffolds, $0.3x10^6$ cells were added; for the 1.2mm high scaffolds, $0.1x10^6$ cells were added. The top-seeded scaffolds were left for three hours at 37˚C in a humidified incubator allowing the cells to settle and attach to the scaffolds. Afterwards, 1000µl of the

culture medium (section 3.5.1) was placed into the wells cultured statically for seven days in 37˚C 5% CO_2 in air in a humidified environment.

3.5.4. Assessment of Cell Viability and Proliferation.

Cell viability and proliferation experiments are assessed to verify the mammalian cell viability when cultured on their scaffolds as an indicator of their biocompatibility. Cells were seeded onto the printed scaffolds and cultured under controlled conditions to assess cell adhesion, and proliferation, within the scaffold environment. This step ensures that the designed scaffolds possess suitable mechanical properties and the ability to support cell attach .

3.5.4.1. Metabolic Activity.

The metabolic activity of the 3T3 o fibroblasts on the scaffolds was assessed using Presto Blue® Cell Viability Reagent (Invitrogen by Thermofisher). The protocol was developed following the manufacturer's instructions. Briefly, scaffolds were removed from the well plate well and added to a new one (so that only cells adherent to the scaffold were detected by the assay). Presto Blue® dye was added at a 1:10 ratio (in culture media) to cover the samples (1 mL). As controls, dilute Presto Blue® reagent was added to empty wells of the well plate (blank), and to scaffolds with no cells seeded (scaffold blank). Dilute Presto Blue® reagent was also added to the wells where the scaffolds were originally seeded. The samples were incubated at 37°C, 5% CO_2 in air for 30 min in a dark environment; each sample 200 µl aliquots were transferred into a 96-well plate and fluorescence measured at an excitation of 560nm and an emission of 590 nm using a Tecan M200 plate reader (TECAN, Austria GmbH) on days 1, 3 and 7. Total cell numbers for the presto blue standard curve were quantified by adding cell concentrations of 0, $0.075x10^6$, $0.15x10^6$, $0.3\ x10^6$, $0.6\ x10^6$, and $1.2\ x10^6$ cells to the plate well with Presto blue aliquot, standard curve is displayed in **Appendix B.**

3.5.4.2. Toluidine Blue O.

Histological staining of cell seeded scaffolds was conducted on days one, three, and seven using Toluidine Blue O. Toluidine Blue O working solution was prepared by dissolving 0.1 g of Toluidine Blue O powder with 100 ml of distilled water while stirring. The samples underwent fixation in 4% paraformaldehyde for an hour at RT. Once fixed, they were washed

in PBS and stained with the toluidine blue aliquot for an hour, followed by 3X washing in PBS. The samples were then sliced in half and observed under the microscope.

3.5.4.3. Cell Viability.

The scaffolds were assessed on day one, day three and day seven. Cell viability was assessed using a LIVE/DEAD™ Viability/Cytotoxicity Kit, for mammalian cells (Molecular Probes, ThermoFisher Scientific, Inc.) as per the manufacturer's protocol**.** The steps followed which included washing the cell-seeded scaffolds in phosphate-buffered saline (PBS) followed by incubation in the dark at RT in the dilute dye solution (10ml of PBS, 5 µl of Calcein AM and 20µl Ethidium Homodimer-1) for 30 min. and then fixed in 4% paraformaldehyde(PFA) for an hour at RT. Measurements were performed on a Zeiss LSM T-PMT 880 Confocal Fluorescence Microscopy (Jena, Germany) for 488-530 nm excitation and fluorescence 530-561 nm with a Leica TCS LSI 0306809 Laser Scanning Confocal Microscope. Live cells were stained green, and dead cells were stained red.

3.5.4.4. DNA Content as a Measure of Cell Number/Proliferation.

DNA content was assessed using the Quant-iT dsDNA HS kit (Invitrogen), following the manufacturer's instructions. DNA content was measured as an indicator of cell proliferation on the scaffolds at day one, day three and day seven. **Figure 3.9** indicates the steps followed; the scaffolds were cut into small pieces and placed in Eppendorf tubes. Lysis freezing solution was prepared by diluting 1.5x Trizma® hydrochloride solution with 8.5x dH_2O and adding 1% Triton X100, this was then mixed until the liquid was homogeneous. This solution was centrifuged at the 4400 rpm for 5 min to stabilise the liquid and to remove bubbles. To each Eppendorf tube (containing scaffold) 1000µl Lysis freezing solution and frozen at - 80˚C.

The samples were defrosted and frozen three times prior to starting the Quant-iT dsDNA HS assay. Samples were first centrifuged at 1000 rpm for 5 min. Using the Quant-iT dsDNA HS kit (Invitrogen), the Quant-iT dsDNA HS buffer was prepared by diluting the reagent 1:200 in dH_2O. A 96-well pate was loaded with 180 µl of the buffer and reagent, and then 20 µl scaffold lysis aliquot in duplicate. Fluorescence was measured with a plate reader (Tecan M200 plate reader (TECAN, Austria GmbH) at the excitation and emission wavelengths of 485 and 535 nm, respectively. Total cell numbers for the DNA standard curve were

quantified using Quant-iT dsDNA HS kit (Invitrogen) from the lysates of known cell number 0, 5, 10,20,40,60,80 and 100 ng/µl, standard curve is displayed in **Appendix C2.**

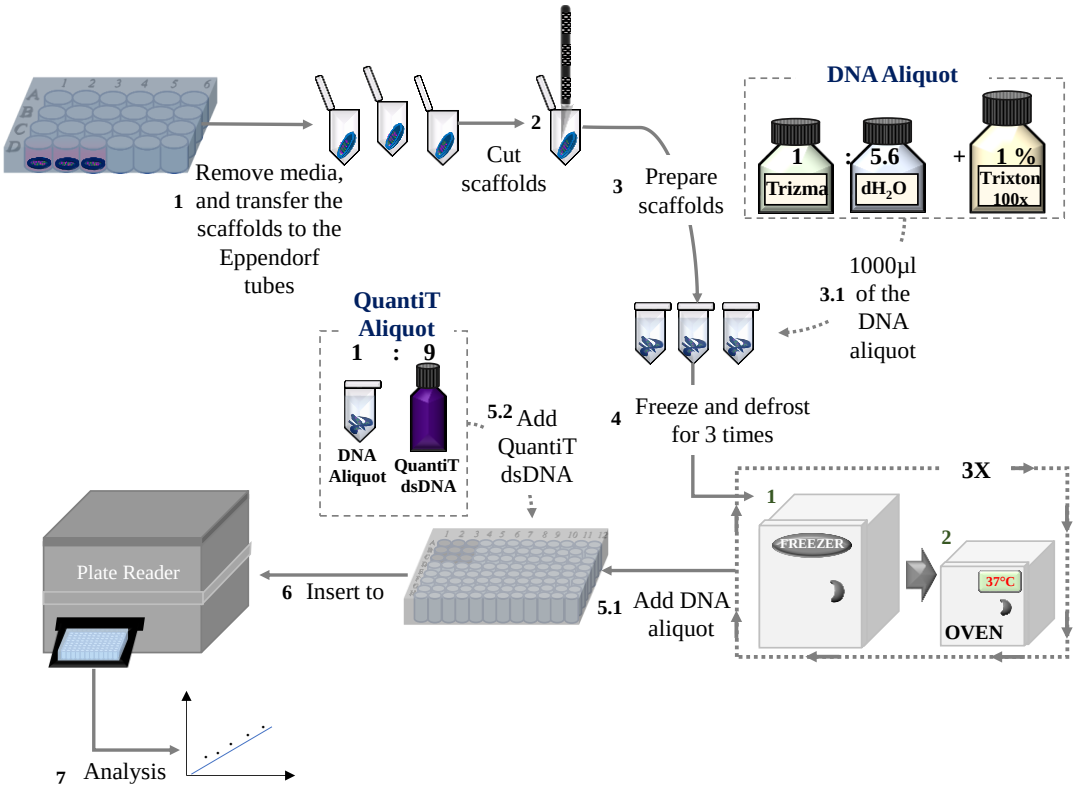


Figure 3.9 Schematic of the DNA quantification using QuantiT dsDNA kit. (1) media was removed, and samples were transferred to the Eppendorf tubes. (2) Samples were sliced and mashed, and (3) 1000ul of Lysis freezing solution was added to each sample. (4) Samples were frozen and defrosted 3X at -80˚C (5) 20ul of the sample aliquot and 180ul of Quant-iT reagent were transferred to a 96 well plate. (6) fluorescence was measured at a: 502/523 nm (7) and analysed.

3.6. Data Analysis and Statistical Analysis.

GraphPad Prism 9 [GraphPad Software Inc., San Diego, USA] was used for the statistical analysis and graphical plotting of data. Compression data is expressed as the average ± standard deviation (S.D.), N=6, n = 3 unless otherwise stated, and analysed for statistical significance using an analysis of variance (ANOVA) test analysis to compare between 3 or more data sets. For cell data ± standard deviation (S.D.), N=3, n = 3 unless otherwise stated, and analysed for statistical significance using an analysis of variance (ANOVA) test analysis to compare between 3 or more data sets. A corresponding p value of < 0.05 * represented a statistically significant difference. is expressed as the average Further levels of statistical significance evaluated included **$p < 0.01$, ***$p < 0.001$, ****$p < 0.0001$ *.

Chapter 4. Characterisation of Polycaprolactone and GelMA for 3D co-printing.

This chapter presents material characterisation work to fully understand the physical properties and behaviour of PCL and GelMA, for the extrusion-based 3D printing scaffolds produced on the RegenHU machine. The materials' rheological properties, swelling ratio, and degradation rates are quantified, since these properties directly influence the mechanical properties and cell behaviour for tissue regeneration. In addition, the implication for design scaffolds to create novel designs for extrusion-based printing and to customise the architecture to meet the required mechanical properties of the tissue.

4.1. Introduction.

An essential element of tissue engineering are the biomaterials that mimic the structure of the native extracellular matrix, promoting cell growth and tissue regeneration. While bone and cartilage differ in composition and mechanics, they converge in the osteochondral tissue. Therefore, the requirements for scaffolds must be meticulously assessed, considering factors such as chemical composition, biological and structural characteristics, degradation behaviour, and fabrication process . (Dwivedi et al., 2020; Grigore, 2017b; E. J. Lee et al., 2014).

Biomaterials for the OC scaffolds can be natural or synthetic, and they can be biodegradable or non-biodegradable. Various synthetic, biodegradable polymers, such as poly lactic acid (PLA) (Esposito Corcione et al., 2019; Kosik-Kozioł et al., 2017; Tamaddon et al., 2016), poly-L-lactide (PLLA), PCL (Nowicki et al., 2020; Patrício et al., 2014; Peng et al., 2018; F. Wang et al., 2022), and poly lactic-glycolic acid (PLGA)(Hiep & Lee, 2010; Kwak et al., 2016; Liang et al., 2018a; Nie & Wang, 2007) copolymers, have been utilised to enhance biomaterial properties in diverse applications. However, their hydrophobic nature often limits their ability to encapsulate cells within physical constructs. Among these synthetic materials, PCL has recently garnered significant attention for the OC applications (Janmohammadi & Nourbakhsh, 2019; Janoušková, 2018; Prasad & Pramanik, 2022).

On the other hand, natural polymers, mostly hydrogels, possess a natural three-dimensional structure and are hydrophilic. Hydrogel biomaterials are being extensively researched due to their resemblance to the extracellular matrix (ECM)(Bryant & Anseth, 2002; Costantini et al., 2016), similar water content, and mechanical properties similar to natural tissues.

Hydrogels derived from sources such as gelatin(Chang et al., 2004; J. Liu et al., 2019b), collagen(Bernhardt et al., 2018; Levingstone, Thompson, et al., 2016c; Parisi et al., 2020), chitosan (Singh & Dutta, 2015; Varoni et al., 2018), cellulose(L. Gu et al., 2020; Isobe et al., 2018), alginate(Filardo et al., 2018; W. Liu et al., 2022), and hyaluronic acid (HyA) (Fischer et al., 2012; Flégeau et al., 2022; Kogan et al., 2007). find broad applications in biological contexts, thanks to their cell viability, cellular interactions, and biodegradability Nevertheless, their limitations include low mechanical strength, uncontrolled structural degradation, susceptibility to contamination, and batch-to-batch variability(Ahmed, 2015; Hoffman, 2012; Vedadghavami et al., 2017).

The aim of this chapter is to investigate and analyse the mechanical properties of PCL and GelMA, specifically focusing on their swelling degradation behaviour and extrudability. This investigation is crucial for understanding the suitability of these materials for OC scaffolds.

4.2. Characterisation of 3D Printing Polycaprolactone.

PCL is characterised in this section by its rheology qualities; it is a flexible thermoplastic semicrystalline polymer that is frequently employed for its advantageous properties such as biocompatibility, biodegradability and simplicity of processing. The glass transition temperature of PCL has been determined to be -60 °C, while the melting point varies between 56 and 65 °C, as mentioned in **chapter 2, Table 2.4.**

4.2.1. Rheological Properties.

Material viscosity is one of the most important parameters in 3D printing. The viscosity of the PCL was measured by changing the temperature from 60 °C (melting temperature) to 160 °C. The measured damping function was employed in the constitutive modelling of the viscoelastic behaviour of the PCL. Molecular weight is the main parameter influencing the flow behaviour of a polymer at temperatures above the glass transition temperature for amorphous materials or melting temperature for semicrystalline polymers (Vinogradov & Malkin, 1980); therefore, different MWs of PCL were investigated.

To study the rheological properties under shear force, the viscosity of PCL with different M_W was measured as a function of increasing shear rate. A constant temperature of 160 °C, was maintained , following the approach of Arraiza et al, to ensure the material a molten

state for accurate viscosity measurements (Arraiza et al., 2007). The shear rate was increased from 0.01 s-1 to 1000 s-1 was applied to PURASORB PC12 (Mw 120,000 g/mol), PCL 45 (M_n 45,000) and PCL 80 (M_n 80,000). PURASORB PC12, compared to the others, is more unstable and extremely viscous in these conditions, oscillating on the 2000 Pa*s **(Figure 4.1 A**). Due to the high viscosity of the PURASORB PC12 material and the limitations of the rheometer, the test was stopped at a shear rate of 10 s^1, and PURASORB PC12 was discarded. PCL 45 showed shear-thinning behaviour at very low shear rates, and a transition to Newtonian behaviour was observed (31Pa*s)(**(Figure 4.1B**). Similar activity was observed for PCL 80 but with a higher viscosity (143Pa*s) **(Figure 4.1 C**).

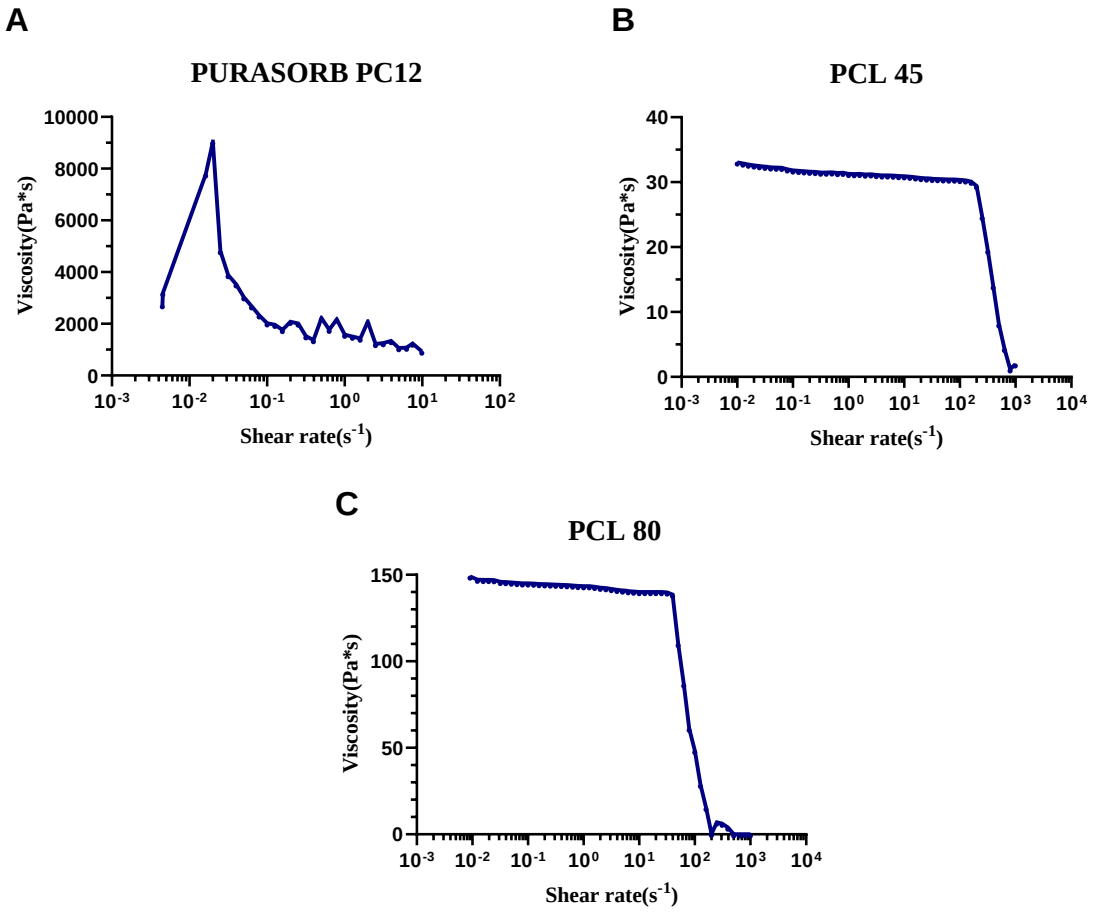


Figure 4.1 Shear viscosity of the PCL. A) PURASORB PC12 B) PCL45, C)PCL 80. Results denote mean± SD (n=3, N=3).

The viscosity of the PCL with different M_w was measured as a function of increasing temperature from 60 °C to 160°C at a constant shear rate of 100 s^{-1}.The shear rate was held

at a constant $100s^{-1}$ for PURASORB PC12 (M_w 120,00), PCL 45 (M_n 45,000) and PCL 80 (M_n 80,000). PURASORB PC12 was not able be measure due to the high viscosity.

The viscosity of PCL depends on temperature and molecular weight; the viscosity values of PCL 45 decreased from 250 Pa-s to 28.65 Pa-s—and PCL 80 viscosity values from 5000 Pa-s to 101 Pa-s (as shown in **Figure 4.2**).

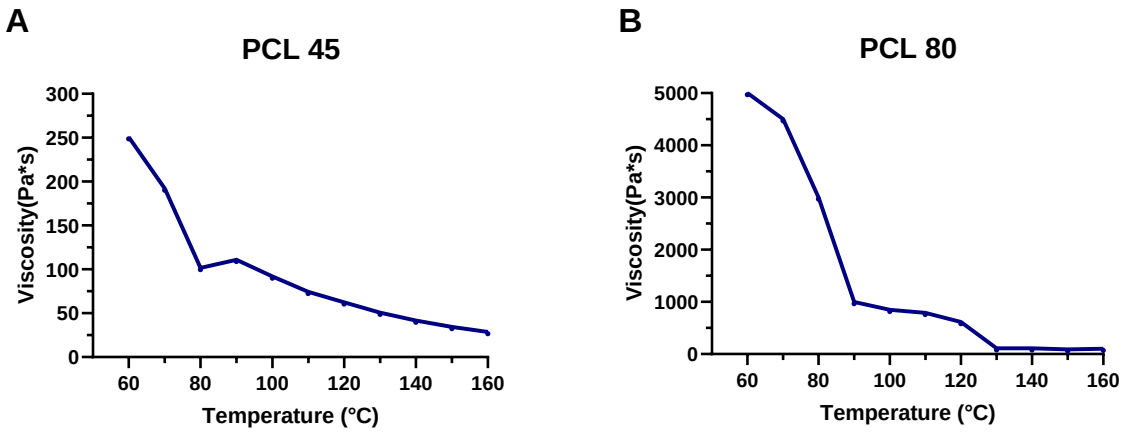


Figure 4.2 Effect of temperature on the PCL. A) PCL45, B)PCL 80. Results denote mean± SD (n=3, N=3).

PCL 45 and PCL 80 have previously been demonstrated as printable materials (Domingos et al. 2009, Hutmacher et al. 2001). Of the two materials, PCL 45 was chosen because the processing temperature is lower than PCL 80, and it prevents thermal degradation.

4.3. Characterisation of 3D Printing GelMA.

The characterisation of GelMA was conducted through an assessment of the degree of methacrylation and rheological analysis. The degree of methacrylation determined its crosslinking potential, influencing its suitability for 3D bioprinting applications., while the rheological testing provided insights into its flow and viscoelastic properties.

4.3.1. Degree of Methacrylation – GelMA.

The DM was measured as stated in **section 3.3.1.2**. The 1H-NMR spectra can be observed in **Figure 4.3**; the phenylalanine signal has been highlighted in red, the methacrylic groups signal in green and the lysine methylene signal in blue. Three different batches of GelMA were compared with gelatin. The phenylalanine signal was used for normalisation.

Compared to unmodified gelatin, new signals could be observed in the spectra of GelMA at 5.3-5.7 ppm, representing the new methacrylate groups and the decreasing of the lysine methylene signal at 2.8 ppm. The data suggest that the gelatin was successfully modified on the molecular level by the conversion of the amino groups. From the quantitative analysis of the NMR spectra, it was calculated that the DM for GelMA 1, 2, 3 and 4 batches was 75%, 87.5 %, 98.13% and 99.88%, respectively. The variation in the DM of the different samples could have been caused by user variability when adding the methacrylic anhydride dropwise. Nichol et al., 2010 showed that the DM affects the mechanical properties of the final GelMA structures, showing that a high degree of DM (81.4%) was best for micro-patterning applications, and a low degree (20%) formed very fragile gels. They also showed that the compressive modulus of high DM was 2-fold higher than medium and 6.6-fold higher than low. Given that the DM has a big effect on the final structures, it is very important to be able to control it and consequently have less batch-to-batch variation. It was therefore decided not to use batch 1 because the DM was very low compared to 2, 3 and 4. The synthesis protocol for the four batches was the same so human error might have caused the discrepancies in DM.

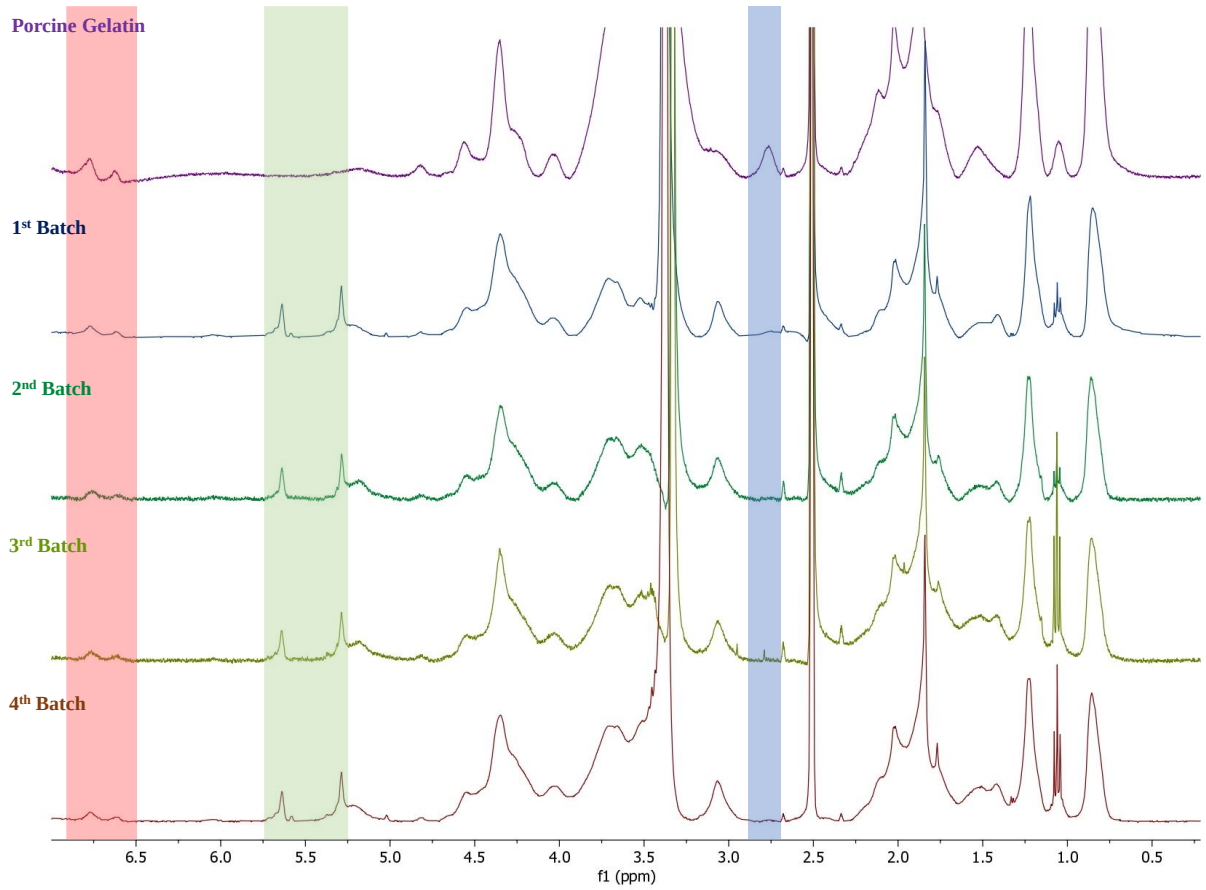


Figure 4.3 1H-NMR spectra of gelatin and GELMA batches. Signals have been highlighted, in red for the phenylalanine signal, the green for the methacrylic groups signal and in blue for the lysine methylene signal.

4.3.2. Rheological Properties.

The effect of different concentrations of GelMA was analysed by conducting rheology measurements over a range of shear rates, between 0.01 s^{-1} to 1000 $s^{-1,}$ determining the different viscosities of GelMA concentrations, as shown in **Figure 4.4**. With a higher concentration of GelMA, there is a significant viscosity increment ($p < 0.0001$) between them. All formulations exhibited shear thinning properties, desirable for extrusion-based printing, at a shear rate of 10^0 values ranging from 0.0025 ±0.0001 to 0.0311 ±0.0054 with increasing concentrations between 5% w/v to 20% w/v of GelMA. However, the data prior shear rate of 10^0 was not considered due to the system equilibration, this initial data was considered inaccurate as the system was stabilising.

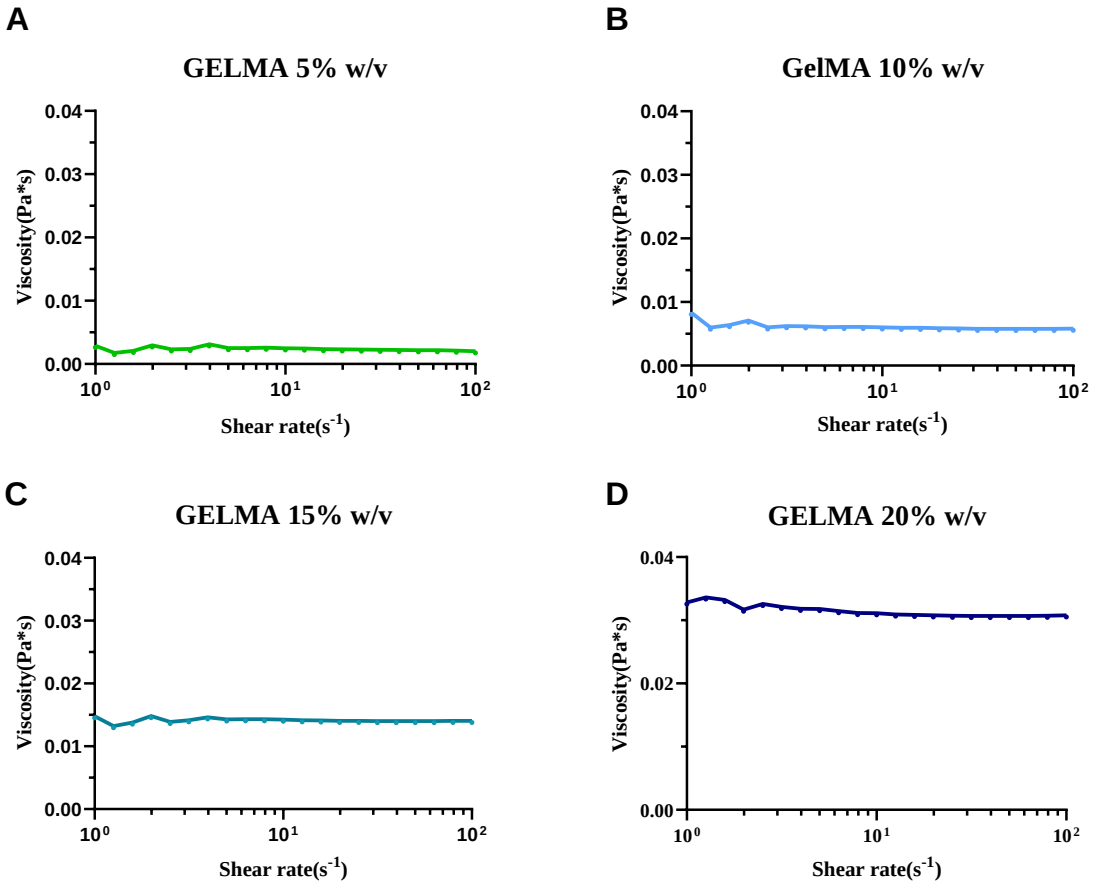


Figure 4.4 Shear rate vs. viscosity for GELMA concentration A) 5%, B) 10%, C) 15% and C) 20%. Results denote mean± SD (n=3, N=3).

During extrusion-based printing, it was anticipated that sufficiently high shear rates would be experienced for the ink viscosity to be applicable. The pressure exerted by the RegenHu machine on the formulations during printing would be constant, although, during periods of inactivity, it could fluctuate at the beginning of the printing. In addition, the results suggest that the GelMA 20% (w/v), due to its high viscosity, may be difficult to print. **Table 4.1** summarises the viscosity values for each GelMA concentration at shear rates of 10^0, 10^1, 10^2.

Table 4.1 Viscosity at different shear rates of the four different concentrations of GelMA. Results denote mean± SD (n=3, N=3).

GelMA	**Viscosity at Shear Rate**		
% (w/v)	**10^0**	**10^1**	**10^2**
5%	0.0025 ±0.0001 (Pa*s)	0.0020 ±0.0002 (Pa*s)	0.0044 ±0.0002 (Pa*s)
10%	0.0060 ±0.0003 (Pa*s)	0.0058 ±0.0002 (Pa*s)	0.0059 ±0.0004 (Pa*s)
15%	0.0142 ±0.0078 (Pa*s)	0.0140 ±0.0062 (Pa*s)	0.0140 ±0.0034 (Pa*s)
20%	0.0311 ±0.0054 (Pa*s)	0.0338 ±0.0077 (Pa*s)	0.0344 ±0.0088 (Pa*s)

Temperature can also alter the viscosity of GelMA, tests were performed by increasing temperature from 10°C to 50°C with a constant shear rate of 100 s^{-1}. GelMA 5% (w/v) shows a really low viscosity, which prevents extruding a filament (**Figure 4.5 A**). GelMA 15% (w/v) and GelMA 20%(w/v) show instability and high viscosity peaks, presenting a change in gelation behaviour when the data are collected at a different set of temperatures (**Figure 4.5** C and **Figure 4.5 D**). In contrast to the 10% (w/v), which shows higher temperature stability and gives a temperature range of 15°C to 20°C at which the viscosity is suitable for printing (**Figure 4.5 B**).

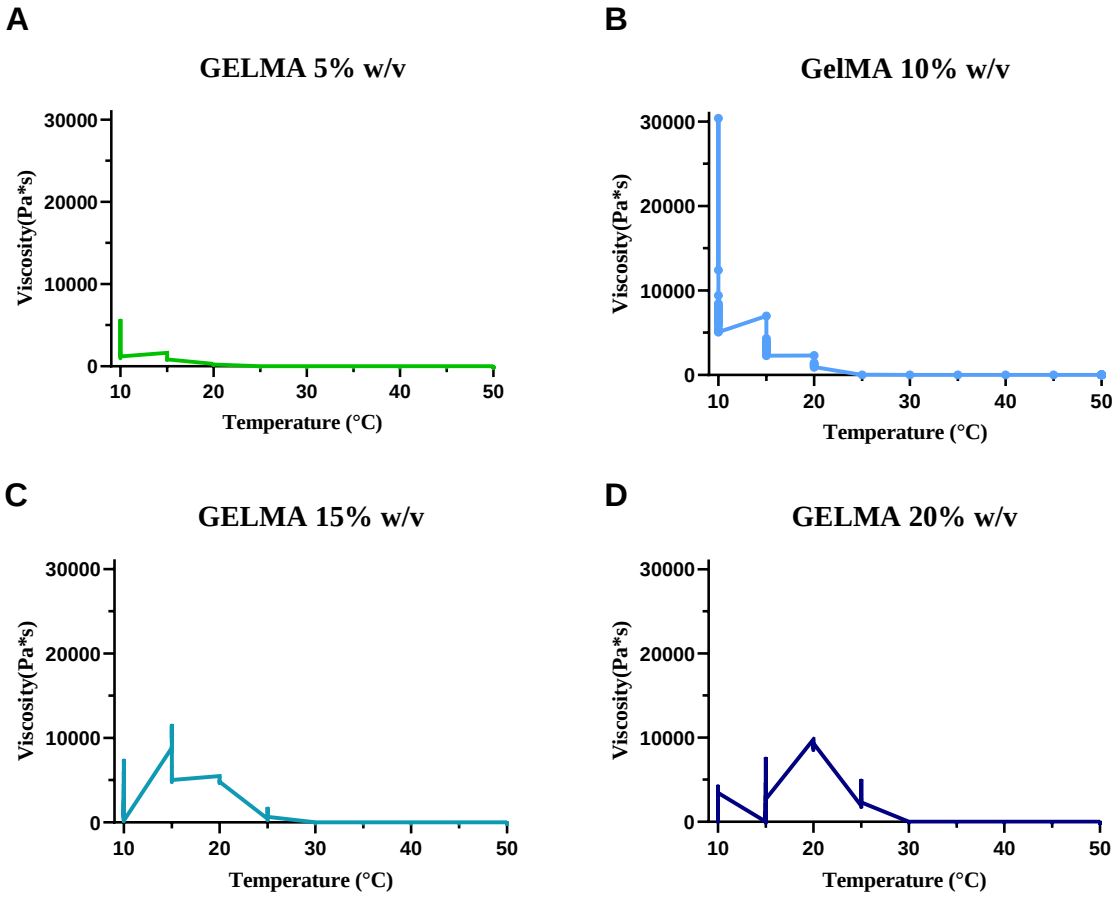


Figure 4.5 Temperature vs. viscosity for GELMA concentration A) 5%, B) 10%, C) 15% and C) 20%. Results denote mean± SD (n=3, N=3).

The viscosity behaviour of GelMA at a concentration of 10% (w/v) was systematically investigated to assess its printability under varying temperature conditions. Within the temperature range of 15°C to 20°C, GelMA 10% (w/v) exhibited a viscosity of 3052.67 Pa*s. Notably, as the temperature surpassed 20°C, a discernible reduction in viscosity occurred, rendering the material less conducive to the printing process. Conversely, when temperatures dropped below 15°C, the viscosity significantly increased to an unstable extent, rendering the material impractical for printing applications.

A comprehensive summary of viscosity values for GelMA at different concentrations is provided in **Table 4.2** around the temperature spectrum from 10°C to 50°C. This tabulated data effectively captures the concentration-dependent viscosity trends, further contributing to a general understanding of GelMAs' rheological behaviour under distinct thermal conditions.

Table 4.2 Viscosity at different temperatures of the four different concentrations of GelMA. Results denote mean± SD (n=3, N=3).

Viscosity at	GelMA 5 % (w/v)	GelMA 10 % (w/v)	GelMA 15 % (w/v)	GelMA 20 % (w/v)
10 °C	1553.33	7728.33	1701.23	3081.69
15 °C	910.54	3052.67	7183.33	1103.12
20 °C	256.67	1053.62	4791.67	9004.00
25 °C	0.12	44.43	798.88	2553.00
30 °C	0.33	0.02	0.034	0.10
35 °C	0.13	0.02	0.013	0.05
40 °C	0.04	0.03	0.02	0.05
45 °C	0.04	0.01	0.02	0.049
50 °C	0.01	0.02	0.01	0.03

Surface tension analysis constitutes a crucial facet of the GelMA characterisation process, providing insights into its physicochemical properties. The experimentation was conducted under controlled conditions at RT, involving the assessment of an average of three droplets per sample. In **Figure 4.6**, a graphical representation is presented for Ethylene Glycol and GelMAs' pressure-versus-time trend, exposing the measured surface tension values corresponding to different GelMA concentrations. The 10% (w/v) GelMA shows a parallel behaviour with potential rheological attributes similar to the Ethylene Glycol, providing anticipation of its flow dynamics under similar conditions with predictable viscosity behaviour.

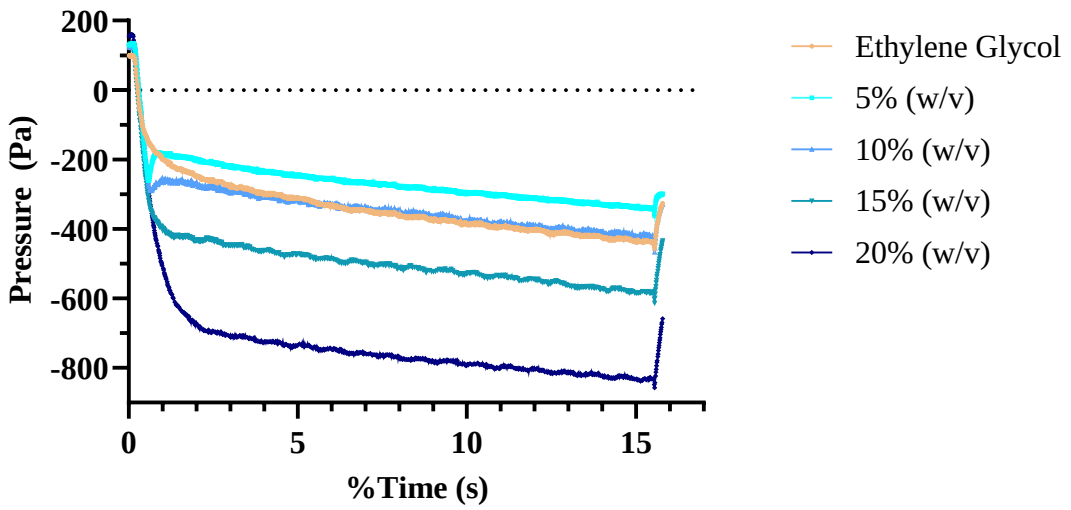


Figure 4.6 Pressure difference in time for the 5% (w/v), 10% (w/v), 15% (w/v) and 20% (w/v). Results denote mean ± SD (n=3, N=3).

The evaluation of surface tension yielded distinct values across the range of GelMA concentrations. Specifically, the surface tension measurements were determined as follows: 59.833 ± 3.836 mN/m, 54.796 ± 3.253 mN/m, 59.348 ± 3.136 mN/m, 59.171 ± 2.552 mN/m for GelMA concentrations of 5% (w/v), 10% (w/v), 15% (w/v), and 20% (w/v), respectively. These outcomes are detailed comprehensively in **Table 4.3**, highlighting the concentration-dependent variations in surface tension characteristics for the GelMA composite.

Table 4.3 Superficial tension, viscosity, and density of GelMA concentrations. Results denote mean ± SD (n=3, N=3).

% (w/v) GelMA	Density (ρ)	Drop mass (g)	Surface Tension (mN/m)	Viscosity (mPa*s)
Ethylene glycol (Control)	1110.0	10.711 ± 4.489	45.633	11.196
5%	839.5	14.041 ± 0.903	59.833 ± 3.836	4.957
10%	881.5	12.861 ± 0.790	54.796 ± 3.253	10.399
15%	881.5	13.932 ± 0.767	59.348 ± 3.136	20.964
20%	904.0	13.889 ± 0.615	59.171 ± 2.552	38.172

As previously, 10% (w/v) GelMA shows 881.5 g/mL of density, 10.39865595 mPa*s of viscosity and 54.796 ± 3.253 mN/m for the surface tension. The behaviour of this hydrogel leads to lower capillary forces and thus decreases water absorption and swelling, making suitable for printing.

Co-printing will be done with PCL, white filament, and GelMA, transparent filament; dying the GelMA was done to provide greater visibility of the material. The added dye concentration was analysed so as not to affect the printing properties and to be as close as possible to the 10% already selected. 10% (w/v) GelMA with different percentages of dye, 0.5%, 1%, 1.5% and 2%, was analysed using the rheometer and at increasing temperature from 10°C to 50°C with a constant shear rate of 100 s^{-1}, as shown in **Figure 4.7A**. As well as the rheology over a range of shear rates, between 0.01 s^{-1} to 1000 s^{-1} at 15°C, determining the difference viscosities, as shown in **Figure 4.7 B**.

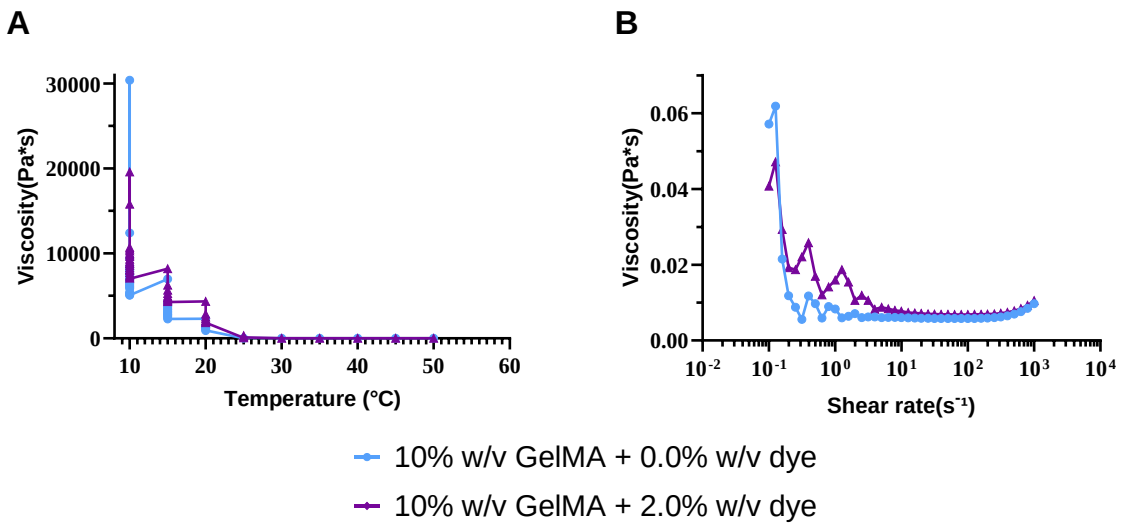


Figure 4.7 10% (w/v) GelMA with and without dye, A) Temperature vs viscosity of 0% and 2% of dye. B) Shear rate vs. viscosity of 0% and 2% of dye. Results denote mean± SD (n=3, N=3).

The graphical depictions presented in **Figure 4.7** provide a visual representation of the limited extent of modification discernible in the viscosity attributes when a dye is introduced to the hydrogel. These graphs vividly demonstrate that alterations in temperature or shear rate yield only marginal changes in the viscosity characteristics, highlighting the inherent stability of the hydrogel-dye composite system.

4.3.3. Swelling Analysis

The swelling capacity of a hydrogel is of considerable importance, as it provides an indirect insight into its water absorption capabilities. This feature, in turn, has the potential to serve as a predictive marker for the hydrogel's degradation timeline. Various factors, including the degree of crosslinking and the dimensions of the pores, play a significant role in influencing the hydrogel's swelling behaviour. It is crucial to emphasise that both the swelling capacity and degradation rate stand as key attributes for the optimal performance of hydrogel scaffolds. The GelMA cast cubes were immersed in dH_2O at 37°C to understand the swelling behaviour. As shown in **Figure 4.8**, swelling ratios of the hydrogels remained mostly swollen between week two and week four; afterwards, degradation started to occur to each of the hydrogel samples. The UV crosslinking significantly affects the network structure, with higher UV exposure leading to more robust crosslinking, which can influence the porosity and swelling behaviour of the hydrogels.

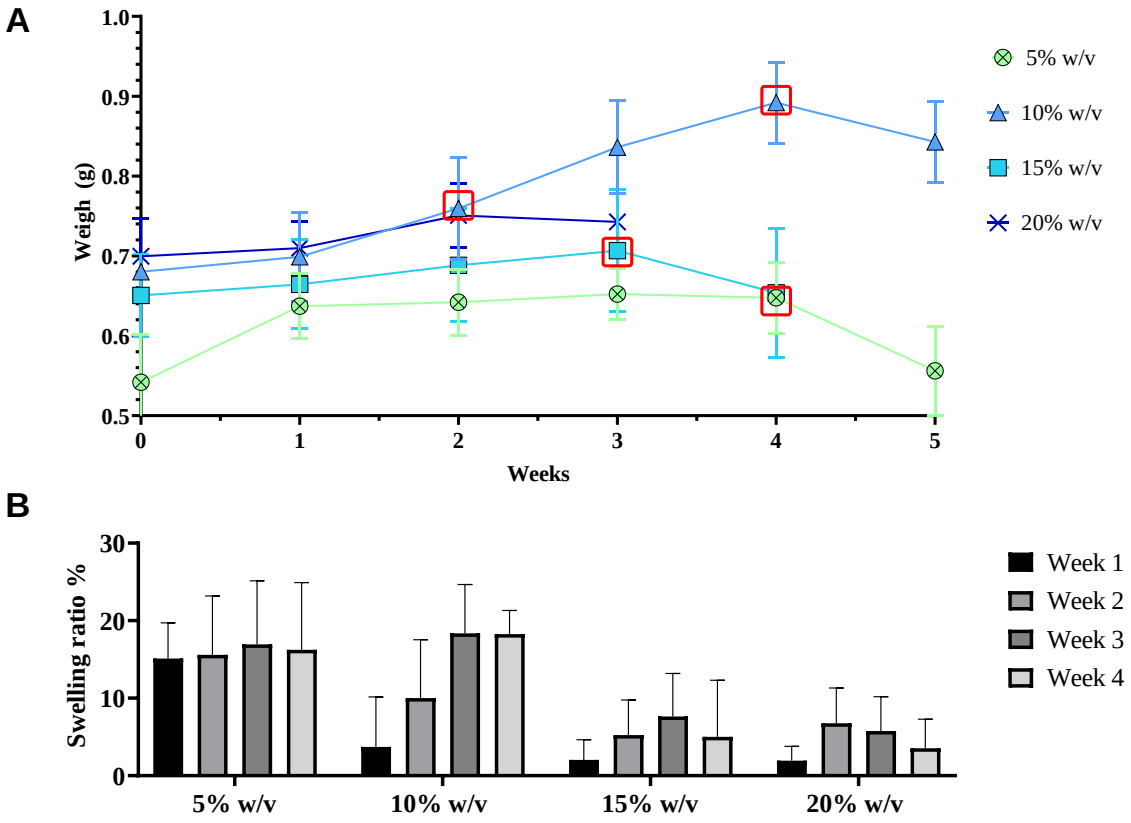


Figure 4.8 Swelling behaviour analysis of GelMA-cast cubes at various concentrations (5% (w/v), 10% (w/v), 15% (w/v), and 20% (w/v)) with 2% (w/v) dye. A) Cube weight variation over the initial 5-week period, investigated at 37°C. B) Percentage swelling ratio at weeks 1, 2, 3, and 4. The graphs provide valuable insights into the swelling characteristics of the GelMA composite across different concentrations and temperature conditions. Results denote mean ± SD (n = 3).

For a more comprehensive characterisation, an investigation into the swelling behaviour was conducted, involving a sequential process of dehydration followed by rehydration aimed at elucidating the hydrogel's response. The dataset presented in the accompanying **Table 4.4** delineates the weights corresponding to their original preparation, the dehydrated state, and subsequent rehydration, conducted at 37°C. Observations reveal a notable reduction in volume during the dehydration phase, ranging from 87.5% to 90.5% across the concentration. As well, the rehydration phase exhibited an increase in volume spanning from 0.5% to 3.2%, depending upon the specific concentration.

Table 4.4 Mass swelling data collected from casted cubes of different concentrations of GelMA, 5%, 10%, 15%, and 20% (w/v). Raw data valuesvat 37°C for each concentration, mass (g), were used to calculate swelling ratio results. Swelling ratio is calculated using Equation (3. Results denote mean ± SD (n = 3).

GelMA samples (%w/v)	Mass(g) as cast	Mass (g) as dried	Mass (g) as rehydrated
5%	0.5419 ±0.0599	0.0561 ±0.0007	0.5550 ±0.0921
10%	0.6801 ±0.0030	0.0851±0.0009	0.6932±0.0242
15%	0.6507 ±0.0521	0.0763±0.0004	0.6638±0.0936
20%	0.6997 ±0.0473	0.0752±0.0005	0.7028±0.0897

Figure 4.9A shows the dehydration process through an illustrative graph, providing a visual representation of the kinetics involved. Particularly, the graph reveals a stabilisation occurring as early as the first day of the dehydration process, understanding the materials swelling under varying conditions. Additionally, images were captured to show the gradual reduction in volume of the casted cube. On the contrary, **Figure 4.9B** illustrates the rehydration process, showing the cubes return to their original dimensions. From this interpretation, it can be deduced that the shape of the cube does not undergo substantial changes following the cycle of dehydration and rehydration. These observations collectively underscore the robustness of the materials' structural integrity throughout these processes.

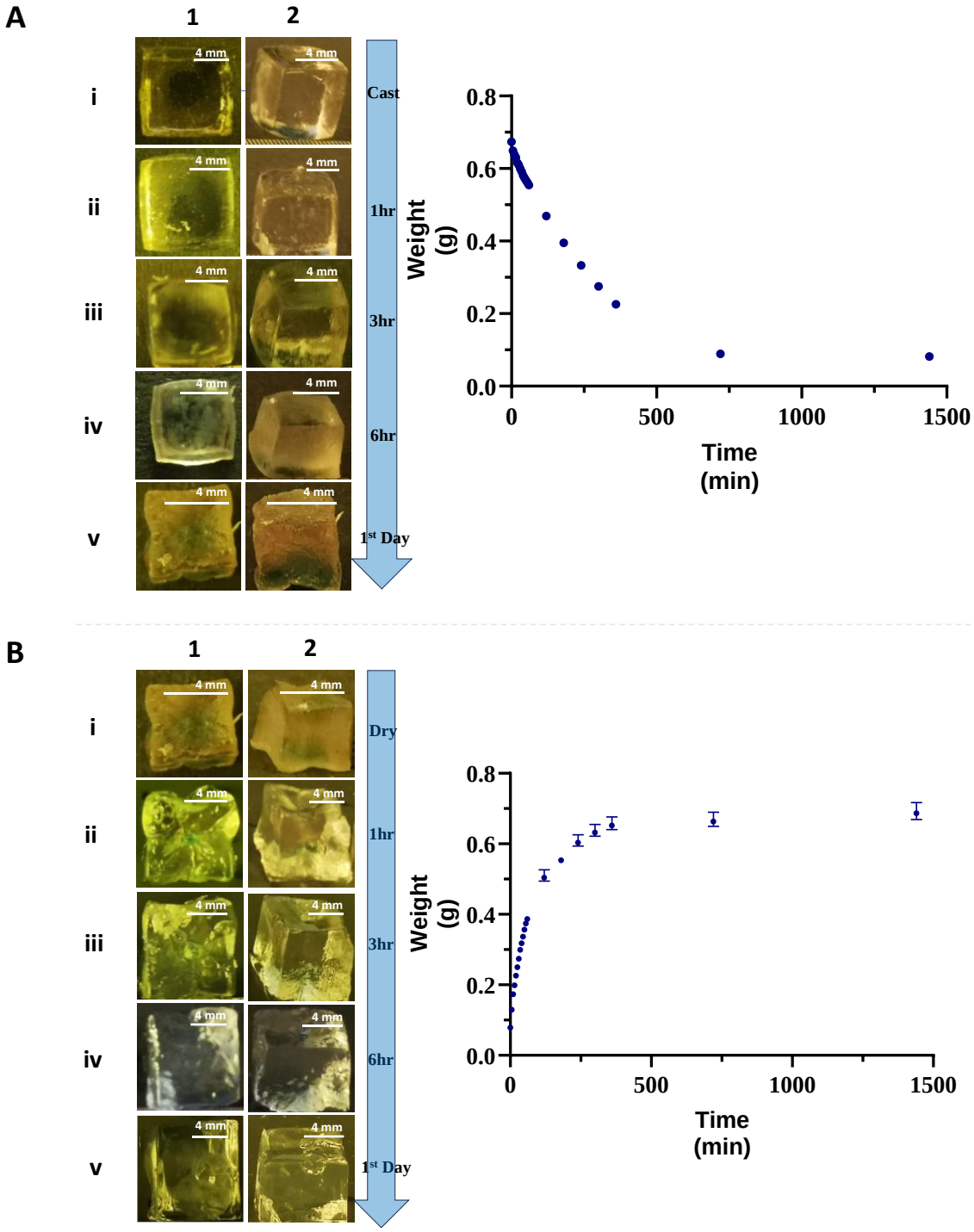


Figure 4.9 Swelling behaviour of 10% (w/v) GelMA + 2% (w/v) dye cubes. A) dehydration of cast cubes over a 24-hour period, and B) hydration of cast cubes within 24-hour timeframe. Rapid response of the material changes in moisture conditions, providing insight into its swelling behaviour. Results denote mean ± SD (n = 3).

4.3.4. Degradation Analysis

The stability of the GelMA hydrogel within a physiological context was evaluated through a degradation test. This degradation was performed by immersing all samples in 5 ml of dH_2O for a duration of 25 weeks at 37°C. Findings reveal a distinct trend wherein higher concentrations of GelMA exhibited comparatively slower rates of degradation when compared against lower concentrations, as shown in **Figure 4.10.** These outcomes highlight the potential implications of GelMA concentration in adapting the materials' biodegradability.

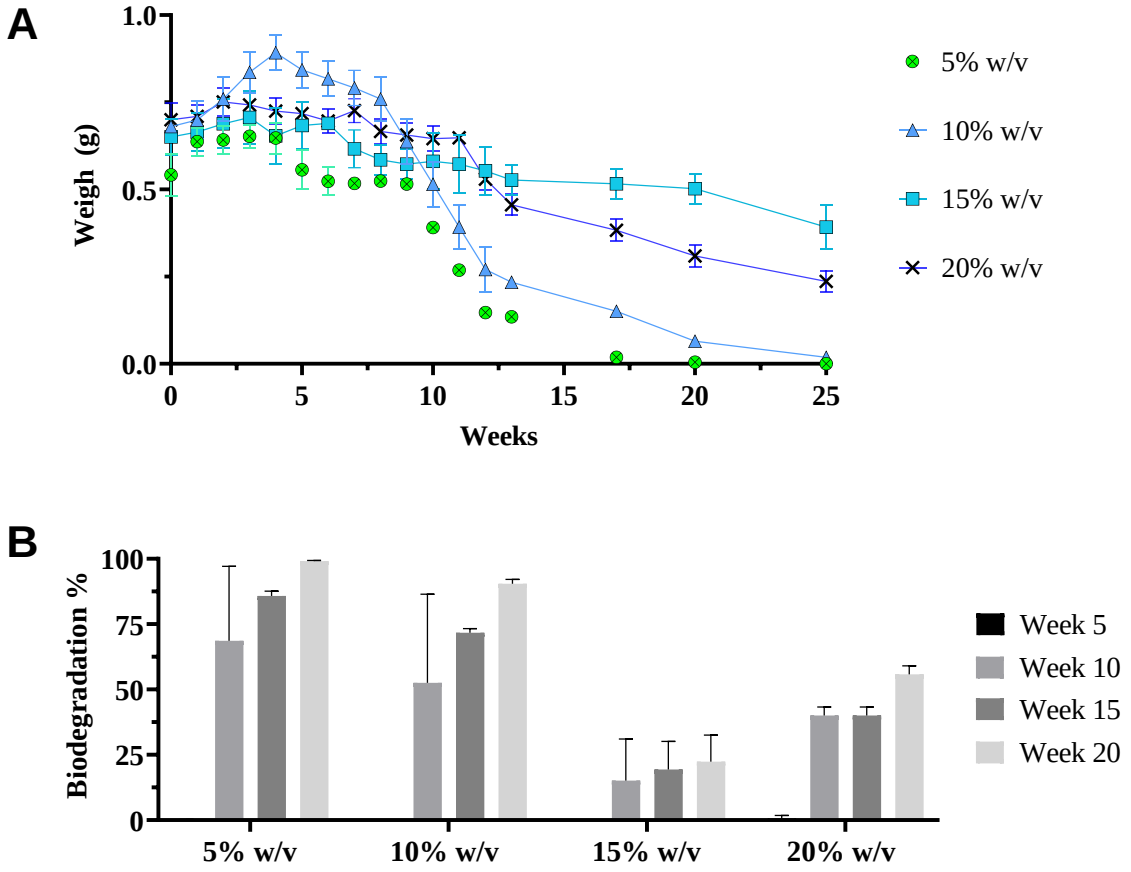


Figure 4.10 Biodegradation analysis of GelMA-cast cubes at varying concentrations (5% (w/v), 10% (w/v), 15% (w/v), and 20% (w/v)) with 2% (w/v) dye. (A) Evolution of cube weight observed over a 25-week period at 37°C. (B) Percentage biodegradation ratio at weeks 5, 10, 15, and 20. Results denote mean ± SD (n = 3).

Table 4.5 provides an insightful interpretation of the biodegradation patterns associated with the different concentrations of GelMA, 5%, 10%, 15%, and 20% w/v with 2% (w/v) dye. The recorded data highlights a consistent trend of progressive disintegration across all concentration levels throughout the observational period; however, there is a general trend of slower mass degradation observed as GelMA concentration increases. Comparing GelMA 5%, 10%, 15%, and 20% (w/v) at 37°C, the mass degradation progresses from 55.11%, 78.67%, 21.33%, to 57.95%, respectively, by week 15, concentration-dependent behaviour suggests that higher GelMA concentrations might offer less structural stability and resistance to biodegradation.

Table 4.5 Mass degradation data collected from cast cubes of different concentrations of GelMA, 5%, 10%, 15%, and 20% (w/v), with 2%(w/v) dye until week 20. Raw data values at 37°C for each concentration, mass (g) used to calculate swelling ratio results. Results denote mean ± SD (n = 3).

GelMA samples (%w/v)	**Mass(g) as cast**	**Mass(g) Week 5**	**Mass (g) Week 10**	**Mass (g) Week 15**	**Mass (g) Week 20**
5%	0.5419 ±0.0599	0.5562 ±0.0559	0.3907 ±0.0183	0.0767 ±0.0098	0.0046 ±0.0012
10%	0.6801 ±0.0030	0.8428 ±0.0507	0.5147 ±0.0643	0.1923 ±0.0113	0.0646 ±0.0124
15%	0.6507 ±0.0521	0.6834 ±0.0662	0.5806 ±0.0800	0.5216 ±0.0425	0.5020 ±0.0432
20%	0.6997 ±0.0473	0.7174 ±0.0346	0.6454 ±0.0361	0.4195 ±0.0308	0.3096 ±0.0289

One of the key observations from the data is the impact of GelMA concentration on the degradation rate of hydrogels. Generally, higher GelMA concentrations exhibit slower degradation rates compared to lower concentrations. For instance, the 5% GelMA samples experienced significant mass loss over the 20-week period, with the mass decreasing from 0.5419 g to 0.0046 g. In contrast, the 20% GelMA samples displayed relatively slower degradation kinetics, retaining a higher mass at the end of the observation period (0.3096 g).

In particular, the interest in the behaviour of 10% (w/v) GelMA with 2% (w/v) dye, subjected to an incubation environment at 37°C, was represented in **Figure 4.11**. Within this context, by week 20, a substantial swelling ratio degradation level of 89% is discernible.

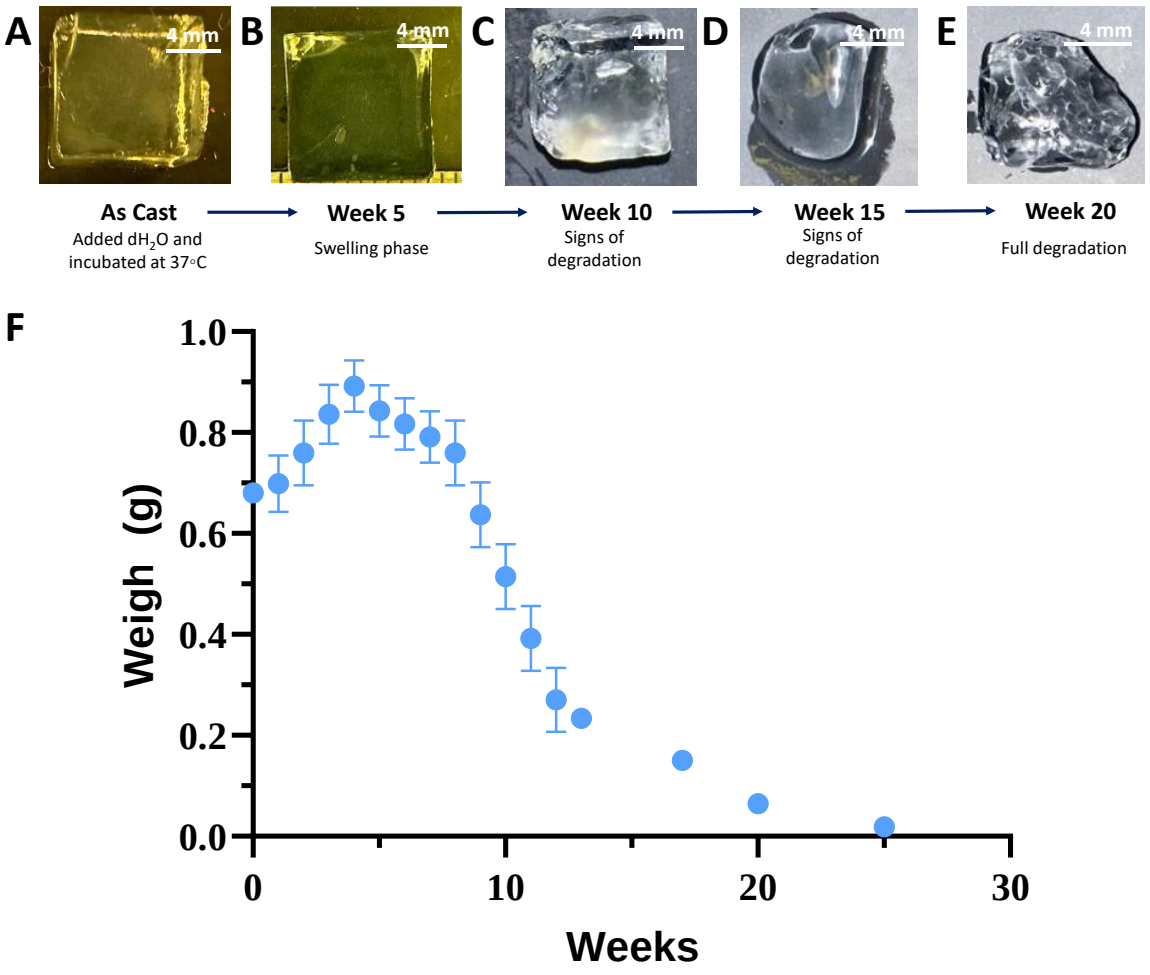


Figure 4.11 Stages of 10% (w/v) GelMA degradation, A) as cast, B) swelling in PBS at 37°C after five weeks, C) signs of degradation at week 15 and D) week 20, E) finally, full degradation at week 25. F) 10% (w/v) GelMA graph during the period of swelling and degradation. Results denote mean ± SD (n = 3).

4.4. Conclusion

This chapter presented the characterisation of PCL and GelMA, both critical materials in 3D printing for the OC scaffolds. The ability to precisely control architecture and composition in 3D printing has revolutionised tissue engineering, opening avenues for constructing intricate structures with tailored mechanical properties. This research incorporated a wide

array of properties and behaviours of PCL and GelMA, each contributing to the optimisation of extrusion-based 3D printing of the OC scaffold.

Rheological properties stand at the forefront of material performance in 3D printing. The analysis of PCL with varying molecular weights showcased significant differences in shear viscosity and flow behaviour under shear force. Notably, PCL 45 emerged as the ideal candidate for printing, with a favourable viscosity profile and processability, as previously demonstrated by other authors (Domingos et al., 2017; Hutmacher et al., 2001; Ruiz-Cantu et al., 2020b). The dependence of PCL viscosity on temperature and molecular weight illuminated the complex interplay guiding its behaviour.

Similarly, the characterisation of GelMA unveiled its unique qualities. The degree of methacrylation served as a predictor of crosslinking potential, a critical determinant of 3D bioprinting suitability. Rheological testing provided insights into GelMA's viscoelastic properties and flow dynamics, showing a shear thinning behaviour as previously demonstrated by Liu et al., 2017. Meanwhile, a sudden decrease of shear rates upon deposition causes a sharp increase in viscosity, resulting in a high printing fidelity (Z. Chen, 2017; Elomaa et al., 2020)

Based on literature and rheological tests the 10% (w/v) concentration showcases favourable behaviour for 3D printing. Likewise, swelling, degradation, and water absorption capacity demonstrated the performance and stability of the material in the scaffold.

In conclusion, this chapter presents integrated work done on material characterisation, scaffold design and 3D printing optimisation. The incorporation of these insights enables the development of biomimetic scaffolds with tailored mechanical properties.

Chapter 5. 3D Bioprinting: characterisation of GelMA/PCL for 3D printing of multi-material for osteochondral defect.

This chapter describes the optimisation process for PCL, GelMA and PCL/GelMA scaffolds through 3D printing extrusion using the 3D Discovery RegenHu machine. This optimisation comprises fine-tuning parameters such as feed rate, pressure, heating and cooling temperatures, which are crucial for achieving precise control over scaffold fabrication. One of the primary objectives of this chapter is to investigate the mechanical properties of these materials and assess how diverse design configurations and pore structures affect their compressive modulus. This knowledge is indispensable to be able to match the mechanical properties of the engineered constructs with those of the target cartilage on the OC tissue.

5.1. Introduction.

3D bio-printing is an important tool that uses biocompatible materials, cells, and supporting components to fabricate complex 3D-printed scaffolds (Mani et al., 2022). The AM technique of extrusion-based bioprinting is characterised by complex geometry that can be fabricated layer-by-layer using two or more biomaterials with the ability to mix cells and biomaterials in the bioink(X. B. Chen et al., 2023; Vanaei et al., 2021). This technique can manipulate different biomaterials, at the same time creating hybrid scaffolds mimicking native tissues in their mechanical and biological properties. Several studies have worked on diverse types of tissues, neuronal tissue, heart valves, cartilage (Duan et al., 2013, 2014; Kesti et al., 2015; W. Liu et al., 2018b; Lozano et al., 2015; Markstedt et al., 2015; F. Wang et al., 2022; Yue et al., 2016)among others, using mechanical or pneumatic pressure (S. Chen et al., 2023; Jo et al., 2023; W. Liu et al., 2018a), to dispense bioink through micro nozzles with an extensive range of materials such as hydrogels, pellets, spheroids, and strands (Flégeau et al., 2022; Malekpour & Chen, 2022). Printing parameters, for instance, printing speed, print orientation, layer thickness and extrusion rate, have been observed to significantly impact both the mechanical and structural properties of the product, as noted in several studies (Brenken et al., 2018; Kichloo et al., 2022; Sing & Yeong, 2021)

Despite the positive results of in vivo studies regarding 3D printing extrusion-based deposition for OC scaffolds (F. Gao et al., 2018; J. Liu et al., 2019c; Monroy et al., 2018; Natarajan et al., 2021), specific challenges have arisen, including limited mechanical and physical stability that can lead to potential scaffold collapse and deformation. Notably, the

utilisation of fibrin glue has exhibited promising improvements in the press-fit fixation of scaffolds during surgery (Filardo et al., 2014), prompting some studies to consider the separate printing of cartilage and bone scaffolds, followed by their combination using fibrin glue. This approach has been implemented due to the previously mentioned issues of limited mechanical and physical stability, which render the scaffolds vulnerable to collapse and deformation. Therefore, the introduction of a monophasic scaffold employing two or more materials may serve as a potential solution to address these concerns. Additionally, the design of the scaffold, particularly in the case of a multiphasic OC scaffold, involves the incorporation of a gradient scaffold, wherein each phase seamlessly transitions into one another, as opposed to a distinct separation (O'Connell et al., 2018).

The previous chapter examined the crucial material components, PCL and GelMA, within the context of 3D printing for tissue engineering. The thorough characterisation of these materials, including rheological properties, cross-linking potential, viscoelastic behaviour, water absorption capacity, and degradation analysis, informed the specific requirements for the extrusion-based 3D printing manufacturing of the OC scaffold.

The aim of this chapter is to consistently and repeatably control the surface porosity and pore size in 3D-printed scaffolds. These surface characteristics are intricately linked to the path taken by the printheads in each layer during the 3D printing process. Therefore, the research has investigated various geometric designs for 3D-printed scaffolds. Through experiments, the modification of surface porosities and pore sizes, all in a concerted effort to the elaborate interaction between these parameters and the resultant mechanical properties of the scaffolds. This chapter is the gateway to a deeper understanding of the steps to engineer osteochondral scaffolds with their mechanical properties.

5.2. RegenHU Bioprinting Configuration.

It is first necessary to examine the configurations and equipment offered by the 3D Discovery RegenHu bioprinter. The configuration of a 3D bioprinting machine is a pivotal factor that profoundly impacts its capabilities and its suitability for achieving specific research objectives. This chapter examines the printability of PCL, GelMA, and a co-printing of PCL and GelMA, which will be employed to construct the OC scaffold. The focus here

is on the individual configuration of printheads, which enables the precise deposition of each material.

The essential components of the RegenHU bioprinter for the OC scaffold fabrication include the following elements: printer heads (DD-135N, HM300H, CF300), build platform, control software, heating system, cooling system, pressure regulator, and UV light source (UV-365NM), as visually represented in **Figure 5.1**. Each of these components plays an integral role in ensuring the success of the printing.

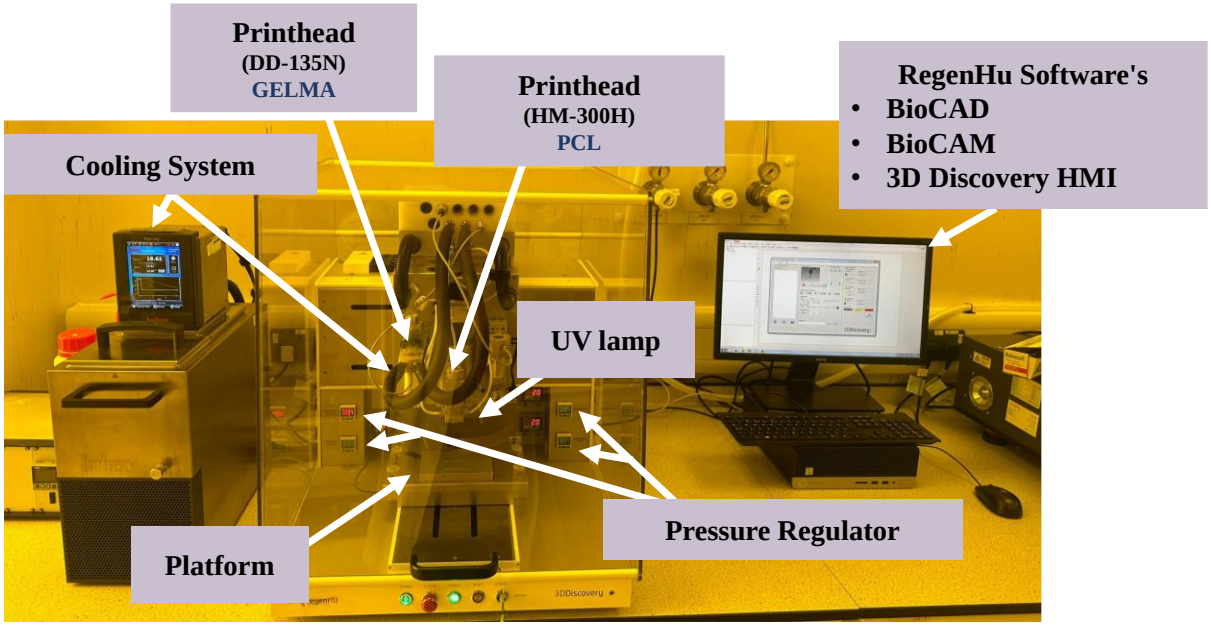


Figure 5.1 3D Biodiscovery RegenHU System Configurations and Equipment. Overview of the configurations and equipment associated with the 3D Biodiscovery RegenHU system, offering an understanding of the technological setup employed.

An outline of the specific configurations and parameters employed for the chosen materials in the bioprinting process, namely PCL and GelMA, use different parts of the printer and are discussed in this section. For the extrusion-based deposition of PCL, the thermo-polymer extruder, HM300H, was selected because of its ability to precisely control the heating system within the printhead and regulate the deposition of PCL pellets. Parameters such as the feed rate, extruder rate and pressure regulation can be adjusted to achieve the desired scaffold properties and structure. In the case of GelMA, the Direct Dispenser (DD-135N) printhead was used in conjunction with the Light Curing Kit (UV-365NM) for photo-polymerisation. The DD-135N printhead is equipped with a round cartridge cooler body connected to a

cooling unit, allowing precise temperature control based on set points, process requirements and internal temperatures. Further customisation can be achieved by adjusting valve dosing, opening, closing, and pressure regulation. Control over UV light parameters such as exposure time and distance are essential for photo-polymerisation.

Figure 5.2 visually represents the configurations and parameters utilised for bioprinting PCL and GelMA materials. This provides valuable insights into the system's versatility and capabilities for biomaterial printing, fundamental to manufacturing an OC scaffold that meet the specific mechanical requirements.

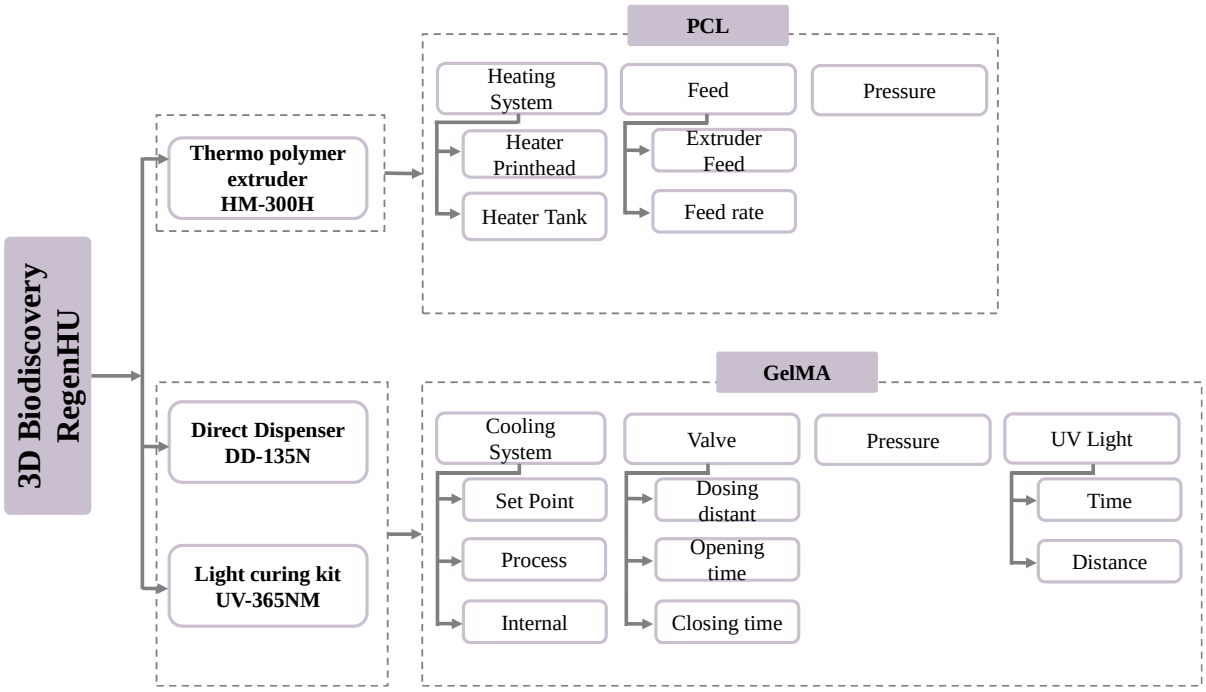


Figure 5.2 3D Biodiscovery RegenHU system tools and variable parameters for PCL and GelMA Printing enable the precise printing of both materials, depending on the printhead.

In the following sections, the experimental results and outcomes of the bioprinting demonstrate how these meticulously selected configurations and equipment have contributed to the successful fabrication of OC scaffolds with tailored properties.

5.3. Optimisation of Polycaprolactone Printing Process.

As mentioned previously, the printhead used to print to extrude the PCL is the thermo-polymer extruder-based (HM-300H) printhead. This printhead exhibits a variety of distinctive characteristics. Firstly, its viscosity range depends on the screw design, ensuring adaptability to a wide range of material viscosities. The printhead has a heated 10ccm tank for fluid storage, facilitating precise temperature control during printing. Furthermore, the nozzle and needle diameter can be adjusted, ranging from 120µm to 800µm, allowing for flexibility in print resolution. The heater integrated into this printhead can reach temperatures of up to 240°C, and it offers individual temperature control for both the tank and the barrier screw, enhancing the control over material extrusion. The dispensing mode employed by this printhead is contact dispensing, ensuring accuracy and consistency in material deposition.

As previously highlighted, the HM-300H printhead possesses many distinctive characteristics that provide both versatility and precision in material deposition. The printing parameters will be further optimised in the following sections to ensure the highest quality and precision in the PCL-based 3D printing processes.

Figure 5.3 presents a visual representation of the strategic selection and utilisation of two needle gauges, G30 and G32, as integral components in the optimisation process of the printing methodology. These needles play a pivotal role in facilitating the creation of precise strands, enabling the formation of printed lines. These lines serve as invaluable indicators, offering a unique perspective into the width dimension of the printed lines.

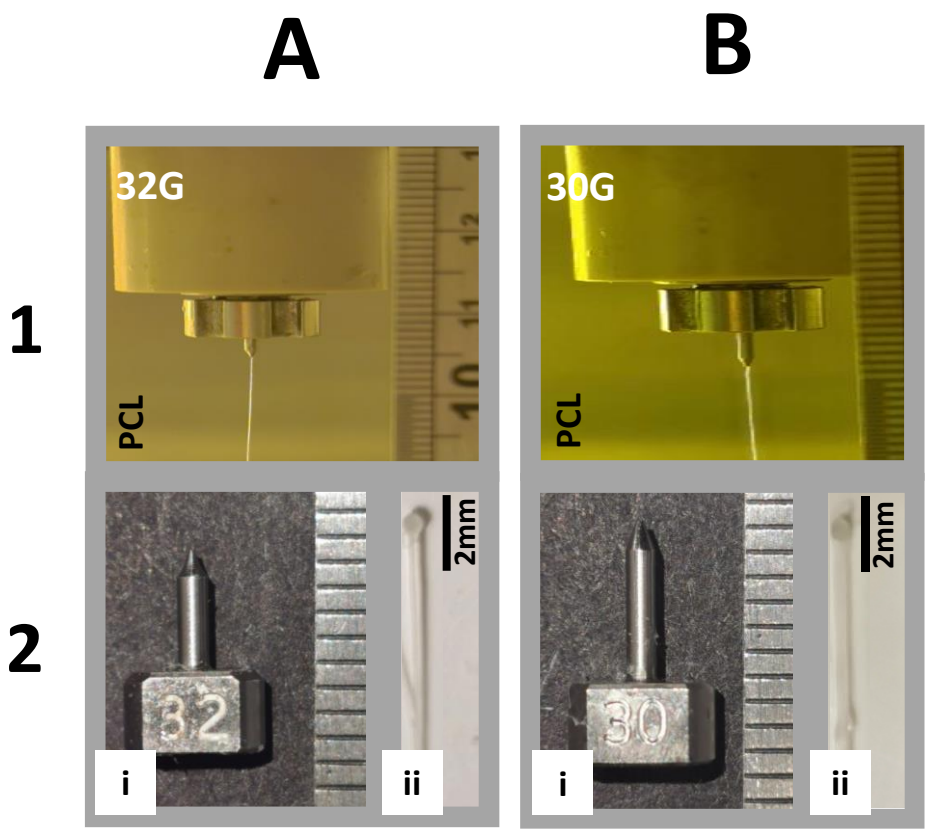


Figure 5.3 Needles optimisation used for the Thermo-Polymer (HM-300H) Printhead. A1- B1) Filaments while printing G32 and G30, showcasing the material flow characteristics. A2i - B2i) Needle dimensions are illustrated in millimetres (mm), providing precise measurements for reference. A2ii-B2ii) Scaled representation of the filament, with a 2mm scale bar.

Based on the designs presented on **Chapter 3-section 3.4,** the gauge chosen to make the optimisation to create different shapes is G32, giving a 250 µm of thickness of the material deposit, which enables the highest levels of accuracy and consistency in the 3D printing, ultimately contributing to the enhancement of the printing processes and the quality of the printed output.

5.3.1. Feeding Rate and Building Speed Optimisation.

Several critical factors require meticulous control to achieve the formation of strands. Among these are two primary variables: the feeding rate and the building speed. The feeding

rate is quantified by the rotations per minute (rpm) of the screw, while the building speed pertains to the velocity of the printing head along the x and y axes.

Figure 5.4 illustrates the pronounced impact of varying rpm values on strand shape. Notably, when the rpm was set at 5 rpm, 10 rpm, and 15 rpm, insufficient material deposition produced notably thinner and structurally weaker strands. Consequently, a decision was made to opt for a more optimal rpm value, settling on 17.5 rpm for the extrusion of PCL.

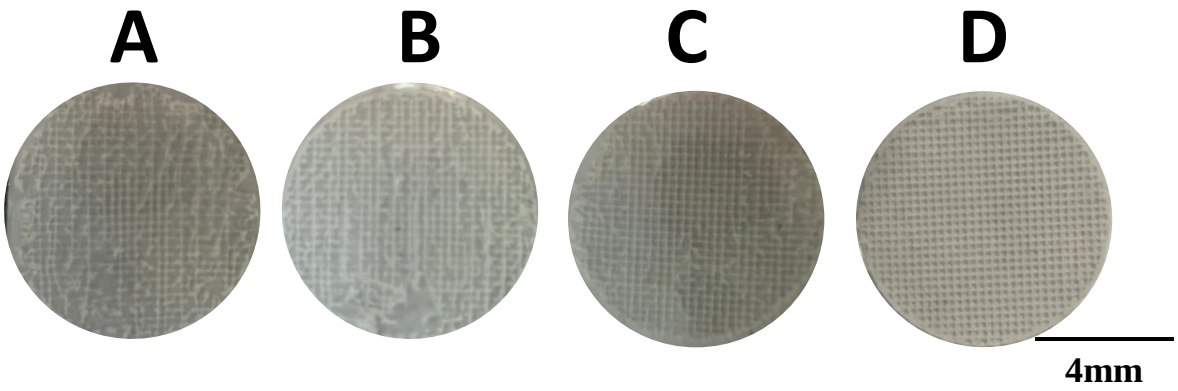


Figure 5.4 3D printing PCL samples at varied feeding rates. A) At 5 rpm, B) 10 rpm, C) 15rpm, and D) 17.5 rpm. The scale bar represents 4mm.

Additionally, the influence of varying building speeds was explored, as depicted in **Figure 5.5.** Among the tested speeds, 20 mm/s emerged as the parameter that yielded the most consistent and uniform strand deposition. These findings emphasise the critical role of both feeding rate and building speed, controlling the dimensions and structural integrity of the generated strands.

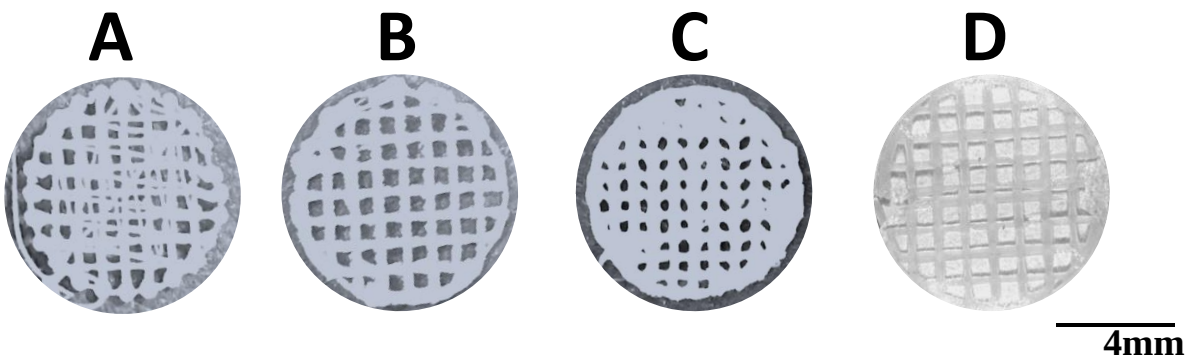


Figure 5.5 3D printing PCL samples at different nozzle speeds. A) At 10mm/s, B) 15mm/s, C) 18mm/s, and D) 20mm/s. The scale bar represents 4mm.

5.3.2. Optimisation of Space Between Strand's Layer Thickness.

The 3D RegenHU printer uses the BioCAD software for printing path design. BioCAD offers freedom in shape and printing path design; however, it requires manual drawing of 3D models within the software. Various functions within the software can be manipulated to create complex 3D models. Given the need for a personalised OC scaffold to meet specific mechanical properties, two critical parameters were identified for optimisation: layer thickness and the ratio between strand diameters.

Figure 5.6 explores PCL scaffolds characterised by a layer thickness of 200μm and varied space ratios, offering crucial insights into their structural attributes. **Figure 5.6 A** offers a comprehensive view of the complete scaffold, delivering an overview of its structure of a dimeter of 8mm. In **Figure 5.6 B**, the focus shifts to the vertical layers, enabling a detailed examination of the printed filaments within a single layer, supported by a microscope scale bar of 500μm for precise dimensional assessment. **Figure 5.6 C** further elucidates the scaffold's intricate architecture by showing the vertical and horizontal filaments within a single layer. This comprehensive visualisation contributes to a deeper understanding of the scaffold's complexity and structural components. Additionally, it is noteworthy that between two PCL strands, there is a consistent space of 1500 μm, emphasising the precise arrangement of structural elements within the scaffold design.

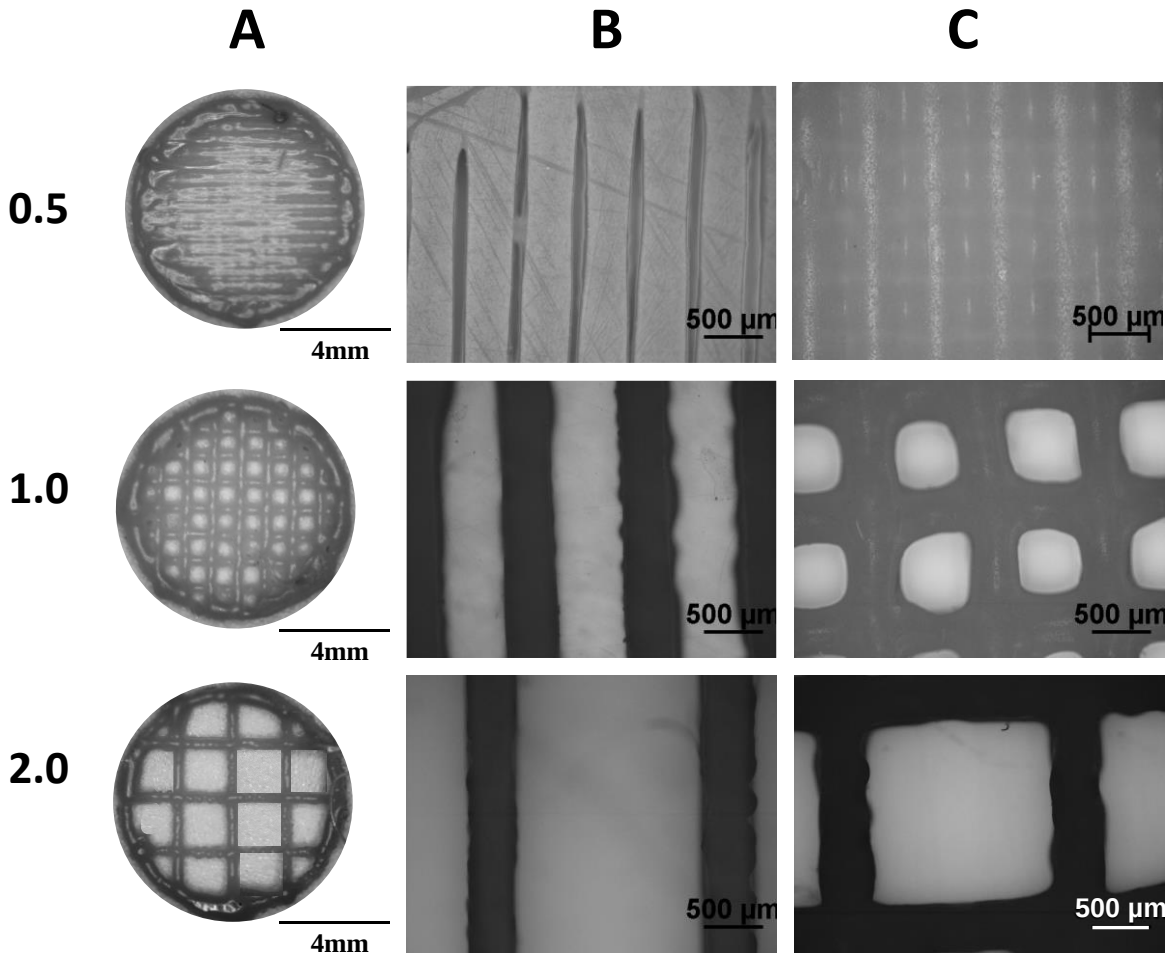


Figure 5.6 Scaffolds with a layer thickness of 200µm and varied space ratios. A) Full scaffold view, providing an overview of the structure (scale bar is 4mm). B) Vertical layers, showcasing the printed filaments within a single layer, allowing for detailed examination. C) Vertical and horizontal filaments are in a single layer, highlighting the complex architecture of the scaffold. A scale bar of 500µm is included in B and C to aid dimensional assessment.

Examining the 500 µm spacing **(Figure 5.6-0.5)** between strands in a range of space ratios, it was observed that a ratio of 1 resulted in a structure with tiny pores and nearly solid characteristics **(Figure 5.6-0.5 C)**. Conversely, a ratio of 0.5 at a spacing of 1000 µm led to pores forming of approximately 500 µm **(Figure 5.6-1.0 C)**. Furthermore, when the spacing between strands was increased to 2000 µm, a ratio of 0.25 resulted in more prominent pores, approximately 1500 µm in size **(Figure 5.6-2.0 C).**

Besides, an essential parameter under consideration is the layer thickness of the scaffold. Since the OC scaffolds are designed to be more than 4mm in height, exploring different layer thicknesses is imperative to optimise the printing conditions for scaffold fabrication. The investigation into layer thickness revealed notable variations in strand spacing between layers. In **Figure 5.7**, a spacing of 250 μm between layers was observed. Notably, the layers displayed deposition issues, particularly in samples with greater height dimensions, leading to the diminished print quality of the strands, where circular and star-shaped strands are well-deposited within a scaffold that reaches a height of 2mm, demonstrating significantly improved printing quality.

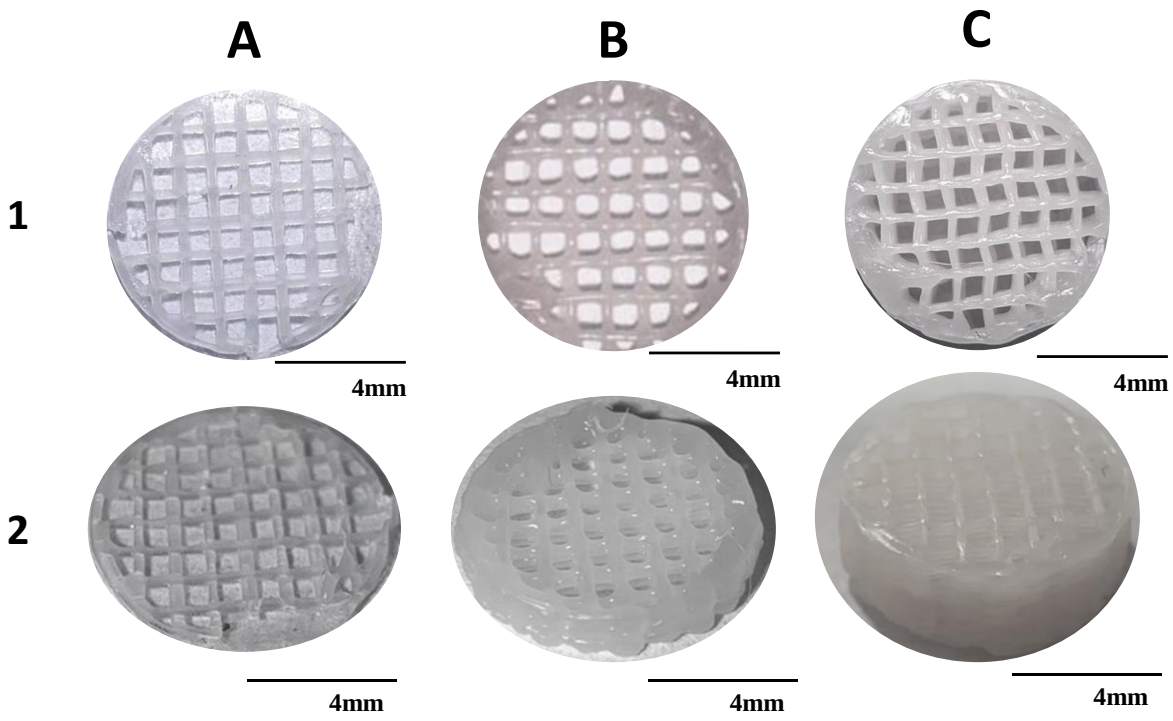


Figure 5.7 Scaffold thickness variation for machine setting parameters. A) layer thickness of 0.25mm, B) scaffold with a thickness of 1.25mm and C) scaffold with a layer thickness of 3.25mm. 1) represents the top view, and 2)the isometric view. Scale bars = 4mm.

5.3.3. Effects of the Heating System on PCL during 3D Printing Process.

High temperatures in 3D printing can lead to various extrusion-related errors. For instance, excessive heat can cause filaments to become overly liquid, resulting in stringing between printed parts and unsightly blobs or zits on the print's surface. It can also exacerbate issues like warping in some cases because the material is extruded at 80˚C and then cooling down and solidify making the material shrink. Moreover, extremely high temperatures can make filament too soft within the hot end, potentially leading to clogs and causing the extruder motor to click or skip steps. To avoid these problems, finding the right balance between temperature and extrusion settings is crucial, adhering to manufacturer-recommended temperature ranges for the specific filament being used and ensuring that the printer is calibrated correctly and maintained.

The presence of delamination and stringing within specific scaffolds was detected as presented in the **Figure 5.8.** These issues were rooted in the critical necessity of meticulously controlling the temperature of the previously deposited layer, which effectively serves as the foundational base for the subsequent layer during the 3D printing process. Maintaining this temperature just slightly below the thermoplastic material's solidification point is principal to secure strong interlayer adhesion, as elucidated in the research of Stansbury & Idacavage, 2015.

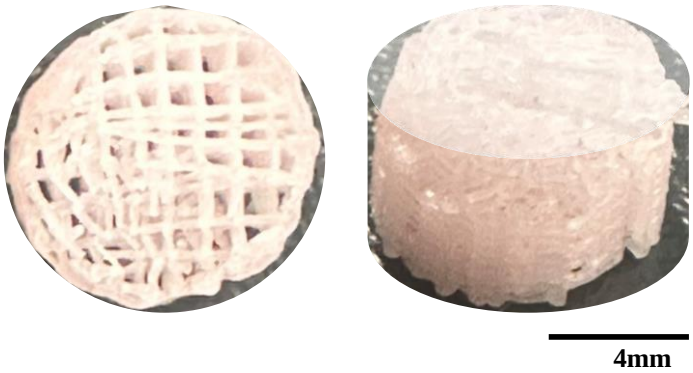


Figure 5.8 3D printing PCL sample with delamination. The scale bar represents 4mm.

In the subsequent phase, the primary objective was to regulate the printing tank and printhead temperature dynamics. These experiments investigated a diverse range of temperature settings and printing durations designed to accommodate various scaffold sizes from small,

medium, and tall structures. This rigorous exploration aimed to find the precise temperature conditions required for achieving optimal interlayer bonding.

Figure 5.9 shows examples of some challenges encountered during the experimentation process. This includes instances where the scaffolds exhibited less than ideal printing quality and cases of clogs within the scaffold structures. These challenges highlight the importance of temperature control in 3D printing. At higher temperatures, the material takes longer to cool down after deposition, resulting in clogs in the scaffold structures, as depicted in **Figure 5.9**. These insights highlight the critical role of temperature control in successfully fabricating 3D-printed scaffolds, thereby advancing the understanding and refinement of this manufacturing process.

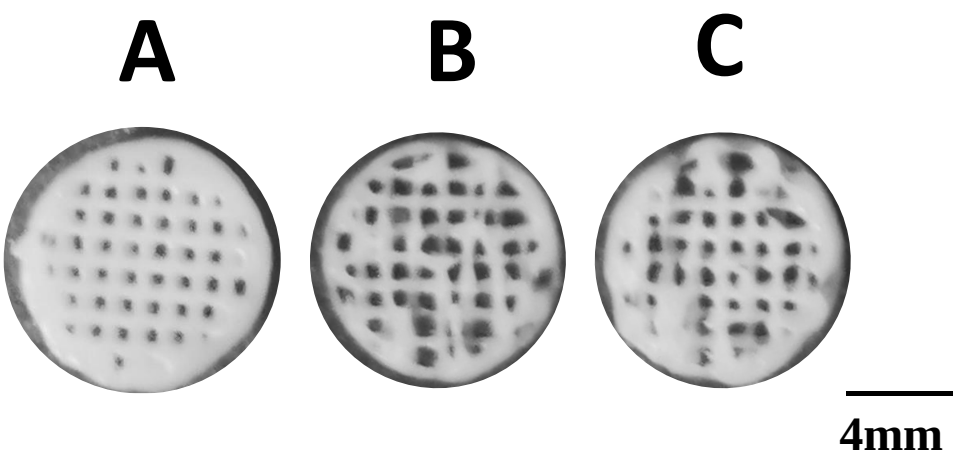


Figure 5.9 3D printing PCL samples using different printhead temperatures. A) Printhead temperature set at 80°C, B) Printhead temperature set at 90°C, and C) Printhead temperature set at 100°C. Scale bar = 4mm.

The optimal temperature conditions for the samples were established with the printhead temperature maintained at 80°C. This value was chosen to prevent layer delamination, and improve the interlayer adhesion, and prevent layer collapse, all while ensuring that the PCL material remained in a sufficiently molten state during the successive layer deposition process.

Figure 5.10 provides a visual illustration of a scaffold with specific dimensions, featuring a height of 4.6mm and a diameter of 8mm. This particular scaffold serves as a tangible

representation of the successful optimisation of the temperature parameters discussed earlier. It exemplifies how these carefully calibrated temperature conditions are well-suited for achieving the desired scaffold dimensions, underscoring their importance in fabrication.

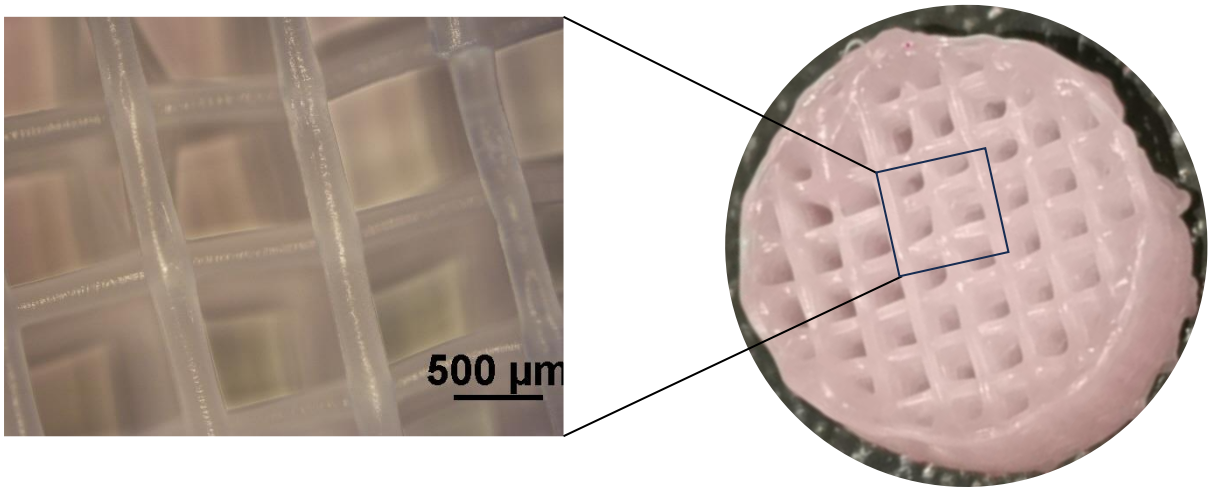


Figure 5.10 PCL Scaffold characteristics and microscope closeup. PCL scaffold with specific dimensions, featuring a thickness of 4.6mm and a diameter of 8mm. Additionally, a microscope closeup view allows for an in-depth exploration of the scaffold's layers at a scale of 500µm.

5.4. Optimisation of Gelatin Methacrylate Printing Process.

As mentioned in **section 5.2**, the printhead used for extruding GelMA is the Time-Pressure dispensing DD-135N (900 002 772) printhead. This printhead boasts several distinctive features, making it well-suited for the task. It operates on a "Time-Pressure" dispensing system, enabling precise dosing directly from the cartridge. The DD-135N (900 002 772) printhead offers versatility in terms of viscosity range, accommodating fluids within the range of 50 to 200,000 mPa*s. Additionally, it supports fluid storage in cartridges of 10ccm, providing ample capacity for the intended application. The nozzle and needle diameter options, ranging from 60µm up to 800µm, allow for fine-tuned control over the extrusion process. Contrasting some printheads, this one does not include a heater; however, a cooling unit (Huber CC-K6 by the Pilot ONE controller) is required to print the GelMA hydrogel. The cooling unit's controller needs an initial setup to ensure seamless operation. This setup

includes configuring essential parameters, such as temperature set point limits, where a minimum of 5°C and a maximum of 35°C are crucial.

Furthermore, the controller facilitates temperature regulation based on an external process sensor. Lastly, the pump speed, pivotal for controlling both cooling efficiency and noise levels, can be adjusted for optimal results achieved when setting the pump speed to 3500 rpm. This comprehensive setup ensures the cooling unit operates at peak performance, successfully maintaining the precise thermal conditions required to fabricate GelMA scaffolds.

Furthermore, the GelMA material is photo cross-linked using the Light Curing lamp UV365-NM (900 002 771), which comprises the Light Curing Kit (900 002 771). This kit facilitates the photo-polymerisation and hydrogel cross-linking required for scaffold formation. The Light Curing lamp emits light at a wavelength of 365nm with a power output of 360mW, ensuring efficient cross-linking. The kit includes essential components such as a control unit and safety goggles to maintain a controlled and safe working environment during cross-linking. These specialised tools and equipment collectively contribute to the precision and success of the GelMA scaffold fabrication process.

The optimisation of the GelMA printing process emerges as a critical undertaking. The chosen DD-135N printhead lays the foundation for this optimisation journey. As previously highlighted, this printhead possesses many distinctive characteristics that promise versatility and precision in material deposition. These parameters for printing will be further optimised in the following sections to ensure the highest quality and precision in the GelMA- 3D printing processes.

The printability results of the rheology test for GelMA 5% w/v, 10% w/v, 15% w/v, and 20% w/v reveal significant viscosity differences among these concentrations. Specifically, 5% w/v exhibits remarkably low viscosity, while 20% w/v demonstrates exceptionally high viscosity. Consequently, a decision was made to evaluate the printability of 10% w/v and 15% w/v concentrations under various printing conditions, including different needle types and pressure settings. The analysis reveals that the 10% w/v concentration is the only suitable option for printing within the RegenHu machine's specified conditions. In contrast, the 15%

w/v concentration demands a higher temperature within the cooling system, rendering it less practical for 3D printing.

Figure 5.11 depicts a graphical representation of the strategic inclusion and application of three gauges, G27, G30, and G32, within the optimisation framework of the printing methodology for the 10% w/v GelMA. These gauges **(Figure 5.11 A2i-B2i-C2i)** assume a central role in streamlining the generation of accurate strands, ultimately creating well-defined printed lines. These lines serve as indispensable tools, providing a distinctive insight into the width aspect of the printed lines.

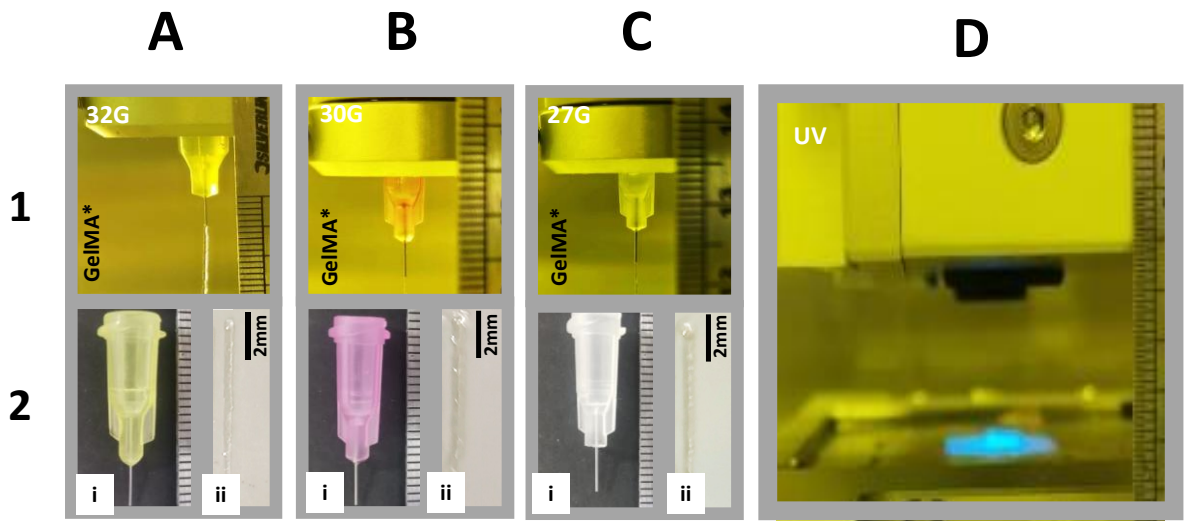


Figure 5.11 Needles optimisation used for the Time-Pressure dispensing DD-135N printhead. A1-B1-C1) Filaments during the printing of G32, G30 and G27 showcasing the material flow characteristics and the influence of needle optimisation on the printing process. A2i-B2i-C2i) Needle dimensions are illustrated in millimetres (mm), providing precise measurements for reference. A2ii-B2ii- C2ii) Scaled representation of the filament, with a 2mm scale bar. D) UV light distance of 4mm for the photocuring of the hydrogel.

Derived from the conceptualisation that GelMA filaments will be positioned between two PCL filaments and utilising G32 as the selected gauge, yielding a width of 0.250mm. This choice underscores the detection of the best precision and uniformity of GelMA 3D printing.

5.4.1. Effects of the Cooling System on GelMA during 3D Printing Process.

The viscosity of GelMA is a fundamental characteristic of a hydrogel extrusion, so maintaining consistent viscosities for all GelMA concentrations during 3D printing is achieved by adjusting the temperature based on rheological findings. Previous research has demonstrated the feasibility of 3D printing lower GelMA concentrations without deformation by lowering the temperature to 4°C (W. Liu et al. 2017). However, the cooling unit's lower limit is 5°C.

The influence of GelMA viscosity on filament formation is notable. GelMA at 5%w/v concentration exhibits low viscosity, requiring temperatures lower than the cooling system's capacity. Conversely, 15% w/v and 20%w/v GelMA concentrations have higher viscosities, demanding temperatures beyond the system's capabilities. To create filaments with the 10% w/v of GelMA, the cooling system is set to an 18°C target to ensure stability, with cooling initiated 30 minutes before scaffold printing. Also, a spread of 10% w/v of GelMA filaments is that upon contact with the substrate, the material's viscosity immediately decreases as it encounters the ambient RT.

5.4.2. Pressure and Speed Optimisation.

An optimisation process is essential to create the formation of strands through the Time-Pressure dispensing printhead, with crucial variables being the pressure and building speed. Pressure corresponds to the dispensing force, while building speed relates to the movement speed of the printing head along the x and y axes. Given the suitability of the 10% w/v GelMA concentration, as illustrated in **Figure 5.12**, it is evident that filaments tend to spread and merge upon deposition. Complete filament merging occurs when a pressure of 2 bar is employed. The impact of different speeds, as depicted in **Figure 5.12**, further underscores this point. At slower speeds, more material is extruded, leading to merging of the material as presented in **Figure 5.12 A** where the nozzle speed is set at 1mm/s. However, among the different tested speeds, 3.5 mm/s is the parameter consistently and uniformly deposits strands, as shown in **Figure 5.14**.

These results underscore the crucial roles played by both pressure and building speed in governing the dimensions and structural integrity of the generated strands.

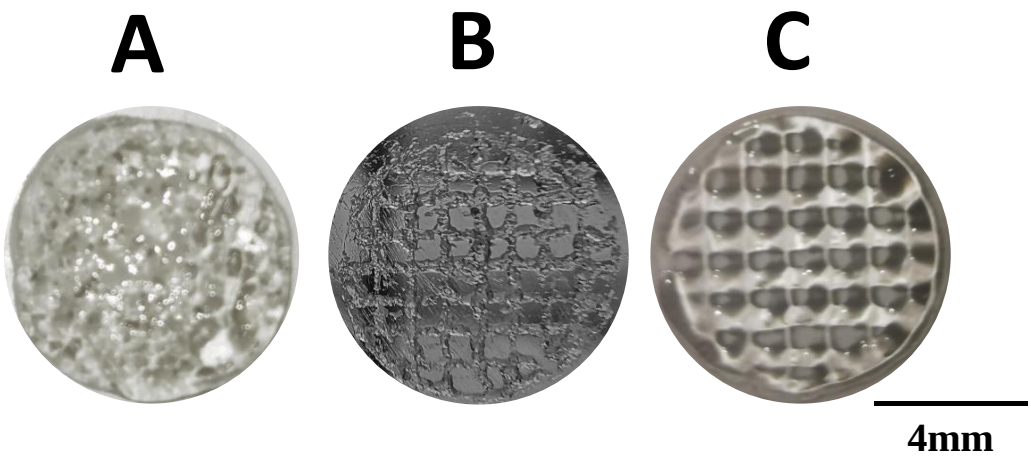


Figure 5.12 3D printing GelMA samples at varied nozzle speeds. A) 1mm/s, B) 2mm/s, and 3 mm/s. The scale bar represents 4mm.

Figure 5.13 presents valuable insights into scaffolds characterised by a 200μm layer thickness and varying space ratios, specifically comparing the 500 μm, 1000 μm, and 2000 μm layer spaces between strands. The figure provides a comprehensive view of the entire scaffold in **Figure 5.13 A**, offering an overview of the structure with a reference scale bar of 4mm. **Figure 5.13 B** shows a closeup of the vertical layers, providing a detailed examination of the printed filaments within a single layer with a scale bar of 500μm. In the case of **Figure 5.13 0.5**, where a spacing of 500μm is used, both images A and B show no pores. However, for **Figure 5.13 1.0** and **Figure 5.13 2.0**, a closer inspection reveals a more precise depiction of the GelMA filaments. This insight is particularly significant for co-printing with PCL in scaffold design, where the strand width is approximately 350μm. It offers crucial information for optimising the co-printing process, enhancing scaffold design, and facilitating improved control over structural characteristics.

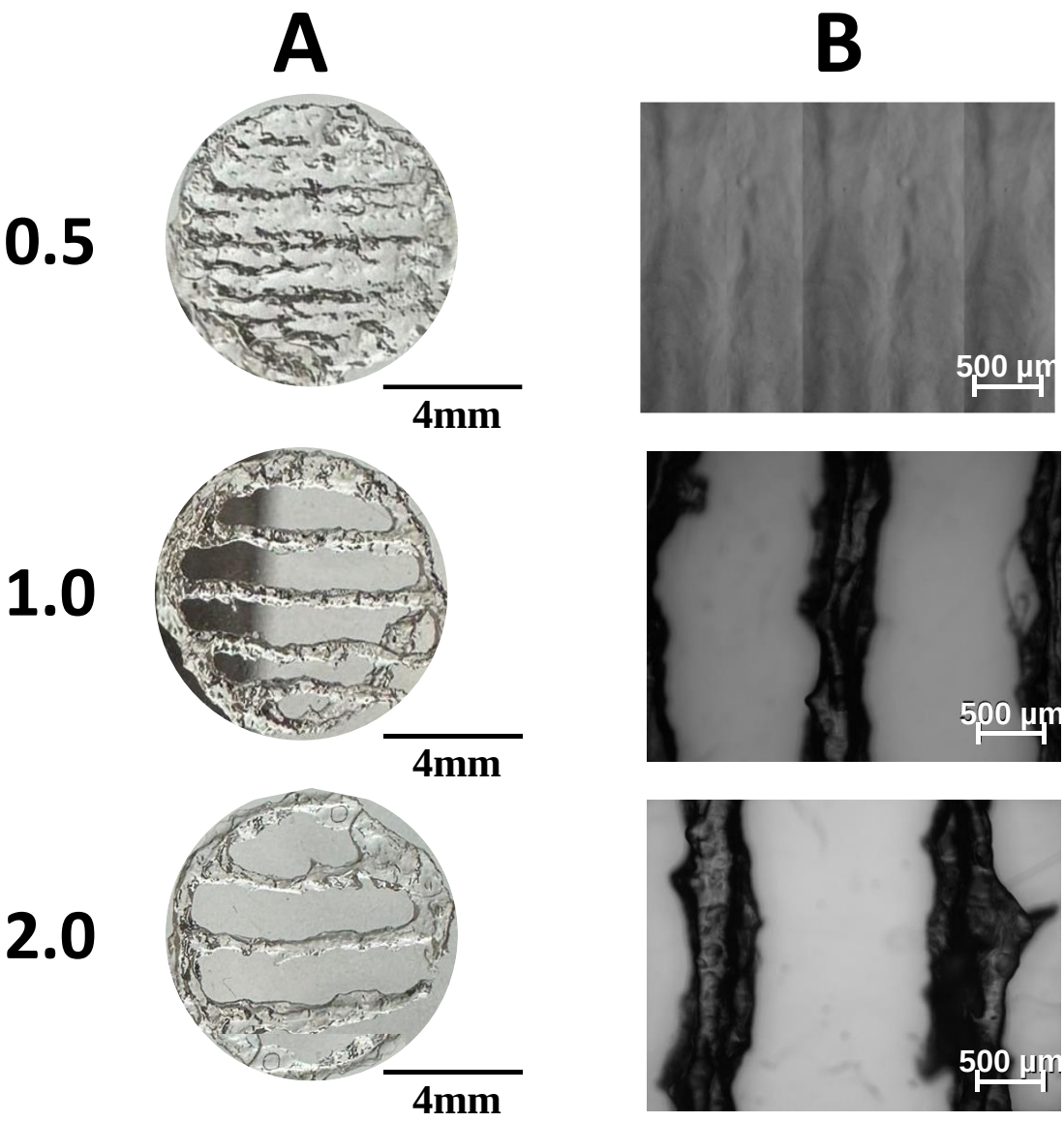


Figure 5.13 Scaffolds with a layer thickness of 200µm and varied space ratios. A) Full scaffold view at a scale of 4mm, providing an overview of the structure with a scale bar of 4mm. B) Vertical layers, showcasing the printed filaments within a single layer, allowing for detailed examination. Scale bar of 500µm.

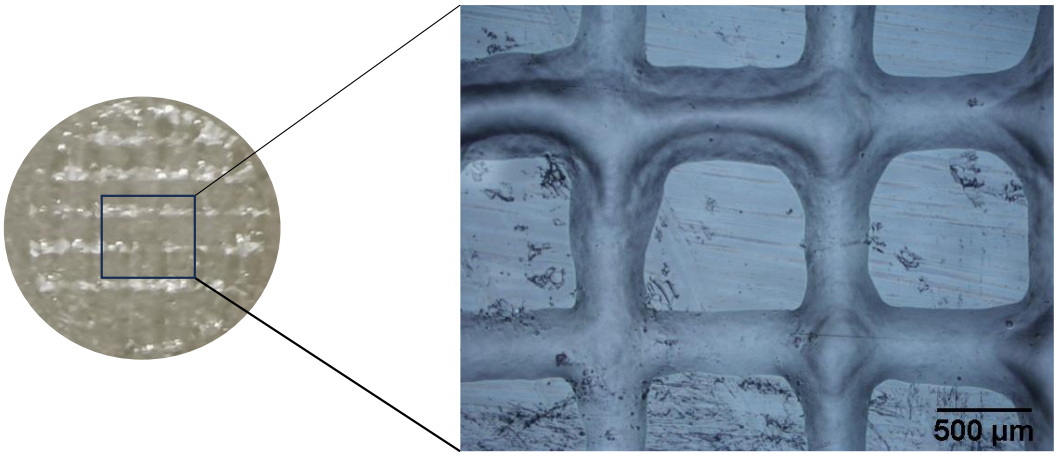


Figure 5.14 GelMA Scaffold characteristics and microscope closeup. GelMA scaffold with specific dimensions, featuring a thickness of 4mm and a diameter of 8mm with a feed rate of 3.5 mm/s. A microscope closeup view for an in-depth exploration of the scaffold's layers at a scale of 500µm.

5.5. 3D printing of PCL/GelMA scaffolds.

5.5.1. Design of PCL/GelMA Scaffolds.

The methodological approach employed in the initial fabrication of scaffold designs was supported by a rigorous screening process, strategically implemented to evaluate their printability before subjecting them to a comprehensive round of mechanical characterisation. Designs ideas were evaluated across the literature of different geometries , Cabreira & Santana presented some of the geometries they used to evaluate performance, while Joyce et al., also contributed to the selection of the designs from a mechanical perspective. However, some designs were disqualified due to limitations of the RegenHu printe and the challenge of the simultaneous printing of PCL and GelMA within the same layer, as one of the primary focus was to ensure the feasibility of simultaneous printing of both materials, which greatly narrowed down the design options. Although infinite possibilities exist, the six chosen structures represent those deemed most feasible and compatible with the printing process. This evaluative phase, rooted in parametric considerations, aimed to discern the printability of diverse scaffold designs. During this examination, the triangle, hexagon, and caracol designs underwent meticulous assessment and were found to exhibit a significant number of interlayer intersections, visibly indicated by numerous toolpath starts, as highlighted by red circles in **Figure 5.19 A, Figure 5.19 B, Figure 5.19 C**. Notably, these intricate toolpaths resulted in a non-homogeneous build-up of material at specific points,

presenting a distinctive by-product attributed to extrusion-based 3D printing process. Consequently, owing to these inherent challenges and material irregularities, the triangle, hexagon and caracol designs were excluded from further in-depth characterisation.

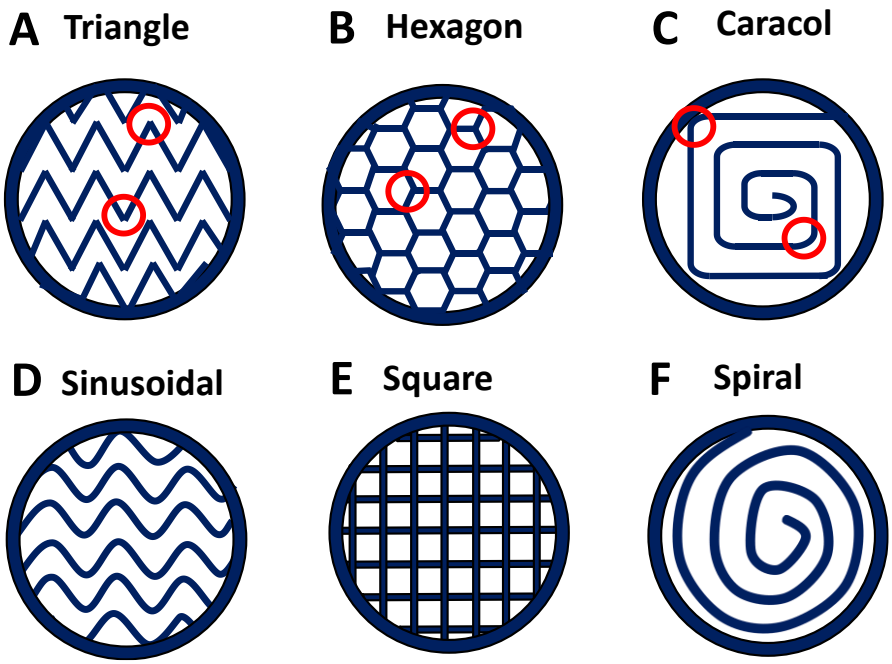


Figure 5.15 Design and fabrication of PCL scaffolds for an OC repair. A,B,C,D) Representative images of single-layer design with a diameter of 8 mm. A) Triangle, B) Hexagon, C) Caracol, D) Sinusoidal, and E) Square, D) Spiral. A, B, C) Highlighting points of intersection and excessive toolpath start and stop points in red circles. D, E,F) 3D-printed PCL scaffolds of sinusoidal, square, and spiral, respectively.

In contrast, square **(Figure 5.19 D**), sinusoidal (**Figure 5.19 E**), and spiral (**Figure 5.19 F**) scaffolds showcased a more favourable characteristic, featuring continuous and non-intersecting toolpaths between layers. This design attribute, considered within the broader parametric framework, proved crucial in mitigating the issues observed in the disqualified designs. Recognising the structural integrity and efficiency of square**,** sinusoidal, and spiral scaffolds, which were identified as promising candidates and, subsequently, advanced for further stages of mechanical testing. This parametric approach, which systematically considered the interplay of design elements, facilitated an understanding of how specific parameters impact the fabrication process.

Personalised scaffolds were constructed after successfully optimising the 3D printing process for PCL and GelMA. These scaffolds incorporated three designs, each individually

printed and subsequently combined into one OC scaffold, as illustrated in **Figure 5.16**. The combination of different geometries is illustrated in **Figure 5.17**, **Figure 5.18**, **Figure 5.19**, **Figure 5.20**. These figures provide a detailed layer-by-layer representation of how the square, spiral, and sinusoidal designs are integrated, as well as how these three designs are combined to create the OC scaffold. This visualisation offers a clear demonstration of the sequential assembly process, highlighting how each design contributes to the final structure. The combination of different designs are illustrated in **Figure 5.17**, **Figure 5.18**, **Figure 5.19**, **Figure 5.20**, it describes a detailed layer-by-layer representation of how the square, spiral, and sinusoidal designs are integrated to form the OC scaffold represented in **Figure 5.16.** This visualisation offers a clear demonstration of the sequential assembly process, highlighting how each design contributes to the final structure. Throughout this process, the printing parameters remained consistent with the specifications outlined in **sections 5.3 and 5.4.** Variations are observed in porosity and strand spacing among the different scaffold designs, as represented in **Figure 5.16.** Despite sharing a uniform 8 mm diameter, each design exhibited unique characteristics in strand spacing. The square design consistently featured a 1 mm spacing between strands, with GelMA deposition occurring between two layers. In contrast, the sinusoidal design incorporated a base layer of PCL with 1 mm spacing between strands, followed by two subsequent layers spaced 2 mm apart, allowing for GelMA deposition between these layers. Finally, the spiral design began with a base layer resembling the sinusoidal pattern, followed by two layers of PCL separated by a 1 mm gap, facilitating the introduction of GelMA between these layers.

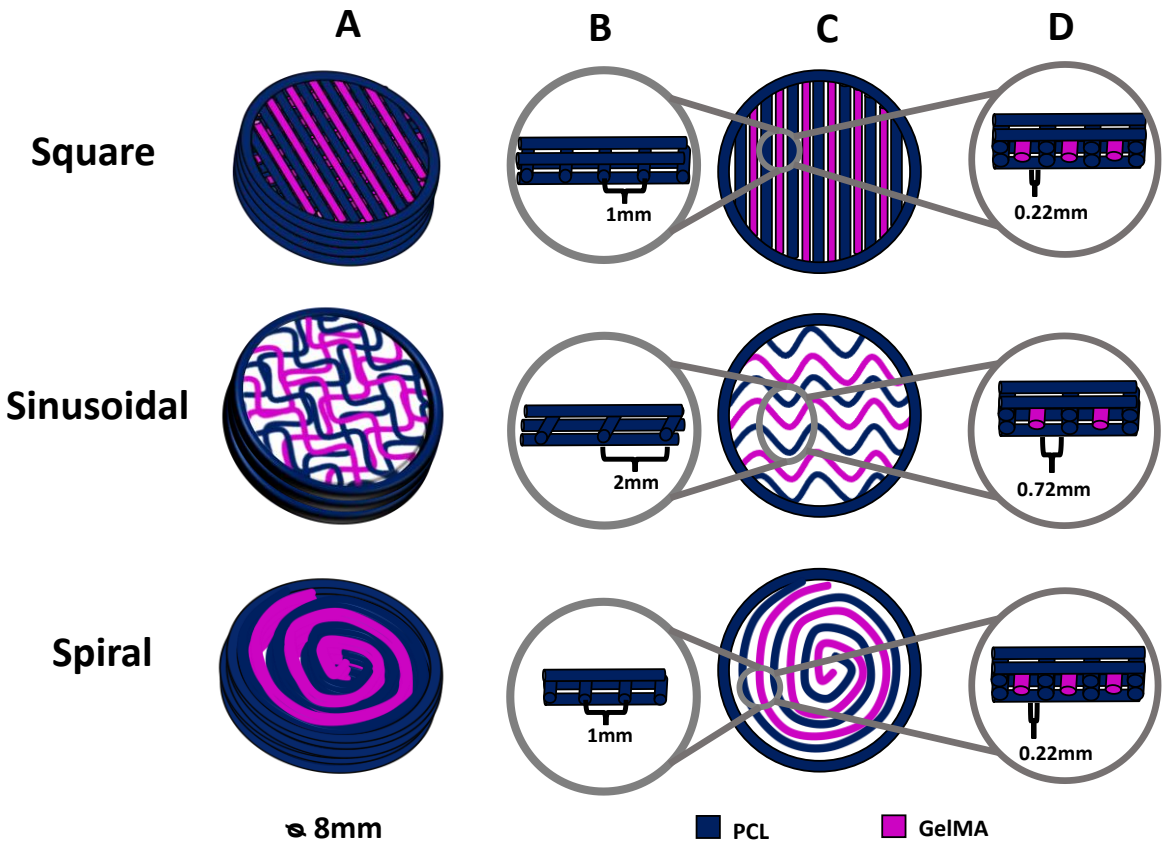


Figure 5.16 Schematic Representations of Multi-Material Bioprinting Designs for PCL/GelMA Composite Scaffolds. A)Frontal view provides a frontal perspective of the scaffold, with a diameter of 8 mm. C) Top view of a single layer D) Cross-section view highlighting the spacing between two PCL strands, varying between 1mm and 2mm depending on the design. C) Cross-section view highlighting the gap between PCL and GelMA strands, ranging from 0.22mm to 0.72mm, depending upon the specific design.

This approach enabled the exploration of diverse structural configurations within a single scaffold, offering insights into their influence on cellular behaviour and potential for tissue regeneration. The variations in porosity and strand spacing underscored the fine-tuning possibilities for crafting scaffolds tailored to specific applications. Integrating these unique designs into the personalised OC scaffold represents a significant advancement, showcasing the potential for customised scaffolds with precisely controllable mechanical properties in tissue engineering.

5.5.2. BioCAD Design.

The scaffold designs encompassed three patterns: square, sinusoidal, and spiral. Each of these designs shared a typical overall size, with an 8mm diameter and a 1.2mm thickness. However, the OC scaffolds possessed slightly new dimensions, featuring an 8mm diameter and a 4.6mm thickness. To create these scaffolds, PCL pellets sourced from Sigma-Aldrich, UK, underwent extrusion at an 80°C temperature, extruding at a rate of 18 mm/s, with a chamber pressure of 2 bar applied to the PCL. The printing strategy involved positioning PCL strands 1mm apart, with GelMA deposited between two adjacent PCL strands in the central region. Notably, one layer of GelMA was printed following every two consecutive layers of PCL, a pattern reflected in **Figure 5.16**.For detailed analysis, each scaffold consisted of six layers of PCL and two layers of GelMA, as represented in **Figure 5.17**, **Figure 5.18** and **Figure 5.19**. The cross-linking of GelMA was executed within a brief 1-minute timeframe for each layer. In the case of the OC scaffold represented in **Figure 5.22**, the configuration consisted of 15 layers of PCL and six layers of GelMA, with the 1-minute cross-linking duration applied in each GelMA layer.

Figure 5.17, **Figure 5.18, Figure 5.19** and **Figure 5.20** provide a detailed sight of the layering process and an indication of the thoughtful incorporation of various materials to realise the desired structural and functional properties in the BioCAD designs. Each image serves as a visual narrative, elucidating how PCL and GelMA are meticulously connected layer by layer, resulting in the complex architecture of this biofabricate structure. These illustrations encapsulate the essence of precision and synergy between materials, representing a critical aspect of successfully implementing this 3D printing technique in tissue engineering and regenerative medicine applications.

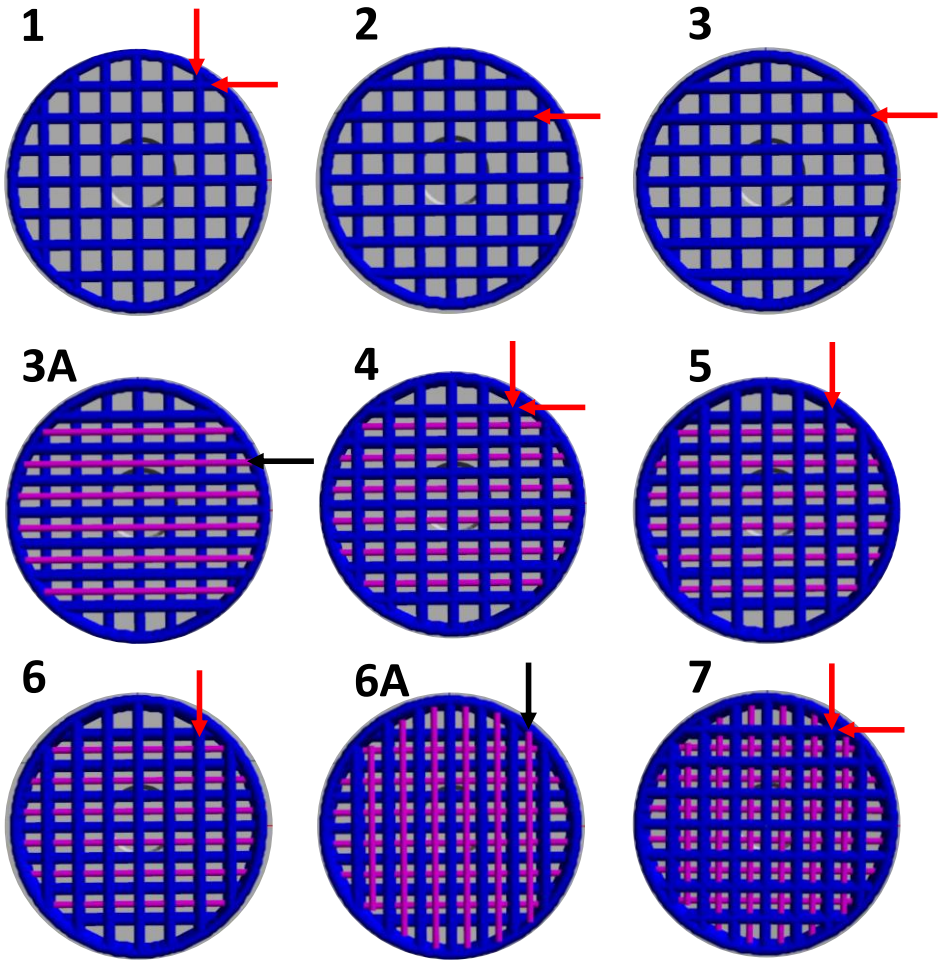


Figure 5.17 Square BioCAD design layer-by-layer provided a comprehensive visual insight into its intricate construction. This design is distinguished by the selective use of two distinct materials. Blue filaments- correspond to PCL serve as the structural framework of the design, providing stability and support. Magenta filaments- represent GelMA layers, which are strategically placed between the layers of PCL, as indicated by the black arrows. These GelMA layers facilitate specific functionalities and biological interactions within the construct.

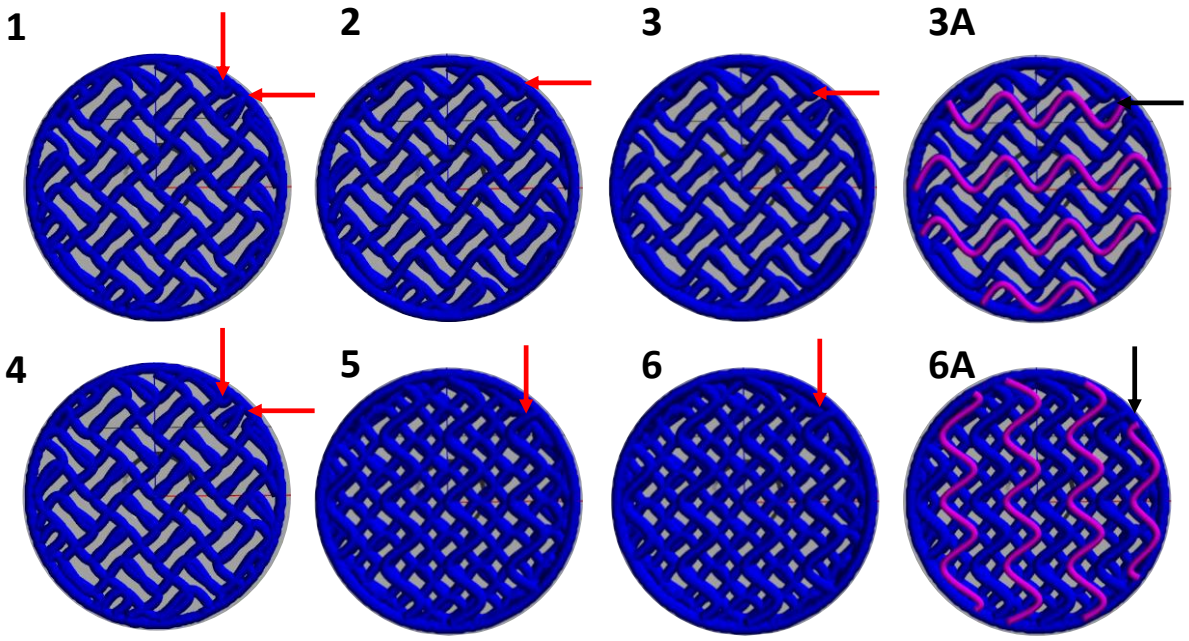


Figure 5.18 Sinusoidal BioCAD design layer-by-layer provided a comprehensive visual insight into its intricate construction. This design is distinguished by the selective use of two distinct materials. Blue filaments- correspond to PCL serve as the structural framework of the design, providing stability and support. Magenta filaments- represent GelMA layers, which are strategically placed between the layers of PCL, as indicated by the black arrows. These GelMA layers facilitate specific functionalities and biological interactions within the construct.

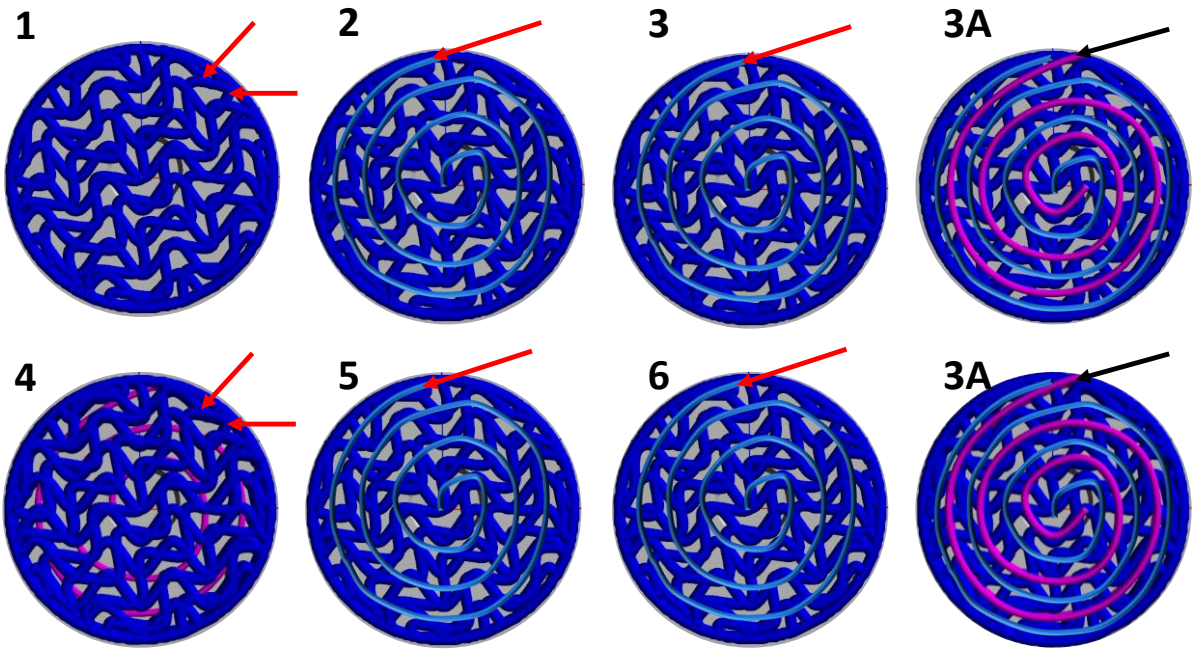


Figure 5.19 Spiral BioCAD design layer-by-layer provided a comprehensive visual insight into its intricate construction. This design is distinguished by the selective use of two distinct materials. Blue filaments- correspond to PCL serve as the structural framework of the design, providing stability and support. Magenta filaments- represent GelMA layers, which are strategically placed between the layers of PCL, as indicated by the black arrows. These GelMA layers facilitate specific functionalities and biological interactions within the construct.

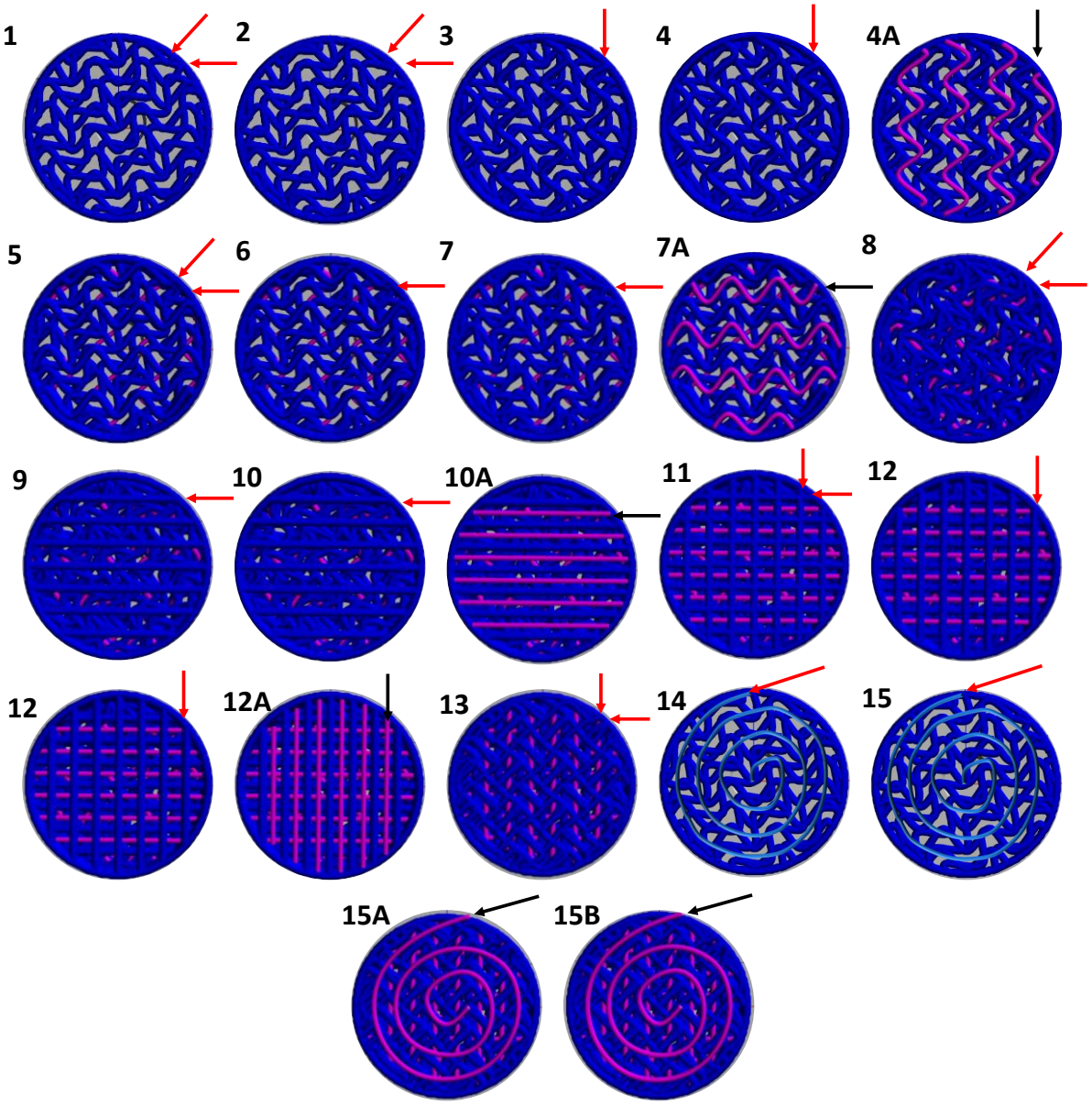


Figure 5.20 OC BioCAD design layer-by-layer represented to emulate the structure of the OC tissue. This design is characterised by the selective use of two distinct materials. Blue filaments- correspond to PCL serve as the structural framework of the design, providing stability and support. Magenta filaments- represent GelMA layers, which are strategically placed between the layers of PCL, as indicated by the black arrows. These GelMA layers facilitate specific functionalities and biological interactions within the construct.

5.5.3. Co-printing.

3D printing a combination of PCL and GelMA, issues like warping can be particularly challenging. PCL is a thermoplastic polymer known for its high melting temperature and rigidity, while GelMA is a water-based material with distinct mechanical properties. Achieving successful PCL/GelMA scaffolds with dissimilar materials requires precise temperature control, optimised printing settings, and possibly support structures to counteract warping tendencies. Additionally, experimenting with different PCL/GelMA combinations and refined the printing parameters to produce more reliable dual-material prints.

5.5.3.1. Effects of Co-printing a Hydrogel with a Polymer.

Co-printing a hydrogel with a polymer, such as GelMA and PCL, using an extrusion-based 3D printing process, it is essential to consider the effects of combining materials with vastly different properties. This combination can present significant challenges, including the potential for warping. As mentioned, contrasting material characteristics often lead to warping during the printing process **(Figure 5.21D, Figure 5.21E**). Warping occurs because PCL typically requires a higher printing temperature, which can cause localised heating and cooling variations when applied alongside the hydrogel. These temperature fluctuations can lead to uneven shrinkage and adhesion problems, resulting in warping and poor interlayer bonding, as shown in **Figure 5.21 Samples 3D co-printed PCL/GelMA. The scale bar** top row represents 4mm and the bottom row 4mm. Successfully co-printing these materials requires careful consideration of extrusion temperatures, optimal print settings, and potentially the use of support structures to address warping issues and achieve accurate and reliable multi-material prints.

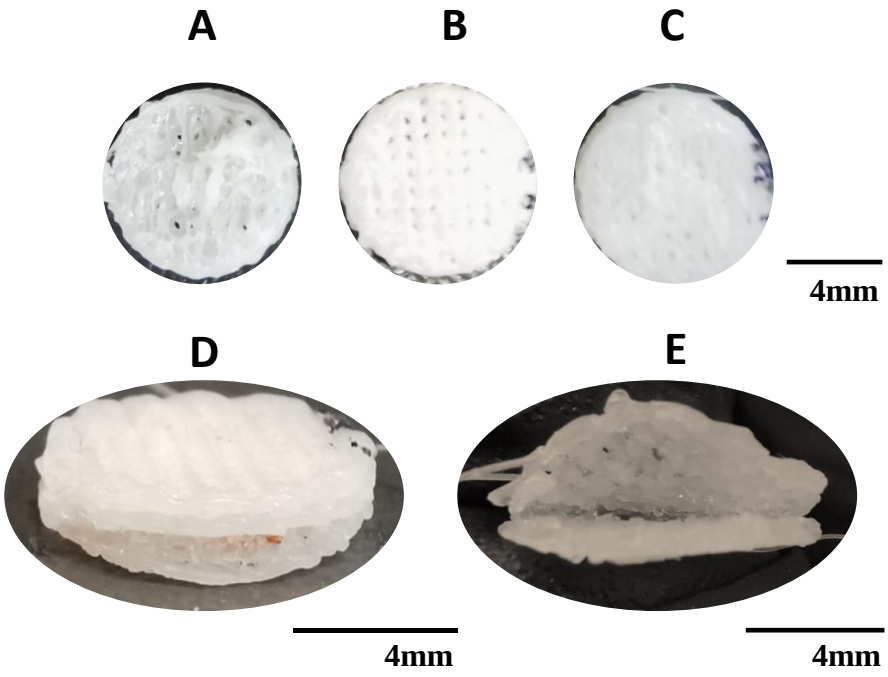


Figure 5.21 Samples 3D co-printed PCL/GelMA. The scale bar top row represents 4mm and the bottom row 4mm.

A strategic design approach is proposed to eliminate the issues depicted in **Figure 5.16,** specifically addressing warping and suboptimal interlayer bonding. In this approach, a singular layer of GelMA was systematically integrated into the printing process, and this GelMA layer was printed between every two consecutive layers of PCL. This novel design strategy was predicted as a viable solution to enhance scaffolds' overall structural integrity and printing performance. By combining the advantageous properties of PCL and GelMA, a successful co-printing of PCL/GelMA scaffolds was made, ultimately addressing the abovementioned challenges associated with warping and subpar interlayer bonding.

5.5.4. Surface Morphology and Porosity Characterisation

The surface morphology and porosity characterisation of PCL/GelMA scaffolds constitute critical aspects of the investigation, offering essential insights into the structural features influencing scaffold performance. Understanding these scaffolds' surface topography and porosity holds significance in assessing their suitability for tissue engineering applications. This characterisation examines the scaffold architecture, illuminating factors such as surface roughness, pore size distribution, and interconnectivity. Such information proves

instrumental in optimising scaffold design to enhance cellular interactions, tissue ingrowth, and overall regenerative potential.

Figure 5.22 provides a comprehensive characterisation of PCL/GelMA scaffolds featuring various designs, including square, sinusoidal, spiral, and OC. Each design shows a fundamental aspect contributing to the scaffold's structural and functional attributes. In the associated SEM images in **Figure 5.22 A, B, C, and D**, a scale bar of 500μm offers an overview of the scaffold's overall structure. Further exploration is facilitated through images **Figure 5.22 A1, B1, C1, and D1** and **Figure 5.22 A2, B2, C2, and D2**, which focus on the GelMA and PCL pores within the scaffold, respectively, with a scale of 200μm. These images closely examine the individual components, enabling a more detailed understanding of the scaffold's intricate composition and architecture.

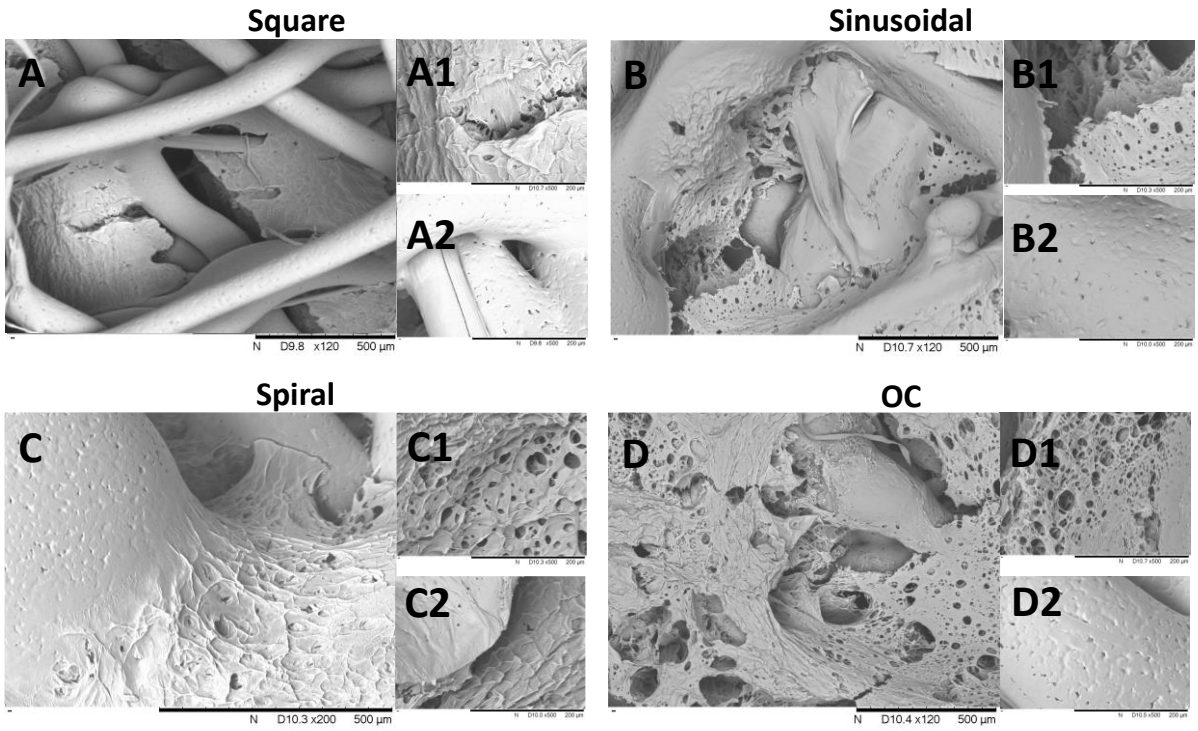


Figure 5.22 Characterisation of PCL/GelMA scaffolds with different geometries, including square, sinusoidal, spiral and OC. Each design A) Square, B) Sinusoidal, , C) Spiral , and D) OC, represents a fundamental aspect of the scaffold's structural and functional attributes. A-D) Scanning Electron Microscopy (SEM) images of section of the PCL/GelMA scaffolds. The scale bar in these images is set at 500µm. A1-D1) GelMA pores within the scaffold. The scale for these images is set at 200µm, providing a closer look at the GelMA component. A2-D2) PCL pores within the scaffold. Similar to A1-D1, the scale is set at 200µm for a detailed examination of the PCL component.

The analysis reveals consistent trends across the various scaffold designs. GelMA consistently demonstrates higher porosity than PCL, with percentages ranging from 8.65% to 6.65% (as represented in **Figure 5.22 A1, B1, C1, and D1**). This higher porosity indicates GelMA's ability to create more interconnected pores within the scaffolds. Additionally, GelMA tends to have larger particle sizes, contributing to its structural characteristics. Conversely, PCL (as represented in **Figure 5.22 A2, B2, C2, and D2**) exhibits lower porosity, ranging from 6.46% to 6.65%, and a filament width of approximately 190.879 ± 10.7635 µm. The lower porosity in PCL suggests a denser scaffold structure compared to GelMA. Analysing the interconnection between GelMA and PCL within the scaffolds

(represented in **Figure 5.22 A, B, C, and D**), it becomes evident that the combination of these materials maintains a porosity of approximately 6.65%. This relationship between GelMA and PCL increases overall scaffold porosity while preserving the structure's integrity.

5.5.5. Swelling and Degradation.

Experiments were conducted to assess the swelling and degradation behaviour of scaffolds co-printed with PCL/GelMA in various designs, including the OC scaffold, over time. Both the swelling capacity and degradation rate are critical attributes for optimal hydrogel performance in these scaffolds. These tests aimed to understand GelMA's long-term behaviour within the scaffolds and its potential impact on cell viability.

5.5.5.1. Swelling.

The hydrogel's swelling capacity is a significant importance as it indirectly reflects its water absorption capabilities. To assess the swelling of the scaffolds, PCL/GelMA scaffolds were submerged in dH_2O at 37°C. The hydrogel swelling ratios predominantly maintained their swollen state on the fourth week, with subsequent degradation in all the hydrogel samples, as shown in **Figure 5.23**

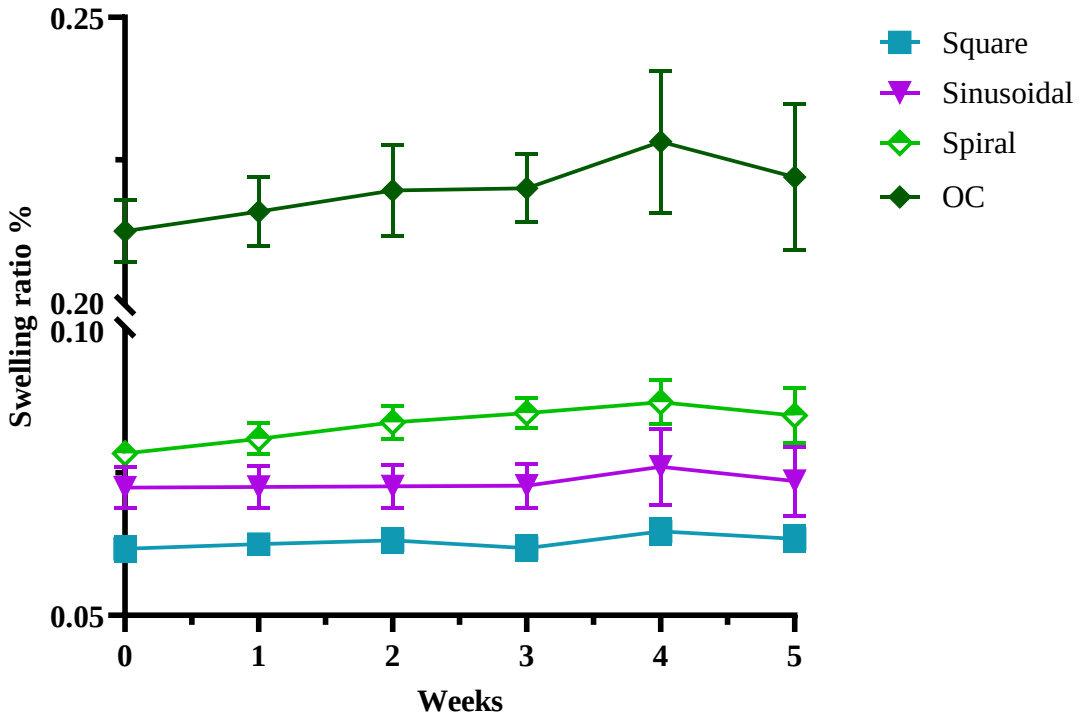


Figure 5.23 Swelling behaviour analysis of PCL/GelMA-scaffolds. PCL/GelMA-scaffolds weight variation over the initial 5-week period, investigated at 37°C. Providing valuable insights into the swelling characteristics of the designs of PCL/GelMA scaffolds and temperature conditions. Results denote mean± S.D. (n=6,N=3).

The observed variations in scaffold dimensions over the five weeks highlight the significant influence of time on scaffold morphology. The data, collected at weekly intervals for different scaffold geometries including square, sinusoidal, and spiral configurations, demonstrate fluctuations in dimensions. For instance, in the square and sinusoidal scaffold designs, it was observed slight increases in dimensions over the first few weeks, followed by relatively stable dimensions thereafter. Conversely, the spiral scaffold design exhibits more pronounced fluctuations in dimensions throughout the observation period. These findings emphasise the importance of considering scaffold geometry and its fundamental properties when designing tissue engineering scaffolds, as variations in dimensions can impact cell behavior and tissue regeneration processes.

Conversely, subjecting scaffolds to dehydration before cell culture has been identified as a potential cause of cell infections, as discussed in detail in **Chapter 7.** Consequently, this dehydrating test was excluded from the considerations and solely relied on the swelling test results to assess scaffold performance.

5.5.5.2. Degradation.

The stability assessment of the PCL/GelMA scaffold was conducted through a degradation test involving the immersion of all samples in 5 ml of dH_2O for ten weeks. Experimental conditions were rigorously maintained at 37°C. Subsequent observations were conducted to analyse the evolution of scaffold degradation behaviour over time within these specified temperature conditions. The obtained results unveiled a distinct trend, with the different geometries of the scaffolds incubated at 37°C exhibiting notably slower degradation rates than their counterparts maintained at lower temperatures, as visually depicted in **Figure 5.24.** These findings underscore the critical role played by the specific design configurations and temperature conditions in influencing the biodegradability of the PCL/GelMA scaffold, offering essential insights into its long-term stability.

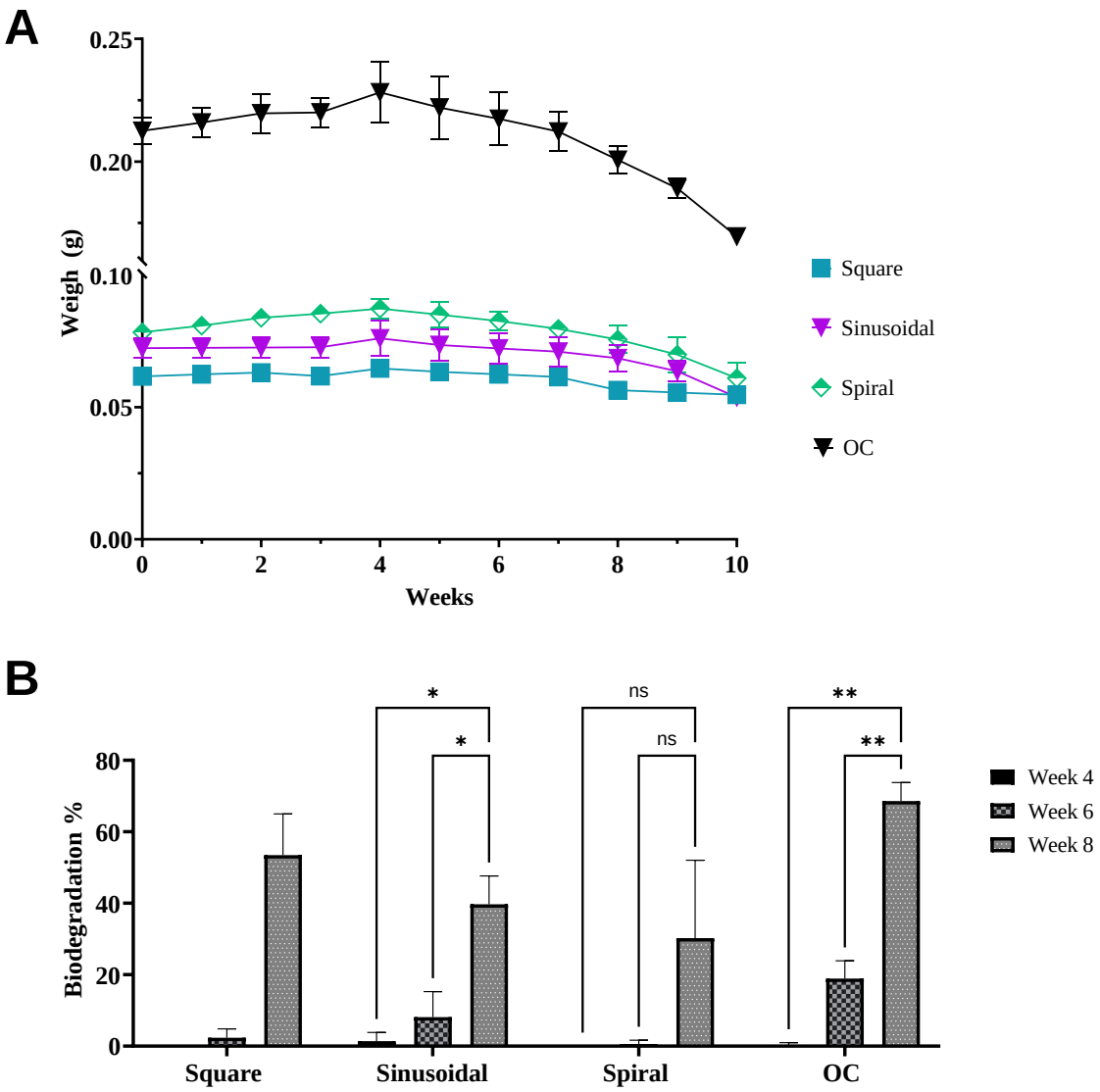


Figure 5.24 Biodegradation analysis of PCL/GelMA scaffolds. (A) Evolution of cube weight observed over ten weeks at 37°C. (B) Percentage biodegradation ratio at weeks 4, 6, and 8. Comprehensive insights are presented into the biodegradation behaviour of the GelMA composite under different conditions and concentration levels. Results denote mean± S.D. (n=6, N=3). Statistical analysis and significance levels are indicated as *** $p < 0.01$ and **** $p < 0.0001$.

Similarly, the OC scaffolds, which incorporate the three distinct designs, offer valuable insights into scaffold degradation behaviour. Notably, as illustrated in **Figure 5.24,** the degradation of the different geometries reveals notable trends in GelMA degradation. Initially, all scaffold designs exhibit relatively stable dimensions, with minimal changes

observed in the first few weeks. However, as the observation period progresses, a gradual decrease in dimensions is observed across all scaffold geometries. Notably, the spiral scaffold design displays the most pronounced decrease in dimensions over time, with an average decrease of approximately 0.0064 gr per week, followed by the sinusoidal and square configurations, which exhibit average decreases of approximately 0.0057 mm and 0.0053 mm per week, respectively. **Table 5.1** presents a comprehensive analysis of the biodegradation characteristics exhibited by the scaffolds, including square, sinusoidal, spiral, and OC. The data underscores a consistent pattern of gradual disintegration observed over the designated period. However, a notable trend emerges, indicating that scaffolds exhibit a slower degradation rate. Comparing the degradation rates of these diverse scaffolds at 37°C, it becomes evident that they display varying degrees of resistance to biodegradation. Specifically, by the eighth week of the observation period, the mass degradation for the square, sinusoidal, spiral, and OC scaffolds stands at 53.44%, 39.73%, 30.2640%, and 68.61%, respectively. This comparative analysis elucidates how the distinct design configurations interact with the biodegradation process, emphasising the particular resistance of the OC scaffolds to biodegradation at this condition.

Table 5.1 Mass degradation data collected of PCL/GelMA scaffolds, square, sinusoidal, spiral, and OC until week 8. Raw data values at 37°C for each scaffold, mass (g) used to calculate swelling ratio results. Results denote mean ± SD (n = 6, N=3).

GelMA samples (%w/v)	**Mass(g) as cast**	**Mass(g) Week 4**	**Mass (g) Week 6**	**Mass (g) Week 8**
Square	0.0617 ±0.0020	0.0647 ±0.0022	0.0624 ±0.0023	0.0564 ±0.0020
Sinusoidal	0.0724 ±0.0644	0.0760 ±0.00661	0.0722 ±0.0057	0.0685 ±0.0049
Spiral	0.0784 ±0.0008	0.0873 ±0.0039	0.08266 ±0.0034	0.0756 ±0.0052
OC	0.2125 ±0.0005	0.2282 ±0.0125	0.2174 ±0.0227	0.2007 ±0.0046

The OC scaffold, comprising square, sinusoidal, and spiral designs, demonstrates varying degradation patterns under different incubation conditions. Several notable trends become apparent when evaluating the mass loss of the OC scaffold over an 8-week period.The OC scaffold initiates with a mass of 0.2125g, progresses to 0.2282g by Week 4, and then reaches 0.2274g by Week 6 and by Week 8 a mass of 0.2007g, showing the degradation of the scaffold. This evaluation, as explained in **Table 5.1**, highlights the influence of incubation temperature on the degradation behaviour of the OC scaffold.

5.6. Mechanical Testing.

5.6.1. Polycaprolactone.

The mechanical properties of a scaffold for the OC defect repair play a pivotal role in its effectiveness and long-term success. These properties comprise key characteristics such as stiffness, elasticity, and load-bearing capacity. An ideal scaffold must mimic the mechanical behaviour of natural osteochondral tissue to provide adequate support during the healing process. This is crucial because improper mechanical properties can lead to issues such as stress shielding, where the scaffold absorbs too much load, preventing the surrounding tissue from bearing its natural share of mechanical stress. Conversely, if the scaffold is too mechanically weak, it might fail to provide the necessary structural support, hindering tissue regeneration. Therefore, achieving the right balance of mechanical properties is imperative to facilitate optimal tissue growth, integration, and functional restoration, making it a critical aspect of scaffold design for osteochondral defect repair. In **Figure 5.25**, an unconfined compression testing overview is presented for both cast PCL cubes and cylindrical printed scaffolds.

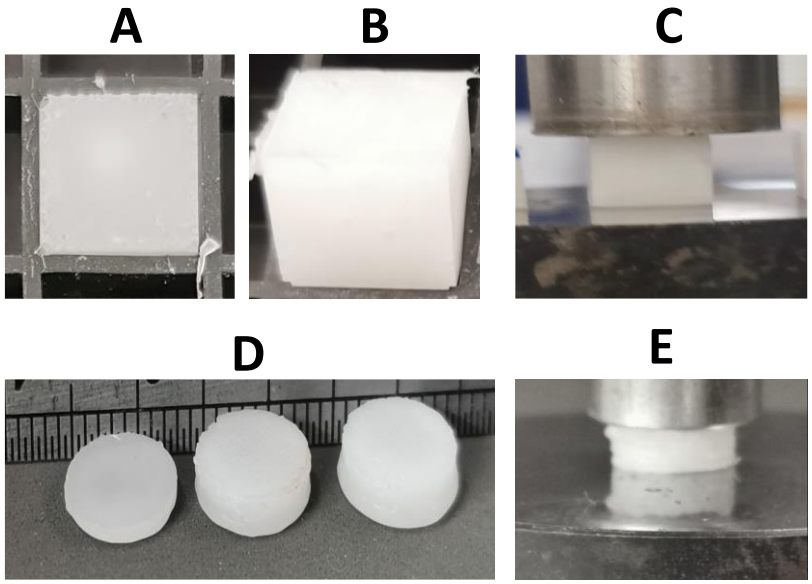


Figure 5.25 Mechanical testing of PCL structures comprising cast cubes and cylindrical printed scaffolds. A-B) PCL cast cubes (10mmx10mmx10mm). C) Illustrates the unconfined compression testing of the PCL cube under axial load. D) Cylindrical scaffolds with varying designs (1.2 mm, 3.6 mm, and 4.2 mm) offer a comparative analysis of their size-dependent mechanical properties. E) Unconfined compression testing of the cylindrical scaffolds.

The compressive mechanical properties of the scaffolds constructed using different materials are graphically presented in **Figure 5.26**. This comprehensive analysis offers valuable insights into the scaffolds varying stiffness and structural characteristics. To contextualise these findings, the Youngs modulus of the PCL casted cubes, as depicted in **Figure 5.26** was determined to be 35.25 ± 2.09 MPa. Comparatively, previous research by Dziadek et al., 2015. reported a Youngs modulus of approximately 38 MPa for pure PCL, aligning with the results obtained in this study.

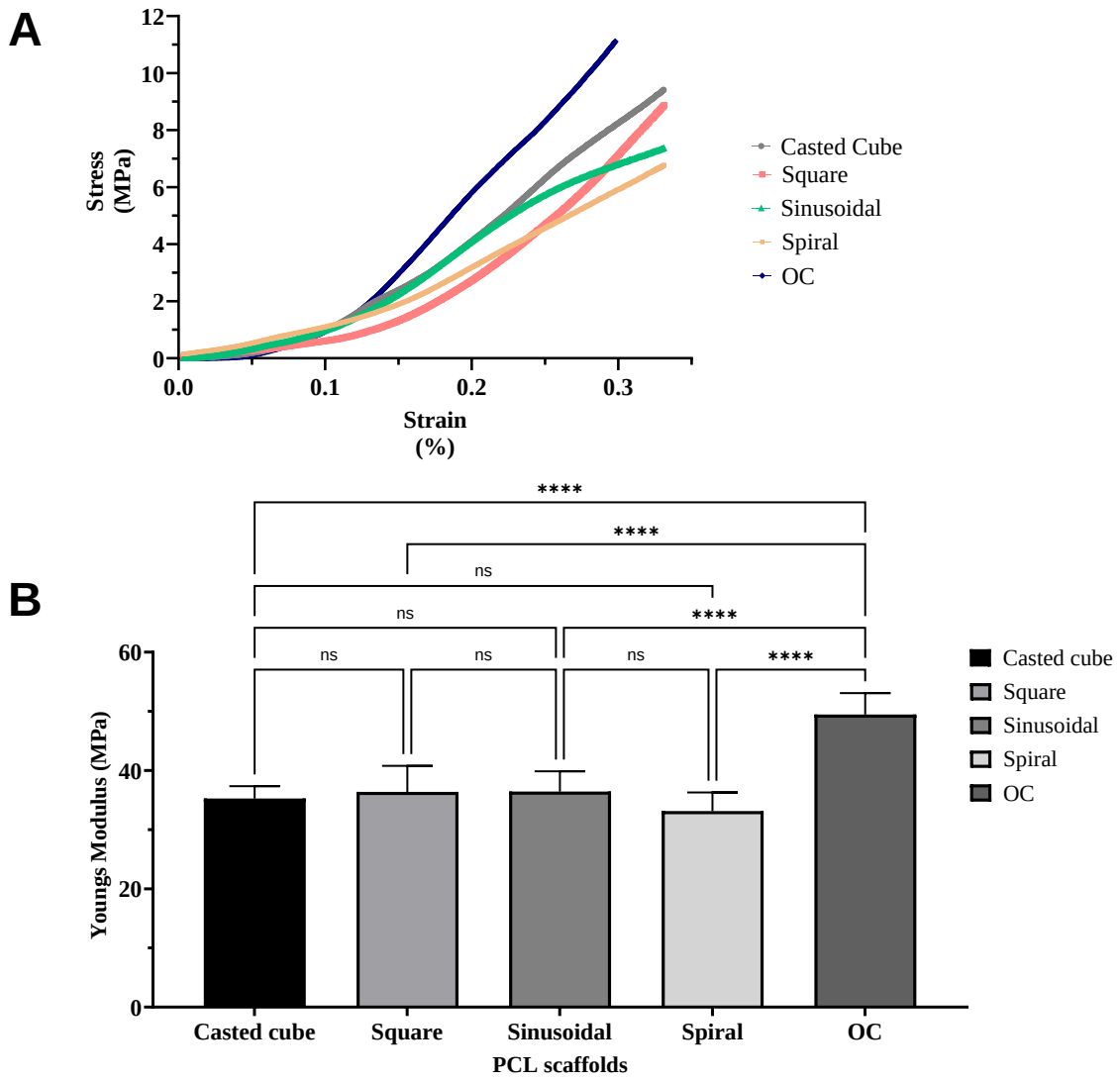


Figure 5.26 Mechanical properties of PCL 3D printed scaffolds and a PCL casted cube. A) Representative stress/strain curves illustrating deformation, the elastic (proportionality) limit, and the plastic region. B) Youngs modulus represents printed samples' compressive stress/strain curves. Results denote mean± S.D. (n=6,N=3). Statistical analysis and significance levels are indicated as ** $p < 0.024$ and **** $p < 0.0001$.

The most notable aspect lies in the considerable variations in stiffness observed across the different scaffold designs. A clear trend emerges when assessing the compressive mechanical properties of the various scaffold designs. In the square, sinusoidal, spiral, and OC designs, the Youngs modulus values were measured as, 36.38 ± 4.40 MPa, 36.44 ± 3.42MPa, 33.13 ± 3.14 MPa, and 49.46 ± 3.62 MPa, respectively as presented on **Table 5.2** . This substantial variation underscores the influence of the different geometries designs on scaffold stiffness.

Table 5.2 Comparative analysis of Youngs modulus for diverse structures, including cast PCL cubes and 3D-printed scaffolds with square, sinusoidal, and spiral designs. Likewise, including OC scaffolds with multiple designs extends the investigation, showcasing the mechanical implications of different geometries. Results denote mean± S.D. (n=6,N=3).

PCL Samples	**Dimensions (mm)**	**Youngs Modulus (MPa)**
Cast cube	10mm x 10 mm x 10mm	35.25 ± 2.09
Square	⌀ = 8.38 ± 0.10 h = 1.12 ± 0.21	36.38 ± 4.40
Sinusoidal	⌀ = 8.55 ± 0.07 h = 1.25 ± 0.11	36.44 ± 3.42
Spiral	⌀ = 8.30 ± 0.15 h = 1.25 ± 0.10	33.13 ± 3.14
OC	⌀ = 8.44 ± 0.20 h = 4.68 ± 0.07	49.46 ± 3.62

The variability in Youngs modulus values was reported in the literature for similar materials. These discrepancies are often attributed to differences in manufacturing techniques, designs and dimensions of the scaffolds, and environmental conditions during testing, as the type of test. As a result, the findings underline the critical importance of carefully selecting scaffold design and material properties, ensuring they align with the specific requirements of diverse tissue engineering applications. This knowledge contributes significantly to understanding scaffold mechanics and informs the selection of appropriate scaffold designs.

5.6.2. Gelatin Methacrylate

Similarly to the evaluation conducted for PCL, an essential examination of GelMA was undertaken to comprehend its impact on the mechanical properties of the OC scaffold. In this context, 10% GelMA compression-casted cubes, each measuring 1x1x1 mm, were subjected to rigorous testing. **Figure 5.27 A-B** visually represents the GelMA casting process, while **Figure 5.27 C** portrays a GelMA cube post-unconfined compression, highlighting the force-induced fracture.

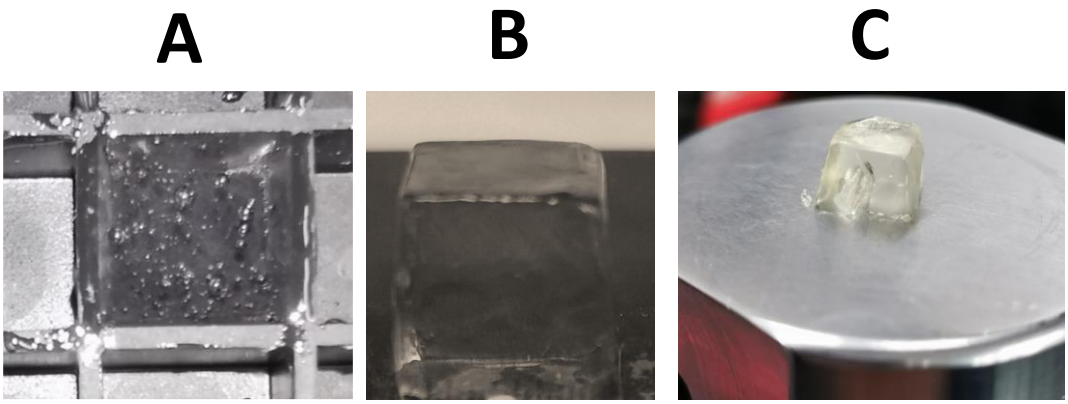


Figure 5.27 Mechanical testing of GelMA casted cubes comprising. A-B) GelMA casted cubes (1mmx1mmx1mm). C) Illustrates the unconfined compression testing of the GelMA cube under axial load.

The stress-strain curves characterising the GelMA samples exhibited notable noise and nonlinearity, as evident in **Figure 5.28**. A linearised average stress-strain relationship was employed to calculate compression Youngs modulus, yielding a value of 0.25 ± 0.14 MPa (refer to **Table 5.3** for further details). This comprehensive evaluation contributes to a deeper understanding of GelMA's mechanical behaviour within the context of the OC scaffold development.

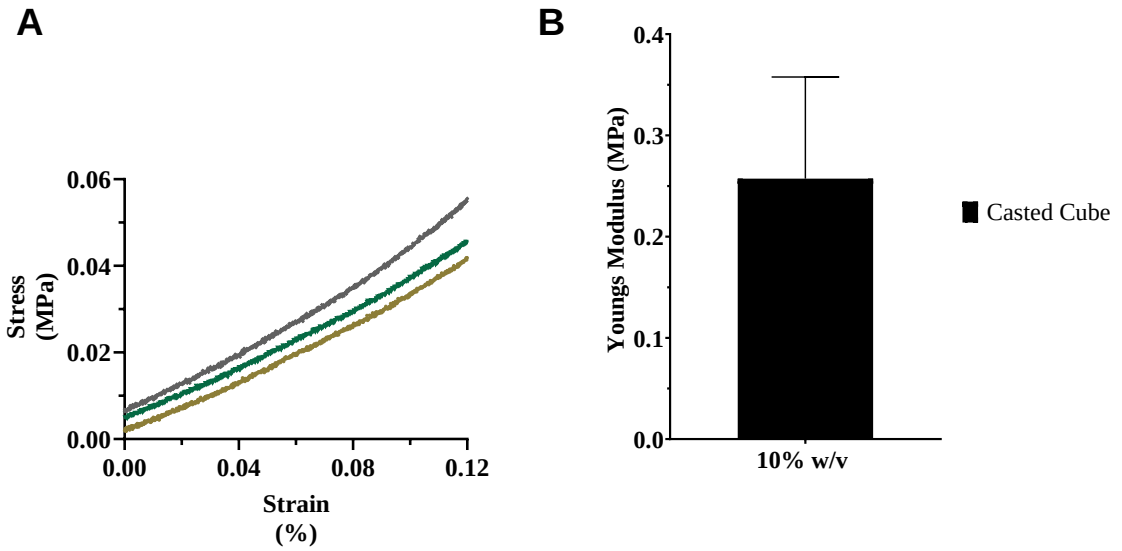


Figure 5.28 Mechanical properties of 10% w/v GelMA casted cube. A) Representative stress/strain curves illustrating deformation, the elastic (proportionality) limit, and the plastic region. B) Youngs modulus representing compressive stress/strain curves of 10% w/v GelMA casted cube. Results denote mean± S.D. (n=6,N=3).

Table 5.3 Comparative analysis of Youngs modulus for diverse structures, including casted GelMA cubes, showcasing the mechanical implications of the material. Results denote mean± S.D. (n=6, N=3).

GelMA Sample	Dimensions (mm)	Youngs Modulus (MPa)
Casted cube	L= 9.56 ± 0.35 h = 9.52 ± .042 w = 9.3 ±0.27	0.25 ± 0.14

5.6.3. PCL/GelMA Scaffolds

The compressive mechanical properties in Figure 5.29, provides critical insights into the varying stiffness of PCL/GelMA scaffold designs This highlights improvements in the mechanical structure regarding the alignment of the filaments in each geometry design and the improvement of bonding by implementing a GelMA filament between the two PCL filaments in each layer of the respectively design. Examining the Youngs modulus values presented on **Table 5.4** for the square, sinusoidal, and spiral designs, which are 36.96 ±

2.49MPa, 38.24 ± 3.75 MPa, and 33.41 ± 3.74 MPa, respectively, it becomes evident that each geometry filament alignment possesses distinct mechanical characteristics. In contrast, the OC scaffold stands out with a higher Youngs modulus of 49.74 ±3.77MPa, signifying its superior stiffness.

However, the significance of these comparisons extends beyond individual design attributes. The collective analysis of the square, sinusoidal, and spiral designs prove the OC design's mechanical behaviour of the scaffold. It illustrates how variations in structural features among these three designs contribute to the OC scaffold's overall stiffness. Such insights underline the fundamental role of scaffold design decisions in tailoring mechanical properties to meet the specific requirements of diverse tissue engineering applications.

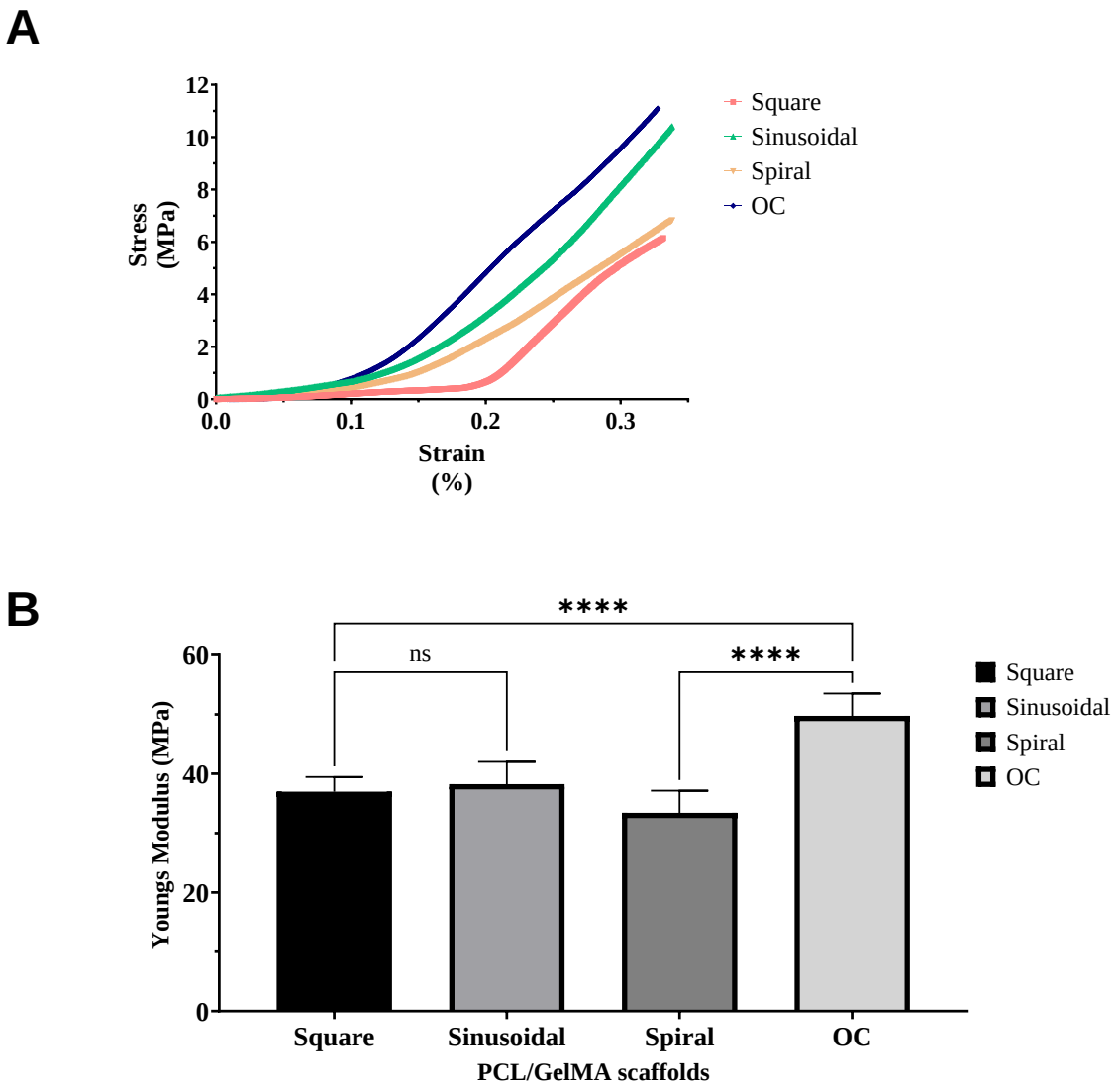


Figure 5.29 Mechanical properties of PCL/GelMA 3D printed scaffolds. A) Representative stress/strain curves illustrating deformation, the elastic (proportionality) limit, and the plastic region. B) Youngs modulus represents printed samples' compressive stress/strain curves. Results denote mean± S.D. (n=6,N=3). Statistical analysis and significance levels are indicated as * $p < 0.0162$, * $p < 0.0014$ and ** $p < 0.001$.

Table 5.4 Comparative analysis of Youngs modulus for diverse structures, including PCL/GelMA, with different square, sinusoidal, and spiral designs. Likewise, including OC scaffolds with multiple designs extends the investigation, showcasing the mechanical implications of different geometries. Results denote mean± S.D. (n=6,N=3).

PCL/GelMA Samples	**Dimensions (mm)**	**Youngs Modulus MPa**
Square	⌀ = 8.35 ± 0.20 h = 1.56 ± 0.72	36.96 ± 2.49
Sinusoidal	⌀ = 8.45 ± 0.16 h = 1.46 ± 0.19	38.24 ± 3.75
Spiral	⌀ = 8.25 ± 0.21 h = 1.48 ± 0.06	33.41 ± 3.74
OC	⌀ = 8.44 ± 0.22 h = 4.68 ± 0.07	49.74 ±3.77

5.6.4. PCL/GelMA/Cells Scaffolds

Evaluating the Youngs modulus values presented on **Table 5.5** for the square, sinusoidal, and spiral designs, measuring 45.09 ± 2.99 MPa, 46.05 ± 2.71 MPa and 42.27 ± 4.89, respectively, a clear divergence in their mechanical behaviour emerges. The OC scaffold incorporates elements from all three designs (square, sinusoidal, and spiral) into a single structure. This integration results in a higher Youngs modulus of the PCL/ of 50.68 ± 3.38 MPa for the OC scaffold, surpassing the individual designs, as presented on Figure 5.30. The interactive effect achieved by combining these three distinct design elements within the OC scaffold contributes to its superior stiffness and remarkable mechanical performance. Furthermore, **Figure 5.31** provides valuable findings into the distinct characteristics of different scaffold designs involving PCL/GelMA/Cells, scaffolds were sterilised, seeded and cultured for 14 days, as explained in **Chapter 7**, which may account for the increment in mechanical properties compared to the PCL/GelMA results.

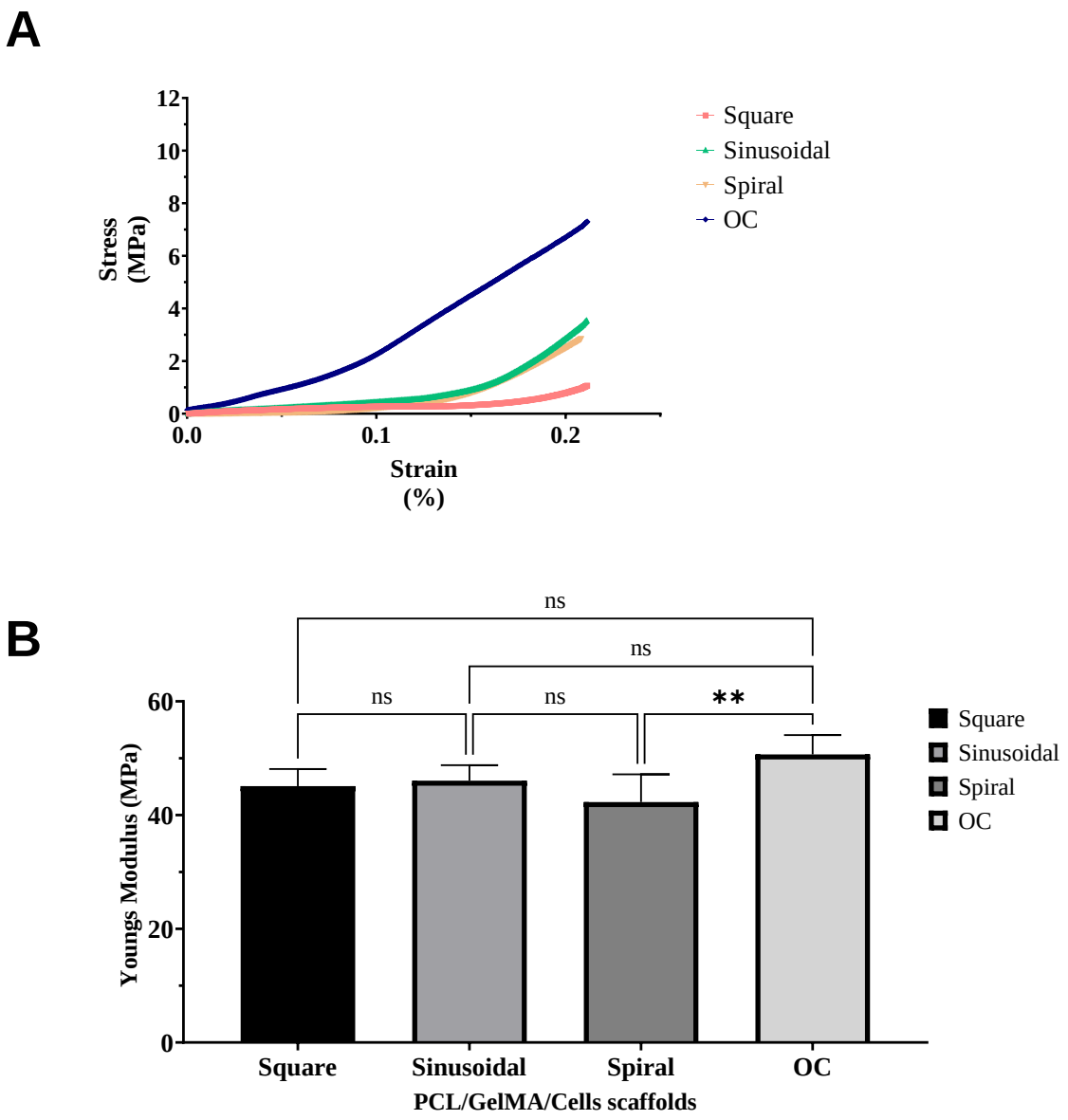


Figure 5.30 Mechanical properties of PCL/GelMA with cells 3D printed scaffolds. A) Representative stress/strain curves illustrating deformation, the elastic (proportionality) limit, and the plastic region. B) Youngs modulus represents printed samples' compressive stress/strain curves. Results denote mean± S.D. (n=6,N=3). Statistical analysis and significance levels are indicated as ** $p < 0.0140$, *** $p < 0.0020$ and **** $p < 0.0001$.

Table 5.5 Comparative analysis of Youngs modulus for diverse structures, including PCL/GelMA with cells with different square, sinusoidal, and spiral designs. Likewise, including the OC scaffolds with multiple designs extends the investigation, showcasing the mechanical implications of different geometries. Results denote mean± S.D. (n=6,N=3).

PCL/GelMA with cells Samples	**Dimensions (mm)**	**Youngs Modulus MPa**
Square	⌀ = 8.35 ± 0.20 h = 1.56 ± 0.72	45.09 ± 2.99
Sinusoidal	⌀ = 8.45 ± 0.16 h = 1.46 ± 0.19	46.05 ± 2.71
Spiral	⌀ = 8.25 ± 0.21 h = 1.48 ± 0.06	42.27 ± 4.89
OC	⌀ = 8.44 ± 0.21 h = 4.68 ± 0.07	50.68 ± 3.38

Comparative analysis of the compressive mechanical properties, as presented in **Figure 5.31,** offers a comprehensive overview of how different scaffold designs perform under varying conditions. The Youngs modulus for each design across different material compositions and cellular environments yields valuable insights.

The results reveal interesting Youngs modulus trends across scaffold designs and conditions. In the case of square PCL scaffolds, Youngs modulus values were found to be 36.38 ± 4.40 MPa, whereas for square PCL/GelMA scaffolds, it slightly increased to 36.96 ± 2.49MPa. Remarkably, when cells were introduced into the square PCL/GelMA scaffold, Youngs modulus further increased to 45.09 ± 2.99 MPa.

Similarly, Sinusoidal PCL scaffolds exhibited a Youngs modulus of 36.44 ± 3.42 MPa. Transitioning to Sinusoidal PCL/GelMA scaffolds resulted in a higher Youngs modulus of 38.24 ± 3.75 MPa, which further increased to 46.05 ± 2.71MPa with the inclusion of cells.

In the case of spiral PCL scaffolds, it had a Youngs modulus of 33.13 ± 3.14MPa. Transitioning to spiral PCL/GelMA scaffolds increased the Youngs modulus to 33.41 ± 3.74MPa, and the inclusion of cells led to a substantial increase to 42.27 ± 4.89MPa.

However, the most significant increase in Youngs modulus was observed in the OC design, which incorporates elements from the square, sinusoidal, and spiral designs into PCL/GelMA scaffolds with cells. The resulting Youngs modulus was notably higher at 50.68 ± 3.38 MPa. This surpasses the individual design performances, indicating a synergistic effect from the combination. These increased the mechanical properties of the OC scaffold as a promising candidate for tissue engineering applications, which require structural support.

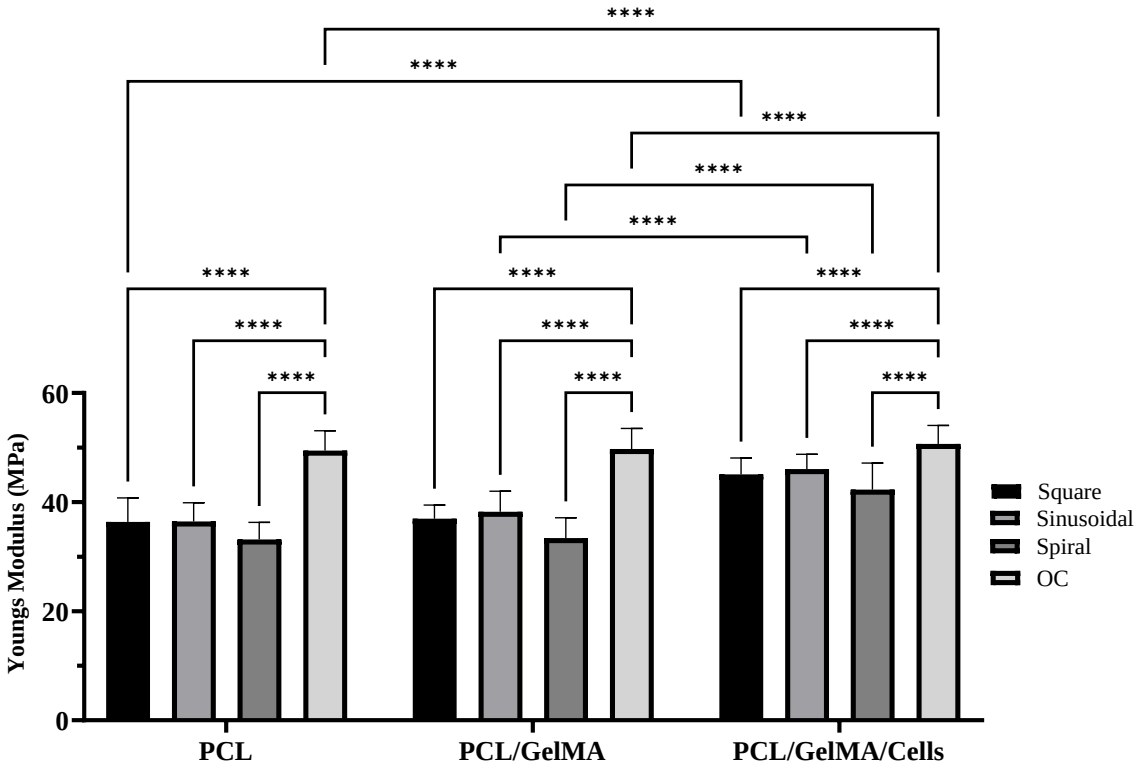


Figure 5.31 Comparative analysis of Youngs modulus representing compressive stress/strain curves of 3D printed scaffolds of PCL, PCL/GelMA, and PCL/GelMA with cells. Results are expressed as mean ± SD (n=6, N=3). Statistical analysis and significance levels are denoted as **** $p < 0.0001$.

As depicted in **Figure 5.31**, a statistical significance of $p = 0.0001$ was observed in the Young's modulus between designs utilising the same material. Furthermore, there is a significant difference between PCL/GelMA and PCL/GelMA/Cells, indicating changes in material conditions when cells are seeded into the scaffold and incubated for 14 days, compared to the conditions of PCL/GelMA scaffolds tested.

These findings demonstrate that scaffold design and different conditions can play a crucial role in designing a scaffold that meets the mechanical requirements of the OC tissue. It is essential to acknowledge that the literature reports varying mechanical property ranges, depending on factors such as cartilage type, donor age, and the specific testing methodologies employed (as reported in **Chapter 2 - Table 2.5**). Additionally, some studies rely on single-donor tissue samples, whereas others incorporate multiple donor tissues into their analyses (Jurvelin et al., 2003; Landínez-Parra et al., 2012; Little et al., 2011; Schoonraad et al., 2021; Thambyah et al., 2006; Vidal-Lesso et al., 2014). However, in a study by Kabir et al., 2021, tissue samples underwent unconfined compression testing, resulting in a compression modulus of 10.60 ± 3.62 MPa. Comparatively, the OC scaffold manufactured and seeded with cells exhibits a Compressive Modulus of 50.68 ± 3.38 MPa. This indicates that OC scaffold successfully meets the required mechanical standards, suggesting its potential suitability for various tissue engineering applications.

5.7. Conclusions.

As detailed in this chapter, the process of 3D printing PCL/GelMA scaffolds is a crucial development in the constantly changing field of tissue engineering and regenerative medicine (Chan & Leong, 2008; Daly & Kelly, 2019; Jian et al., 2020; Schipani, Scheurer, et al., 2020). The process commenced with the optimisation of the 3D printing methodology for PCL and GelMA. This initial phase provided of develop customised OC scaffolds, layered constructs has been explored in the literature (Levingstone et al., 2014b; K. Q. Liu et al., 2020; Pereira et al., 2018), the approach used by three different geometries designs: square, sinusoidal, and spiral. Though sharing the same dimensions, these designs introduced a new level of variation due to their distinct filament alignment, strand spacing and structure, facilitating a comprehensive exploration into scaffold architecture, and their impact on cellular behaviour.

One of the research's breakthroughs was the effective co-printing of PCL with GelMA, which was not without challenges. The difference in mechanical characteristics of these two materials created challenges such as wrapping, bending and inadequate interlayer bonding while optimising the printing. However, these difficulties were overcome by design tactics such as combining GelMA layers between PCL, adopting a similar approach as (Ruiz-Cantu et al., 2020b). As a result, the scaffolds' structural integrity and printing performance

improved significantly. This achievement shows the way for the development of scaffolds with increased mechanical properties and the ability to regulate their characteristics during printing. Surface porosity characterisation was another critical aspect of this study, which revealed the fascinating discrepancies between GelMA and PCL. The contrast of these materials highlighted their complementary functions in preserving the scaffold's integrity, with insights into surface roughness, pore size distribution, and interconnectivity being crucial for optimising scaffold design (Joyce et al., 2023; Nava et al., 2016). Swelling and degradation studies were critical in determining the scaffolds' long-term behaviour. The regulated modulation of swelling at various temperatures proved beneficial, particularly in applications requiring precise control of pore size. Furthermore, the findings from degradation experiments offer information on the durability of the scaffolds over time, with temperature conditions playing a crucial influence. This understanding is critical for assuring the scaffolds' long-term survival in practical applications.

Mechanical testing conducted in this thesis revealed the variations in the stiffness of scaffold geometries. Schipani et al. further demonstrated how architecture configurations influence the Youngs modulus, by manufacturing a PCL scaffold with a square design and altering the configuration with a double offset, showing that the Youngs modulus decreases for the offset configuration (Schipani, Scheurer, et al., 2020). Notably, the OC scaffold manufactured achieved a higher compression modulus by combining design geometries from various configurations, in the contrary of Daly & Kelly, who reported a PCL/GelMA/Pluronic square scaffold with lower compression Youngs modulus due printing configuration (Daly & Kelly, 2019). This result underscores the importance of design geometries in adapting the mechanical attributes of scaffolds to meet specific tissue engineering requirements. The OC scaffold's mechanical performance shows a promising behaviour for fulfilling the mechanical properties. This study represents the 3D printing of PCL/GelMA scaffolds by co-printing different geometries with different mechanical properties in order to create an OC scaffold with a higher compression modulus as previous reported by Daly & Kelly and Schipani (Daly & Kelly, 2019; Schipani, Scheurer, et al., 2020). The findings shown in this chapter can offer a different perspective to manufacture a customisable, versatile, and mechanically scaffold for tissue engineering applications.

Chapter 6. FE Modelling of the designs for osteochondral scaffolds.

This chapter describes a comprehensive exploration of the mechanical properties of the 3D-printed OC scaffold by employing finite element (FE) analysis . The primary objective is to develop a predictive model to assess and validate the scaffold's mechanical characteristics. This computational framework serves as a powerful tool for predictive analysis, offering insights into the scaffolds behaviour under varying conditions and loading scenarios. Through the application of FE, a deeper understanding of the structural integrity and performance of the OC scaffold.

6.1. Introduction.

The design and evaluation of the OC scaffolds have increasingly employed finite element (FE) as a novel technique. This approach provides a comprehensive means to delve deeper into the scaffold's architectural, material, and mechanical properties, thereby ensuring optimal cell differentiation, a critical factor impacting tissue scaffold performance(Cahill et al., 2009; Koh et al., 2019; Sahai & Gogoi, 2020) The suitability of a scaffold for tissue engineering on interrelated factors that collectively contribute to achieving biocompatibility and cell proliferation. Notably, it entails attaining a level of porosity and pore interconnectivity that effectively facilitates cellular migration and the seamless transport of nutrients and waste products into and out of the scaffolds (Doyle et al., 2014b).

However, when manufacturing processes result in complex geometries, as seen in the case of 3D printed scaffolds, the applicability of these models can become limited, necessitating the adoption of FE. FE anlysis is a numerical methodology used to resolve differential equations through discretisation. This technique becomes especially powerful in creating mechanical models for complex geometries by breaking them down into a network of simpler, solvable elements. FE is also instrumental in modelling structures composed of multiple materials (Khennane, 2013). As a result, FE analysis has frequently become an integral component of the 3D-printed scaffold design process (Hairui, Yu, & Ling, 2021). Zhang *et al.* used lay-down angles, filament diameters, inter-filament spacing, and layer overlaps in the simulation using compressive loading conditions to create a 3D-printed scaffold. The study revealed that by increasing the porosity in the scaffold, the Youngs modulus will decrease. Additionally, a gradient transition in the scaffold assembling by

layers with different lay-down angles was achieved, demonstrating the connection between the mechanical properties and the pore geometry (B. Zhang, Guo, et al., 2020).

Tan et al.'s research introduced the development of in silico models guiding the design of poro-elastic mimics of articular cartilage, revealing the necessity of incorporating stiff fibres within a fibre-reinforced poro-elastic framework to amplify the fraction of load supported by fluid pressure. This proposal emphasised the fundamental role of a stiffer fibrous phase in developing physiological mimics of articular cartilage, underscoring the importance of the structural framework in achieving optimal load distribution and biomechanical functionality, crucial for the effective performance and longevity of tissue-engineered constructs (Tan et al., 2023).

This chapter aims to predicting the mechanical properties of scaffolds through the utilisation of data gathered from the unconfined compression tests conducted on various materials and scaffold geometries in previous chapters. The primary objective is to employ a FE analysis approach, to validate the structural designs of the OC scaffolds. The application of FE serves as a crucial method for substantiating the structural integrity and mechanical characteristics required for the OC scaffold by understanding each zone of the native tissue properties.

6.2. CAD Geometries.

The geometries generated from BioCAD software (RegenHU, Switzerland) for the 3D extrusion-based printing are not compatible with ABAQUS software. Geometries of square, sinusoidal, spiral and OC scaffold were replicated in SolidWorks (Dassault Systèmes) as a cylindrical three-dimensional object with a diameter of 8mm and a height of 1.2 mm for each geometry and for the OC scaffold a diameter of 8mm and a height of 4.6mm.

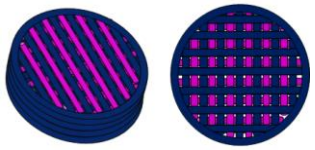
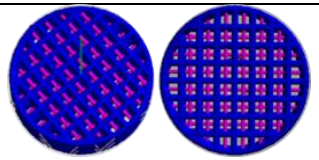
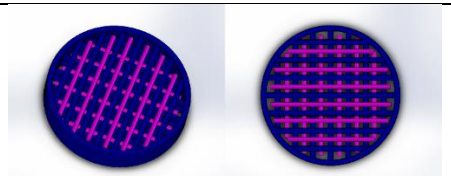
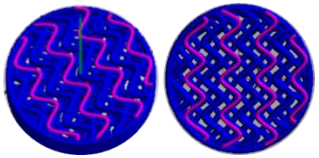
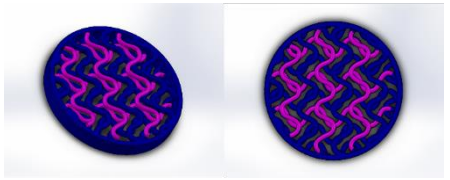
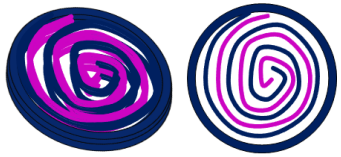
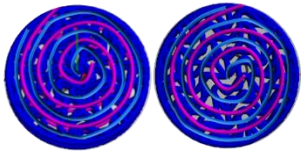
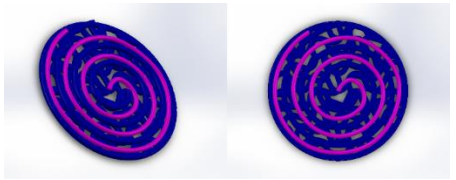
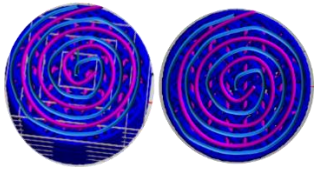
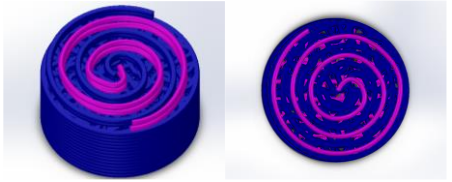
6.2.1. Development of CAD scaffolds.

The geometries were developed through SolidWorks (Dassault Systems, France) by creating layer-by-layer extrusion parameters from BIOCAD and adjusting dimensions based on experimental measurements. An iterative approach was adopted in CAD model design, with a focus on responsiveness to experimental findings. In the initial iteration, the square scaffold geometry was utilised to validate setup parameters. To validate the FE model, measured print parameters from fabricated scaffolds such as fibre spacing, fibre diameter,

and layer height were used as geometric inputs. The compressive Young's modulus was employed as the optimization variable. The parameters were iteratively varied to determine a minimum in the absolute standard error of the predictions compared to the experimental values.

Each geometry of the extruded PCL and GelMA was modelled using ongoing experimental insights, as illustrated in **Table 6.1**. This was a foundational step in ensuring the CAD model's fidelity to experimental conditions. The development of the CAD model aimed to assess how geometries variations affect mechanical properties from experimental tests. All print parameter values considered are detailed in **Chapter 5**.

Table 6.1 Samples designs of the three different geometries using BioCAD and SolidWorks based on the sketch design.

Sample Design Code	Sample Design Sketch	Sample Design BioCAD RegenHU	Sample Design SolidWorks
Geometry A Square			
Geometry B Sinusoidal			
Geometry C Spiral			
Geometry D OC Scaffold	------		

6.3. Finite Element Analysis.

The Parasolid Model Part file (.X_T) of the model created on SolidWorks was imported into ABAQUS CAE 2022 (Dassault Systemes, France). Meshing was performed using the quadratic tetrahedral element. An ABAQUS assembly was set up to simulate the loading case of unconfined compression, with each scaffold and its respective GelMA components enclosed between two rigid planar shell elements.

In the ABAQUS simulation setup, an assembly was configured to replicate the unconfined compression loading scenario. In this setup, each geometry scaffold was encapsulated between two rigid planar shell elements, as illustrated in **Figure 6.1C.** Compression analysis involved subjecting each PCL and PCL-GelMA scaffold to compression forces and compressive loads on the top plate with magnitudes of 1N and 5N, aiming to induce small strains. The analyses were executed utilising the ABAQUS Explicit solver, initiating with a time increment of 0.01s and setting a minimum time increment of 1E-8s. The solver was allowed to iteratively converge to a solution, during which stress distributions and displacements were.

The determination of scaffold stiffness in the downward loading direction involved a two-step calculation process. Firstly, compressive stress was computed by dividing the applied scaffold load by the top surface area, determined from the measured scaffold width. Subsequently, the compressive strain was ascertained by dividing the maximum simulated displacement of the top plate by the measured original scaffold length. This comprehensive approach allowed for a precise and comprehensive assessment of the scaffold's stiffness characteristics under specific loading conditions, providing valuable insights into its mechanical behaviour. Material properties were defined by linear stiffness values, and the data obtained from compressive tests of PCL and GelMA was incorporated. Boundary conditions were established to ensure stability during the simulation. Specifically, the bottom compression plate was fixed at its centroid, while the top plate was constrained in all directions except the vertical axis. Likewise, contact conditions were implemented in the model, incorporating a coefficient of friction set at 0.1 to mitigate any potential sliding between components. This comprehensive simulation framework aimed to capture the mechanical behaviour of the PCL-GelMA scaffolds under unconfined compression, providing a thorough understanding of their response to applied loads.

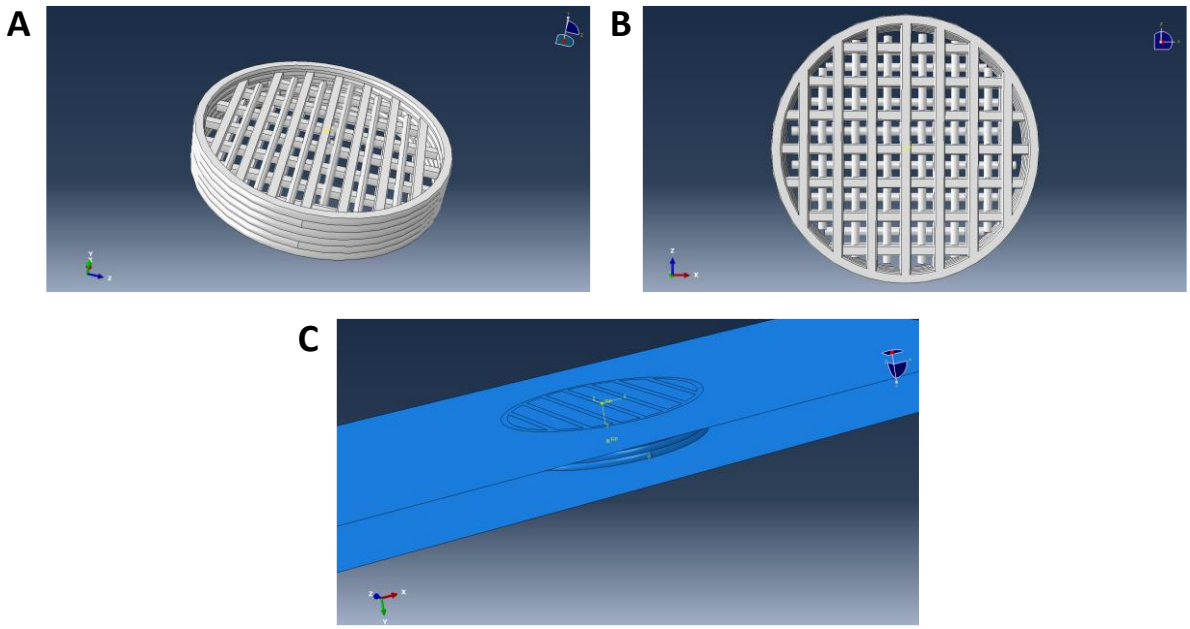


Figure 6.1 Square PCL/GelMA Scaffold. A) Side view, B) top view, and C) geometry scaffold encapsulated between two rigid planar shells.

6.4. Simulations Conditions.

The compression analysis of the PCL cubes and GelMA cubes, both with a dimension of 10X10X10mm, is presented in **chapter 5, section 5.3 and section 5.4**, respectively. PCL cube Youngs modulus 35.25 ± 2.09MPa, and GelMA cube Youngs modulus 0.25±0.14 MPa. The literature suggests a Poisson's ratio for PCL between 0.3-0.45, but the most common is 0.45, which was selected for the analysis (Doyle et al., 2014c; Eshraghi & Das, 2010; Meng et al., 2020; P. Zhang et al., 2018). PCL exhibited a density of $11.6E^{-03}g.mm^{\wedge-3}$.

6.4.1. Mesh.

Mesh sensitivity analysis on the FE model was performed by comparing the predicted elastic modulus using different mesh sizes. The meshing of tetrahedral elements is subject to specific criteria limits representing the minimum allowed volume-to-surface ratio, which is set at 0.0001. This ensures that the tetrahedral elements possess a certain degree of regularity to maintain accuracy in the analysis. Additionally, the smaller face corner angle must be greater than 5 degrees, and the larger face corner angle should be less than 170 degrees.

These criteria contribute to the avoidance of excessively distorted or degenerate tetrahedral elements that may compromise the reliability of FE simulations. Lastly, a uniform aspect ratio limit of 10 is applied across tetrahedra, emphasising the importance of maintaining reasonable element proportions for effective and stable numerical analyses. These specific elements were detected through the utilisation of evaluate mesh functionality. In the event that more than 0.1% of elements within the mesh exceeded these predefined thresholds or if there was a concentration of failed elements within a singular geometric feature, a decision was made to initiate a re-meshing process for the entire model, as visually represented in **Figure 6.2**. The strategies employed for re-meshing were multifaceted, involving a combination of partitioning, global mesh refinement, localised mesh refinement, curvature control, and minimum size control. These parameters underwent meticulous adjustments iteratively until the mesh quality conformed to the predefined limits. In scenarios where time constraints were not prohibitive, a finer mesh with an input sizing of 0.05mm was implemented**.** Conversely, for larger mesh sizes, such as 0.1mm, for the OC scaffold. This approach ensured that the mesh adhered to the specified criteria, maintaining the structural integrity and accuracy of the model.

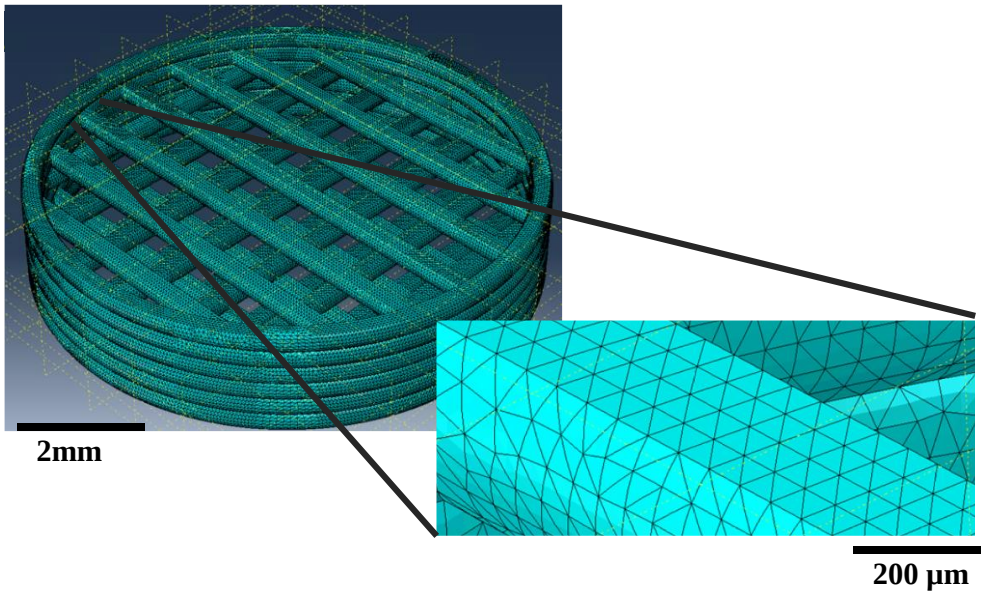


Figure 6.2 Tetrahedral mesh (0.05mm element size) of the Square Scaffold with 200µm Contact Width.

6.4.2. Compression Properties.

The FE analysis was utilised to predict Youngs modulus of PCL scaffolds with various geometries, including square, sinusoidal, spiral, and OC structures. The predicted values, 36.10 MPa, 34.96MPa, 32.85883 MPa, and 48.503 MPa for square, sinusoidal, spiral, and OC scaffolds, respectively, demonstrate the efficacy of the FE model in capturing the mechanical behaviour of these complex structures. The predictions are closely aligned with the experimentally measured compression Youngs modulus values. The experimentally obtained results show a compression Youngs modulus of 36.38 ± 4.40MPa, 36.44 ± 3.42 MPa, 33.1 ± 3.14MPa, and 49.46 ± 3.62MPa for square, sinusoidal, spiral, and OC scaffolds respectively. The close correlation indicates that the FE model successfully captures the mechanical response of PCL scaffolds across geometries configurations, as shown in **Figure 6.3.**

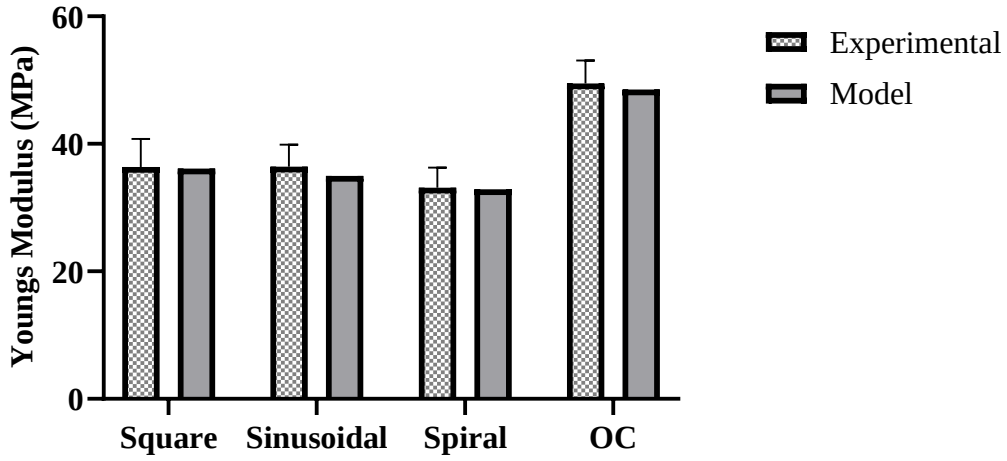


Figure 6.3 Experimental results vs. model Youngs modulus comparison of PCL scaffolds. Experimental results are expressed as mean ± SD (n=6, N=3).

For PCL/GelMA scaffolds, the experimental assessment revealed distinct Youngs modulus values across various scaffold geometries. Specifically, Youngs modulus was determined as 36.96 ± 2.49 MPa, 38.24 ± 3.75 MPa, 33.41 ± 3.74 MPa and 49.74 ±3.77 MPa for square, sinusoidal, spiral, and OC scaffolds respectively as shown in **chapter 5, section 5.6.** The FE model, employed to predict the mechanical behaviour of these scaffolds, projected Youngs modulus values that closely mirrored the experimental findings. The model anticipated

Youngs modulus values of 36.67 MPa, 36.76 MPa, 33.13 MPa, and 48.48MPa for square, sinusoidal, spiral, and OC scaffolds, respectively, as visually represented in **Figure 6.4.**

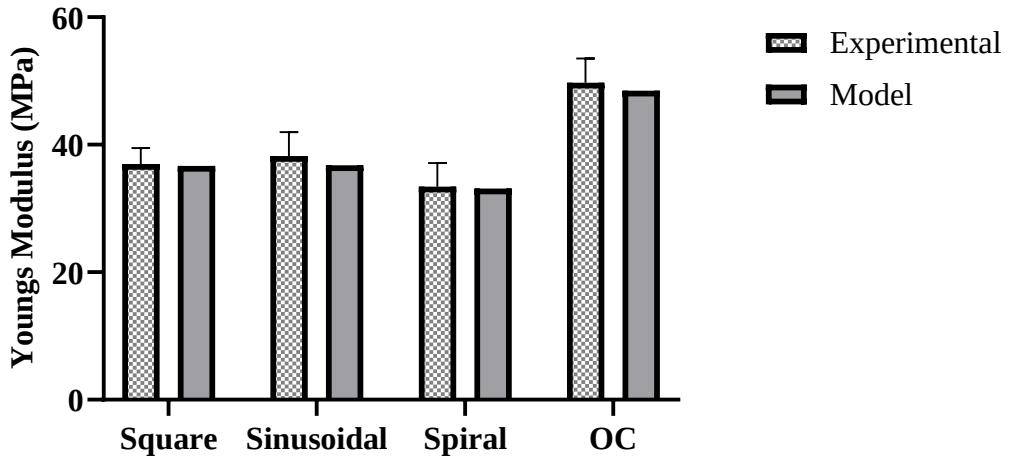


Figure 6.4 Experimental results vs. model Youngs modulus comparison of PCL/GelMA scaffolds. Experimental results are expressed as mean ± SD (n=6, N=3).

Figure 6.5 D represents the comparison of the experimental and model predicted Youngs modulus values for both PCL/GelMA and PCL scaffolds. There is notable agreement in the trends observed. In PCL/GelMA scaffolds, the experimental and predicted values demonstrate a consistent order of stiffness across different scaffold geometries. The model captures the relative differences in Youngs modulus between square, sinusoidal, spiral, and OC structures. The experimental and computational results indicate the reliability and accuracy of the computational model in simulating the mechanical properties of PCL/GelMA scaffolds. This alignment across different scaffold geometries underscores the model's versatility and its ability to capture the complex mechanical behaviour of structures with diverse shapes. It is essential to acknowledge the limitations of any computational model, and further validation through additional experimental studies may provide a more comprehensive understanding of the scaffold's mechanical behaviour.

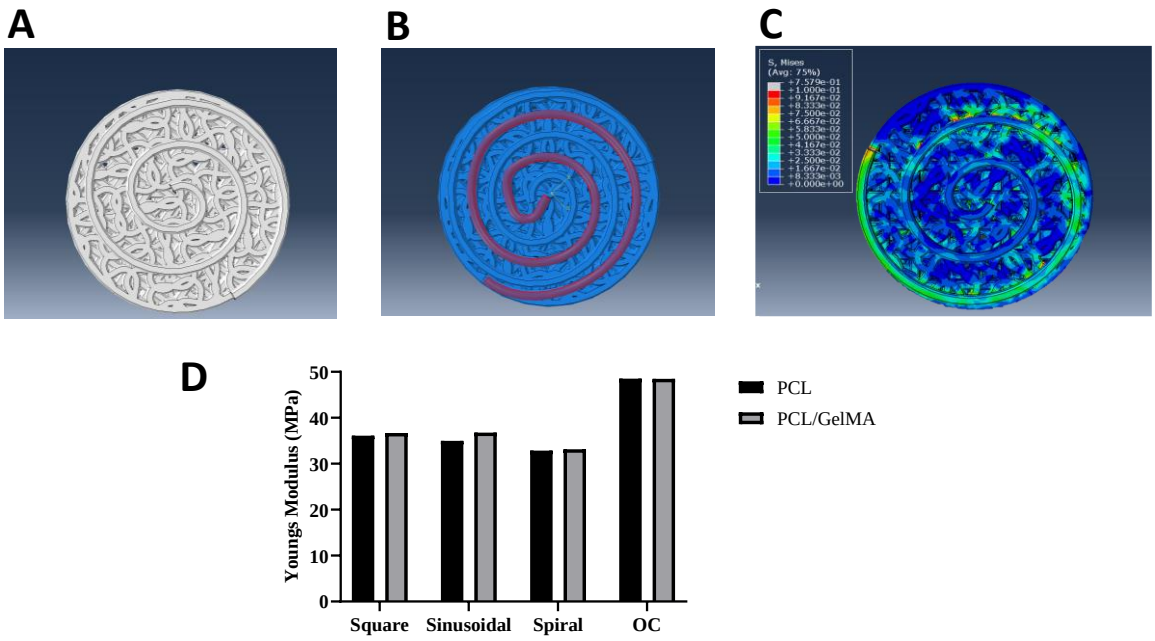


Figure 6.5 Youngs modulus of scaffold geometries, A) PCL OC scaffold representation, B) PCL/GelMA scaffolds representation, C) representation of the stress distribution of the OC scaffold and D) Graph showing the data of PCL and PC/GelMA of the model.

6.5. Conclusions.

This chapter provides a comprehensive exploration of the mechanical properties of 3D-printed OC scaffolds using FE analysis. The primary objective is to develop a predictive model for assessing and validating the scaffold's mechanical characteristics, offering insights into its behaviours under varying conditions and loading scenarios. This computational framework serves as a powerful tool for predictive analysis, contributing to a deeper understanding of the scaffold's structural integrity and performance.

FE analysis has become integral in the design and evaluation of the OC scaffolds. It offers a comprehensive means to understand their architectural, material, and mechanical properties for achieving optimal cell differentiation and tissue scaffold performance (Koh et al., 2019; Schipani et al., 2020; Wieding et al., 2013). The complexity introduced by 3D-printed scaffold geometries necessitates the adoption of FE analysis to capture their mechanical responses accurately.

FE analysis, a numerical methodology resolving differential equations through discretisation, proves indispensable in modelling complex geometries and structures composed of multiple materials. The approach has become a cornerstone in 3D-printed scaffold design processes, allowing for precise simulations and predictions. Studies such as Zhang et al. and Tan et al. showcase the efficacy of FE analysis in understanding the relationship between scaffold properties, pore geometry, and mechanical behaviours (Tan et al., 2023; B. Zhang, Huang, Narayan, et al., 2020).

The CAD geometries generated from BioCAD software were adapted in SolidWorks for compatibility with ABAQUS. The iterative development process focused on responsiveness to experimental findings, ensuring the fidelity of simulated geometries to real-world scenarios. The FE simulation setup involved importing the Parasolid Model Part file into ABAQUS CAE, with meshing performed using quadratic tetrahedral elements. The unconfined compression loading scenario provided insights into stress distributions and displacements. Simulation conditions included compressive loading on PCL and GelMA cubes, with Youngs modulus values obtained from experimental tests. Mesh sensitivity analysis ensured the reliability of the FE model, with stringent criteria for element regularity and proportions. The meshing process involved meticulous adjustments, and the resulting mesh adhered to predefined limits.

FE analysis successfully predicted Youngs modulus of PCL scaffolds with different geometries, demonstrating close alignment with experimentally measured values. The comparative analysis highlights the agreement between experimental and model-predicted Youngs modulus, reinforcing the accuracy and reliability of the FE model. For PCL/GelMA scaffolds, experimental assessments and FE model predictions revealed consistent trends across various scaffold geometries. The experimental and model-predicted Youngs modulus values affirm the reliability and accuracy of the model. The alignment across diverse scaffold shapes underscores the versatility of the model in capturing complex mechanical behaviours.

Moreover, a dynamic seeding assessment simulated using SolidWorks provided insights into fluid flow profiles within different scaffold designs. The flow velocities and patterns associated with square, sinusoidal, spiral, and OC designs. The interplay between seeding

dynamics and flow distribution offers valuable insights into potential mechanisms for enhancing cellular proliferation within specific scaffold designs.

In conclusion, this chapter contributes to the understanding of the OC scaffold mechanical properties through a robust FE analysis approach. The alignment between experimental and model-predicted results signifies the reliability of the computational model. Future directions could involve further validation through experimental studies and exploring additional complexities in scaffold behaviours. The insights gained from this study advance the field of tissue engineering, providing a foundation for optimising scaffold design strategies based on predictive mechanical assessments.

Chapter 7. Characterisation of cell viability on the OC scaffold.

This chapter presents the viability assessment of PCL/GelMA scaffolds. The comprehensive characterisation of cell viability encompasses the analysis of sterilisation and seeding processes on various design types of the scaffold. Additionally, the study inspects cell distribution, metabolic activity, viability, and proliferation of the scaffolds. These investigations aim to contribute valuable insights towards the cell attachment in PCL/GelMA scaffolds with different geometries for the manufacturing of the OC scaffolds.

7.1. Introduction.

Tissue engineering holds great promise for regenerating and repairing damaged tissues and organs, and the development of suitable scaffolds is crucial in this field. The design of these scaffolds, particularly their pore structure and material composition, has a significant impact on cell viability and behaviour within the scaffold (Chan & Leong, 2008; Jian et al., 2020)

Cell distribution within tissue engineering scaffolds plays a pivotal role in facilitating nutrient diffusion and cellular migration, essential for successful tissue regeneration. The presence of pores within scaffolds is a critical feature influencing these processes. Kang et al. (2016) emphasised the significance of pores in bio-printed scaffolds, showing their pivotal role in cellular behaviour (H.-W. Kang et al., 2016). In a study by Campos Mora et al., porous scaffolds based on PCL/PGA with varying pore sizes demonstrated favourable mechanical properties, high chondrocyte adhesion, proliferation, and GAG secretion, showcasing the importance of scaffold porosity and pore size for tissue repair (Campos Mora, 2022) Additionally, the 3D structure of scaffolds has been identified as a significant factor influencing new tissue formation, impacting both mechanical properties and cell behaviours (Woodfield et al., 2004).

Cellular metabolism refers to the processes involved in energy production and consumption, while proliferation indicates the ability of cells to divide and multiply (Chaudhary et al., 2023; W. Wei & Dai, 2021c). Both factors are crucial indicators of cell health and functionality. Pore size, distribution, and interconnectivity within scaffolds play a vital role in facilitating nutrient diffusion, waste removal, and cell-cell interactions(Nava et al., 2016). By varying these parameters, cellular metabolic activity and proliferation rates are affected

by the pore designs (Browe et al., 2022). Likewise, the composite OC scaffold is specifically designed to support the regeneration of osteochondral tissues, necessitating careful consideration of the materials used. By evaluating cell viability on the different geometries that comprise the OC scaffold, the specific impact of each material on mammalian cell metabolic activity and proliferation can be determined.

Addressing the challenges in the OC defect repair, scaffold-based tissue engineering emerges as a promising approach, providing an ideal environment for cell growth and differentiation. The 3D structure of scaffolds, beyond porosity and pore size, significantly influences new tissue formation, nutrient transport, and cell-matrix interactions. Inspired by the hierarchical structure of natural bone, researchers have designed scaffold architectures at various scales, including macroscale, microscale, and nanoscale. While some recent studies have introduced novel design patterns, the comprehensive analysis of these staggered structures remains limited. The functionality of scaffolds, including permeability and mechanical and biological properties, is crucial for their effectiveness (Hollister, 2005; Joyce et al., 2023; Rosenzweig et al., 2015; Z. Yang et al., 2021)

Researchers have explored different scaffold fabrication methods to achieve specific architectures. Rosenzweig et al. utilised the FDM method to print orthogonal scaffolds with suitable pore sizes for chondrocyte and nucleus pulposus (NP) cell growth and extracellular matrix production (Rosenzweig et al., 2015). Yang et al. reported a bifunctional PCL/GelMA/DCECM scaffold co-printed with aptamer-GE bioink, providing both mechanical strength and anatomical structure(Z. Yang et al., 2021). Joyce et al.'s study highlighted the gyroid design's ability to maintain axial porosity under load-bearing forces, promoting cellular migration and maintaining an interconnected architecture (Joyce et al., 2023).

In previous chapters, the physical properties and behaviour of both PCL and GelMA were examined in the context of extrusion-based 3D printing. Following this, the optimisation process for extrusion-based 3D printing of PCL/GelMA scaffolds was performed. The optimisation involved distinct designs implemented across different zones to enhance the mechanical properties in each respective area. Likewise, a FEA model to assess and validate the mechanical properties as a predictive analysis of the 3D printed OC scaffold.

The aim of this chapter is to comprehend the viability within PCL/GelMA scaffolds, encompassing distinct designs such as square, sinusoidal, and spiral, with a specific focus on the OC scaffold using these three configurations. The main objective of this chapter was to establish a comparative analysis of cell viability, showing the influences of each design and their distinct impacts on cell distribution, metabolic, viability and proliferation activity in the scaffolds that strategically incorporates essential physical cues, thereby influencing cellular attachment for the OC scaffold repair.

7.2. Viability Studies of 3T3 Cells for PCL/GelMA Scaffolds.

7.2.1. Effect of Scaffold Sterilisation.

Scaffold sterilisation was performed as mentioned in the methodology **Chapter 3, section 3.5.2.** A comprehensive exploration of diverse sterilisation methodologies for scaffolds was conducted, yielding a comparative framework for their effectiveness using visual observation of the media containing the scaffolds, after a 20-day incubation at 37˚C, as the determinant of infection (cloudy media with green bacteria at the top was considered contaminated, clear media was considered not infected). The investigated strategies are visually delineated in **Figure 7.1**, offering an understanding of their application. **Figure 7.1 A** encompassed an initial immersion of the scaffolds in dH_2O after printed and followed by UV light disinfection for 40min.

Conversely, for **Figure 7.1 B, C, and D**, the scaffolds were not immersed in dH_2O, and GelMA was dehydrated. **In Figure 7.1 B,** the same process of sterilisation as on A was performed, involving the direct UV disinfection of scaffolds. A distinct variant approach in **Figure 7.1 C** targeted disinfection by covering the scaffolds with AB/AM for one day, subsequently, the AB/AM was removed, and the scaffolds were submerged in PBS for three days. Finally, **Figure 7.1 D** extended this protocol by incorporating a sequential procedure, followed by submersion in AB/AM for a day and finally in PBS for two days, prior to final UV light disinfection. These methodologies provide valuable insights into the diverse strategies employed to ensure scaffold sterility, thereby contributing to the enhancement of biocompatibility and overall performance.

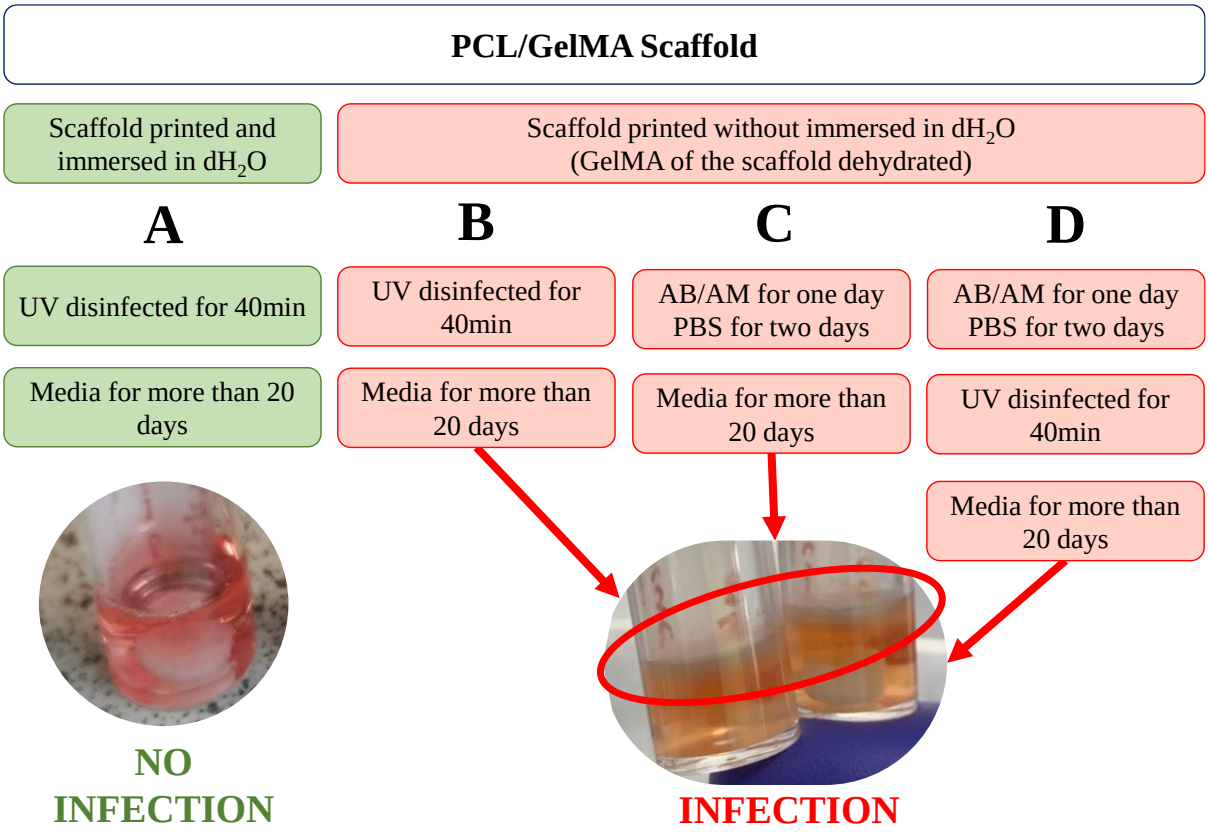


Figure 7.1 Comparative illustration of distinct sterilisation approaches employed for the scaffolds. A) Scaffolds underwent a treatment involving submersion in dH_2O followed by UV disinfection. B) Direct UV disinfection of scaffolds after allowing them to dry without prior immersion in dH_2O. C) Scaffolds were dried and subsequently disinfected with AB/AM. D) Scaffolds were dried and disinfection protocol involved submerging them into AB/AM and PBS prior to UV disinfection. Cloudy media with green bacteria at the top was considered contaminated, clear media was considered not infected.

Dehydration reveals that regardless of the array of sterilisation methods employed, bacterial proliferation occurs, leading to scaffold contamination at distinct phases. As a result, the methodology illustrated in **Figure 7.1A** was selected as the preferred approach.

7.2.2. Cells Seeding with Static method.

A static seeding method was employed to assess the impact of cell viability and proliferation within the scaffolds, involving the introduction of mammalian 3T3-E291 cells onto the scaffold designs, as shown in **Figure 7.2.** The seeding density was tailored to the surface area of the respective designs: the square, sinusoidal, and spiral scaffolds with a high of 1.2mm were seeded at a density of $0.1X10^6$ cells, whereas the OC scaffold high of 4.6mm with a density of the cells were $0.3X10^6$ cells as explained in the methodology **chapter 3 section 3.5.3.**

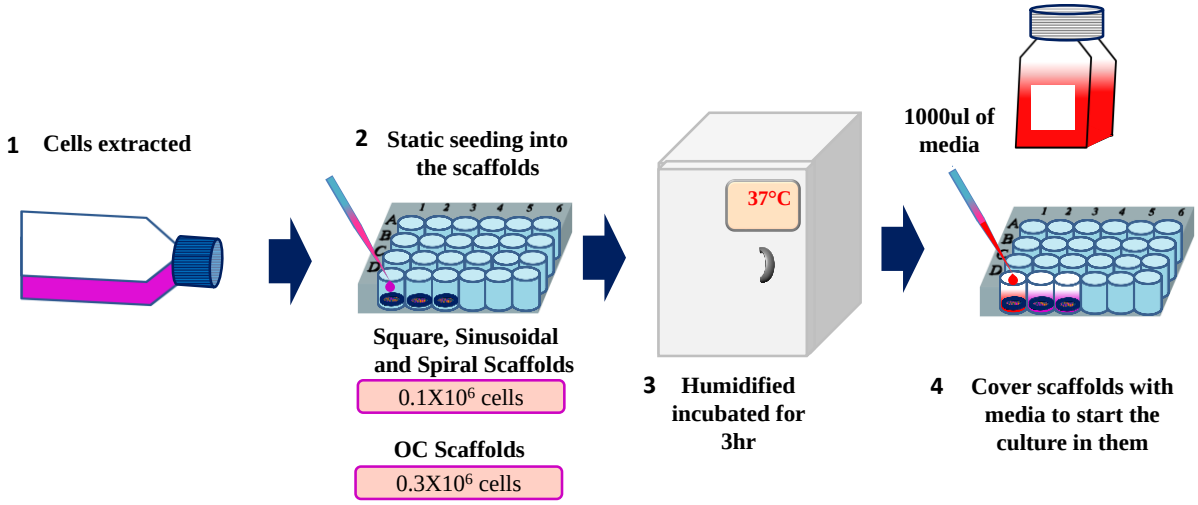


Figure 7.2 Schematic showing the methodology for static cell seeding in the scaffolds. (1) Mammalian cells 3T3-E291 were extracted. (2) Scaffolds were top-seeded by pipetting the cells. (3) Samples were incubated for 3hr at 37˚C (4). 1000 µl f media was added aliquots added to the scaffolds in the well plates.

7.3. Cell Distribution, Proliferation, and Viability Analysis.

PCL/GelMA hybrid constructs were synthesised to facilitate their application in an OC tissue regeneration. PCL, chosen for its robust mechanical properties, served as a reinforcing component for the fabrication of three-dimensional constructs that offer structural stability. In the formulation, 10% GelMA was selected primarily due to its enhanced printability using extrusion-based methods, as evidenced in the findings outlined in **Chapter 4**. The OC PCL/GelMA scaffold design achieved the mechanical properties of 50.68 ± 3.38 MPa, as shown in **chapter 5- section 5.6**. The design also influences cell distribution, which can be

impacted by the pore architecture of the scaffolds, as suggested in the literature. In this regard, the PCL/GelMA scaffolds were top-seeded and assayed on day 1, 3 and 7 for attachment, distribution, proliferation, and viability utilising Toluidine Blus O., Presto Blue®, LIVE/DEAD™ Viability/Cytotoxicity, and Quant-iT dsDNA HS assays, as represented in **Figure 7.3.**

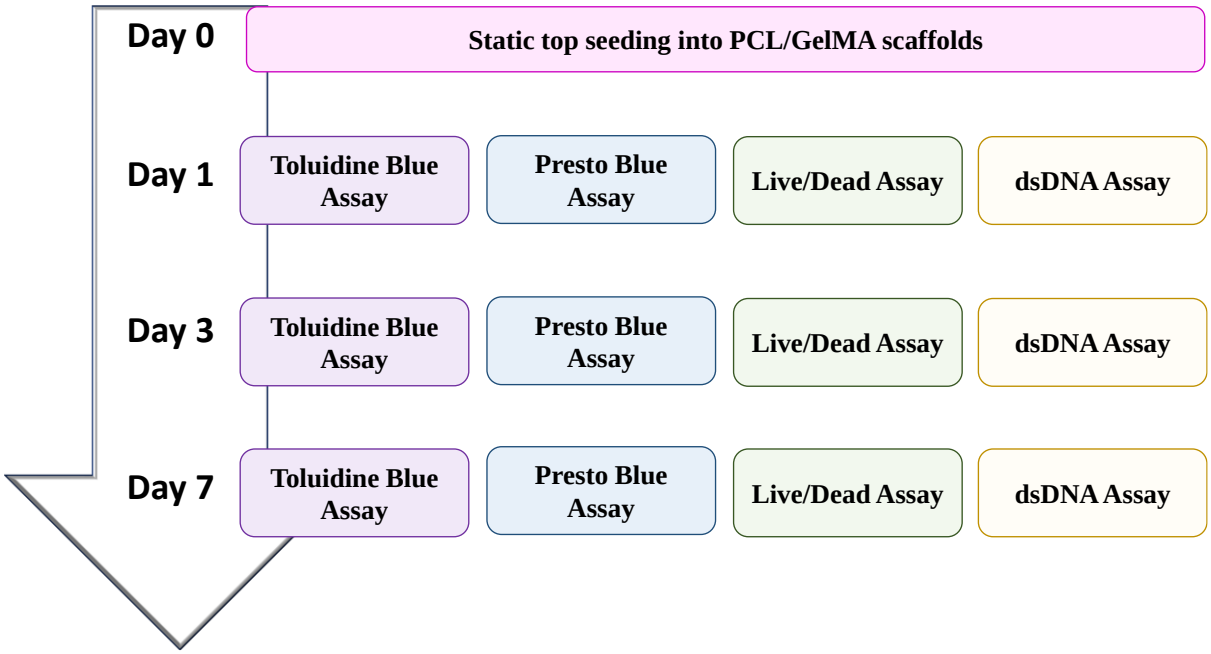


Figure 7.3 Schematic overview of the experimental setup to assess the ability of PCL/GelMa scaffold to support cell culture.

In **Figure 7.4**, a comprehensive depiction of cell distribution on day seven across distinct designs is presented. While **Figure 7.4A** provides an overview of the complete 3D printed scaffold, **Figure 7.4 B** offers a comprehensive visualisation of the cells on the scaffold using Live/Dead™ stain. Images were captured using a Zeiss LSM T-PMT 880 Confocal Fluorescence Microscopy. Moreover, **Figure 7.4C** captures an image of a scaffold section, effectively illustrating the localised cellular population within this microenvironment at higher magnification.

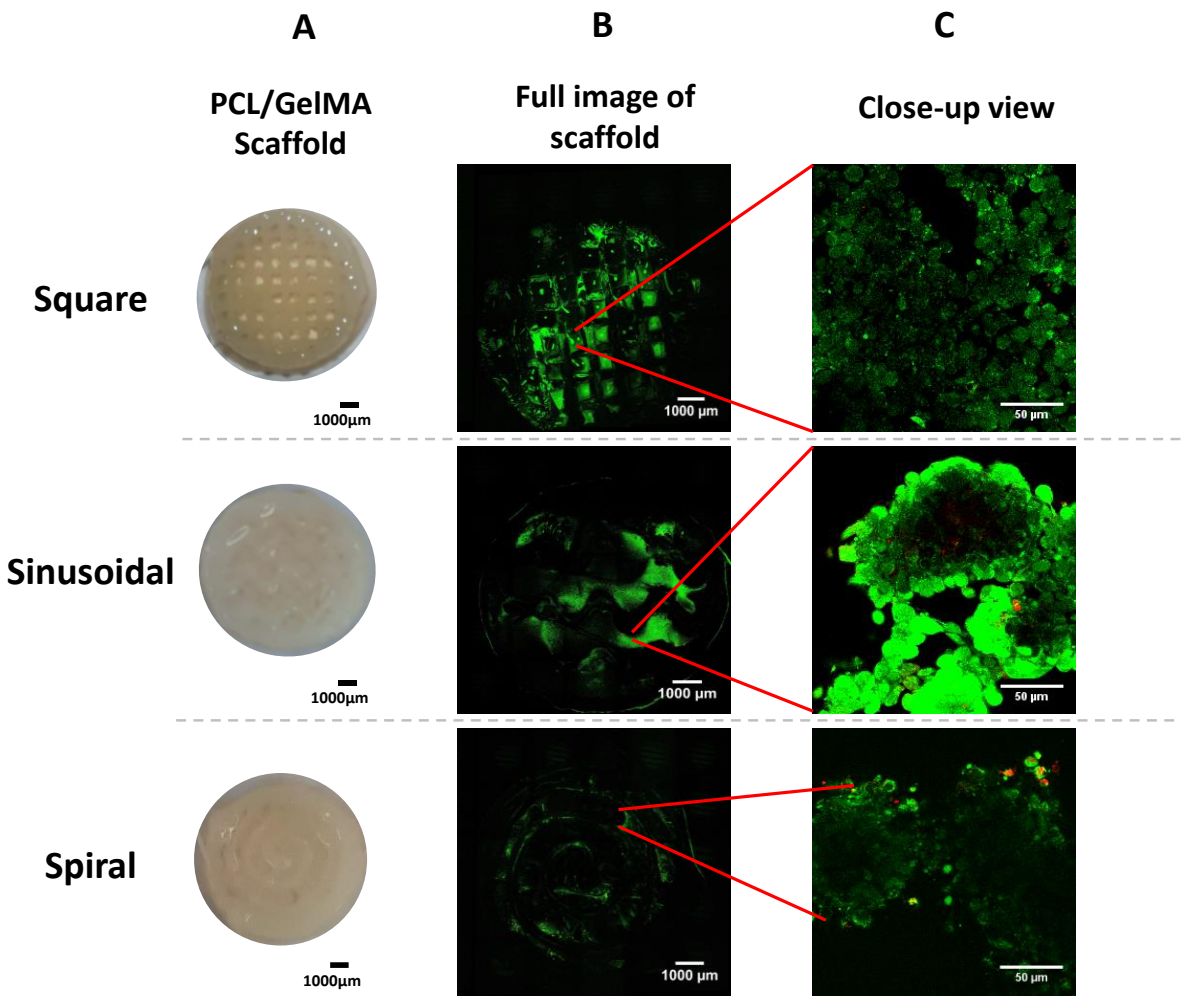


Figure 7.4 Representative images of the cell distribution on the top of the scaffold at day 7. A) Printed PCL/GelMA scaffold image representing the designs B) Full scaffold structure is depicted, and the imaging was conducted utilising the Leica TCS LSI 0306809 Laser Scanning Confocal Microscope. scale bar representing 1000 µm. C) A specific section is highlighted, providing enhanced visibility of the cells. The imaging was conducted utilising the Zeiss LSM T-PMT 880 Confocal Fluorescence Microscopy with a 40x objective, with the scale bar representing 50 µm.

The cells follow the pattern of the printed GelMA and a notable attachment in all three designs of PCL/GelMA scaffolds in the seven day. For an in-depth analysis of the temporal progression, **section 7.3.3** looks into the specifics, offering a detailed breakdown of the cellular attachment on days 1, 3, and 7 for each PCL/GelMA scaffold variant.

7.3.1. Cell Distribution.

The 3T3 cells were seeded onto cylindrical GelMA/PCL scaffolds and cultivated for seven days. Afterwards, the samples were stained with toluidine blue to facilitate the visualisation of the cell distribution, as explained in **chapter 3 – section 3.5.4.2** and represented on the schematic **Figure 7.5.**

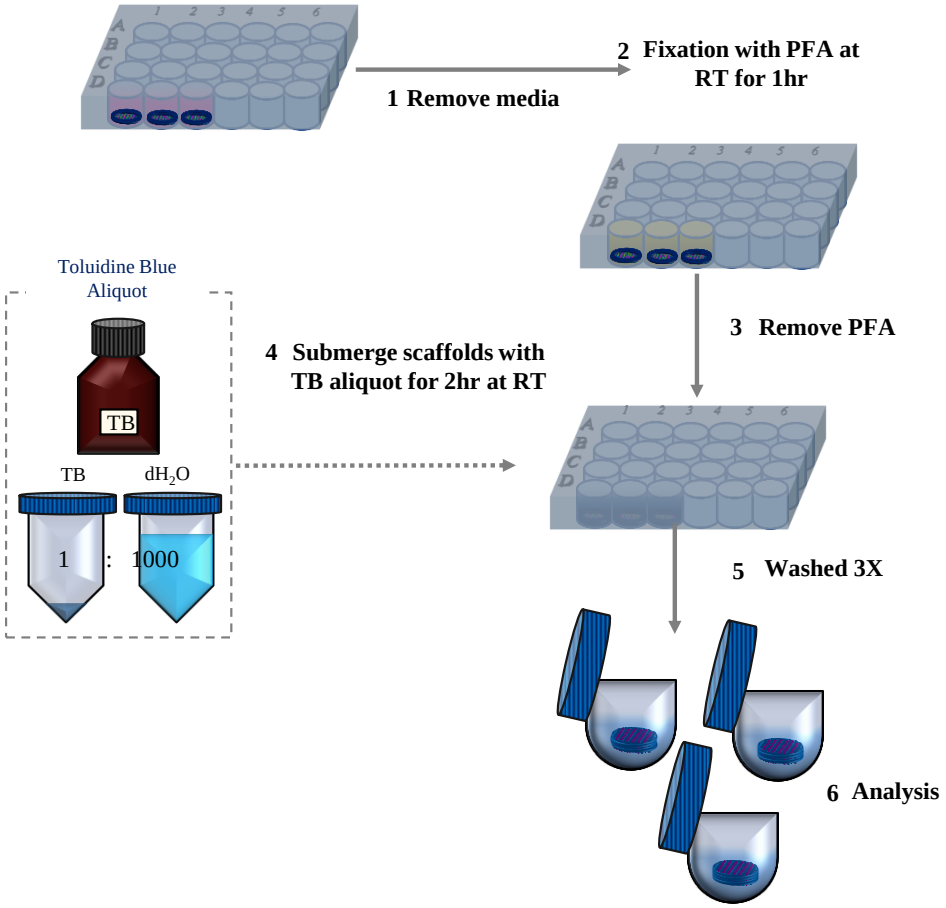


Figure 7.5 Schematic describing the visualisation of mammalian cells on the scaffolds using Toluidine Blue O. The protocol followed consists of (1) removing the media from the samples. (2) Fixing the samples using PFA for one hour at room temperature (3) removal of the PFA from the sample. (4) Samples were submerged into the toluidine blue O solution for two hours (5) Samples were washed 3X with PBS. (6). Samples were visualised with a microscope.

Following staining, the samples were cut in half, as demonstrated in **Figure 7.6**. It was observed that the cell population had appeared to increase between days 1 and 7 on the surface of the scaffolds on all the different scaffold designs, represented in blue **(Figure 7.6**). Additionally, it was noticed that the shape and size of the scaffolds were maintained after the seven days of culture. The square, spiral, and sinusoidal scaffold designs were sectioned in half, denoted as **Figure 7.6A** (surface of the scaffold) and **Figure 7.6B** (mid-section). In contrast, due to its increased height, the OC scaffold was bisected into two parts, denoted **Figure 7.6C** and **Figure 7.6D**) to enable enhanced visualisation of cell distribution throughout the scaffold.

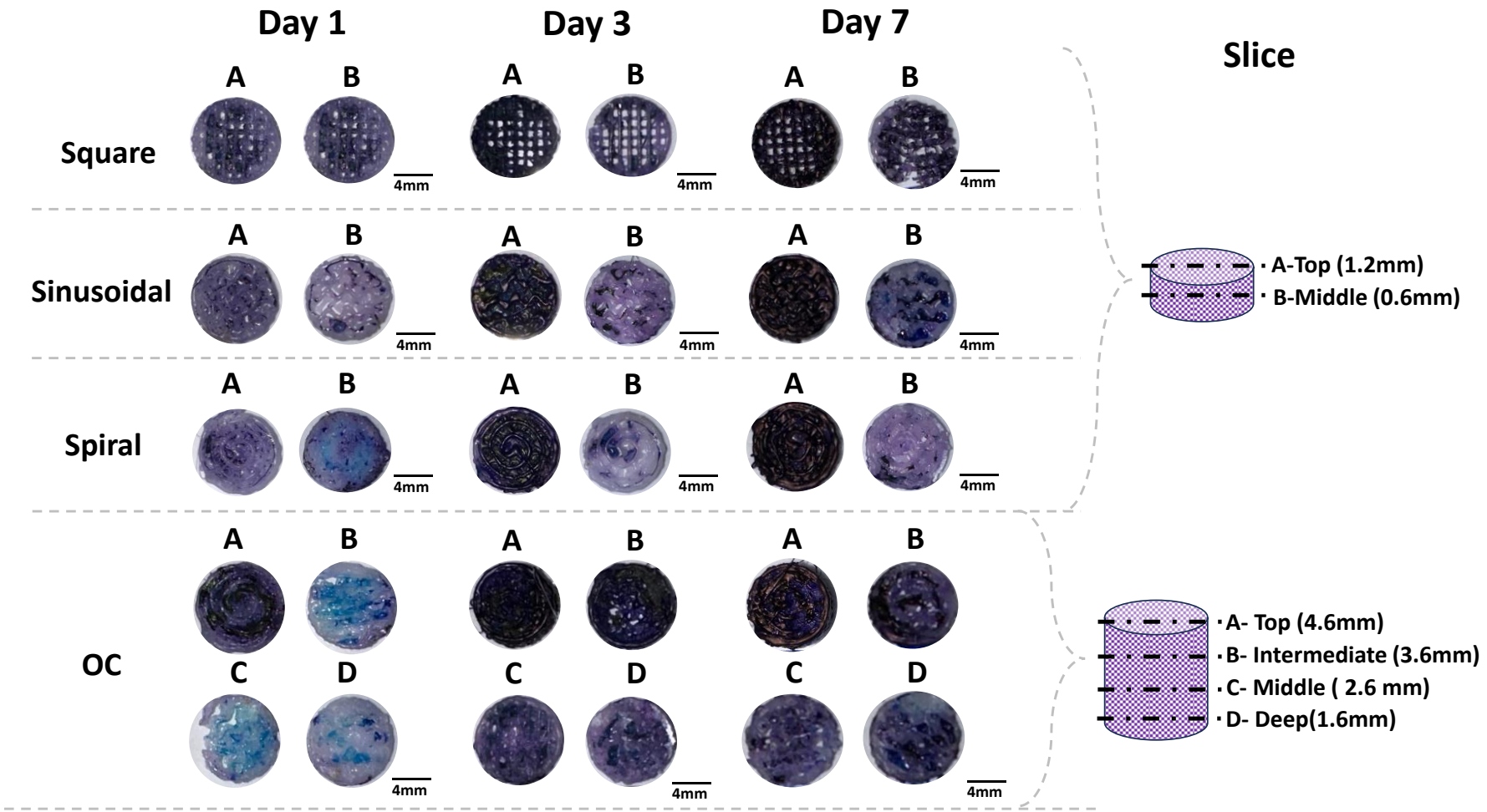


Figure 7.6 Cell proliferation is examined alongside the OC scaffold across square, sinusoidal, and spiral scaffold designs. Representative images of 3T cells stained with toluidine blue after seven days illustrate cell attachment and distribution throughout the scaffold. Both, front and middle views are presented for each design on days 1, 3 and 7 in scaffolds seeded at the top. Scale bars: 4 mm.

Throughout the experiment, increased cell attachment and distribution across the surface of all scaffold types was observed. In the OC scaffold, cell attachment and distribution increased throughout the full height of the scaffold as the days progressed up to day 7. This phenomenon might be attributed to the OC design, which consists of the spiral design at the top, followed by the square design, and finally, the sinusoidal design. These findings underscore the intricate interplay between scaffold architecture and cell behaviour, exposing how design can influence cell distribution over time.

7.3.2. Metabolic Activity.

To assess the metabolic activity of the 3T3 fibroblast on PCL/GelMA **scaffolds on days 1, 3, and 7**, Presto Blue® Cell Viability Reagent from Invitrogen by Thermofisher was employed following the manufacturer's protocol, as explained in **chapter 3 – section 3.5.4.1** and represented on the schematic **Figure 7.7.**

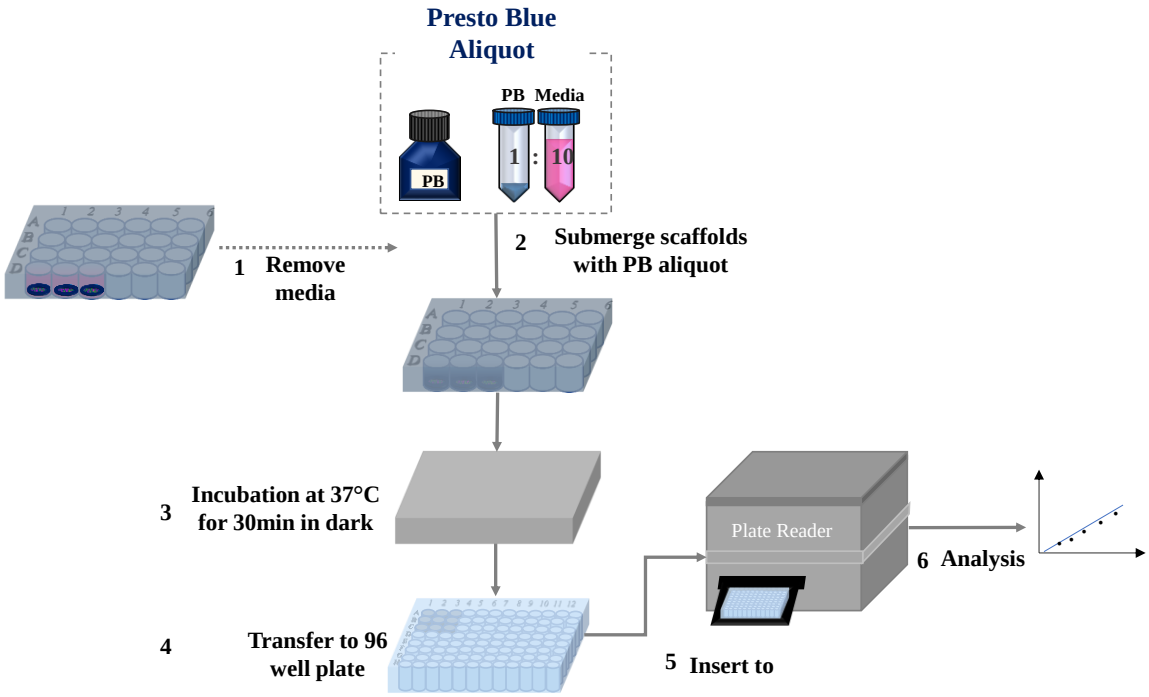


Figure 7.7 Schematic showing the methodology for the metabolic activity using Presto Blue® protocol. (1) Media was removed from the samples. (2) Presto Blue Working Reagent was made and 1 mL was added to the scaffold. (3)Samples were incubated for 30 min in a dark environment at 37˚C (4). 100 µl aliquots were taken and added to the 96 well plates in triplicates. (5) Plate reader was used to(6) measure fluorescence, providing a quantitative measure of viability and proliferation of cells.

In **Figure 7.8**, the assessment of seeding efficiency across each scaffold design was carried out on day one, including square, sinusoidal, spiral, and OC scaffolds with their respective untreated well plate. The seeding efficiency was quantified utilising the formula: $seeding\ efficiency\ (\%) = \left(1 - \frac{cells_u}{cells_t}\right) * 100$, where $cells_u$ represents the number of cells initially seeded and $cells_t$ indicates the count of unattached cells in the untreated well plate.

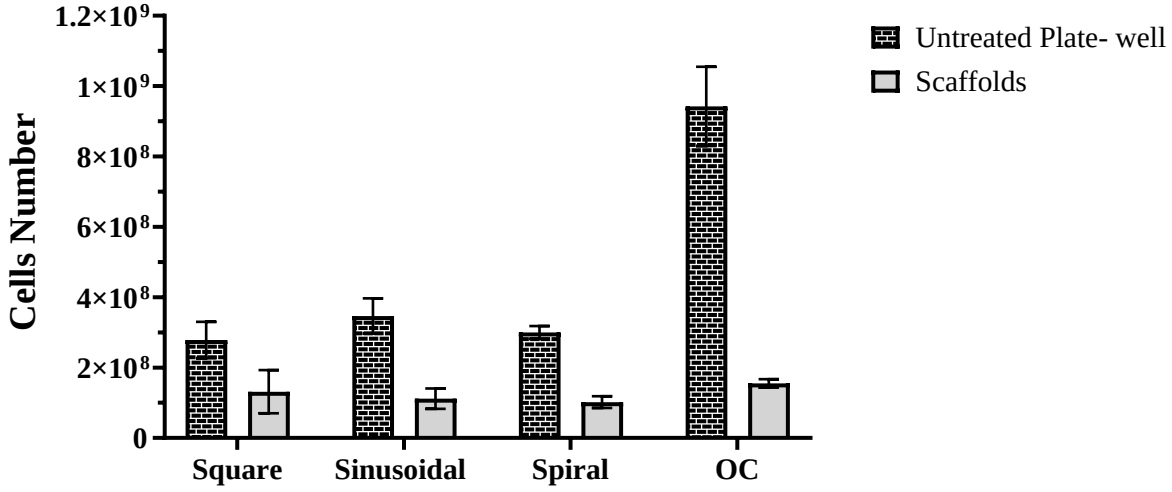


Figure 7.8 3T3 cell metabolic activity to determine seeding efficiency using the Presto Blue assay following one day after seeding for each design, square, sinusoidal, spiral, and OC untreated plate well. Results denote mean± S.D. (n=3, N=3). Statistical analysis and significance levels are indicated as ** $p < 0.0041$, *** $p = 0.0004$ and **** $p < 0.0001$

The seeding efficiency percentages were as follows: square (32%), sinusoidal (24%), spiral (25%), and OC (14%). The observed data indicates a lower seeding efficiency on the OC scaffold, showcasing a profound impact on cellular attachment and subsequent metabolic activity. This incongruence challenges the notion of the OC scaffold's superior performance in terms of cellular attachment, raising questions about its potential impact on overall metabolic response.

In the context of the viability assays, the fluorescence levels exhibited a consistent increase across all experimental days, spanning from day 1 through day 7, for all scaffold variations. As indicated in **Figure 7.9**, the metabolic activity of the 3T3 fibroblasts on the scaffolds remained relatively similar from day 1 to day 3, demonstrating no significance on the metabolic activity except for the sinusoidal scaffold. However, by day 7, a significant increase in absorbance was evident across all scaffold designs, underscoring heightened metabolic activity at this later time point.

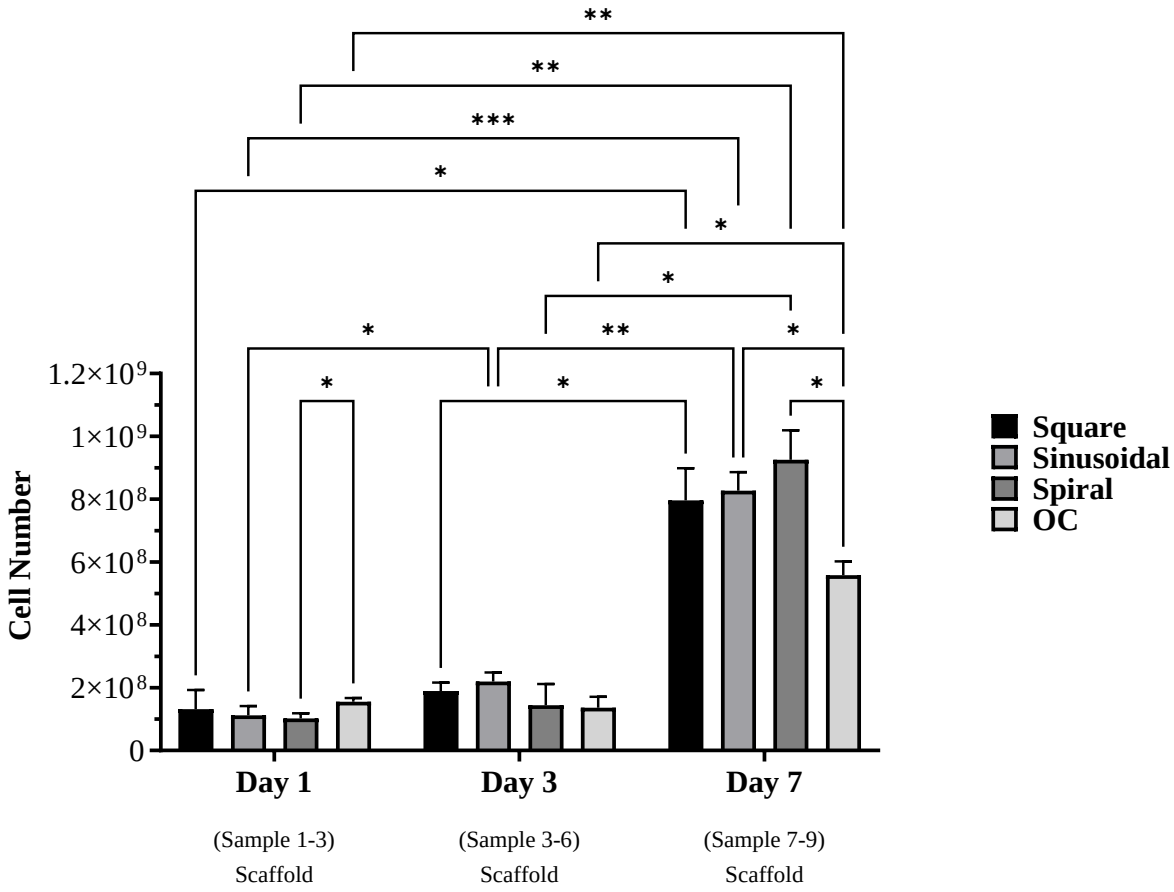


Figure 7.9 Metabolic activity across scaffold designs at different time points: day 1, day 3, and day 7. Results denote mean± S.D. (n=3,N=3). Statistical analysis and significance levels are indicated as **** $p \leq 0.01$, **** $p \leq 0.001$ and **** $p \leq 0.0001$.

The variation in cell metabolic activity among different scaffold designs was evident throughout the experiment, as represented in **Figure 7.9.** On day one, the square scaffold exhibited a cell number of $1.31x10^{+8} \pm 5.01x10^{+7}$, followed by the sinusoidal scaffold with $1.12x10^{+8} \pm 2.38x10^{+7}$, the spiral scaffold with 1.02x10+8 ± $1.38x10^{+7}$, and the OC scaffold with $1.55x10^{+8} \pm 9.99x10^{+6}$. Progressing to day three, the square scaffold displayed an increase to $1.89x10^{+8} \pm 2.20x10^{+7}$, while the sinusoidal scaffold experienced a more pronounced rise to $2.20x10^{+8} \pm 2.32x10^{+7}$. Conversely, the spiral scaffold showed a relatively modest elevation to $1.44x10^{+8} \pm 5.51x10^{+7}$, and the OC scaffold registered a slight decline to $1.36x10^{+8} \pm 2.84x10^{+8.}$

The most notable rise in metabolic activity was observed on day seven. The cells on the square scaffold recorded an increase to $7.96x10^{+8} \pm 8.36x10^{+7}$, while the sinusoidal scaffold

closely followed with $8.27x10^{+8} \pm 4.85x10^{+7}$. Similarly, cells cultured on the spiral scaffold exhibited an increase in metabolic activity to $9.25x10^{+8} \pm 7.66x10^{+7}$. Particularly noteworthy was the rise seen when cells were cultured on the OC scaffold to $5.58x10^{+9} \pm 3.59x10^{+8}$.

Moreover, the evaluation of the dataset reveals distinctive trends across different scaffold designs over three temporal points: day one, day three, and day seven. On day one, a significant change of 0.0453 is observed between the spiral and the OC designs. Conversely, the square and sinusoidal designs do not exhibit any statistically significant alterations at this early time point. Then, on day three, no statistically significant change was observed between the designs, suggesting relative stability in cellular behaviour across the scaffold variations. Finally, by day seven, the sinusoidal and OC designs display a significant difference with p-values of 0.0140, while the spiral and OC designs exhibit a significance of 0.0297. At this point, no further statistically significant changes are noted among the other design comparisons.

However, upon closer inspection of individual designs, distinct patterns of significance changes appear. For the square design, minimal significance is observed between day one and day seven ($p = 0.372$) and between day three and day seven ($p = 0.0191$). No significance is detected between day one and day three. Conversely, the sinusoidal design showcases a significant change of 0.0335 between day one and day three, a heightened significance of 0.0002 between day one and day seven, and a significance of 0.0046 between day three and day 7. The spiral design reveals slight significance between day one and day three ($p = 0.0072$) and between day three and day seven ($p = 0.0110$), yet no significance is noted between day one and day three. Similarly, the OC design also exhibits slight significance between day one and day three ($p = 0.0051$) and between day three and day seven ($p = 0.0150$), while no significance is present between day one and day three.

These comprehensive insights underline the relationship between scaffold designs, cellular metabolic activity, and the corresponding significance changes, revealing how distinct designs influence the metabolic behaviour of cells over the experimental time.

7.3.3. Cell Viability.

The capability of cells to adhere and spread onto hydrogels forms a fundamental requirement for tissue regeneration. To assess cell viability and proliferation on scaffolds with distinct designs of PCL/GelMA, cells were stained with Live/Dead™ stain and visualised, as explained in **chapter 3 – section 3.5.4.3** and represented on the schematic **Figure 7.10.**

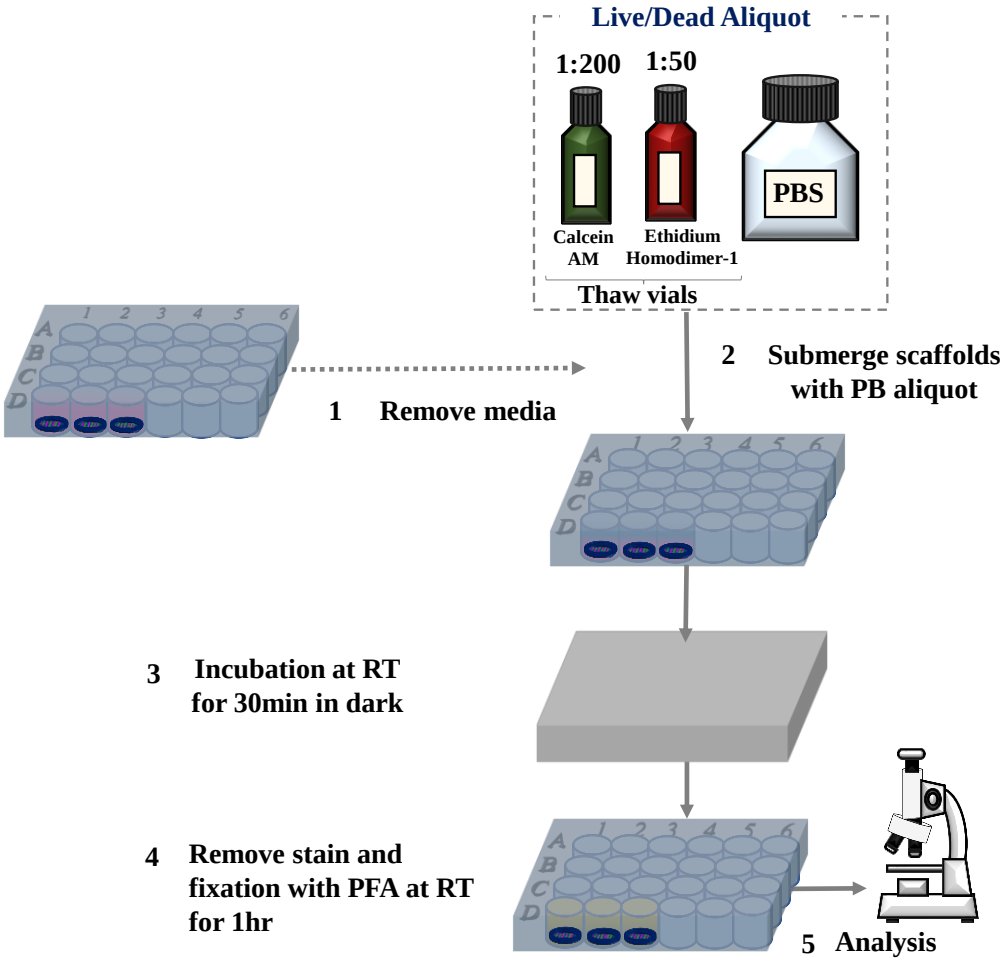


Figure 7.10 Schematic showing the Live/Dead™ protocol for cell viability. (1) media was removed from the scaffolds. (2) Live/Dead™ working solution was added to the well containing the scaffolds, (3) and incubated at room temperature in the dark for 30 min. (4) Live/Dead™ stain was removed, and PFA was added and incubated for an hour. (5) Samples were visualised using confocal microscopy, where green are the live cells and red are dead.

The visual evidence presented in **Figure 7.11** supports the capability of cells to attach to the square-patterned PCL/GelMA scaffold. By day 7, a notable internal organisation is discernible across the different scaffold layers designated as A, B, C, and D in **Figure 7.11**. This arrangement predominantly aligns with the hydrogel's upper zone D, where cell adherence is most pronounced. The analysis extends to **Figure 7.12** and **Figure 7.13**, representing the sinusoidal PCL/GelMA scaffold and the spiral PCL/GelMA scaffolds, respectively. Cells are observed to attach to the GelMA pattern of the scaffolds. However, it is notable that the spiral PCL/GelMA scaffold in **Figure 7.13** shows a comparatively slight increase in visible adherence in comparison to the others. These findings demonstrate that scaffold design can influence cellular behaviour and the ability to use GelMA as a way to pattern cell adhesion.

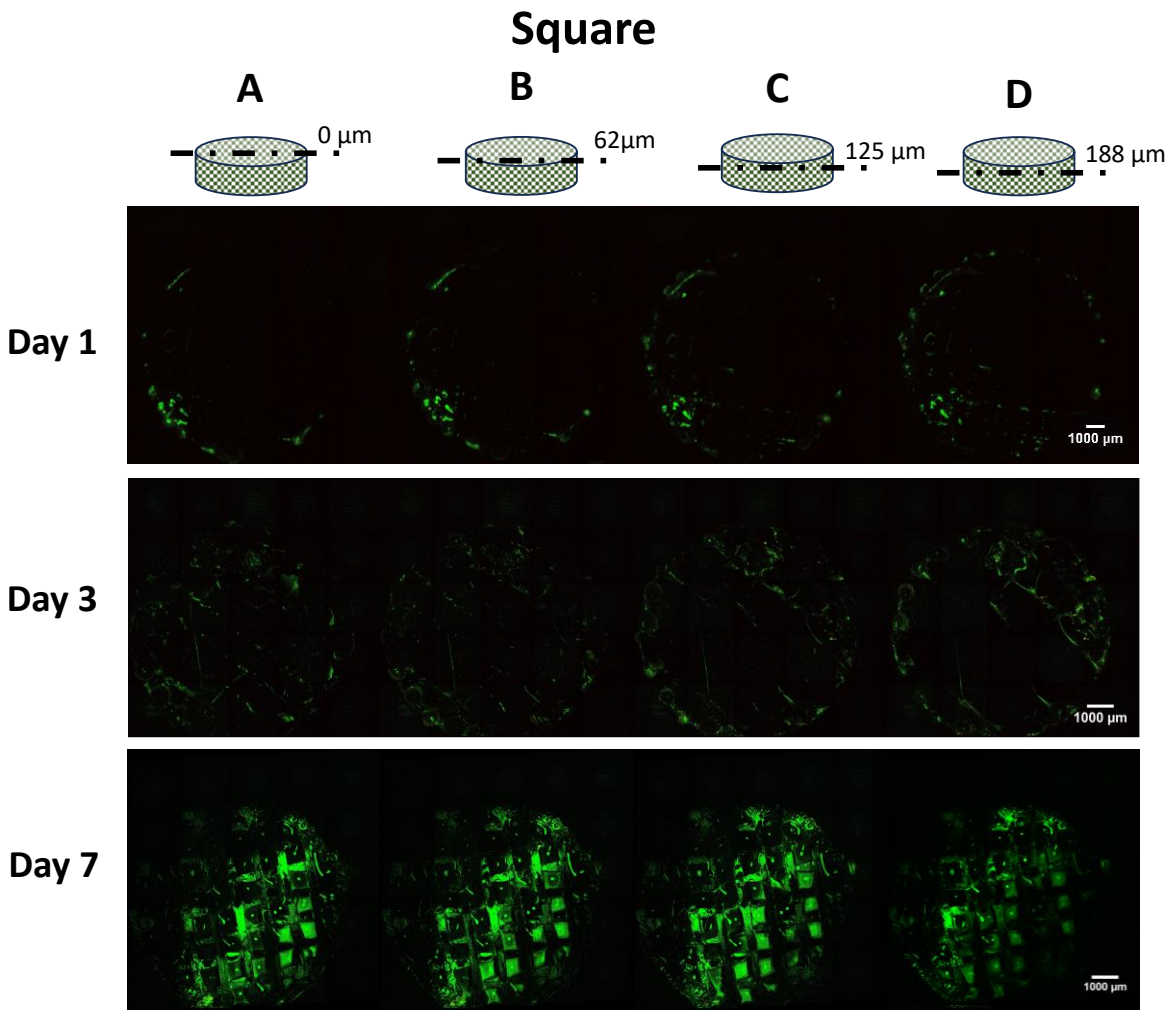


Figure 7.11 Representative fluorescence images of 3T3 cells adherent on the square scaffold at day 1, day 3, and day 7. Live and dead cells were discriminated using the LIVE/DEAD™ Viability/Cytotoxicity Kit for mammalian cells, employing green fluorescent calcein-AM for live cell identification based on intracellular esterase activity and red-fluorescent ethidium homodimer-1 to discern compromised plasma membrane integrity in dead cells. Cellular imaging was conducted utilising the Leica TCS LSI 0306809 Laser Scanning Confocal Microscope, with the scale bar representing 1000 µm for accurate assessment of live/dead staining.

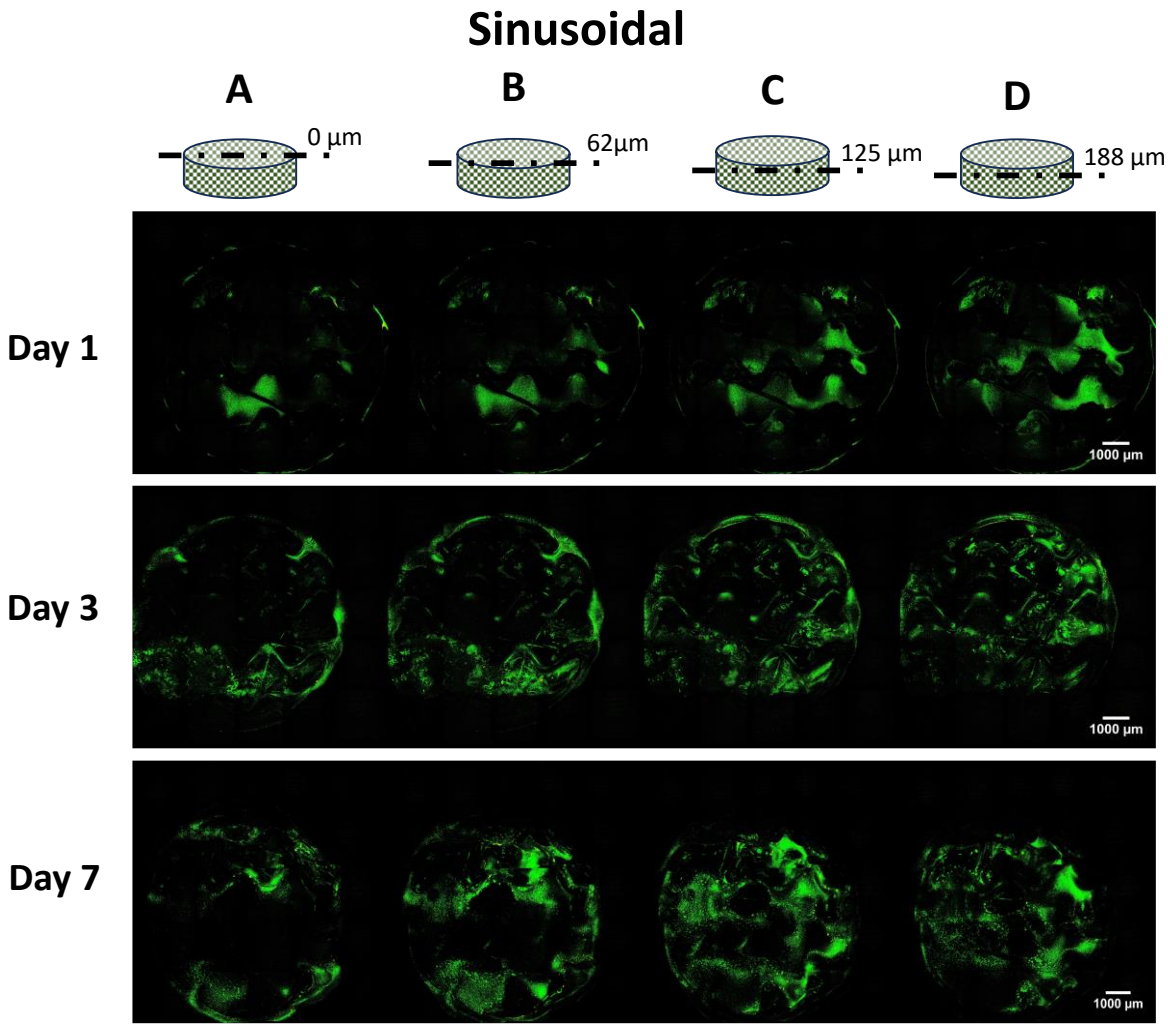


Figure 7.12 Visual representation of full sinusoidal scaffold for adhesion and viability assessment of 3T3 cells at day 1, day 3, and day 7. Live and dead cells were discriminated using the LIVE/DEAD™ Viability/Cytotoxicity Kit for mammalian cells, employing green fluorescent calcein-AM for live cell identification based on intracellular esterase activity and red-fluorescent ethidium homodimer-1 to discern compromised plasma membrane integrity in dead cells. Cellular imaging was conducted utilising the Leica TCS LSI 0306809 Laser Scanning Confocal Microscope, with the scale bar representing 1000 µm for accurate assessment of live/dead staining.

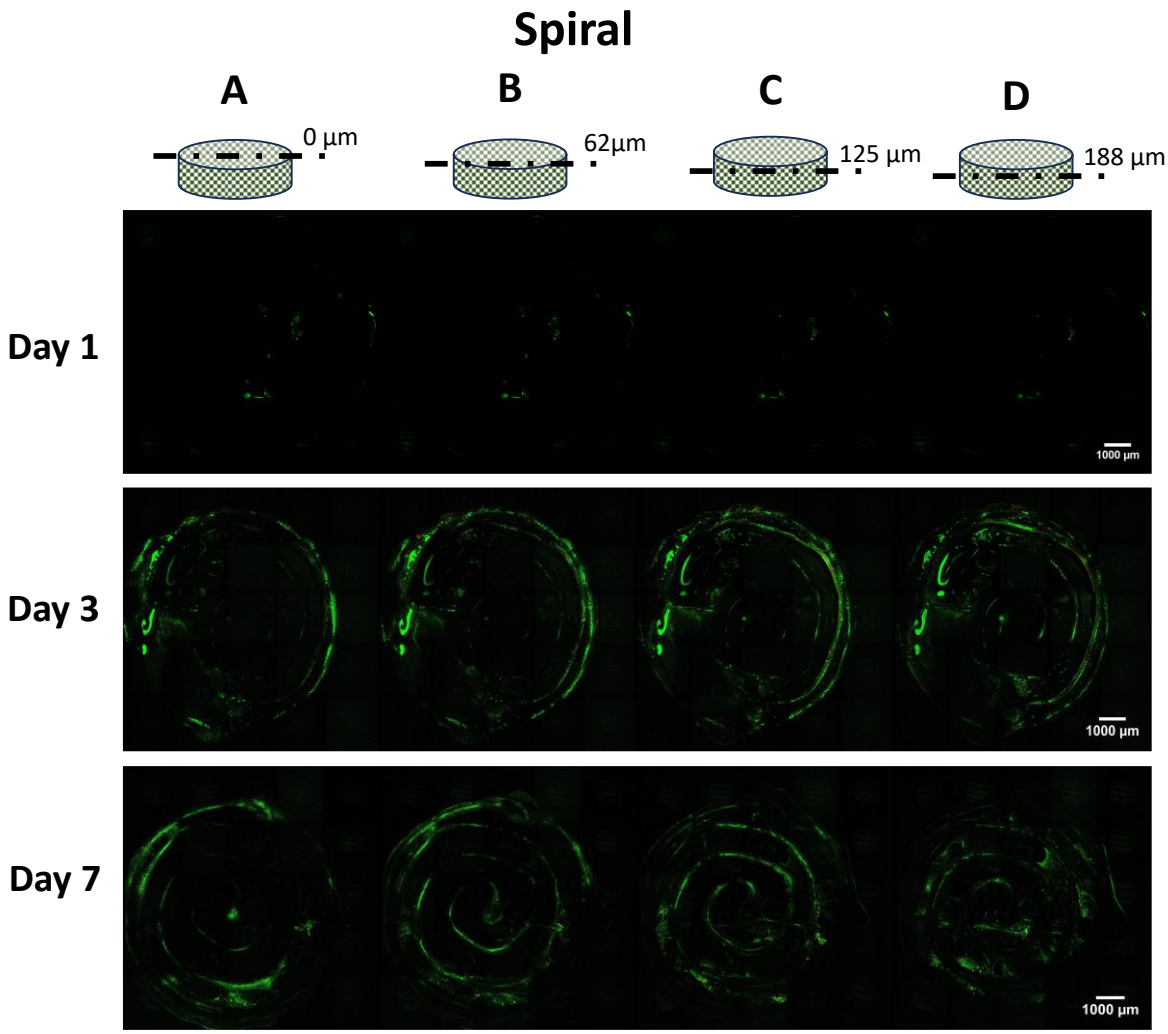


Figure 7.13 Visual representation of full spiral scaffold for adhesion and viability assessment of 3T3 cells at day 1, day 3, and day 7. Live and dead cells were discriminated using the LIVE/DEAD™ Viability/Cytotoxicity Kit for mammalian cells, employing green fluorescent calcein-AM for live cell identification based on intracellular esterase activity and red-fluorescent ethidium homodimer-1 to discern compromised plasma membrane integrity in dead cells. Cellular imaging was conducted utilising the Leica TCS LSI 0306809 Laser Scanning Confocal Microscope, with the scale bar representing 1000 µm for accurate assessment of live/dead staining.

Live/dead assays were carried out on days 1, 3, and 7 to facilitate a more in-depth analysis of the distinct layers (A, B, C, and D) within different design configurations, including square, sinusoidal, spiral, and OC, as illustrated in **Figure 7.14, Figure 7.15, Figure 7.16 and Figure 7.17**, respectively. At each time point of the conducted assays, a predominance

of live cells, indicated by the green fluorescence signal, is discernible. Conversely, only a sparse presence of dead cells(red) is evident. Across the different layers (A, B, C, and D) on each assessment day, an increment in the presence of live cells is consistently observed.

A notable commonality among the different geometries lies in the observation that, across the different layers, the innermost region (A) tends to exhibit a slightly higher presence of deceased cells, as evidenced by the red fluorescence signal. Conversely, an analogous trend emerges in the innermost part (D), characterised by an increased proliferation of live cells illustrated in green. This cumulative observation underscores the proficient cellular behaviour and viability within the context of the diverse scaffold designs over the specified assessment intervals.

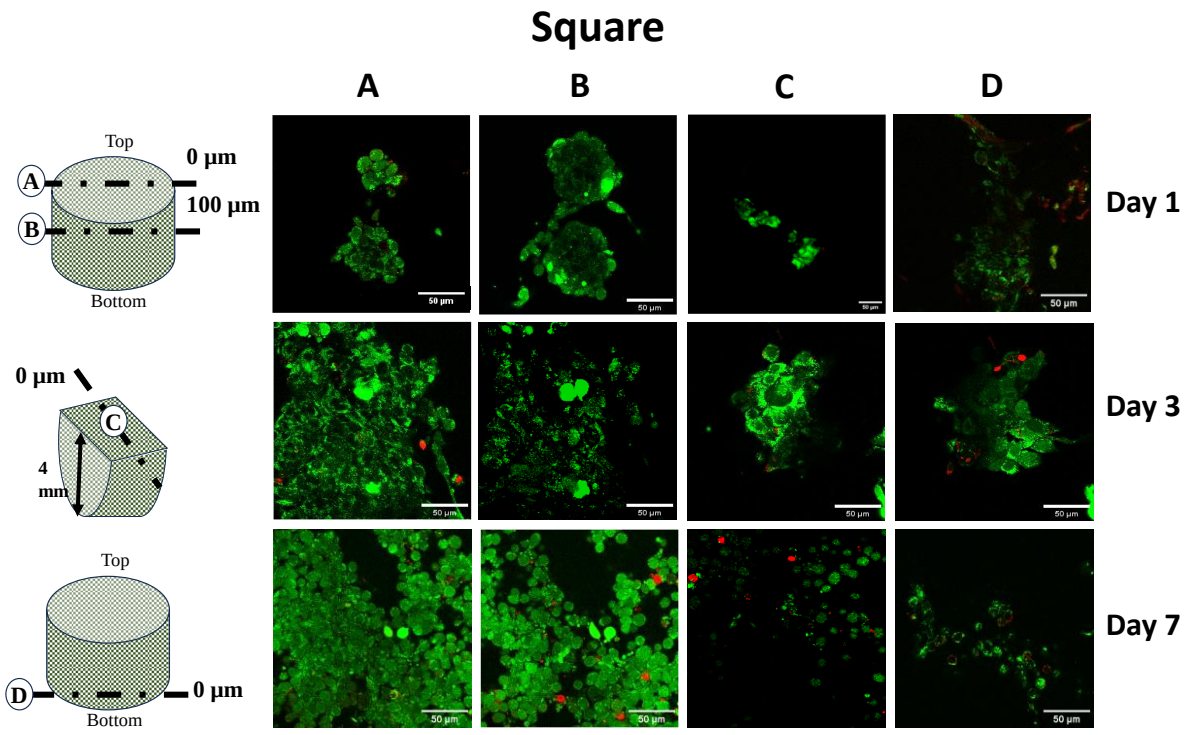


Figure 7.14 Adhesion and viability assessment of 3T3 cells on square scaffolds on day 1, day 3, and day 7. Live and dead cells were discriminated using the LIVE/DEAD™ Viability/Cytotoxicity Kit for mammalian cells, employing green-fluorescent calcein-AM for live cell identification based on intracellular esterase activity and red-fluorescent ethidium homodimer-1 to discern compromised plasma membrane integrity in dead cells. Notably, the micrographs vividly illustrate the robust adhesion and extensive spreading of 3T3 cells across all scaffold variations. Cellular imaging was conducted utilising the Zeiss LSM T-PMT 880 Confocal Fluorescence Microscopy equipped with a 40x objective, with the scale bar representing 50 µm for accurate assessment of live/dead staining.

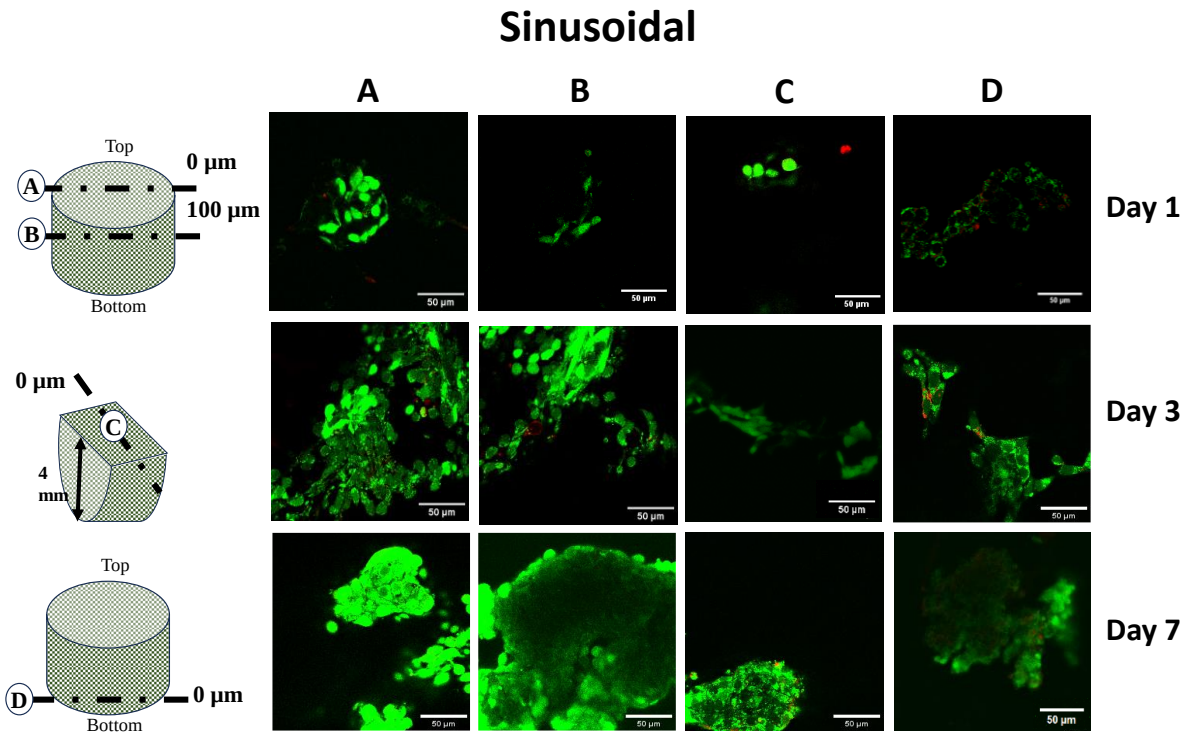


Figure 7.15 Adhesion and viability assessment of 3T3 cells on sinusoidal scaffolds at day 1, day 3, and day 7. Live and dead cells were discriminated using the LIVE/DEAD™ Viability/Cytotoxicity Kit for mammalian cells, employing green-fluorescent calcein-AM for live cell identification based on intracellular esterase activity and red-fluorescent ethidium homodimer-1 to discern compromised plasma membrane integrity in dead cells. Notably, the micrographs vividly illustrate the robust adhesion and extensive spreading of 3T3 cells across all scaffold variations. Cellular imaging was conducted utilising the Zeiss LSM T-PMT 880 Confocal Fluorescence Microscopy equipped with a 40x objective, with the scale bar representing 50 µm for accurate assessment of live/dead staining.

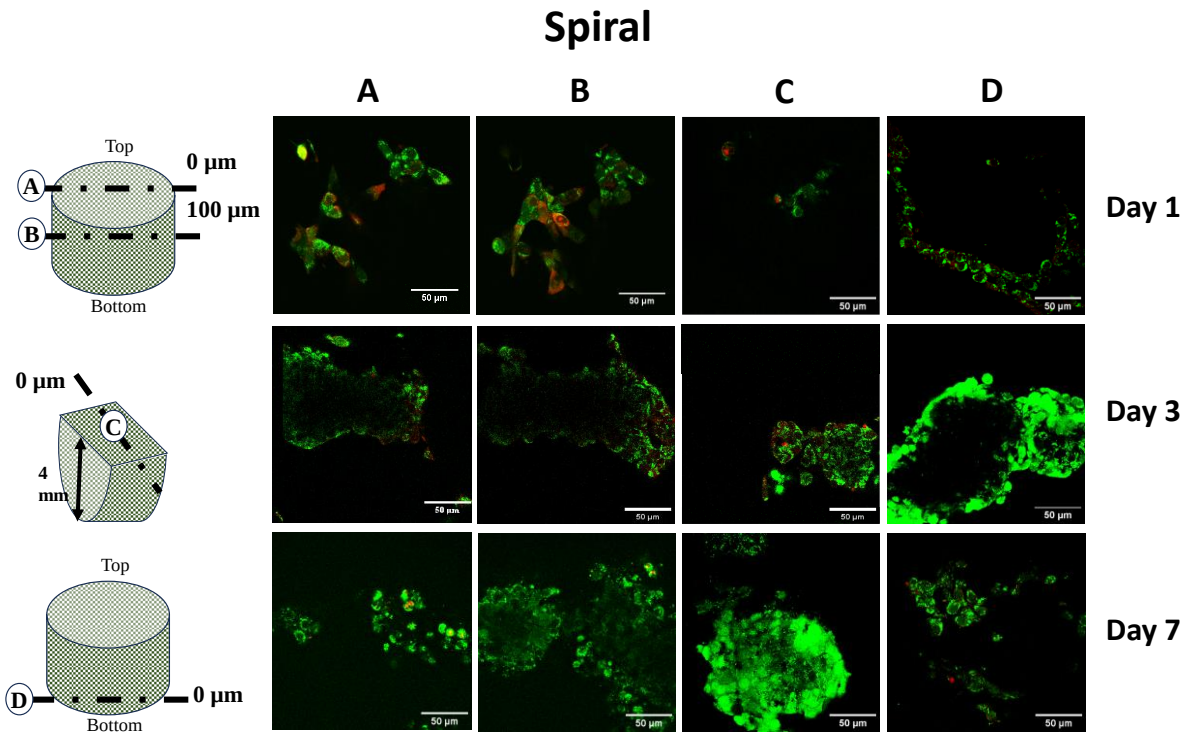


Figure 7.16 Adhesion and viability assessment of 3T3 cells on spiral scaffolds at day 1, day 3, and day 7. Live and dead cells were discriminated using the LIVE/DEAD™ Viability/Cytotoxicity Kit for mammalian cells, employing green-fluorescent calcein-AM for live cell identification based on intracellular esterase activity and red-fluorescent ethidium homodimer-1 to discern compromised plasma membrane integrity in dead cells. Notably, the micrographs vividly illustrate the robust adhesion and extensive spreading of 3T3 cells across all scaffold variations. Cellular imaging was conducted utilising the Zeiss LSM T-PMT 880 Confocal Fluorescence Microscopy equipped with a 40x objective, with the scale bar representing 50 µm for accurate assessment of live/dead staining.

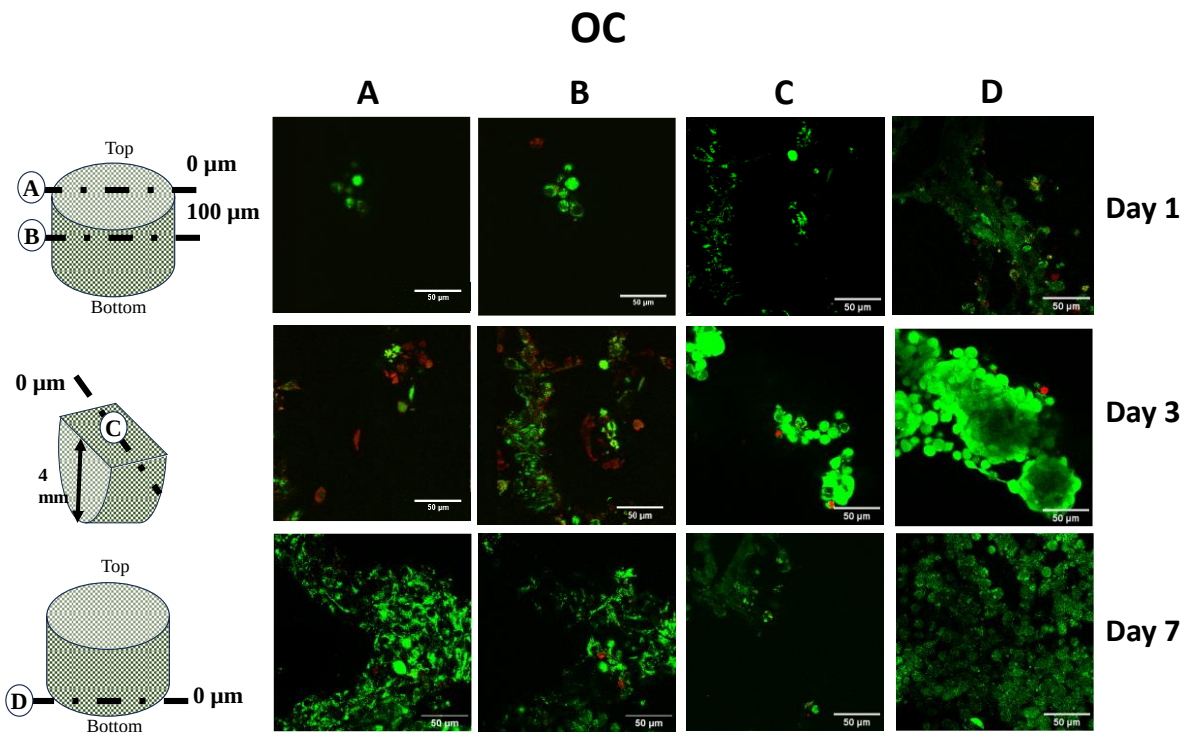


Figure 7.17 Adhesion and viability assessment of 3T3 cells on OC scaffolds at day 1, day 3, and day 7. Live and dead cells were discriminated using the LIVE/DEAD™ Viability/Cytotoxicity Kit for mammalian cells, employing green-fluorescent calcein-AM for live cell identification based on intracellular esterase activity and red-fluorescent ethidium homodimer-1 to discern compromised plasma membrane integrity in dead cells. Notably, the micrographs vividly illustrate the robust adhesion and extensive spreading of 3T3 cells across all scaffold variations. Cellular imaging was conducted utilising the Zeiss LSM T-PMT 880 Confocal Fluorescence Microscopy equipped with a 40x objective, with the scale bar representing 50 µm for accurate assessment of live/dead staining.

To quantify cell viability on day 1, 3, and 7 were manually counted in the four points: two at the top, one in the middle and one at the bottom per sample in each design and OC scaffold. Finally, the data from samples were statistically analysed using ImageJ software. The outcomes, as illustrated in **Figure 7.18**, show the viability among the different scaffold designs. On day 1, the sinusoidal scaffold showed the highest cell viability at 92.73%, followed closely by the OC scaffold at 93.75% ± 5.89%. In contrast, cells on the square and spiral designs exhibit slightly lower viabilities of 89.83% ± 3.55% and 71.03% ± 4.63%, respectively. On day 3, the sinusoidal scaffold exhibits a viability of 80.48% ± 6.18%. Following, the square and spiral scaffolds indicate viabilities of 83.41% ± 2.18% and 81.36% ± 13.6%, respectively. On the same day, the OC scaffold showed a slightly lower viability

of 77.4% ± 12.8%. Finally, by day 7, the sinusoidal scaffold maintains a high viability of 95.1% ± 2.92%, the OC scaffold exhibits a viability of 97.34% ± 1.16%, the square 92.36% ± 3.09%, and cells cultured on the spiral scaffold a lower viability of 71% ± 13.5%. These observations between scaffold design and cellular viability in all scaffold types, contain a notable and consistent viability throughout the experimental period.

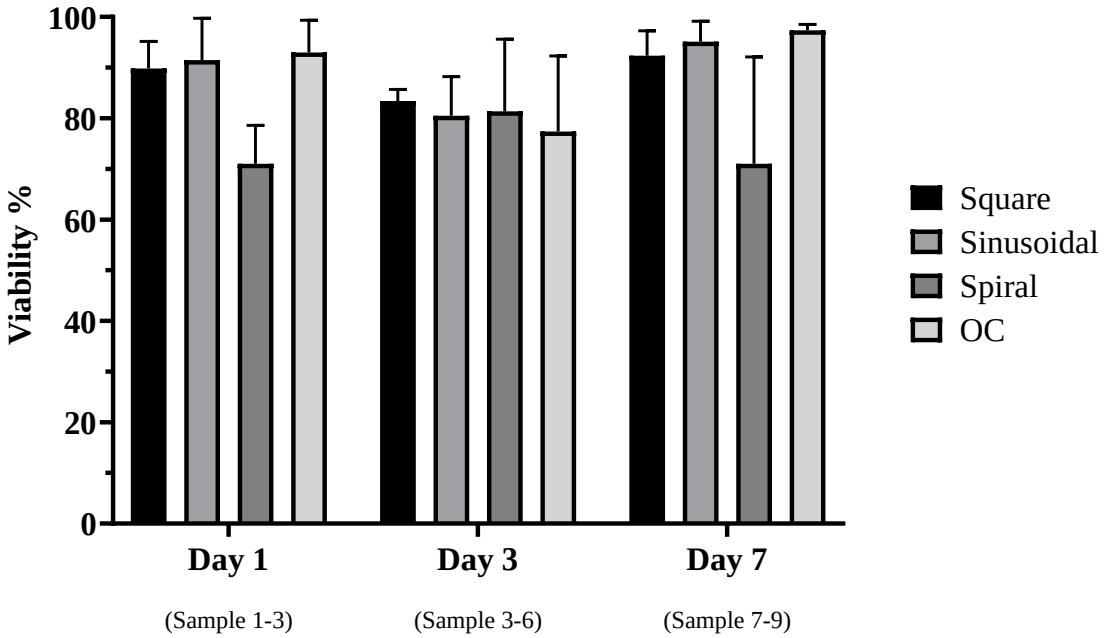


Figure 7.18 Cell viability assessment employing the live/dead cell assay conducted on day 1, day 3, and day 7 for the different geometries and the OC scaffold. The quantification analysis was carried out utilising ImageJ/Fiji software. T. Results denote mean± SD (n=3, N=3).

7.3.4. Cell Proliferation.

As shown in **Figure 7.19**, the DNA assay results provide valuable insights into the cell content within the scaffold designs. Specifically, the only instances of statistical significance were observed in the spiral design. Notably, the spiral design exhibited significant differences in DNA content between day one and day three of $p = 0.0026$, as well as between day one and day seven of $p = 0.0149$. Conversely, the square, sinusoidal, and OC designs did not exhibit any statistically significant variations in DNA content.

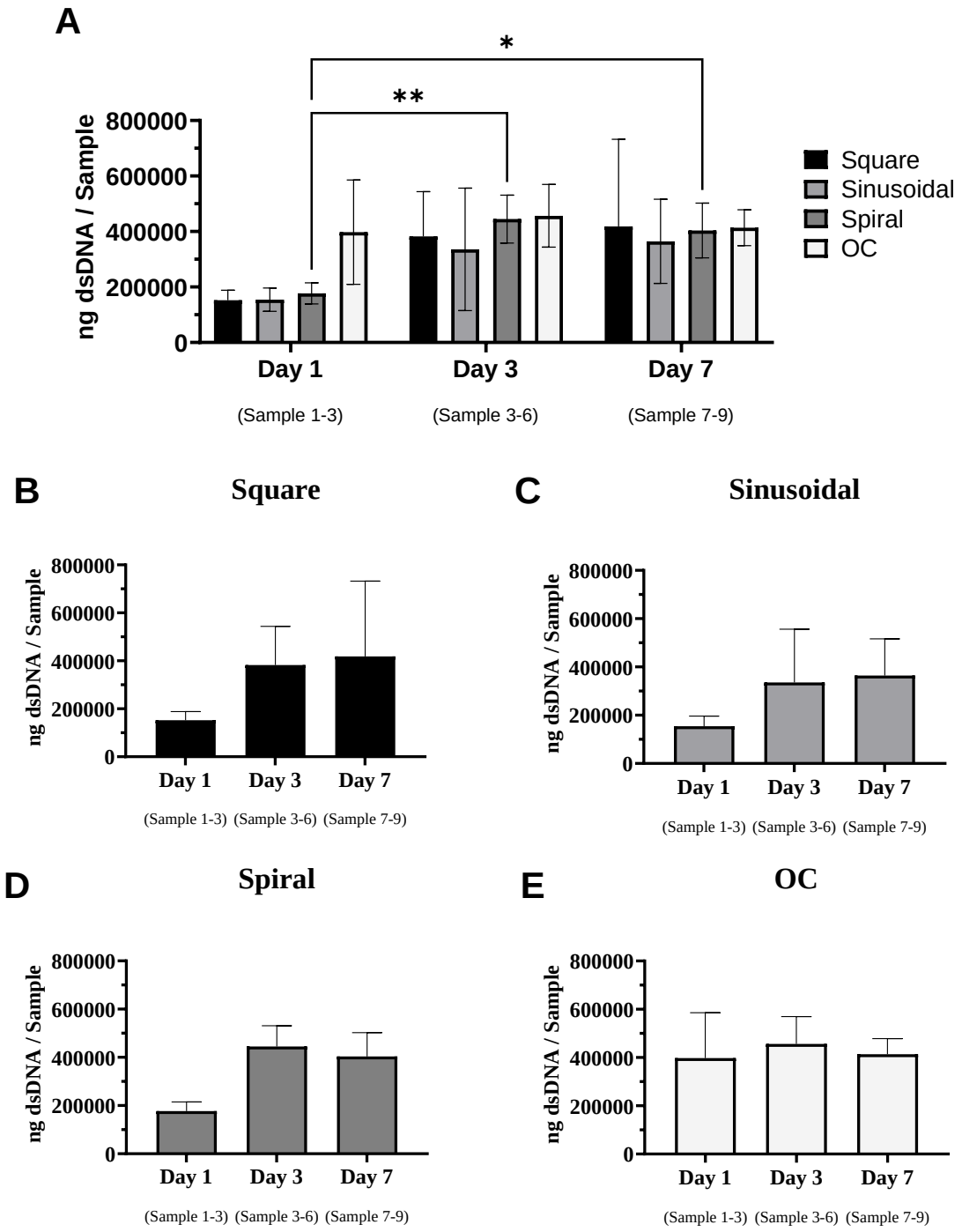


Figure 7.19 Cell Proliferation as assessed by dsDNA content at day 1, day 3, and day 7. A) Cell Proliferation using dsDNA assay comparing square, sinusoidal, spiral and OC scaffolds at day 1, day 3, and day 7. B) Square scaffolds. C) Sinusoidal scaffolds. D) Spiral scaffolds. E) OC scaffolds. Results denote mean± S.D. (n=3,N=3). Statistical analysis and significance levels are indicated as $p < 0.01$,** $p < 0.001$.

Cell expansion findings support the observed trends in DNA content as indicative of proliferation. The DNA content assessments underscore a consistent rise in cell numbers across all scaffold designs. By day three of the culture period, cell proliferation had occurred $3.82x10^5 \pm 1.47\ x10^5$, $3.36x10^5 \pm 2.02x10^5$ and $4.45x10^5 \pm 7.89\ x10^4$ for the square, sinusoidal and spiral, respectively. Contrary, the OC scaffolds keep the DNA content of $4.57x10^5 \pm 1.03\ x10^5$ between day 1 and day 3 (as shown in **Figure 7.19**).

However, an interesting pattern emerged by day 7. The spiral design and the OC scaffold, represented in **Figure 7.19D** and **Figure 7.19E**, respectively, displayed a decline in their DNA content. The spiral design showed a decrease to $4.04\ x10^5 \pm 9.00\ x10^4$, and the OC scaffold exhibited a comparable reduction to $4.14\ x10^5 \pm 5.91\ x10^4$.

The observed reduction in DNA content raises the possibility of altered cell dynamics within these designated designs. Such a trend suggests the potential for a plateau or even a decline in cell proliferation as the extended culture period progresses. In order to comprehensively evaluate cell proliferation under these circumstances, dynamic seeding methods would be deployed to facilitate an internal flow. This approach ensures sustained nutrient availability and effective waste removal, enhancing the potential for continuous cellular activity.

Through this comparative exploration, significant differences in cell proliferation trajectories become evident. This emphasises scaffold design's profound impact on cell behaviour's temporal evolution. The variations in proliferation dynamics underscore the intricate interplay between the microenvironment provided by the scaffold and the cellular responses.

7.4. Conclusions.

In conclusion, this chapter presents the extensive characterisation of cell viability on the OC scaffold, aiming to disclose the relationship between scaffold design, cellular metabolism, and proliferation. The importance of scaffold design in tissue engineering implies that the pore structure and material composition significantly influence cell behaviour within the scaffold matrix (Chan & Leong, 2008; Jian et al., 2020). This evaluation is fundamental in the context of the OC scaffold, where the optimisation of these parameters holds the key to promoting successful tissue regeneration.

A comprehensive analysis of cell viability was conducted, considering factors such as metabolic activity, proliferation, and attachment. Evaluation of cellular responses across different scaffold geometries (square, sinusoidal, spiral) along with the OC scaffold revealed distinct behaviour patterns, aligning with existing literature on scaffold architecture influence (Browe et al., 2022; Nava et al., 2016). Recognising the key role of pore size, distribution, and interconnectivity to facilitate nutrient diffusion, waste removal, and cell-cell interactions reflect by previous studies (Campos Mora, 2022). These geometries patterns were found to influence cellular metabolic activity and proliferation rates across each geometry design. The OC scaffold, designed for osteochondral tissue regeneration, demonstrated unique characteristics driven by the influence of the spiral design on cell distribution.

Assessment of the metabolic activity revealed interesting trends over time, emphasising how scaffold design dictates cellular responses. Insights from studies by Joyce et al. , Rosenzweig et al. , and Yang et al., et al. provided additional context, offering insights into different scaffold architectures and fabrication techniques (Joyce et al., 2023; Rosenzweig et al., 2015; Yang et al., 2021). Although the initial metabolic activity remained relatively stable, a significant rise was observed on the seventh day in all designs. The OC scaffold exhibited a notable increase in metabolic activity, underscoring its potential to produce a robust cellular response. DNA content measurements further validate the scaffolds, with significant increases in cell amount observed across designs. However, intriguingly, the spiral design and the OC scaffold demonstrated a decrease in DNA content by day seven, hinting at altered cellular dynamics over extended culture periods.

In summary, the examination of cell viability in the OC scaffold revealed deep insights into the layers between scaffold design, cell proliferation, and binding efficiency. These findings, aligning with existing literature, guide the development of optimised scaffold designs to enhance tissue regeneration and repair (Campos Mora, 2022; H. W. Kang et al., 2016). This study highlights the importance of understanding the interaction between scaffold characteristics and cellular behaviour for osteochondral tissue regeneration.

Chapter 8. Summary and future directions.

The field of 3D printing, particularly within the field of medical applications offers opportunities for innovation and customisation of medical devices. Among the various 3D printing technologies, extrusion-based methods have been extensively explored for their versatility and applicability in healthcare. Extrusion-based 3D printing grants the freedom to produce intricate and diverse designs, catering to the specific needs of medical applications. This technology ensures repeatability in structure, enabling the creation of complex geometries for tissue engineering. Furthermore, the utilisation of biomaterials in extrusion-based 3D printing allows for the fabrication of patient-specific implants and tissues. This convergence of 3D printing, extrusion-based techniques, medical applications, design flexibility, structural consistency, and biomaterial integration underscores potential of this technology in shaping the future of personalised healthcare.

The landscape of medical interventions for osteochondral defects has been significantly influenced by the emergence of 3D printing technologies, with extrusion-based methods taking a prominent role in this transformative process. Osteochondral defects, characterised by damage to both the articular cartilage and underlying bone, present challenges for conventional treatments. Existing approaches often include autografts, allografts, or microfracture procedures, yet these methods fall short in achieving optimal tissue regeneration and functional restoration. Extrusion-based 3D printing is one of the most common manufacturing methodologies. It is cheap, easy, and readily accessible to non-expert users, making it suitable for fabricating scaffolds. This method generates continuous filaments through extrusion force, allowing for the creation of precise geometries. Moreover, this manufacturing technique is compatible with various biomaterial viscosities and different concentrations of cells, enabling the construction of tissue structures through multi-material printing.

The overall aim of this thesis was the design and fabrication of a multiphasic-graded articular OC scaffold. The integrated and graded mechanical properties of the scaffold components were designed to reflect the unique characteristics of the different zones within the tissues (bone and cartilage). The fundamental hypothesis guiding this research proposed was that implementing a graded interface, achieved through multi-material material and different geometries across the scaffold, would effectively align the mechanical properties. Likewise,

the designs involved in creating the OC were analysed to ensure an environment conducive to optimal cell attachment and proliferation within the scaffold structure.

In **Chapter 4,** PCL and GelMA were 3D printed, using extrusion methods, into a 3D structure with integrated yet distinct zones representing the structure of the OC tissue within a singular scaffold. PCL, chosen for its thermoplastic properties, was evaluated as a potential structural support material for the scaffold. Due to PCL's exposure to degradation at elevated temperatures, material characterisation post 3D printing was performed. The conclusive findings indicated that the material properties of PCL remained unaffected by the 3D printing process, establishing it as a suitable supportive material for the osteochondral scaffold. Similarly, the characterisation of different concentrations of GelMA (5% w/v, 10% w/v, 15% w/v, and 20% w/v) was conducted. All concentrations have exhibited shear-thinning behaviour, as previously demonstrated by Liu et al. and Ruiz-Cantu et al (W. Liu et al., 2017; Ruiz-Cantu et al., 2020b). Meanwhile, the viscosity of GelMA is influenced by temperature and concentrations. When GelMA is subjected to high shear rates inside a nozzle during extrusion 3D printing, a decrease in viscosity or shear stress is expected. This phenomenon has been observed in studies by Schuurman et al and Schuwab et al (Schuurman et al., 2013; Schwab et al., 2020). Rheological tests suggested that 10% w/v GelMA possesses the required rheological profile for extrusion 3D printing. Therefore, 10% w/v GelMA was selected as the material for 3D printing to provide cell support in the multi-material scaffold.

In **Chapter 5,** the objective was to achieve mechanical properties in the OC scaffold similar to the native OC tissue, specifically a compressive Youngs modulus. The investigation focused on scaffold design and material selection influenced by 3D extrusion base printing. The 3D printing parameters of the materials selected were evaluated by varying the pressures (2-4 bar), needle gauges (G27, G30, G32), and temperature (80°C-100°C for PCL and 14°C-20°C for GelMA). Simultaneously, different geometries were explored in the scaffold design to create a comprehensive structure with varied mechanical properties in a multi-material graded scaffold. Geometries such as square, sinusoidal, and spiral were selected based on printability. The mechanical properties of these geometries exhibited variations in Youngs modulus, as Schipani, Scheurer, et al. provided evidence of PCL scaffolds with a square design and modifying the configuration with a double offset, revealing a decrease in the Youngs modulus for the offset configuration, showing that architectural configurations in scaffolds impact the Youngs modulus (Schipani, Scheurer, et al., 2020). The outcome

demonstrated that, by judiciously selecting materials and optimising scaffold geometries through 3D printing, it is indeed feasible to achieve overall mechanical properties comparable to those of the OC tissue, exemplified by a Youngs modulus of 49.74 ±3.77MPa in the final PCL/GelMA OC design. Comparing the experimental findings in this thesis with those of Kabir et al., who conducted unconfined compression tests on human femoral condyles tissue. Kabir et al. reported a compressive modulus of 10.60 ± 3.62 MPa in their experiments related to the articular OC tissue (Kabir et al., 2021). This result demonstrates the feasibility of achieving higher mechanical properties comparable to those of the cartilage OC tissue through the material selection and scaffold optimisation via 3D. This result aligns closely with the OC scaffold Youngs modulus. In contrast, Daly and Kelly study, which employed a PCL/GelMA/Pluronic scaffold for the OC defects, yielded mechanical properties that were notably lower. Using the same unconfined compression technique, the mechanical property of the scaffold was reported as 3000 KPa after 10 weeks of cell culture (Daly & Kelly, 2019). This variance in results emphasizes the impact of the scaffold design choices on the mechanical performance of the OC scaffold. In **Chapter 6,** key parameters and assumptions made for constructing a predictive FE model of mechanical behaviour of the OC scaffold were established. The FE model constructed in this study provides a prediction of the mechanical behaviour of the OC scaffolds.

Finally, in **Chapter 7,** how different scaffold geometry designs can enhance cell adhesion and proliferation, creating a favourable environment for cellular growth within the OC scaffold was explored. The geometries, square, sinusoidal, and spiral, supported cell adhesion to these areas and an increase in cell proliferation was observed over 7 days, in accordance with established studies highlighting the impact of scaffold architecture (Browe et al., 2022; Nava et al., 2016). However, it was observed that, for the OC scaffold, comprising these three designs and with a height four times greater than the individual geometries, the proliferation of cells within the scaffold was seen to decrease by day 7. Daly and Kelly show a scaffold with similar dimensions and materials seeded statically and dynamically, with the dynamic seeding showing a beneficial culture conditions into the core of the scaffold (Daly & Kelly, 2019). The use of MSCs, dynamic seeding and evaluation of cell differentiation (e.g. the secretion of collagens) would form the next steps towards an in vivo evaluation of the scaffolds.

The work outlined in this thesis showcases the 3D printing of a multiphasic graded OC scaffold using multiple materials, with a primary focus on aligning the scaffold's mechanical properties with those of the OC tissue and without interfaces between the different scaffold zones/materials. Emphasising the importance of printing requirements, established through a predictive modelling and an experimental approach using extrusion printing, has successfully demonstrated a graded OC scaffold with geometries that can be used to modulate the Youngs modulus of the scaffold. In conclusion, the novelty in the presented research focuses on created a multiphasic graded OC scaffold mimicking the mechanical properties, this thesis has significantly advanced the understanding of mechanical property variation through varying geometries. Joyce et al demonstrate that a square geometry is slightly lower in the mechanical properties than a gyroid geometry (Joyce et al., 2023).The combined influence of optimised materials, scaffold design, and fabrication techniques holds promise for the future development of the OC scaffolds with improved functionality and broader applicability in tissue engineering.

8.1. Future Work.

This section discusses the recommendations for future work to further investigate **the** characterisation of materials for extrusion-base 3D printing, 3D printing of multi-material for osteochondral defect, predictive FE Modelling and characterisation of cell viability for the OC scaffold.

Characterisation of materials for extrusion-base 3D printing- This thesis involves the characterisation of PCL and GelMA materials for multi-material extrusion-based 3D printing. However, limitations were noted in the compressive material properties of PCL and GelMA. Notably, the thesis does not explore the incorporation of a third material, presenting an avenue for future research to investigate the impact of introducing a new material and its potential contribution to enhancing the compressive Youngs modulus, particularly in the subchondral zone. Furthermore, maintaining the graded scaffold by simultaneously extruding three materials using extrusion-based 3D printing justifies further examination in future studies.

3D printing of multi-material for osteochondral defect- This thesis assessed the compressive Youngs modulus of various zones in the OC scaffold, through the fabrication of three geometries employed in manufacturing the OC scaffold. However, potential future investigations could concentrate on enhancing and evaluating alternative designs to meet

mechanical properties and promote cell viability. Furthermore, as technology advances, employing the same design approaches but with different 3D printing modalities could facilitate the creation of more complex designs that align with the specific mechanical requirements of each tissue zone.

Predictive FE Modelling- The use of a finite element FE model in this thesis emerges as a valuable tool for predicting scaffold behaviour. However, this thesis does not explore the establishment of a robust FE model that could involve incorporating additional material properties, identifying key parameters, and delineating the assumptions integral to the model. Notably, a more sophisticated FE model could account for interactions between the scaffold and its external environment, such as the walls with which the scaffold interacts during the transplantation process. Expanding the scope of the FE model to address these refined factors would contribute to a more accurate and insightful simulation of scaffold dynamics.

Characterisation of cell differentiation for the OC scaffold- In this thesis, scaffolds were evaluated for cell viability and proliferation. However, due to time restrictions, the decision was made to assess cell viability using mammalian 3T3 cells as a preliminary measure for evaluating viability conditions within the scaffolds. Subsequent steps would involve utilising mesenchymal stem cells (MSCs), implementing dynamic seeding, and assessing cell expansion, differentiation, and collagen secretion. This progression aligns logically with the aim of advancing towards an in vivo evaluation of the scaffolds.

8.2. Concluding Statement of Research Purpose and Novelty.

The literature reveals various attempts at creating OC scaffolds using diverse materials, manufacturing processes, and approaches. However, there remains a gap in the exploration of fulfilling the distinct mechanical properties of each zone within the OC tissue. Consequently, this gap prompts an investigation into the feasibility of employing 3D printing to create an OC scaffold that meets the mechanical properties of each zone within the tissue. The novelty in the presented research focuses on the creation of a multiphasic graded OC scaffold designed to replicate the mechanical properties of the native articular OC tissue. This is achieved by modifying the design across different zones, utilising an integrated materials approach and 3D extrusion printing, with the goal of attaining the compression modulus specific to each zone. The underlying intention is to gain a deeper understanding

of how to meet the mechanical property requirements of the regenerated articular OC tissue through the design and 3D printing of an OC scaffold.

The potential significance lies in a better understanding of these aspects, employing design for manufacture and creating a scaffold with varying compressive modulus. This understanding opens up the possibility of similar approaches being applied to develop scaffolds for other tissues. Finally, this developmental process holds promise for generating diverse designs in the future and creating novel scaffolds tailored to the specific mechanical properties required by different tissues.

REFERENCES

Ahmadi Soufivand, A., Faber, J., Hinrichsen, J., & Budday, S. (2023). Multilayer 3D bioprinting and complex mechanical properties of alginate-gelatin mesostructures. *Scientific Reports 2023 13:1*, *13*(1), 1–14. https://doi.org/10.1038/s41598-023-38323-2

Ahmed, E. M. (2015). Hydrogel: Preparation, characterisation, and applications: A review. In *Journal of Advanced Research* (Vol. 6, Issue 2, pp. 105–121). Elsevier B.V. https://doi.org/10.1016/j.jare.2013.07.006

Ai, C., Lee, Y. H. D., Tan, X. H., Tan, S. H. S., Hui, J. H. P., & Goh, J. C. H. (2021). Osteochondral tissue engineering: Perspectives for clinical application and preclinical development. *Journal of Orthopaedic Translation*, *30*, 93–102. https://doi.org/10.1016/J.JOT.2021.07.008

Al-Munajjed, A. A., Hien, M., Kujat, R., Gleeson, J. P., & Hammer, J. (2008). Influence of pore size on tensile strength, permeability and porosity of hyaluronan-collagen scaffolds. *Journal of Materials Science: Materials in Medicine*, *19*(8), 2859–2864. https://doi.org/10.1007/S10856-008-3422-5/FIGURES/5

Ansari, S., Khorshidi, S., & Karkhaneh, A. (2019). Engineering of gradient osteochondral tissue: From nature to lab. *Acta Biomaterialia*, *87*, 41–54. https://doi.org/10.1016/J.ACTBIO.2019.01.071

Archer, E., Torretti, M., & Madbouly, S. (2021). Biodegradable polycaprolactone (PCL) based polymer and composites. *Physical Sciences Reviews*, *0*(0). https://doi.org/10.1515/psr-2020-0074

Arraiza, A. L., Sarasua, J. R., Verdu, J., & Colin, X. (2007). Rheological behavior and modeling of thermal degradation of poly(ε-caprolactone) and poly(L-lactide). *International Polymer Processing*, *22*(5), 389–394. https://doi.org/10.3139/217.2067

Askari, M., Afzali Naniz, M., Kouhi, M., Saberi, A., Zolfagharian, A., & Bodaghi, M. (2021). Recent progress in extrusion 3D bioprinting of hydrogel biomaterials for tissue regeneration: A comprehensive review with focus on advanced fabrication

techniques. In *Biomaterials Science* (Vol. 9, Issue 3, pp. 535–573). Royal Society of Chemistry. https://doi.org/10.1039/d0bm00973c

Azimi, B., Nourpanah, P., Rabiee, M., & Arbab, S. (n.d.). *Poly (ε-caprolactone) Fiber: An Overview*. *9*. Retrieved October 19, 2023, from http://www.jeffjournal.org

Azimi, B., Nourpanah, P., Rabiee, M., & Arbab, S. (2014). Poly (ε-caprolactone) fiber: An overview. *Journal of Engineered Fibers and Fabrics*, *9*(3), 74–90. https://doi.org/10.1177/155892501400900309

Badami, A. S., Kreke, M. R., Thompson, M. S., Riffle, J. S., & Goldstein, A. S. (2006). Effect of fiber diameter on spreading, proliferation, and differentiation of osteoblastic cells on electrospun poly(lactic acid) substrates. *Biomaterials*, *27*(4), 596–606. https://doi.org/10.1016/j.biomaterials.2005.05.084

Bartnikowski, M., Klein, T. J., Melchels, F. P. W., & Woodruff, M. A. (2014). Effects of scaffold architecture on mechanical characteristics and osteoblast response to static and perfusion bioreactor cultures. *Biotechnology and Bioengineering*, *111*(7), 1440–1451. https://doi.org/10.1002/BIT.25200

Bartnikowski, M., Wellard, R. M., Woodruff, M., & Klein, T. (2015). Tailoring Hydrogel Viscoelasticity with Physical and Chemical Crosslinking. *Polymers 2015, Vol. 7, Pages 2650-2669*, *7*(12), 2650–2669. https://doi.org/10.3390/POLYM7121539

Bas, O., De-Juan-Pardo, E. M., Meinert, C., D'Angella, D., Baldwin, J. G., Bray, L. J., Wellard, R. M., Kollmannsberger, S., Rank, E., Werner, C., Klein, T. J., Catelas, I., & Hutmacher, D. W. (2017). Biofabricated soft network composites for cartilage tissue engineering. *Biofabrication*, *9*(2), 025014. https://doi.org/10.1088/1758-5090/AA6B15

Bayrak, E., & Ozcan, B. (2016). Cartilage-Bone Interface Features, Scaffold and Cell Options for Regeneration. *Journal of Tissue Science & Engineering*, *7*(2). https://doi.org/10.4172/2157-7552.1000174

Beatrice, C. A. G., Shimomura, K. M. B., Backes, E. H., Harb, S. V., Costa, L. C., Passador, F. R., & Pessan, L. A. (2021). Engineering printable composites of poly

(ε-polycaprolactone) / β-tricalcium phosphate for biomedical applications. *Polymer Composites*, *42*(3), 1198–1213. https://doi.org/10.1002/pc.25893

Bernhardt, A., Paul, B., & Gelinsky, M. (2018). Biphasic scaffolds from marine collagens for regeneration of osteochondral defects. *Marine Drugs*, *16*(3), 91. https://doi.org/10.3390/md16030091

Billiet, T., Gevaert, E., De Schryver, T., Cornelissen, M., & Dubruel, P. (2014). The 3D printing of gelatin methacrylamide cell-laden tissue-engineered constructs with high cell viability. *Biomaterials*, *35*(1), 49–62. https://doi.org/10.1016/j.biomaterials.2013.09.078

Bittner, S. M., Smith, B. T., Diaz-Gomez, L., Hudgins, C. D., Melchiorri, A. J., Scott, D. W., Fisher, J. P., & Mikos, A. G. (2019a). Fabrication and mechanical characterisation of 3D printed vertical uniform and gradient scaffolds for bone and osteochondral tissue engineering. *Acta Biomaterialia*, *90*, 37–48. https://doi.org/10.1016/j.actbio.2019.03.041

Borsøe, B., Casper, C. •, Foldager, B., Hansen, O. M., Asger, •, Kristiansen, A., Dang, •, Svend, Q., Agnete, L. •, Nielsen, D., Vinge, J., Cody, N. •, Bü, E., & Lind, M. (n.d.). *A novel nano-structured porous polycaprolactone scaffold improves hyaline cartilage repair in a rabbit model compared to a collagen type I/III scaffold: in vitro and in vivo studies*. https://doi.org/10.1007/s00167-011-1692-9

Boschetti, F., Pennati, G., Gervaso, F., Peretti, G. M., & Dubini, G. (2004). Biomechanical properties of human articular cartilage under compressive loads. *Biorheology*, *41*(3–4), 159–166. https://europepmc.org/article/med/15299249

Boushell, M. K. (2016). Scaffold Design and Optimization for Integrative Cartilage Repair. *ProQuest Dissertations and Theses*, 185.

Boushell, M. K., Hung, C. T., Hunziker, E. B., Strauss, E. J., & Lu, H. H. (2017). Current strategies for integrative cartilage repair. *Connective Tissue Research*, *58*(5), 393–406. https://doi.org/10.1080/03008207.2016.1231180

Brandt, K. D., Radin, E. L., Dieppe, P. A., & Putte, L. van de. (2006). Yet more evidence that osteoarthritis is not a cartilage disease. *Annals of the Rheumatic Diseases*, *65*(10), 1261–1264. https://doi.org/10.1136/ARD.2006.058347

Brenken, B., Barocio, E., Favaloro, A., Kunc, V., & Pipes, R. B. (2018). Fused filament fabrication of fiber-reinforced polymers: A review. *Additive Manufacturing*, *21*, 1–16. https://doi.org/10.1016/J.ADDMA.2018.01.002

Brittberg, M., Gomoll, A. H., Canseco, J. A., Far, J., Lind, M., & Hui, J. (2016). Cartilage repair in the degenerative ageing knee. *Acta Orthopaedica*, *87*(sup363), 26–38. https://doi.org/10.1080/17453674.2016.1265877

Brittberg, M., Lindahl, A., Nilsson, A., Ohlsson, C., Isaksson, O., & Peterson, L. (1994). Treatment of Deep Cartilage Defects in the Knee with Autologous Chondrocyte Transplantation. *Https://Doi.Org/10.1056/NEJM199410063311401*, *331*(14), 889–895. https://doi.org/10.1056/NEJM199410063311401

Browe, D. C., Díaz-Payno, P. J., Freeman, F. E., Schipani, R., Burdis, R., Ahern, D. P., Nulty, J. M., Guler, S., Randall, L. D., Buckley, C. T., Brama, P. A. J., & Kelly, D. J. (2022). Bilayered extracellular matrix derived scaffolds with anisotropic pore architecture guide tissue organization during osteochondral defect repair. *Acta Biomaterialia*, *143*, 266–281. https://doi.org/10.1016/J.ACTBIO.2022.03.009

Bruyas, A., Lou, F., Stahl, A. M., Gardner, M., Maloney, W., Goodman, S., & Yang, Y. P. (2018). Systematic characterisation of 3D-printed PCL/β-TCP scaffolds for biomedical devices and bone tissue engineering: influence of composition and porosity. *Journal of Materials Research*, *33*(14), 1948. https://doi.org/10.1557/JMR.2018.112

Bryant, S. J., & Anseth, K. S. (2002). Hydrogel properties influence ECM production by chondrocytes photoencapsulated in poly(ethylene glycol) hydrogels. *Journal of Biomedical Materials Research*, *59*(1), 63–72. https://doi.org/10.1002/JBM.1217

Buzgo, M., Mickova, A., Rampichova, M., & Doupnik, M. (2018). Blend electrospinning, coaxial electrospinning, and emulsion electrospinning techniques. In *Core-Shell Nanostructures for Drug Delivery and Theranostics* (pp. 325–347). Elsevier. https://doi.org/10.1016/B978-0-08-102198-9.00011-9

Cabreira, V., & Santana, R. M. C. (2020). Effect of infill pattern in fused filament fabrication (FFF) 3D printing on materials performance. *Revista Materia*, *25*(3), 1–9. https://doi.org/10.1590/S1517-707620200003.1126

Cahill, S., Lohfeld, S., & McHugh, P. E. (2009). Finite element predictions compared to experimental results for the effective modulus of bone tissue engineering scaffolds fabricated by selective laser sintering. *Journal of Materials Science. Materials in Medicine*, *20*(6), 1255–1262. https://doi.org/10.1007/S10856-009-3693-5

Camacho, P., Busari, H., Seims, K. B., Schwarzenberg, P., Dailey, H. L., & Chow, L. W. (2019). 3D printing with peptide-polymer conjugates for single-step fabrication of spatially functionalized scaffolds. *Biomaterials Science*, *7*, 4237. https://doi.org/10.1039/c9bm00887j

Camacho, P., Fainor, M., Seims, K. B., Tolbert, J. W., & Chow, L. W. (2021). Fabricating spatially functionalized 3D-printed scaffolds for osteochondral tissue engineering. *Journal of Biological Methods*, *8*(1), e146. https://doi.org/10.14440/jbm.2021.353

Campbell, S. E., Ferguson, V. L., & Hurley, D. C. (2012). Nanomechanical mapping of the osteochondral interface with contact resonance force microscopy and nanoindentation. *Acta Biomaterialia*, *8*(12), 4389–4396. https://doi.org/10.1016/J.ACTBIO.2012.07.042

Campos Mora, Y. (2022). *Multilayer porous scaffolds for cartilage tissue engineering*. https://hdl.handle.net/1887/3455223

Cano-Vicent, A., Tambuwala, M. M., Hassan, S. S., Barh, D., Aljabali, A. A. A., Birkett, M., Arjunan, A., & Serrano-Aroca, Á. (2021). Fused deposition modelling: Current status, methodology, applications and future prospects. *Additive Manufacturing*, *47*, 102378. https://doi.org/10.1016/J.ADDMA.2021.102378

Cao, L., Youn, I., Guilak, F., & Setton, L. A. (2006). *Compressive Properties of Mouse Articular Cartilage Determined in a Novel Micro-Indentation Test Method and Biphasic Finite Element Model*. https://doi.org/10.1115/1.2246237

Cao, Y., Cheng, P., Sang, S., Xiang, C., An, Y., Wei, X., Yan, Y., & Li, P. (2021). 3D printed PCL/GelMA biphasic scaffold boosts cartilage regeneration using co-culture of mesenchymal stem cells and chondrocytes: In vivo study. *Materials & Design*, *210*, 110065. https://doi.org/10.1016/J.MATDES.2021.110065

Carla, A., Sato, K., & Cunha, R. L. (n.d.). *Effect of collagen fiber and gelatin on gelling properties of alginate gels*. 1–4.

Castro, N. J., O'Brien, J., & Zhang, L. G. (2015). Integrating biologically inspired nanomaterials and table-top stereolithography for 3D printed biomimetic osteochondral scaffolds. *Nanoscale*, *7*(33), 14010–14022. https://doi.org/10.1039/C5NR03425F

Castro, N. J., Patel, R., & Zhang, L. G. (2015). Design of a Novel 3D Printed Bioactive Nanocomposite Scaffold for Improved Osteochondral Regeneration. *Cellular and Molecular Bioengineering*, *8*(3), 416–432. https://doi.org/10.1007/s12195-015-0389-4

Ceretti, E., Ginestra, P., Neto, P. I., Fiorentino, A., & Da Silva, J. V. L. (2017). Multi-layered Scaffolds Production via Fused Deposition Modeling (FDM) Using an Open Source 3D Printer: Process Parameters Optimization for Dimensional Accuracy and Design Reproducibility. *Procedia CIRP*, *65*, 13–18. https://doi.org/10.1016/J.PROCIR.2017.04.042

Chan, B. P., & Leong, A. K. W. (n.d.). *Scaffolding in tissue engineering: general approaches and tissue-specific considerations*. https://doi.org/10.1007/s00586-008-0745-3

Chang, C. H., Lin, F. H., Lin, C. C., Chou, C. H., & Liu, H. C. (2004). Cartilage tissue engineering on the surface of a novel gelatin–calcium-phosphate biphasic scaffold in a double-chamber bioreactor. *Journal of Biomedical Materials Research Part B: Applied Biomaterials*, *71B*(2), 313–321. https://doi.org/10.1002/JBM.B.30090

Chaudhary, S., Ghosal, D., Tripathi, P., & Kumar, S. (2023). Cellular metabolism: a link connecting cellular behaviour with the physiochemical properties of biomaterials for bone tissue engineering. *Biomaterials Science*, *11*(7), 2277–2291. https://doi.org/10.1039/D2BM01410F

Chen, G., Sato, T., Tanaka, J., & Tateishi, T. (2006). Preparation of a biphasic scaffold for osteochondral tissue engineering. *Materials Science and Engineering: C*, *26*(1), 118–123. https://doi.org/10.1016/J.MSEC.2005.07.024

Chen, H., Gonnella, G., Huang, J., & Di-Silvio, L. (2023). Fabrication of 3D Bioprinted Bi-Phasic Scaffold for Bone–Cartilage Interface Regeneration. *Biomimetics*, *8*(1), 87. https://doi.org/10.3390/BIOMIMETICS8010087/S1

Chen, L., Wei, L., Su, X., Qin, L., Xu, Z., Huang, X., Chen, H., & Hu, N. (2023). Preparation and Characterisation of Biomimetic Functional Scaffold with Gradient Structure for Osteochondral Defect Repair. *Bioengineering 2023, Vol. 10, Page 213*, *10*(2), 213. https://doi.org/10.3390/BIOENGINEERING10020213

Chen, S., Tomov, M. L., Ning, L., Gil, C. J., Hwang, B., Bauser-Heaton, H., Chen, H., & Serpooshan, V. (2023). Extrusion-Based 3D Bioprinting of Adhesive Tissue Engineering Scaffolds Using Hybrid Functionalized Hydrogel Bioinks. *Advanced Biology*, *7*(7), 2300124. https://doi.org/10.1002/ADBI.202300124

Chen, X. B., Fazel Anvari-Yazdi, A., Duan, X., Zimmerling, A., Gharraei, R., Sharma, N. K., Sweilem, S., & Ning, L. (2023). Biomaterials / bioinks and extrusion bioprinting. *Bioactive Materials*, *28*, 511–536. https://doi.org/10.1016/J.BIOACTMAT.2023.06.006

Chen, Z. (2017). Fabrication and research of 3D complex scaffolds for bone tissue engineering based on extrusion deposition technique Fabrication and Research of 3D Complex Scaffolds for Bone Tissue Engineering Based on Extrusion Deposition Technique By. *Thesis*, 211.

Cipitria, A., Skelton, A., Dargaville, T. R., Dalton, P. D., & Hutmacher, D. W. (2011). Design, fabrication and characterisation of PCL electrospun scaffolds - A review. *Journal of Materials Chemistry*, *21*(26), 9419–9453. https://doi.org/10.1039/c0jm04502k

Cometa, S., Bonifacio, M. A., Tranquillo, E., Gloria, A., Domingos, M., & De Giglio, E. (2021). A 3d printed composite scaffold loaded with clodronate to regenerate osteoporotic bone: In vitro characterisation. *Polymers*, *13*(1), 1–17. https://doi.org/10.3390/POLYM13010150

Cong, B., Sun, T., Zhao, Y., & Chen, M. (2023). Current and Novel Therapeutics for Articular Cartilage Repair and Regeneration. *Therapeutics and Clinical Risk Management*, *19*, 485. https://doi.org/10.2147/TCRM.S410277

Costantini, M., Idaszek, J., Szöke, K., Jaroszewicz, J., Dentini, M., Barbetta, A., Brinchmann, J. E., & Święszkowski, W. (2016). 3D bioprinting of BM-MSCs-loaded ECM biomimetic hydrogels for in vitro neocartilage formation. *Biofabrication*, *8*(3), 035002. https://doi.org/10.1088/1758-5090/8/3/035002

Critchley, S., Sheehy, E. J., Cunniffe, G., Diaz-Payno, P., Carroll, S. F., Jeon, O., Alsberg, E., Brama, P. A. J., & Kelly, D. J. (2020). 3D printing of fibre-reinforced cartilaginous templates for the regeneration of osteochondral defects. *Acta Biomaterialia*, *113*, 130–143. https://doi.org/10.1016/J.ACTBIO.2020.05.040

Csaki, C., Schneider, P. R. A., & Shakibaei, M. (2008). Mesenchymal stem cells as a potential pool for cartilage tissue engineering. In *Annals of Anatomy* (Vol. 190, Issue 5, pp. 395–412). Urban & Fischer. https://doi.org/10.1016/j.aanat.2008.07.007

Cui, X., Breitenkamp, K., Finn, M. G., Lotz, M., & D'Lima, D. D. (2012). Direct Human Cartilage Repair Using Three-Dimensional Bioprinting Technology. *Https://Home.Liebertpub.Com/Tea*, *18*(11–12), 1304–1312. https://doi.org/10.1089/TEN.TEA.2011.0543

Cui, X., Gao, G., Yonezawa, T., & Dai, G. (2014). Human cartilage tissue fabrication using three-dimensional inkjet printing technology. *Journal of Visualized Experiments*, *88*. https://doi.org/10.3791/51294

Daly, A. C., Critchley, S. E., Rencsok, E. M., & Kelly, D. J. (2016). A comparison of different bioinks for 3D bioprinting of fibrocartilage and hyaline cartilage. *Biofabrication*, *8*(4), 045002. https://doi.org/10.1088/1758-5090/8/4/045002

Daly, A. C., Freeman, F. E., Gonzalez-Fernandez, T., Critchley, S. E., Nulty, J., & Kelly, D. J. (2017a). 3D Bioprinting for Cartilage and Osteochondral Tissue Engineering. *Advanced Healthcare Materials*, *6*(22), 1700298. https://doi.org/10.1002/adhm.201700298

Daly, A. C., & Kelly, D. J. (2019). Biofabrication of spatially organised tissues by directing the growth of cellular spheroids within 3D printed polymeric microchambers. *Biomaterials*, *197*, 194–206. https://doi.org/10.1016/J.BIOMATERIALS.2018.12.028

de Ruijter, M., Ribeiro, A., Dokter, I., Castilho, M., & Malda, J. (2019). Simultaneous Micropatterning of Fibrous Meshes and Bioinks for the Fabrication of Living Tissue Constructs. *Advanced Healthcare Materials*, *8*(7). https://doi.org/10.1002/ADHM.201800418

Dellaquila, A., Campodoni, E., Tampieri, A., & Sandri, M. (2020). Overcoming the Design Challenge in 3D Biomimetic Hybrid Scaffolds for Bone and Osteochondral Regeneration by Factorial Design. *Frontiers in Bioengineering and Biotechnology*, *8*, 743. https://doi.org/10.3389/fbioe.2020.00743

Deng, C., Chang, J., & Wu, C. (2019). Bioactive scaffolds for osteochondral regeneration. *Journal of Orthopaedic Translation*, *17*, 15–25. https://doi.org/10.1016/J.JOT.2018.11.006

Deng, C., Zhu, H., Li, J., Feng, C., Yao, Q., Wang, L., Chang, J., & Wu, C. (2018a). Bioactive scaffolds for regeneration of cartilage and subchondral bone interface. *Theranostics*, *8*(7), 1940–1955. https://doi.org/10.7150/thno.23674

Di Luca, A., Van Blitterswijk, C., & Moroni, L. (2015). The osteochondral interface as a gradient tissue: From development to the fabrication of gradient scaffolds for regenerative medicine. *Birth Defects Research Part C - Embryo Today: Reviews*, *105*(1), 34–52. https://doi.org/10.1002/bdrc.21092

Domingos, M., Gloria, A., Coelho, J., Bartolo, P., & Ciurana, J. (2017). Three-dimensional printed bone scaffolds: The role of nano/micro-hydroxyapatite particles on the adhesion and differentiation of human mesenchymal stem cells. *Proceedings of the Institution of Mechanical Engineers, Part H: Journal of Engineering in Medicine*, *231*(6), 555–564. https://doi.org/10.1177/0954411916680236

Dormer, N. H., Singh, M., Zhao, L., Mohan, N., Berkland, C. J., & Detamore, M. S. (2012). Osteochondral interface regeneration of the rabbit knee with macroscopic

gradients of bioactive signals. *Journal of Biomedical Materials Research - Part A*, *100 A*(1), 162–170. https://doi.org/10.1002/jbm.a.33225

Doube, M., Firth, E. C., Boyde, A., & Bushby, A. J. (2010). Combined nanoindentation testing and scanning electron microscopy of bone and articular calcified cartilage in an equine fracture predilection site. *European Cells & Materials*, *19*, 242–251. https://doi.org/10.22203/ECM.V019A23

Doyle, H., Lohfeld, S., & McHugh, P. (2014a). Predicting the elastic properties of selective laser sintered PCL/β-TCP bone scaffold materials using computational modelling. *Annals of Biomedical Engineering*, *42*(3), 661–677. https://doi.org/10.1007/S10439-013-0913-4

Du, X. (2018). 3D Bio-Printing Review. *IOP Conference Series: Materials Science and Engineering*, *301*(1), 012023. https://doi.org/10.1088/1757-899X/301/1/012023

Du, Y., Liu, H., Yang, Q., Wang, S., Wang, J., Ma, J., Noh, I., Mikos, A. G., & Zhang, S. (2017). Selective laser sintering scaffold with hierarchical architecture and gradient composition for osteochondral repair in rabbits. *Biomaterials*, *137*, 37–48. https://doi.org/10.1016/J.BIOMATERIALS.2017.05.021

Duan, B., Hockaday, L. A., Kang, K. H., & Butcher, J. T. (2013). 3D bioprinting of heterogeneous aortic valve conduits with alginate/gelatin hydrogels. *Journal of Biomedical Materials Research. Part A*, *101*(5), 1255–1264. https://doi.org/10.1002/JBM.A.34420

Duan, B., Kapetanovic, E., Hockaday, L. A., & Butcher, J. T. (2014). Three-dimensional printed trileaflet valve conduits using biological hydrogels and human valve interstitial cells. *Acta Biomaterialia*, *10*(5), 1836–1846. https://doi.org/10.1016/J.ACTBIO.2013.12.005

Duncan, H., Jundt, J., Riddle, J., Pitchford, W., & Christopherson, T. (1987). *The tibial subchondral plate. A scanning electron microscopic study*.

Dutta, P. K. (2015). Chitin and Chitosan for Regenerative Medicine. In *Chitin and Chitosan for Regenerative Medicine* (Issue December 2017). https://doi.org/10.1007/978-81-322-2511-9

Dwivedi, R., Kumar, S., Pandey, R., Mahajan, A., Nandana, D., Katti, D. S., & Mehrotra, D. (2020). Polycaprolactone as biomaterial for bone scaffolds: Review of literature. *Journal of Oral Biology and Craniofacial Research*, *10*(1), 381. https://doi.org/10.1016/J.JOBCR.2019.10.003

Dziadek, M., Menaszek, E., Zagrajczuk, B., Pawlik, J., & Cholewa-Kowalska, K. (2015). New generation poly(ε-caprolactone)/gel-derived bioactive glass composites for bone tissue engineering: Part I. Material properties. *Materials Science and Engineering: C*, *56*, 9–21. https://doi.org/10.1016/J.MSEC.2015.06.020

Elomaa, L., Keshi, E., Sauer, I. M., & Weinhart, M. (2020). Development of GelMA/PCL and dECM/PCL resins for 3D printing of acellular in vitro tissue scaffolds by stereolithography. *Materials Science and Engineering: C*, *112*, 110958. https://doi.org/10.1016/J.MSEC.2020.110958

Eltom, A., Zhong, G., & Muhammad, A. (2019). Scaffold Techniques and Designs in Tissue Engineering Functions and Purposes: A Review. *Advances in Materials Science and Engineering*, *2019*, 1–13. https://doi.org/10.1155/2019/3429527

Eshraghi, S., & Das, S. (2010). Mechanical and microstructural properties of polycaprolactone scaffolds with one-dimensional, two-dimensional, and three-dimensional orthogonally oriented porous architectures produced by selective laser sintering. *Acta Biomaterialia*, *6*(7), 2467–2476. https://doi.org/10.1016/J.ACTBIO.2010.02.002

Esposito Corcione, C., Gervaso, F., Scalera, F., Padmanabhan, S. K., Madaghiele, M., Montagna, F., Sannino, A., Licciulli, A., & Maffezzoli, A. (2019). Highly loaded hydroxyapatite microsphere/ PLA porous scaffolds obtained by fused deposition modelling. *Ceramics International*, *45*(2), 2803–2810. https://doi.org/10.1016/J.CERAMINT.2018.07.297

Fan, C., & Wang, D. A. (2015). A biodegradable PEG-based micro-cavitary hydrogel as scaffold for cartilage tissue engineering. *European Polymer Journal*, *72*, 651–660. https://doi.org/10.1016/J.EURPOLYMJ.2015.02.038

Fan, M., Qiang, L., Wang, Y., Liu, Y., Zhuang, H., Guo, R., Ben, Y., Li, Q., & Zheng, P. (2023). 3D bioprinted hydrogel/polymer scaffold with factor delivery and mechanical support for growth plate injury repair. *Frontiers in Bioengineering and Biotechnology*, *11*, 1210786. https://doi.org/10.3389/FBIOE.2023.1210786/BIBTEX

Felfel, R. M., Gideon-Adeniyi, M. J., Zakir Hossain, K. M., Roberts, G. A. F., & Grant, D. M. (2019). Structural, mechanical and swelling characteristics of 3D scaffolds from chitosan-agarose blends. *Carbohydrate Polymers*, *204*, 59–67. https://doi.org/10.1016/J.CARBPOL.2018.10.002

Fereshteh, Z., Fathi, M., Bagri, A., & Boccaccini, A. R. (2016b). Preparation and characterisation of aligned porous PCL/zein scaffolds as drug delivery systems via improved unidirectional freeze-drying method. *Materials Science and Engineering C*, *68*, 613–622. https://doi.org/10.1016/j.msec.2016.06.009

Ferguson, V. L., Bushby, A. J., & Boyde, A. (2003). Nanomechanical properties and mineral concentration in articular calcified cartilage and subchondral bone. *Journal of Anatomy*, *203*(2), 191–202. https://doi.org/10.1046/J.1469-7580.2003.00193.X

Filardo, G., Drobnic, M., Perdisa, F., Kon, E., Hribernik, M., & Marcacci, M. (2014). Fibrin glue improves osteochondral scaffold fixation: study on the human cadaveric knee exposed to continuous passive motion. *Osteoarthritis and Cartilage*, *22*(4), 557–565. https://doi.org/10.1016/J.JOCA.2014.01.004

Filardo, G., Perdisa, F., Gelinsky, M., Despang, F., Fini, M., Marcacci, M., Parrilli, A. P., Roffi, A., Salamanna, F., Sartori, M., Schütz, K., & Kon, E. (2018). Novel alginate biphasic scaffold for osteochondral regeneration: an in vivo evaluation in rabbit and sheep models. *Journal of Materials Science: Materials in Medicine*, *29*(6), 1–13. https://doi.org/10.1007/S10856-018-6074-0/TABLES/4

Fina, F., Gaisford, S., & Basit, A. W. (2018). Powder bed fusion: The working process, current applications and opportunities. *AAPS Advances in the Pharmaceutical Sciences Series*, *31*, 81–105. https://doi.org/10.1007/978-3-319-90755-0_5/COVER

Fischer, R. L., McCoy, M. G., & Grant, S. A. (2012). Electrospinning collagen and hyaluronic acid nanofiber meshes. *Journal of Materials Science: Materials in Medicine*, *23*(7), 1645–1654. https://doi.org/10.1007/s10856-012-4641-3

Flégeau, K., Puiggali-Jou, A., & Zenobi-Wong, M. (2022). Cartilage tissue engineering by extrusion bioprinting utilizing porous hyaluronic acid microgel bioinks. *Biofabrication*, *14*(3), 034105. https://doi.org/10.1088/1758-5090/AC6B58

Fu, L., Yang, Z., Gao, C., Li, H., Yuan, Z., Wang, F., Sui, X., Liu, S., & Guo, Q. (2020). Advances and prospects in biomimetic multilayered scaffolds for articular cartilage regeneration. *Regenerative Biomaterials*, *7*(6), 527–542. https://doi.org/10.1093/RB/RBAA042

Gao, F., Xu, Z., Liang, Q., Liu, B., Li, H., Wu, Y., Zhang, Y., Lin, Z., Wu, M., Ruan, C., Liu, W., Gao, F., Xu, Z., Liu, B., Li, H., Wu, Y., Zhang, Y., Liu, W., Liang, Q., … Ruan, C. (2018). Direct 3D Printing of High Strength Biohybrid Gradient Hydrogel Scaffolds for Efficient Repair of Osteochondral Defect. *Advanced Functional Materials*, *28*(13), 1706644. https://doi.org/10.1002/ADFM.201706644

Gao, J., Chen, S., Tang, D., Jiang, L., Shi, J., & Wang, S. (2019). Mechanical Properties and Degradability of Electrospun PCL/PLGA Blended Scaffolds as Vascular Grafts. *Transactions of Tianjin University*, *25*(2), 152–160. https://doi.org/10.1007/S12209-018-0152-8/FIGURES/6

Gao, J., Ding, X., Yu, X., Chen, X., Zhang, X., Cui, S., Shi, J., Chen, J., Yu, L., Chen, S., Ding, J., Gao, J., Yu, X., Chen, X., Cui, S., Shi, J., Yu, L., Ding, J., Ding, X., … Chen, S. (2021). Cell-Free Bilayered Porous Scaffolds for Osteochondral Regeneration Fabricated by Continuous 3D-Printing Using Nascent Physical Hydrogel as Ink. *Advanced Healthcare Materials*, *10*(3), 2001404. https://doi.org/10.1002/ADHM.202001404

Geng, P., Zhao, J., Wu, W., Ye, W., Wang, Y., Wang, S., & Zhang, S. (2019). Effects of extrusion speed and printing speed on the 3D printing stability of extruded PEEK filament. *Journal of Manufacturing Processes*, *37*, 266–273. https://doi.org/10.1016/J.JMAPRO.2018.11.023

Gerçek, I., Tiğli, R. S., & Gumusderelioglu, M. (2008a). A novel scaffold based on formation and agglomeration of PCL microbeads by freeze-drying. *Journal of Biomedical Materials Research - Part A*, *86*(4), 1012–1022. https://doi.org/10.1002/jbm.a.31723

Gerçek, I., Tiğli, R. S., & Gumusderelioglu, M. (2008b). A novel scaffold based on formation and agglomeration of PCL microbeads by freeze-drying. *Journal of Biomedical Materials Research - Part A*, *86*(4), 1012–1022. https://doi.org/10.1002/jbm.a.31723

Getgood, A. M. J. J., Kew, S. J., Brooks, R., Aberman, H., Simon, T., Lynn, A. K., & Rushton, N. (2012). Evaluation of early-stage osteochondral defect repair using a biphasic scaffold based on a collagen-glycosaminoglycan biopolymer in a caprine model. *Knee*, *19*(4), 422–430. https://doi.org/10.1016/j.knee.2011.03.011

Ghasemi-Mobarakeh, L., Prabhakaran, M. P., Morshed, M., Nasr-Esfahani, M. H., & Ramakrishna, S. (2008). Electrospun poly(ε-caprolactone)/gelatin nanofibrous scaffolds for nerve tissue engineering. *Biomaterials*, *29*(34), 4532–4539. https://doi.org/10.1016/j.biomaterials.2008.08.007

Ghorbani, F., Sahranavard, M., Mousavi Nejad, Z., Li, D., Zamanian, A., & Yu, B. (2020b). Surface Functionalization of Three Dimensional-Printed Polycaprolactone-Bioactive Glass Scaffolds by Grafting GelMA Under UV Irradiation. In *Frontiers in Materials* (Vol. 7). https://doi.org/10.3389/fmats.2020.528590

Gille, J., Behrens, P., Volpi, P., De Girolamo, L., Reiss, E., Zoch, W., & Anders, S. (2013). Outcome of Autologous Matrix Induced Chondrogenesis (AMIC) in cartilage knee surgery: Data of the AMIC Registry. *Archives of Orthopaedic and Trauma Surgery*, *133*(1), 87–93. https://doi.org/10.1007/s00402-012-1621-5

Global RA Network » About Arthritis and RA. (n.d.). Retrieved May 26, 2020, from https://globalranetwork.org/project/disease-info/

Gong, L., Li, J., Zhang, J., Pan, Z., Liu, Y., Zhou, F., Hong, Y., Hu, Y., Gu, Y., Ouyang, H., Zou, X., & Zhang, S. (2020). An interleukin-4-loaded bi-layer 3D printed

scaffold promotes osteochondral regeneration. *Acta Biomaterialia*, *117*, 246–260. https://doi.org/10.1016/J.ACTBIO.2020.09.039

González-González, A. M., Cruz, R., Rosales-Ibáñez, R., Hernández-Sánchez, F., Carrillo-Escalante, H. J., Rodríguez-Martínez, J. J., Velasquillo, C., Talamás-Lara, D., & Ludert, J. E. (2023). In Vitro and In Vivo Evaluation of a Polycaprolactone (PCL)/Polylactic-Co-Glycolic Acid (PLGA) (80:20) Scaffold for Improved Treatment of Chondral (Cartilage) Injuries. *Polymers*, *15*(10). https://doi.org/10.3390/POLYM15102324/S1

Grigore, M. E. (2017a). Biomaterials for Cartilage Tissue Engineering. *Journal of Tissue Science & Engineering*, *08*(01), 4–9. https://doi.org/10.4172/2157-7552.1000192

Gross, R. A., & Kalra, B. (2002). Biodegradable polymers for the environment. *Science*, *297*(5582), 803–807. https://doi.org/10.1126/SCIENCE.297.5582.803/ASSET/F574722D-03B6-4ED9-9117-3EF2634AD946/ASSETS/GRAPHIC/SE3020739002.JPEG

Gu, L., Li, T., Song, X., Yang, X., Li, S., Chen, L., Liu, P., Gong, X., Chen, C., & Sun, L. (2020). Preparation and characterisation of methacrylated gelatin/bacterial cellulose composite hydrogels for cartilage tissue engineering. *Regenerative Biomaterials*, *7*(2), 195–202. https://doi.org/10.1093/rb/rbz050

Gu, X., Zha, Y., Li, Y., Chen, J., Liu, S., Du, Y., Zhang, S., & Wang, J. (2022a). Integrated polycaprolactone microsphere-based scaffolds with biomimetic hierarchy and tunable vascularization for osteochondral repair. *Acta Biomaterialia*, *141*, 190–197. https://doi.org/10.1016/J.ACTBIO.2022.01.021

Gupta, H. S., Schratter, S., Tesch, W., Roschger, P., Berzlanovich, A., Schoeberl, T., Klaushofer, K., & Fratzl, P. (2005). Two different correlations between nanoindentation modulus and mineral content in the bone-cartilage interface. *Journal of Structural Biology*, *149*(2), 138–148. https://doi.org/10.1016/J.JSB.2004.10.010

Haaparanta, A. (2016). *Highly Porous Freeze-Dried Composite Scaffolds for Cartilage and Osteochondral Tissue Engineering* (Issue 2015).

Han, Y., Lian, M., Zhang, C., Jia, B., Wu, Q., Sun, B., Qiao, Z., Sun, B., & Dai, K. (2022). Study on bioactive PEGDA/ECM hybrid bi-layered hydrogel scaffolds fabricated by electro-writing for cartilage regeneration. *Applied Materials Today*, *28*, 101547. https://doi.org/10.1016/J.APMT.2022.101547

Hargrave-Thomas, E., van Sloun, F., Dickinson, M., Broom, N., & Thambyah, A. (2015). Multi-scalar mechanical testing of the calcified cartilage and subchondral bone comparing healthy vs early degenerative states. *Osteoarthritis and Cartilage*, *23*(10), 1755–1762. https://doi.org/10.1016/J.JOCA.2015.05.012

Heuijerjans, A., Wilson, W., Ito, K., & van Donkelaar, C. C. (2018). Osteochondral resurfacing implantation angle is more important than implant material stiffness. *Journal of Orthopaedic Research*, *36*(11), 2911. https://doi.org/10.1002/JOR.24101

Hiep, N. T., & Lee, B. T. (2010). Electro-spinning of PLGA/PCL blends for tissue engineering and their biocompatibility. *Journal of Materials Science: Materials in Medicine*, *21*(6), 1969–1978. https://doi.org/10.1007/S10856-010-4048-Y/FIGURES/9

Hoffman, A. S. (2012). Hydrogels for biomedical applications. *Advanced Drug Delivery Reviews*, *64*(SUPPL.), 18–23. https://doi.org/10.1016/J.ADDR.2012.09.010

Hollister, S. J. (2005). Porous scaffold design for tissue engineering. *Nature Materials 2005 4:7*, *4*(7), 518–524. https://doi.org/10.1038/nmat1421

Holmes, B., Zhu, W., Li, J., Lee, J. D., & Zhang, L. G. (2014). Development of Novel Three-Dimensional Printed Scaffolds for Osteochondral Regeneration. *Https://Home.Liebertpub.Com/Tea*, *21*(1–2), 403–415. https://doi.org/10.1089/TEN.TEA.2014.0138

Howell, M., Liao, Q., & Gee, C. W. (2021). Surgical Management of Osteochondral Defects of the Knee: An Educational Review. *Current Reviews in Musculoskeletal Medicine*, *14*(1), 60–66. https://doi.org/10.1007/S12178-020-09685-1/FIGURES/3

Hu, M. Y., & Nukavarapu, S. (2019). Scaffolds for cartilage tissue engineering. In *Handbook of Tissue Engineering Scaffolds: Volume One*. Elsevier Ltd. https://doi.org/10.1016/B978-0-08-102563-5.00011-3

Huang, A., Jiang, Y., Napiwocki, B., Mi, H., Peng, X., & Turng, L.-S. (2017). Fabrication of poly(ε-caprolactone) tissue engineering scaffolds with fibrillated and interconnected pores utilizing microcellular injection molding and polymer leaching. *RSC Advances*, *7*(69), 43432–43444. https://doi.org/10.1039/C7RA06987A

Hutmacher, D. W., Schantz, T., Zein, I., Ng, K. W., Teoh, S. H., & Tan, K. C. (2001). *Mechanical properties and cell cultural response of polycaprolactone scaffolds designed and fabricated via fused deposition modeling*. https://doi.org/10.1002/1097-4636

Ikada, Y., & Tsuji, H. (2000). Biodegradable polyesters for medical and ecological applications. *Macromol. Rapid Commun*, *21*, 117–132. https://doi.org/10.1002/(SICI)1521-3927(20000201)21:3

Im, G. Il, & Lee, J. H. (2010). Repair of osteochondral defects with adipose stem cells and a dual growth factor-releasing scaffold in rabbits. *Journal of Biomedical Materials Research - Part B Applied Biomaterials*, *92*(2), 552–560. https://doi.org/10.1002/jbm.b.31552

Imhof, Prof. Dr. H., Breitenseher, P. . Dr. M., Kainberger, Prof. Dr. F., T., R., & Trattning, Prof. Dr. S. (1999). Importance of Subchondral Bone to Articular Cartilagein Health and Disease. *Topics in Llagnetic Resononce Imaging*, *Lippincott*, 180–192.

Inzana, J. A., Olvera, D., Fuller, S. M., Kelly, J. P., Graeve, O. A., Schwarz, E. M., Kates, S. L., & Awad, H. A. (2014). 3D printing of composite calcium phosphate and collagen scaffolds for bone regeneration. *Biomaterials*, *35*(13), 4026–4034. https://doi.org/10.1016/J.BIOMATERIALS.2014.01.064

Isobe, N., Kimura, S., Wada, M., & Deguchi, S. (2018). Poroelasticity of cellulose hydrogel. *Journal of the Taiwan Institute of Chemical Engineers*, *92*, 118–122. https://doi.org/10.1016/J.JTICE.2018.02.017

Janmohammadi, M., & Nourbakhsh, M. S. (2019). Electrospun polycaprolactone scaffolds for tissue engineering: a review. *International Journal of Polymeric Materials and Polymeric Biomaterials*, *68*(9), 527–539. https://doi.org/10.1080/00914037.2018.1466139

Janoušková, O. (2018). Synthetic polymer scaffolds for soft tissue engineering. *Physiological Research*, *67*, s335–s348. https://doi.org/10.33549/PHYSIOLRES.933983

Jeon, J. E., Vaquette, C., Klein, T. J., & Hutmacher, D. W. (2014). Perspectives in Multiphasic Osteochondral Tissue Engineering. *The Anatomical Record*, *297*(1), 26–35. https://doi.org/10.1002/ar.22795

Jia, S., Wang, J., Zhang, T., Pan, W., Li, Z., He, X., Yang, C., Wu, Q., Sun, W., Xiong, Z., & Hao, D. (2018a). Multilayered Scaffold with a Compact Interfacial Layer Enhances Osteochondral Defect Repair [Research-article]. *ACS Applied Materials and Interfaces*, *10*(24), 20296–20305. https://doi.org/10.1021/acsami.8b03445

Jian, Z., Zhuang, T., Qinyu, T., Liqing, P., Kun, L., Xujiang, L., Diaodiao, W., Zhen, Y., Shuangpeng, J., Xiang, S., Jingxiang, H., Shuyun, L., Libo, H., Peifu, T., Qi, Y., & Quanyi, G. (2020). 3D bioprinting of a biomimetic meniscal scaffold for application in tissue engineering. *Bioactive Materials*, *6*(6), 1711–1726. https://doi.org/10.1016/J.BIOACTMAT.2020.11.027

Jiang, G., Li, S., Yu, K., He, B., Hong, J., Xu, T., Meng, J., Ye, C., Chen, Y., Shi, Z., Feng, G., Chen, W., Yan, S., He, Y., & Yan, R. (2021). A 3D-printed PRP-GelMA hydrogel promotes osteochondral regeneration through M2 macrophage polarization in a rabbit model. *Acta Biomaterialia*. https://doi.org/10.1016/j.actbio.2021.04.010

Jo, S. Y., Lee, J. U., Lee, H., Ryu, D., & Kim, G. H. (2023). The one-step fabrication of porous hASC-laden GelMa constructs using a handheld printing system. *Npj Regenerative Medicine 2023 8:1*, *8*(1), 1–16. https://doi.org/10.1038/s41536-023-00307-1

Joyce, M., Hodgkinson, T., Lemoine, M., González-Vázquez, A., Kelly, D. J., & O'brien, F. J. (2023). DEVELOPMENT OF A 3D-PRINTED

BIOABSORBABLE COMPOSITE SCAFFOLD WITH MECHANICAL PROPERTIES SUITABLE FOR TREATING LARGE, LOAD-BEARING ARTICULAR CARTILAGE DEFECTS. *European Cells and Materials*, *45*, 158–172. https://doi.org/10.22203/eCM.v045a11

Jurvelin, J. S., Buschmann, M. D., & Hunziker, E. B. (2003). Mechanical anisotropy of the human knee articular cartilage in compression. *Http://Dx.Doi.Org/10.1243/095441103765212712*, *217*(3), 215–219. https://doi.org/10.1243/095441103765212712

Kabir, W., Di Bella, C., Choong, P. F. M., & O'Connell, C. D. (2021). Assessment of Native Human Articular Cartilage: A Biomechanical Protocol. *Cartilage*, *13*(2_suppl), 427S-437S. https://doi.org/10.1177/1947603520973240/ASSET/IMAGES/LARGE/10.1177_1947603520973240-FIG4.JPEG

Kang, H. W., Lee, S. J., Ko, I. K., Kengla, C., Yoo, J. J., & Atala, A. (2016). A 3D bioprinting system to produce human-scale tissue constructs with structural integrity. *Nature Biotechnology*, *34*(3), 312–319. https://doi.org/10.1038/nbt.3413

Kauppinen, S., Karhula, S. S., Thevenot, J., Ylitalo, T., Rieppo, L., Kestilä, I., Haapea, M., Hadjab, I., Finnilä, M. A., Quenneville, E., Garon, M., Gahunia, H. K., Pritzker, K. P. H., Buschmann, M. D., Saarakkala, S., & Nieminen, H. J. (2019). 3D morphometric analysis of calcified cartilage properties using micro-computed tomography. *Osteoarthritis and Cartilage*, *27*(1), 172–180. https://doi.org/10.1016/j.joca.2018.09.009

Kesti, M., Eberhardt, C., Pagliccia, G., Kenkel, D., Grande, D., Boss, A., & Zenobi-Wong, M. (2015). Bioprinting Complex Cartilaginous Structures with Clinically Compliant Biomaterials. *Advanced Functional Materials*, *25*(48), 7406–7417. https://doi.org/10.1002/ADFM.201503423

Khanarian, N. T., Haney, N. M., Burga, R. A., & Lu, H. H. (2012). A functional agarose-hydroxyapatite scaffold for osteochondral interface regeneration. *Biomaterials*, *33*(21), 5247–5258. https://doi.org/10.1016/j.biomaterials.2012.03.076

Kichloo, A. F., Raina, A., Haq, M. I. U., & Wani, M. S. (2022). Impact of Carbon Fiber Reinforcement on Mechanical and Tribological Behavior of 3D-Printed Polyethylene Terephthalate Glycol Polymer Composites—An Experimental Investigation. *Journal of Materials Engineering and Performance*, *31*(2), 1021–1038. https://doi.org/10.1007/S11665-021-06262-6

Kilian, D., Ahlfeld, T., Akkineni, A. R., Bernhardt, A., Gelinsky, M., & Lode, A. (2020). 3D Bioprinting of osteochondral tissue substitutes – in vitro-chondrogenesis in multi-layered mineralized constructs. *Scientific Reports*, *10*(1), 8277. https://doi.org/10.1038/s41598-020-65050-9

Kim, H.-W., Lee, H.-H., & Knowles, J. C. (2006). Electrospinning biomedical nanocomposite fibers of hydroxyapatite/poly(lactic acid) for bone regeneration. *Journal of Biomedical Materials Research Part A*, *79A*(3), 643–649. https://doi.org/10.1002/jbm.a.30866

Kim, H.-W. W., Yu, H.-S. S., & Lee, H.-H. H. (2008). Nanofibrous matrices of poly(lactic acid) and gelatin polymeric blends for the improvement of cellular responses. *Journal of Biomedical Materials Research - Part A*, *87*(1), 25–32. https://doi.org/10.1002/jbm.a.31677

Kingsbury, S. R., Gross, H. J., Isherwood, G., & Conaghan, P. G. (n.d.). *Osteoarthritis in Europe: impact on health status, work productivity and use of pharmacotherapies in five European countries*. https://doi.org/10.1093/rheumatology/ket463

Kiviranta, P., Lammentausta, E., Töyräs, J., Kiviranta, I., & Jurvelin, J. S. (2008). Indentation diagnostics of cartilage degeneration. *Osteoarthritis and Cartilage*, *16*(7), 796–804. https://doi.org/10.1016/J.JOCA.2007.10.016

Kogan, G., Šoltés, L., Stern, R., & Gemeiner, P. (2007). Hyaluronic acid: A natural biopolymer with a broad range of biomedical and industrial applications. *Biotechnology Letters*, *29*(1), 17–25. https://doi.org/10.1007/s10529-006-9219-z

Koh, Y.-G. G., Lee, J.-A. A., Kim, Y. S., Lee, H. Y., Kim, H. J., & Kang, K.-T. T. (2019). Optimal mechanical properties of a scaffold for cartilage regeneration

using finite element analysis. *Journal of Tissue Engineering*, *10*, 204173141983213. https://doi.org/10.1177/2041731419832133

Kolambkar, Y. M., Dupont, K. M., Boerckel, J. D., Huebsch, N., Mooney, D. J., Hutmacher, D. W., & Guldberg, R. E. (2011). An alginate-based hybrid system for growth factor delivery in the functional repair of large bone defects. *Biomaterials*, *32*(1), 65–74. https://doi.org/10.1016/j.biomaterials.2010.08.074

Korhonen, R. K., Laasanen, M. S., Töyräs, J., Rieppo, J., Hirvonen, J., Helminen, H. J., & Jurvelin, J. S. (2002). Comparison of the equilibrium response of articular cartilage in unconfined compression, confined compression and indentation. *Journal of Biomechanics*, *35*(7), 903–909. https://doi.org/10.1016/S0021-9290(02)00052-0

Korpayev, S., Kaygusuz, G., Şen, M., Orhan, K., Oto, Ç., & Karakeçili, A. (2020). Chitosan/collagen based biomimetic osteochondral tissue constructs: A growth factor-free approach. *International Journal of Biological Macromolecules*, *156*, 681–690. https://doi.org/10.1016/j.ijbiomac.2020.04.109

Kosik-Kozioł, A., Costantini, M., Bolek, T., Szöke, K., Barbetta, A., Brinchmann, J., & Święszkowski, W. (2017). PLA short sub-micron fiber reinforcement of 3D bioprinted alginate constructs for cartilage regeneration. *Biofabrication*, *9*(4), 044105.

Kosik-Kozioł, A., Costantini, M., Mróz, A., Idaszek, J., Heljak, M., Jaroszewicz, J., Kijeńska, E., Szöke, K., Frerker, N., Barbetta, A., Brinchmann, J. E., & Święszkowski, W. (2019). *3D bioprinted hydrogel model incorporating β-tricalcium phosphate for calcified cartilage tissue engineering*. https://doi.org/10.1088/1758-5090/ab15cb

Kosik-Kozioł, A., Heljak, M., & Święszkowski, W. (2020a). Mechanical properties of hybrid triphasic scaffolds for osteochondral tissue engineering. *Materials Letters*, *261*. https://doi.org/10.1016/j.matlet.2019.126893

Kwak, S., Haider, A., Gupta, K. C., Kim, S., & Kang, I.-K. K. (2016). Micro/Nano Multilayered Scaffolds of PLGA and Collagen by Alternately Electrospinning for

Bone Tissue Engineering. *Nanoscale Research Letters*, *11*(1), 323. https://doi.org/10.1186/s11671-016-1532-4

Labet, M., & Thielemans, W. (2009). Synthesis of polycaprolactone: a review. *Chemical Society Reviews*, *38*(12), 3484–3504. https://doi.org/10.1039/B820162P

Landínez-Parra, N. S., Garzón-Alvarado, D. A., Vanegas-Acosta, J. C., Landínez-Parra, N. S., Garzón-Alvarado, D. A., & Vanegas-Acosta, J. C. (2012). Mechanical Behavior of Articular Cartilage. *Injury and Skeletal Biomechanics*. https://doi.org/10.5772/48323

Lausch, A. J., Chong, L. C., Uludag, H., & Sone, E. D. (2018a). Multiphasic Collagen Scaffolds for Engineered Tissue Interfaces. *Advanced Functional Materials*, *28*(48), 1804730. https://doi.org/10.1002/adfm.201804730

Lee, E. J., Kasper, F. K., & Mikos, A. G. (2014). Biomaterials for Tissue Engineering. *Annals of Biomedical Engineering*, *42*(2), 323. https://doi.org/10.1007/S10439-013-0859-6

Lee, K. W., Wang, S., Fox, B. C., Ritman, E. L., Yaszemski, M. J., & Lu, L. (2007). Poly(propylene fumarate) bone tissue engineering scaffold fabrication using stereolithography: Effects of resin formulations and laser parameters. *Biomacromolecules*, *8*(4), 1077–1084. https://doi.org/10.1021/bm060834v

Lee, K. Y., & Mooney, D. J. (2012). Alginate: Properties and biomedical applications. *Progress in Polymer Science (Oxford)*, *37*(1), 106–126. https://doi.org/10.1016/j.progpolymsci.2011.06.003

Lee, M., & Wu, B. M. (2012). Recent advances in 3D printing of tissue engineering scaffolds. *Methods in Molecular Biology (Clifton, N.J.)*, *868*, 257–267. https://doi.org/10.1007/978-1-61779-764-4_15

Lee, W. D., Hurtig, M. B., Pilliar, R. M., Stanford, W. L., & Kandel, R. A. (2015). Engineering of hyaline cartilage with a calcified zone using bone marrow stromal cells. *Osteoarthritis and Cartilage*, *23*(8), 1307–1315. https://doi.org/10.1016/j.joca.2015.04.010

Leng, P., Ding, C. R., Zhang, H. N., & Wang, Y. Z. (2012). Reconstruct large osteochondral defects of the knee with hIGF-1 gene enhanced Mosaicplasty. *Knee*, *19*(6), 804–811. https://doi.org/10.1016/j.knee.2012.03.009

Levett, P. A., Melchels, F. P. W., Schrobback, K., Hutmacher, D. W., Malda, J., & Klein, T. J. (2014). A biomimetic extracellular matrix for cartilage tissue engineering centered on photocurable gelatin, hyaluronic acid and chondroitin sulfate. *Acta Biomaterialia*, *10*(1), 214–223. https://doi.org/10.1016/J.ACTBIO.2013.10.005

Levingstone, T. J., Matsiko, A., Dickson, G. R., O'Brien, F. J., & Gleeson, J. P. (2014). A biomimetic multi-layered collagen-based scaffold for osteochondral repair. *Acta Biomaterialia*, *10*(5), 1996–2004. https://doi.org/10.1016/j.actbio.2014.01.005

Levingstone, T. J., Ramesh, A., Brady, R. T., Brama, P. A. J., Kearney, C., Gleeson, J. P., & O'Brien, F. J. (2016). Cell-free multi-layered collagen-based scaffolds demonstrate layer specific regeneration of functional osteochondral tissue in caprine joints. *Biomaterials*, *87*, 69–81. https://doi.org/10.1016/j.biomaterials.2016.02.006

Levingstone, T. J., Thompson, E., Matsiko, A., Schepens, A., Gleeson, J. P., & O'brien, F. J. (2016a). Multi-layered collagen-based scaffolds for osteochondral defect repair in rabbits. *Acta Biomaterialia*, *32*, 149–160. https://doi.org/10.1016/j.actbio.2015.12.034

Levingstone, T. J., Thompson, E., Matsiko, A., Schepens, A., Gleeson, J. P., & O'brien, F. J. (2016c). Multi-layered collagen-based scaffolds for osteochondral defect repair in rabbits. *Acta Biomaterialia*, *32*, 149–160. https://doi.org/10.1016/j.actbio.2015.12.034

Li, H., Yin, Y., Xiang, Y., Liu, H., & Guo, R. (2020c). A novel 3D printing PCL/GelMA scaffold containing USPIO for MRI-guided bile duct repair. *Biomedical Materials*, *15*(4), 045004. https://doi.org/10.1088/1748-605X/AB797A

Li, X., Ding, J., Wang, J., Zhuang, X., & Chen, X. (2015). Biomimetic biphasic scaffolds for osteochondral defect repair. *Regenerative Biomaterials*, *2*(3), 221–228. https://doi.org/10.1093/rb/rbv015

Liang, X., Duan, P., Gao, J., Guo, R., Qu, Z., Li, X., He, Y., Yao, H., & Ding, J. (2018a). Bilayered PLGA/PLGA-HAp Composite Scaffold for Osteochondral Tissue Engineering and Tissue Regeneration. *ACS Biomaterials Science and Engineering*, *4*(10), 3506–3521. https://doi.org/10.1021/ACSBIOMATERIALS.8B00552/ASSET/IMAGES/LARGE/AB-2018-005524_0010.JPEG

Lin, H., Zhang, D., Alexander, P. G., Yang, G., Tan, J., Cheng, A. W. M., & Tuan, R. S. (2013). Application of visible light-based projection stereolithography for live cell-scaffold fabrication with designed architecture. *Biomaterials*, *34*(2), 331–339. https://doi.org/10.1016/J.BIOMATERIALS.2012.09.048

Lin, X., Chen, J., Qiu, P., Zhang, Q., Wang, S., Su, M., Chen, Y., Jin, K., Qin, A., Fan, S., Chen, P., & Zhao, X. (2018). Biphasic hierarchical extracellular matrix scaffold for osteochondral defect regeneration. *Osteoarthritis and Cartilage*, *26*(3), 433–444. https://doi.org/10.1016/j.joca.2017.12.001

Little, C. J., Bawolin, N. K., & Chen, X. (2011). Mechanical properties of natural cartilage and tissue-engineered constructs. *Tissue Engineering - Part B: Reviews*, *17*(4), 213–227. https://doi.org/10.1089/ten.teb.2010.0572

Liu, F., Zhang, D. Z., Zhang, P., Zhao, M., & Jafar, S. (2018). Mechanical properties of optimized diamond lattice structure for bone scaffolds fabricated via selective laser melting. *Materials*, *11*(3). https://doi.org/10.3390/ma11030374

Liu, J., Li, L., Suo, H., Yan, M., Yin, J., & Fu, J. (2019a). 3D printing of biomimetic multi-layered GelMA/nHA scaffold for osteochondral defect repair. *Materials and Design*, *171*, 107708. https://doi.org/10.1016/j.matdes.2019.107708

Liu, J., Li, L., Suo, H., Yan, M., Yin, J., & Fu, J. (2019c). 3D printing of biomimetic multi-layered GelMA/nHA scaffold for osteochondral defect repair. *Materials & Design*, *171*, 107708. https://doi.org/10.1016/J.MATDES.2019.107708

Liu, K. Q., Liu, Y. N., Duan, Z. G., Ma, X. X., & Fan, D. Di. (2020). A biomimetic bi-layered tissue engineering scaffolds for osteochondral defects repair. *Science China Technological Sciences*. https://doi.org/10.1007/s11431-020-1597-4

Liu, M., Yu, X., Huang, F., Cen, S., Zhong, G., & Xiang, Z. (2013). Tissue engineering stratified scaffolds for articular cartilage and subchondral bone defects repair. *Orthopedics*, *36*(11), 868–873. https://doi.org/10.3928/01477447-20131021-10

Liu, W., Heinrich, M. A., Zhou, Y., Akpek, A., Hu, N., Liu, X., Guan, X., Zhong, Z., Jin, X., Khademhosseini, A., & Zhang, Y. S. (2017). Extrusion Bioprinting of Shear-Thinning Gelatin Methacryloyl Bioinks. *Advanced Healthcare Materials*, *6*(12), 1601451. https://doi.org/10.1002/adhm.201601451

Liu, W., Madry, H., & Cucchiarini, M. (2022). Application of Alginate Hydrogels for Next-Generation Articular Cartilage Regeneration. *International Journal of Molecular Sciences*, *23*(3). https://doi.org/10.3390/IJMS23031147

Liu, W., Zhong, Z., Hu, N., Zhou, Y., Maggio, L., Miri, A. K., Fragasso, A., Jin, X., Khademhosseini, A., & Zhang, Y. S. (2018a). Coaxial extrusion bioprinting of 3D microfibrous constructs with cell-favorable gelatin methacryloyl microenvironments. *Biofabrication*, *10*(2), 024102. https://doi.org/10.1088/1758-5090/aa9d44

Liu, X., Liu, S., Liu, S., & Cui, W. (2014). Evaluation of oriented electrospun fibers for periosteal flap regeneration in biomimetic triphasic osteochondral implant. *Journal of Biomedical Materials Research Part B: Applied Biomaterials*, *102*(7), 1407–1414. https://doi.org/10.1002/jbm.b.33119

Logli, A. L., Bernard, C. D., O'Driscoll, S. W., Sanchez-Sotelo, J., Morrey, M. E., Krych, A. J., & Camp, C. L. (2019). Osteochondritis dissecans lesions of the capitellum in overhead athletes: a review of current evidence and proposed treatment algorithm. *Current Reviews in Musculoskeletal Medicine*, *12*(1), 1–12. https://doi.org/10.1007/S12178-019-09528-8/FIGURES/5

Lopa, S., & Madry, H. (2014). Bioinspired Scaffolds for Osteochondral Regeneration. *Https://Home.Liebertpub.Com/Tea*, *20*(15–16), 2052–2076. https://doi.org/10.1089/TEN.TEA.2013.0356

Loy, B. N., Zimel, M., Gowda, A. L., Tooley, T. R., Maerz, T., Bicos, J., & Guettler, J. (2018). A Biomechanical and Structural Comparison of Articular Cartilage and Subchondral Bone of the Glenoid and Humeral Head. *Orthopaedic Journal of Sports Medicine*, *6*(7), 2325967118785854. https://doi.org/10.1177/2325967118785854

Lozano, R., Stevens, L., Thompson, B. C., Gilmore, K. J., Gorkin, R., Stewart, E. M., in het Panhuis, M., Romero-Ortega, M., & Wallace, G. G. (2015). 3D printing of layered brain-like structures using peptide modified gellan gum substrates. *Biomaterials*, *67*, 264–273. https://doi.org/10.1016/J.BIOMATERIALS.2015.07.022

Lyons, T. J., Stoddart, R. W., McClure, S. F., & McClure, J. (2005). The tidemark of the chondro-osseous junction of the normal human knee joint. *Journal of Molecular Histology*, *36*(3), 207–215. https://doi.org/10.1007/s10735-005-3283-x

Madry, H., van Dijk, C. N., & Mueller-Gerbl, M. (2010a). The basic science of the subchondral bone. *Knee Surgery, Sports Traumatology, Arthroscopy*, *18*(4), 419–433. https://doi.org/10.1007/s00167-010-1054-z

Makris, E. A., Gomoll, A. H., Malizos, K. N., Hu, J. C., & Athanasiou, K. A. (2015). Repair and tissue engineering techniques for articular cartilage. *Nature Reviews. Rheumatology*, *11*(1), 21. https://doi.org/10.1038/NRRHEUM.2014.157

Malekpour, A., & Chen, X. (2022). Printability and Cell Viability in Extrusion-Based Bioprinting from Experimental, Computational, and Machine Learning Views. *Journal of Functional Biomaterials*, *13*(2). https://doi.org/10.3390/JFB13020040

Mani, M. P., Sadia, M., Jaganathan, S. K., Khudzari, A. Z., Supriyanto, E., Saidin, S., Ramakrishna, S., Ismail, A. F., & Faudzi, A. A. M. (2022). A review on 3D printing in tissue engineering applications. *Journal of Polymer Engineering*, *42*(3), 243–265. https://doi.org/10.1515/POLYENG-2021-0059/ASSET/GRAPHIC/J_POLYENG-2021-0059_FIG_004.JPG

Marcelino, P., Silva, J. C., Moura, C. S., Meneses, J., Cordeiro, R., Alves, N., Pascoal-Faria, P., & Ferreira, F. C. (2023). A Novel Approach for Design and

Manufacturing of Curvature-Featuring Scaffolds for Osteochondral Repair. *Polymers*, *15*(9), 2129. https://doi.org/10.3390/POLYM15092129/S1

Markstedt, K., Mantas, A., Tournier, I., Martínez Ávila, H., Hägg, D., & Gatenholm, P. (2015). 3D Bioprinting Human Chondrocytes with Nanocellulose-Alginate Bioink for Cartilage Tissue Engineering Applications. *Biomacromolecules*, *16*(5), 1489–1496. https://doi.org/10.1021/ACS.BIOMAC.5B00188

Marras-Marquez, T., Peña, J., & Veiga-Ochoa, M. D. (2014). Agarose drug delivery systems upgraded by surfactants inclusion: Critical role of the pore architecture. *Carbohydrate Polymers*, *103*(1), 359–368. https://doi.org/10.1016/j.carbpol.2013.12.026

Matsiko, A., Levingstone, T. J., O'Brien, F. J., & Gleeson, J. P. (2012). Addition of hyaluronic acid improves cellular infiltration and promotes early-stage chondrogenesis in a collagen-based scaffold for cartilage tissue engineering. *Journal of the Mechanical Behavior of Biomedical Materials*, *11*, 41–52. https://doi.org/10.1016/j.jmbbm.2011.11.012

Meng, Z., He, J., Cai, Z., Wang, F., Zhang, J., Wang, L., Ling, R., & Li, D. (2020). Design and additive manufacturing of flexible polycaprolactone scaffolds with highly-tunable mechanical properties for soft tissue engineering. *Materials & Design*, *189*, 108508. https://doi.org/10.1016/J.MATDES.2020.108508

Mente, P. L., & Lewis, J. L. (1994). Elastic modulus of calcified cartilage is an order of magnitude less than that of subchondral bone. *Journal of Orthopaedic Research : Official Publication of the Orthopaedic Research Society*, *12*(5), 637–647. https://doi.org/10.1002/JOR.1100120506

Monroy, D. A. P., Bravo, J. M. C., Mercado, I. E. S., & Gómez, L. J. V. (2018). Gelatin and Collagen Nanofiber Scaffolds for Tissue Engineering. In *Tissue Regeneration*. InTech. https://doi.org/10.5772/intechopen.73316

Munir, N., & Callanan, A. (2018). Novel phase separated polycaprolactone/collagen scaffolds for cartilage tissue engineering. *Biomedical Materials (Bristol)*, *13*(5), 051001. https://doi.org/10.1088/1748-605X/aac91f

Naghieh, S., Foroozmehr, E., Badrossamay, M., & Kharaziha, M. (2017). Combinational processing of 3D printing and electrospinning of hierarchical poly(lactic acid)/gelatin-forsterite scaffolds as a biocomposite: Mechanical and biological assessment. *Materials & Design*, *133*, 128–135. https://doi.org/10.1016/J.MATDES.2017.07.051

Naing, M. W., Chua, C. K., Leong, K. F., & Wang, Y. (2005). Fabrication of customised scaffolds using computer-aided design and rapid prototyping techniques. *Rapid Prototyping Journal*, *11*(4), 249–259. https://doi.org/10.1108/13552540510612938

Natarajan, A., Sivadas, V. P., & Nair, P. D. (2021). 3D-printed biphasic scaffolds for the simultaneous regeneration of osteochondral tissues. *Biomedical Materials*, *16*(5), 054102. https://doi.org/10.1088/1748-605X/AC14CB

Nava, M. M., Draghi, L., Giordano, C., & Pietrabissa, R. (2016). The effect of scaffold pore size in cartilage tissue engineering. *Journal of Applied Biomaterials and Functional Materials*, *14*(3), e223–e229. https://doi.org/10.5301/jabfm.5000302

Neill, S. O. (2016). *Mechanical Evaluation of 3D Printed Scaffolds for Articular Cartilage Tissue Engineering*. *September*. http://www.tcd.ie/calendar

Nichol, J. W., Koshy, S. T., Bae, H., Hwang, C. M., Yamanlar, S., & Khademhosseini, A. (2010). Cell-laden microengineered gelatin methacrylate hydrogels. *Biomaterials*, *31*(21), 5536–5544. https://doi.org/10.1016/J.BIOMATERIALS.2010.03.064

Nie, H., & Wang, C. H. (2007). Fabrication and characterisation of PLGA/HAp composite scaffolds for delivery of BMP-2 plasmid DNA. *Journal of Controlled Release*, *120*(1–2), 111–121. https://doi.org/10.1016/j.jconrel.2007.03.018

Niu, X., Li, N., Du, Z., & Li, X. (2023). Integrated gradient tissue-engineered osteochondral scaffolds: Challenges, current efforts and future perspectives. *Bioactive Materials*, *20*, 574–597. https://doi.org/10.1016/J.BIOACTMAT.2022.06.011

Nooeaid, P., Roether, J. A., Weber, E., Schubert, D. W., & Boccaccini, A. R. (2014). Technologies for Multilayered Scaffolds Suitable for Interface Tissue Engineering. *Advanced Engineering Materials*, *16*(3), 319–327. https://doi.org/10.1002/ADEM.201300072

Nooeaid, P., Salih, V., Beier, J. P., & Boccaccini, A. R. (2012a). Osteochondral tissue engineering: Scaffolds, stem cells and applications. *Journal of Cellular and Molecular Medicine*, *16*(10), 2247–2270. https://doi.org/10.1111/j.1582-4934.2012.01571.x

Nowicki, M., Zhu, W., Sarkar, K., Rao, R., & Zhang, L. G. (2020). 3D printing multiphasic osteochondral tissue constructs with nano to micro features via PCL based bioink. *Bioprinting*, *17*, e00066. https://doi.org/10.1016/J.BPRINT.2019.E00066

Nukavarapu, S. P., & Dorcemus, D. L. (2013a). Osteochondral tissue engineering: Current strategies and challenges. *Biotechnology Advances*, *31*(5), 706–721. https://doi.org/10.1016/j.biotechadv.2012.11.004

O'Brien, F., Gleeson, J., & Plunkett, N. (2008). *Collagen/hydroxyapatite composite scaffold, and process for the production thereof.* (Patent WO 2008/096334 A2).

O'Connell, C. D., Zhang, B., Onofrillo, C., Duchi, S., Blanchard, R., Quigley, A., Bourke, J., Gambhir, S., Kapsa, R., Di Bella, C., Choong, P., & Wallace, G. G. (2018). Tailoring the mechanical properties of gelatin methacryloyl hydrogels through manipulation of the photocrosslinking conditions. *Soft Matter*, *14*(11), 2142–2151. https://doi.org/10.1039/C7SM02187A

Osteochondritis Dissecans - OrthoInfo - AAOS. (n.d.). Retrieved May 27, 2020, from https://orthoinfo.aaos.org/en/diseases--conditions/osteochondritis-dissecans/

Pan, Y., Zhou, C., & Chen, Y. (2012). A fast mask projection stereolithography process for fabricating digital models in minutes. *Journal of Manufacturing Science and Engineering*, *134*(5). https://doi.org/10.1115/1.4007465/474915

Panjapheree, K., Kamonmattayakul, S., & Meesane, J. (2018). Biphasic scaffolds of silk fibroin film affixed to silk fibroin/chitosan sponge based on surgical design

for cartilage defect in osteoarthritis. *Materials and Design*, *141*, 323–332. https://doi.org/10.1016/j.matdes.2018.01.006

Parisi, C., Salvatore, L., Veschini, L., Serra, M. P., Hobbs, C., Madaghiele, M., Sannino, A., & Di Silvio, L. (2020). Biomimetic gradient scaffold of collagen–hydroxyapatite for osteochondral regeneration. *Journal of Tissue Engineering*, *11*, 204173141989606. https://doi.org/10.1177/2041731419896068

Patel, J. M., Wise, B. C., Bonnevie, E. D., & Mauck, R. L. (2019). A Systematic Review and Guide to Mechanical Testing for Articular Cartilage Tissue Engineering. *Tissue Engineering. Part C, Methods*, *25*(10), 593. https://doi.org/10.1089/TEN.TEC.2019.0116

Patrício, T., Domingos, M., Gloria, A., D'Amora, U., Coelho, J. F. F., & Bártolo, P. J. J. (2014). Fabrication and characterisation of PCL and PCL/PLA scaffolds for tissue engineering. *Rapid Prototyping Journal*, *20*(2), 145–156. https://doi.org/10.1108/RPJ-04-2012-0037

Peng, C., Zheng, J., Chen, D., Zhang, X., Deng, L., Chen, Z., & Wu, L. (2018). Response of hPDLSCs on 3D printed PCL/PLGA composite scaffolds in vitro. *Molecular Medicine Reports*, *18*(2), 1335–1344. https://doi.org/10.3892/MMR.2018.9076/HTML

Pepelanova, I., Kruppa, K., Scheper, T., & Lavrentieva, A. (2018a). Gelatin-methacryloyl (GelMA) hydrogels with defined degree of functionalization as a versatile toolkit for 3D cell culture and extrusion bioprinting. *Bioengineering*, *5*(3), 55. https://doi.org/10.3390/bioengineering5030055

Pereira, D. R., Reis, R. L., & Oliveira, J. M. (2018). Layered Scaffolds for Osteochondral Tissue Engineering. In *Advances in Experimental Medicine and Biology* (Vol. 1058, pp. 193–218). Springer New York LLC. https://doi.org/10.1007/978-3-319-76711-6_9

Pérez-Silos, V., Moncada-Saucedo, N. K., Peña-Martínez, V., Lara-Arias, J., Marino-Martínez, I. A., Camacho, A., Romero-Díaz, V. J., Lara Banda, M., García-Ruiz, A., Soto-Dominguez, A., Rodriguez-Rocha, H., López-Serna, N., Tuan, R. S., Lin, H., & Fuentes-Mera, L. (2019). A Cellularized Biphasic Implant Based on a

Bioactive Silk Fibroin Promotes Integration and Tissue Organization during Osteochondral Defect Repair in a Porcine Model. *International Journal of Molecular Sciences*, *20*(20), 5145. https://doi.org/10.3390/ijms20205145

Pillai, C. K. S., & Sharma, C. P. (2010). Review Paper: Absorbable Polymeric Surgical Sutures: Chemistry, Production, Properties, Biodegradability, and Performance. *Http://Dx.Doi.Org/10.1177/0885328210384890*, *25*(4), 291–366. https://doi.org/10.1177/0885328210384890

Pitrolino, K. A., Felfel, R. M., Pellizzeri, L. M., McLaren, J., Popov, A. A., Sottile, V., Scotchford, C. A., Scammell, B. E., Roberts, G. A. F., & Grant, D. M. (2022). Development and in vitro assessment of a bi-layered chitosan-nano-hydroxyapatite osteochondral scaffold. *Carbohydrate Polymers*, *282*, 119126. https://doi.org/10.1016/J.CARBPOL.2022.119126

Prasad, P., & Pramanik, K. (2022). Polycaprolactone-based composite biomaterials and their applications in the treatment of arthritis. *Polycaprolactone: Applications, Synthesis and Characterisation*, 151–181.

Qin, C., Ma, J., Chen, L., Ma, H., Zhuang, H., Zhang, M., Huan, Z., Chang, J., Ma, N., & Wu, C. (2021). 3D bioprinting of multicellular scaffolds for osteochondral regeneration. *Materials Today*, *49*, 68–84. https://doi.org/10.1016/J.MATTOD.2021.04.016

Raeisdasteh Hokmabad, V., Davaran, S., Ramazani, A., & Salehi, R. (2017). Design and fabrication of porous biodegradable scaffolds: a strategy for tissue engineering. *Journal of Biomaterials Science, Polymer Edition*, *28*(16), 1797–1825. https://doi.org/10.1080/09205063.2017.1354674

Ramis, J. M. (2021). *Production Of Precipitated Biopolymers With Modification For Crosslinking* (Patent Volume 25 Number 107). Intellectual Property Center, Office Of The Philippines.

Re'Em, T., Witte, F., Willbold, E., Ruvinov, E., & Cohen, S. (2012). Simultaneous regeneration of articular cartilage and subchondral bone induced by spatially presented TGF-beta and BMP-4 in a bilayer affinity binding system. *Acta Biomaterialia*, *8*(9), 3283–3293. https://doi.org/10.1016/j.actbio.2012.05.014

Reneker DH, Yarin AL, Fong H, K. S. (2000). *Bending Instability in Electrospinning of Electrically Charged Liquid Jets of Polymer Solutions in Electrospinning,*.

Reyes, R., Delgado, A., Sánchez, E., Fernández, A., Hernández, A., & Evora, C. (2012). Repair of an osteochondral defect by sustained delivery of BMP-2 or TGFβ1 from a bilayered alginate-PLGA scaffold. *Journal of Tissue Engineering and Regenerative Medicine*, *8*(7), n/a-n/a. https://doi.org/10.1002/term.1549

Richter, D. L., Schenck, R. C., Wascher, D. C., & Treme, G. (2016). Knee Articular Cartilage Repair and Restoration Techniques: A Review of the Literature. *Sports Health*, *8*(2), 153–160. https://doi.org/10.1177/1941738115611350

Riewruja, K., Aguglia, A. M., Hines, S., Makarcyzk, M. J., Honsawek, S., & Lin, H. (2022). PEG Reinforced Scaffold Promotes Uniform Distribution of Human MSC-Created Cartilage Matrix. *Gels*, *8*(12), 794. https://doi.org/10.3390/GELS8120794/S1

Rosenzweig, D. H., Carelli, E., Steffen, T., Jarzem, P., & Haglund, L. (2015). 3D-Printed ABS and PLA Scaffolds for Cartilage and Nucleus Pulposus Tissue Regeneration. *International Journal of Molecular Sciences*, *16*(7), 15118–15135. https://doi.org/10.3390/IJMS160715118

Roth, E. A., Xu, T., Das, M., Gregory, C., Hickman, J. J., & Boland, T. (2004). Inkjet printing for high-throughput cell patterning. *Biomaterials*, *25*(17), 3707–3715. https://doi.org/10.1016/j.biomaterials.2003.10.052

Ruiz-Cantu, L., Gleadall, A., Faris, C., Segal, J., Shakesheff, K., & Yang, J. (2020a). Multi-material 3D bioprinting of porous constructs for cartilage regeneration. *Materials Science and Engineering C*, *109*(February 2019). https://doi.org/10.1016/j.msec.2019.110578

Sahai, N., & Gogoi, M. (2020). Computer aided designing and finite element analysis for development of porous 3D tissue scaffold – A review. *International Journal of Biomedical Engineering and Technology*, *33*(2), 174–197. https://doi.org/10.1504/IJBET.2020.107712

Sahoo, S., Teh, T. K., He, P., Toh, S. L., & Goh, J. C. (2011). Interface tissue engineering: Next phase in musculoskeletal tissue repair. *Annals of the Academy of Medicine Singapore*, *40*(5), 246–251.

Sánchez-Pech, J. C., Rosales-Ibáñes, R., Cauich-Rodriguez, J. V., Carrillo-Escalante, H. J., Rodríguez-Navarrete, A., Avila-Ortega, A., & Hernández-Sánchez, F. (2020). Design, synthesis, characterisation, and cytotoxicity of PCL/PLGA scaffolds through plasma treatment in the presence of pyrrole for possible use in urethral tissue engineering. *Journal of Biomaterials Applications*, *34*(6), 840–850. https://doi.org/10.1177/0885328219882638/ASSET/IMAGES/LARGE/10.1177_0885328219882638-FIG9.JPEG

Sarin, J. K., te Moller, N. C. R., Mancini, I. A. D., Brommer, H., Visser, J., Malda, J., van Weeren, P. R., Afara, I. O., & Töyräs, J. (2018). Arthroscopic near infrared spectroscopy enables simultaneous quantitative evaluation of articular cartilage and subchondral bone in vivo. *Scientific Reports*, *8*(1), 1–10. https://doi.org/10.1038/s41598-018-31670-5

Schaefer, D., Martin, I., Jundt, G., Seidel, J., Heberer, M., Grodzinsky, A., Bergin, I., Vunjak-Novakovic, G., & Freed, L. E. (2002). Tissue-engineered composites for the repair of large osteochondral defects. *Arthritis & Rheumatism*, *46*(9), 2524–2534. https://doi.org/10.1002/art.10493

Schek, R. M., Taboas, J. M., Segvich, S. J., Hollister, S. J., & Krebsbach, P. H. (2004). Engineered osteochondral grafts using biphasic composite solid free-form fabricated scaffolds. *Tissue Engineering*, *10*(9–10), 1376–1385. https://doi.org/10.1089/ten.2004.10.1376

Schipani, R., Nolan, D. R., Lally, C., & Kelly, D. J. (2020a). Integrating finite element modelling and 3D printing to engineer biomimetic polymeric scaffolds for tissue engineering. *Connective Tissue Research*, *61*(2), 174–189. https://doi.org/10.1080/03008207.2019.1656720

Schipani, R., Nolan, D. R., Lally, C., & Kelly, D. J. (2020b). Integrating finite element modelling and 3D printing to engineer biomimetic polymeric scaffolds for tissue

engineering. *Connective Tissue Research*, *61*(2), 174–189. https://doi.org/10.1080/03008207.2019.1656720

Schipani, R., Scheurer, S., Florentin, R., Critchley, S. E., & Kelly, D. J. (2020). Reinforcing interpenetrating network hydrogels with 3D printed polymer networks to engineer cartilage mimetic composites. *Biofabrication*, *12*(3). https://doi.org/10.1088/1758-5090/AB8708

Schoonraad, S. A., Fischenich, K. M., Eckstein, K. N., Crespo-Cuevas, V., Savard, L. M., Muralidharan, A., Tomaschke, A. A., Uzcategui, A. C., Randolph, M. A., McLeod, R. R., Ferguson, V. L., & Bryant, S. J. (2021). Biomimetic and mechanically supportive 3D printed scaffolds for cartilage and osteochondral tissue engineering using photopolymers and digital light processing. *Biofabrication*, *13*(4). https://doi.org/10.1088/1758-5090/AC23AB

Schuurman, W., Levett, P. A., Pot, M. W., van Weeren, P. R., Dhert, W. J. A., Hutmacher, D. W., Melchels, F. P. W., Klein, T. J., & Malda, J. (2013). Gelatin-Methacrylamide Hydrogels as Potential Biomaterials for Fabrication of Tissue-Engineered Cartilage Constructs. *Macromolecular Bioscience*, *13*(5), 551–561. https://doi.org/10.1002/MABI.201200471

Schwab, A., Levato, R., D'Este, M., Piluso, S., Eglin, D., & Malda, J. (2020). Printability and Shape Fidelity of Bioinks in 3D Bioprinting. In *Chemical Reviews* (Vol. 120, Issue 19, pp. 11028–11055). American Chemical Society. https://doi.org/10.1021/acs.chemrev.0c00084

Seo, S. J., Mahapatra, C., Singh, R. K., Knowles, J. C., & Kim, H. W. (2014a). Strategies for osteochondral repair: Focus on scaffolds. In *Journal of Tissue Engineering* (Vol. 5). SAGE Publications Ltd. https://doi.org/10.1177/2041731414541850

Serra, T. (2014). *Development of 3D-printed biodegradable composite scaffolds for tissue engineering applications*. *1*, 1 recurs electrònic (177).

Shen, T., Dai, Y., Li, X., Xu, S., Gou, Z., & Gao, C. (2018a). Regeneration of the Osteochondral Defect by a Wollastonite and Macroporous Fibrin Biphasic

Scaffold. *ACS Biomaterials Science and Engineering*, *4*(6), 1942–1953. https://doi.org/10.1021/acsbiomaterials.7b00333

Shepherd, D. E. T., & Seedhom, B. B. (1999). The "instantaneous" compressive modulus of human articular cartilage in joints of the lower limb. *Rheumatology*, *38*, 124–132. https://academic.oup.com/rheumatology/article/38/2/124/1783577

Shie, M. Y., Lee, J. J., Ho, C. C., Yen, S. Y., Ng, H. Y., & Chen, Y. W. (2020). Effects of Gelatin Methacrylate Bio-ink Concentration on Mechano-Physical Properties and Human Dermal Fibroblast Behavior. *Polymers 2020, Vol. 12, Page 1930*, *12*(9), 1930. https://doi.org/10.3390/POLYM12091930

Shimomura, K., Moriguchi, Y., Murawski, C. D., Yoshikawa, H., & Nakamura, N. (2014). Osteochondral tissue engineering with biphasic scaffold: Current strategies and techniques. In *Tissue Engineering - Part B: Reviews* (Vol. 20, Issue 5, pp. 468–476). Mary Ann Liebert Inc. https://doi.org/10.1089/ten.teb.2013.0543

Sing, S. L., & Yeong, W. Y. (2021). Process–Structure–Properties in Polymer Additive Manufacturing. *Polymers*, *13*(7). https://doi.org/10.3390/POLYM13071098

Singh, B. K., & Dutta, P. K. (2015). Chitin, chitosan, and silk fibroin electrospun nanofibrous scaffolds: A prospective approach for regenerative medicine. In *Chitin and Chitosan for Regenerative Medicine* (pp. 151–189). Springer India. https://doi.org/10.1007/978-81-322-2511-9_7

Sinha, V. R., Bansal, K., Kaushik, R., Kumria, R., & Trehan, A. (2004). Poly-ϵ-caprolactone microspheres and nanospheres: an overview. *International Journal of Pharmaceutics*, *278*(1), 1–23. https://doi.org/10.1016/J.IJPHARM.2004.01.044

Skoog, S. A., Goering, P. L., & Narayan, R. J. (2014). Stereolithography in tissue engineering. *Journal of Materials Science: Materials in Medicine*, *25*(3), 845–856. https://doi.org/10.1007/s10856-013-5107-y

Stansbury, J. W., & Idacavage, M. J. (2015). *ScienceDirect 3D printing with polymers: Challenges among expanding options and opportunities*. https://doi.org/10.1016/j.dental.2015.09.018

Subramanian, A., Vu, D., Larsen, G. F., & Lin, H. Y. (2005). Preparation and evaluation of the electrospun chitosan/PEO fibers for potential applications in cartilage tissue engineering. *Journal of Biomaterials Science, Polymer Edition*, *16*(7), 861–873. https://doi.org/10.1163/1568562054255682

Sun, H., Mei, L., Song, C., Cui, X., & Wang, P. (2006). The in vivo degradation, absorption and excretion of PCL-based implant. *Biomaterials*, *27*(9), 1735–1740. https://doi.org/10.1016/J.BIOMATERIALS.2005.09.019

Sun, J., Hou, X. kui, & Zheng, Y. xin. (2016). Restore a 9 mm diameter osteochondral defect with gene enhanced tissue engineering followed mosaicplasty in a goat model. *Acta Orthopaedica et Traumatologica Turcica*, *50*(4), 464–469. https://doi.org/10.1016/j.aott.2016.05.003

Suo, H., Chen, Y., Liu, J., Wang, L., & Xu, M. (2021a). 3D printing of biphasic osteochondral scaffold with sintered hydroxyapatite and polycaprolactone. *Journal of Materials Science*, *56*(29), 16623–16633. https://doi.org/10.1007/S10853-021-06229-X/FIGURES/7

Swieszkowski, W., Tuan, B. H. S., Kurzydlowski, K. J., & Hutmacher, D. W. (2007a). Repair and regeneration of osteochondral defects in the articular joints. *Biomolecular Engineering*, *24*(5), 489–495. https://doi.org/10.1016/J.BIOENG.2007.07.014

Tamaddon, M., Blunn, G., & Liu, C. (2016). *3D printed PLA / collagen hybrid scaffolds for bone-cartilage interface tissue engineering*. *32*(page 113), 103516.

Tamaddon, M., Wang, L., Liu, Z., & Liu, C. (2018a). Osteochondral tissue repair in osteoarthritic joints: clinical challenges and opportunities in tissue engineering. *Bio-Design and Manufacturing*, *1*(2), 101–114. https://doi.org/10.1007/s42242-018-0015-0

Tan, W. S., Moore, A. C., & Stevens, M. M. (2023). Minimum design requirements for a poroelastic mimic of articular cartilage. *Journal of the Mechanical Behavior of Biomedical Materials*, *137*. https://doi.org/10.1016/J.JMBBM.2022.105528

Tang, Y., Muzzy, J. D., Henderson, C. L., Rosen, D. W., Ludovice, P. J., & Hernandez, R. (2005). *STEREOLITHOGRAPHY CURE PROCESS MODELING A Dissertation Presented to The Academic Faculty*.

Tappa, K., & Jammalamadaka, U. (2018). Novel Biomaterials Used in Medical 3D Printing Techniques. *Journal of Functional Biomaterials*, *9*(1), 17. https://doi.org/10.3390/jfb9010017

Taylor, S. D., Tsiridis, E., Ingham, E., Jin, Z., Fisher, J., & Williams, S. (2012). Comparison of human and animal femoral head chondral properties and geometries. *Proceedings of the Institution of Mechanical Engineers, Part H: Journal of Engineering in Medicine*, *226*(1), 55–62. https://doi.org/10.1177/0954411911428717/ASSET/IMAGES/LARGE/10.1177_0954411911428717-FIG9.JPEG

Thambyah, A., Nather, A., & Goh, J. (2006). Mechanical properties of articular cartilage covered by the meniscus. *Osteoarthritis and Cartilage*, *14*(6), 580–588. https://doi.org/10.1016/J.JOCA.2006.01.015

The Lancet: New study reveals the most common form of arthritis, osteoarthritis, affects 15% of the global population over the age of 30 | The Institute for Health Metrics and Evaluation. (n.d.). Retrieved October 5, 2023, from https://www.healthdata.org/news-events/newsroom/news-releases/lancet-new-study-reveals-most-common-form-arthritis

Tillman, B. W., Yazdani, S. K., Lee, S. J., Geary, R. L., Atala, A., & Yoo, J. J. (2009). The in vivo stability of electrospun polycaprolactone-collagen scaffolds in vascular reconstruction. *Biomaterials*, *30*(4), 583–588. https://doi.org/10.1016/j.biomaterials.2008.10.006

Toom, D. A. den, Rieke, M., Elbadawi, A., & Kösters, C. (2023). 2-year results of middle-aged patients with two-compartment cartilage lesions in one knee treated with two patient specific metal implants. *Journal of Experimental Orthopaedics*, *10*(1). https://doi.org/10.1186/S40634-023-00648-2

Upmeier, H., Brüggenjürgen, B., Weiler, A., Flamme, C., Laprell, H., & Willich, S. N. (2007). Follow-up costs up to 5 years after conventional treatments in patients with

cartilage lesions of the knee. *Knee Surgery, Sports Traumatology, Arthroscopy*, *15*(3), 249–257. https://doi.org/10.1007/S00167-006-0182-Y/FIGURES/3

Valentinčič, J., Peroša, M., Jerman, M., Sabotin, I., & Lebar, A. (2017). Low cost printer for DLP stereolithography. *Strojniski Vestnik/Journal of Mechanical Engineering*, *63*(10), 559–566. https://doi.org/10.5545/SV-JME.2017.4591

Van De Velde, K., & Kiekens, P. (2002a). Biopolymers: overview of several properties and consequences on their applications. *Polymer Testing*, *21*(4), 433–442. https://doi.org/10.1016/S0142-9418(01)00107-6

Vanaei, S., Parizi, M. S., Vanaei, S., Salemizadehparizi, F., & Vanaei, H. R. (2021). An Overview on Materials and Techniques in 3D Bioprinting Toward Biomedical Application. *Engineered Regeneration*, *2*, 1–18. https://doi.org/10.1016/J.ENGREG.2020.12.001

Varoni, E. M., Vijayakumar, S., Canciani, E., Cochis, A., De Nardo, L., Lodi, G., Rimondini, L., & Cerruti, M. (2018). Chitosan-Based Trilayer Scaffold for Multitissue Periodontal Regeneration. *Journal of Dental Research*, *97*(3), 303–311. https://doi.org/10.1177/0022034517736255

Vedadghavami, A., Minooei, F., Mohammadi, M. H., Khetani, S., Rezaei Kolahchi, A., Mashayekhan, S., & Sanati-Nezhad, A. (2017). Manufacturing of hydrogel biomaterials with controlled mechanical properties for tissue engineering applications. *Acta Biomaterialia*, *62*, 42–63. https://doi.org/10.1016/J.ACTBIO.2017.07.028

Vidal-Lesso, A., Ledesma-Orozco, E., Daza-Benítez, L., & Lesso-Arroyo, R. (2014). Mechanical Characterisation of Femoral Cartilage Under Unicompartimental Osteoarthritis. *Ingeniería Mecánica, Tecnología y Desarrollo*, *4*(6), 239–246. http://www.scielo.org.mx/scielo.php?script=sci_arttext&pid=S1665-73812014000100006&lng=es&nrm=iso&tlng=en

Vidal-Lesso, A., Ledesma-Orozco, E., Lesso-Arroyo, R., & Daza-Benitez, L. (2012). Nonlinear Dynamic Viscoelastic Model for Osteoarthritic Cartilage Indentation Force. *ASME 2011 International Mechanical Engineering Congress and*

Exposition, IMECE 2011, *2*, 215–220. https://doi.org/10.1115/IMECE2011-64387

Viidik, L., Vesala, J., Laitinen, R., Korhonen, O., Ketolainen, J., Aruväli, J., Kirsimäe, K., Kogermann, K., Heinämäki, J., Laidmäe, I., & Ervasti, T. (2021). Preparation and characterisation of hot-melt extruded polycaprolactone-based filaments intended for 3D-printing of tablets. *European Journal of Pharmaceutical Sciences*, *158*, 105619. https://doi.org/10.1016/j.ejps.2020.105619

Vijayavenkataraman, S., Yan, W.-C. C., Lu, W. F., Wang, C. H., Fuh, J. Y. H., Wang, C. H., & Fuh, J. Y. H. (2018). 3D bioprinting of tissues and organs for regenerative medicine. *Advanced Drug Delivery Reviews*, *132*, 296–332. https://doi.org/10.1016/j.addr.2018.07.004

Vijayavenkataraman, S., Zhang, L., Zhang, S., Fuh, J. Y. H., & Lu, W. F. (2018). Triply periodic minimal surfaces sheet scaffolds for tissue engineering applications: An optimization approach toward biomimetic scaffold design [Research-article]. *ACS Applied Bio Materials*, *1*(2), 259–269. https://doi.org/10.1021/acsabm.8b00052

Vinogradov, G. V., & Malkin, A. Ya. (1980). *Rheology of Polymers*. https://doi.org/10.1007/978-3-642-52204-8

Wang, F., Tankus, E. B., Santarella, F., Rohr, N., Sharma, N., Märtin, S., Michalscheck, M., Maintz, M., Cao, S., & Thieringer, F. M. (2022). Fabrication and Characterisation of PCL/HA Filament as a 3D Printing Material Using Thermal Extrusion Technology for Bone Tissue Engineering. *Polymers*, *14*(4), 669. https://doi.org/10.3390/POLYM14040669/S1

Wang, K. C., Cotter, E. J., Davey, A., Oliver-Welsh, L., W Griffin, J., Meyer, M. A., Gitelis, M. E., & Cole, B. J. (2016). *A Treatment Approach for Articular Cartilage Defects | Journal of Clinical Orthopaedics*. https://jcorth.com/2016/07/10/a-treatment-approach-for-articular-cartilage-defects/

Wang, P., Sun, Y., Li, D., Ma, Z., Zhang, B., Diao, L., & Liu, H. (2023). Extrusion-based 3D co-printing: Printing material design and novel workflow for fabricating patterned heterogeneous tissue structures. *Materials & Design*, *227*, 111737. https://doi.org/10.1016/J.MATDES.2023.111737

Wang, W., Caetano, G. F., Chiang, W. H., Braz, A. L., Blaker, J. J., Frade, M. A. C., & Bártolo, P. J. (2016). Morphological, mechanical and biological assessment of PCL/pristine graphene scaffolds for bone regeneration. *International Journal of Bioprinting*, *2*(2), 95–104. https://doi.org/10.18063/IJB.2016.02.009

Wang, W., Nie, W., Zhou, X., Feng, W., Chen, L., Zhang, Q., You, Z., Shi, Q., Peng, C., & He, C. (2018). Fabrication of heterogeneous porous bilayered nanofibrous vascular grafts by two-step phase separation technique. *Acta Biomaterialia*, *79*, 168–181. https://doi.org/10.1016/J.ACTBIO.2018.08.014

Wang, X., Grogan, S. P., Rieser, F., Winkelmann, V., Maquet, V., La Berge, M., & Mainil-Varlet, P. (2004). Tissue engineering of biphasic cartilage constructs using various biodegradable scaffolds: An in vitro study. *Biomaterials*. https://doi.org/10.1016/j.biomaterials.2003.10.102

Wasyłeczko, M., Sikorska, W., & Chwojnowski, A. (2020). Review of Synthetic and Hybrid Scaffolds in Cartilage Tissue Engineering. *Membranes*, *10*(11), 1–28. https://doi.org/10.3390/MEMBRANES10110348

Wei, P., Xu, Y., Zhang, H., & Wang, L. (2021). Continued sustained insulin-releasing PLGA nanoparticles modified 3D-Printed PCL composite scaffolds for osteochondral repair. *Chemical Engineering Journal*, *422*, 130051. https://doi.org/10.1016/J.CEJ.2021.130051

Wei, W., & Dai, H. (2021a). Articular cartilage and osteochondral tissue engineering techniques: Recent advances and challenges. *Bioactive Materials*, *6*(12), 4830–4855. https://doi.org/10.1016/j.bioactmat.2021.05.011

Wieding, J., Souffrant, R., Mittelmeier, W., & Bader, R. (2013). Finite element analysis on the biomechanical stability of open porous titanium scaffolds for large segmental bone defects under physiological load conditions. *Medical Engineering & Physics*, *35*(4), 422–432. https://doi.org/10.1016/J.MEDENGPHY.2012.06.006

Winarso, R., Anggoro, P. W., Ismail, R., Jamari, J., & Bayuseno, A. P. (2022). Application of fused deposition modeling (FDM) on bone scaffold manufacturing process: A review. *Heliyon*, *8*(11). https://doi.org/10.1016/J.HELIYON.2022.E11701

Woodfield, T. B. F., Bezemer, J. M., Pieper, J. S., Van Blitterswijk, C. A., & Riesle, J. (2002). Scaffolds for tissue engineering of cartilage. In *Critical Reviews in Eukaryotic Gene Expression* (Vol. 12, Issue 3, pp. 209–236). Begel House Inc. https://doi.org/10.1615/CritRevEukaryotGeneExpr.v12.i3.40

Woodfield, T. B. F., Malda, J., De Wijn, J., Péters, F., Riesle, J., & Van Blitterswijk, C. A. (2004). Design of porous scaffolds for cartilage tissue engineering using a three-dimensional fiber-deposition technique. *Biomaterials*, *25*(18), 4149–4161. https://doi.org/10.1016/J.BIOMATERIALS.2003.10.056

Woodruff, M. A., & Hutmacher, D. W. (2010). The return of a forgotten polymer - Polycaprolactone in the 21st century. In *Progress in Polymer Science (Oxford)* (Vol. 35, Issue 10, pp. 1217–1256). Elsevier Ltd. https://doi.org/10.1016/j.progpolymsci.2010.04.002

Xiao, H., huang, W., Xiong, K., ruan, S., Yuan, C., Mo, G., Tian, R., Zhou, S., She, rongfeng, Ye, P., Liu, B., & Deng, J. (2019). Osteochondral repair using scaffolds with gradient pore sizes constructed with silk fibroin, chitosan, and nano-hydroxyapatite. *International Journal of Nanomedicine*, *14*, 2011–2027. https://doi.org/10.2147/IJN.S191627

Xiao, H., Huang, W., Xiong, K., Ruan, S., Yuan, C., Mo, G., Tian, R., Zhou, S., She, R., Ye, P., Liu, B., & Deng, J. (2019). Osteochondral repair using scaffolds with gradient pore sizes constructed with silk fibroin, chitosan, and nano-hydroxyapatite. *International Journal of Nanomedicine*, *14*, 2011–2027. https://doi.org/10.2147/IJN.S191627

Xu, T., Binder, K. W., Albanna, M. Z., Dice, D., Zhao, W., Yoo, J. J., & Atala, A. (2012). Hybrid printing of mechanically and biologically improved constructs for cartilage tissue engineering applications. *Biofabrication*, *5*(1), 015001. https://doi.org/10.1088/1758-5082/5/1/015001

Xu, T., Binder, K. W., Albanna, M. Z., Dice, D., Zhao, W., Yoo, J. J., & Atala, A. (2013). Hybrid printing of mechanically and biologically improved constructs for cartilage tissue engineering applications. *IOP PUBLISHING BIOFABRICATION Biofabrication*, *5*, 15001–15010. https://doi.org/10.1088/1758-5082/5/1/015001

Xu, T., Rohozinski, J., Zhao, W., Moorefield, E. C., Atala, A., & Yoo, J. J. (2009). Inkjet-mediated gene transfection into living cells combined with targeted delivery. *Tissue Eng. A*, *15*(1), 95–101. https://doi.org/10.1089/ten.tea.2008.0095

Yan, J., Demirci, E., Ganesan, A., & Gleadall, A. (2022). Extrusion width critically affects fibre orientation in short fibre reinforced material extrusion additive manufacturing. *Additive Manufacturing*, *49*, 102496. https://doi.org/10.1016/J.ADDMA.2021.102496

Yang, X., Liu, P., Zhang, Y., Lu, J., & Zhao, H. (2023). Bioprinting-Enabled Biomaterials: A Cutting-Edge Strategy for Future Osteoarthritis Therapy. *International Journal of Nanomedicine*, *18*, 6213–6232. https://doi.org/10.2147/IJN.S432468

Yang, Y., Feng, Y., Qu, R., Li, Q., Rong, D., Fan, T., Yang, Y., Sun, B., Bi, Z., Khan, A. U., Deng, T., Dai, J., & Ouyang, J. (2020). Synthesis of aligned porous polyethylene glycol/silk fibroin/hydroxyapatite scaffolds for osteoinduction in bone tissue engineering. *Stem Cell Research and Therapy*, *11*(1), 1–17. https://doi.org/10.1186/S13287-020-02024-8/FIGURES/7

Yang, Z., Zhao, T., Gao, C., Cao, F., Li, H., Liao, Z., Fu, L., Li, P., Chen, W., Sun, Z., Jiang, S., Tian, Z., Tian, G., Zha, K., Pan, T., Li, X., Sui, X., Yuan, Z., Liu, S., & Guo, Q. (2021). 3D-Bioprinted Difunctional Scaffold for In Situ Cartilage Regeneration Based on Aptamer-Directed Cell Recruitment and Growth Factor-Enhanced Cell Chondrogenesis. *ACS Applied Materials & Interfaces*, *13*(20), 23369–23383. https://doi.org/10.1021/ACSAMI.1C01844

Yousefi, A. M., Hoque, M. E., Prasad, R. G. S. V., & Uth, N. (2015a). Current strategies in multiphasic scaffold design for osteochondral tissue engineering: A review. *Journal of Biomedical Materials Research - Part A*, *103*(7), 2460–2481. https://doi.org/10.1002/jbm.a.35356

Yousefi, A. M., Hoque, M. E., Prasad, R. G. S. V., & Uth, N. (2015c). Current strategies in multiphasic scaffold design for osteochondral tissue engineering: A review. *Journal of Biomedical Materials Research - Part A*, *103*(7), 2460–2481. https://doi.org/10.1002/jbm.a.35356

Yu, P., Ning, C., Zhang, Y., Tan, G., Lin, Z., Liu, S., Wang, X., Yang, H., Li, K., Yi, X., Zhu, Y., & Mao, C. (2017). Bone-inspired spatially specific piezoelectricity induces bone regeneration. *Theranostics*, *7*(13), 3387–3397. https://doi.org/10.7150/THNO.19748

Yue, Z., Liu, X., Coates, P. T., & Wallace, G. G. (2016). Advances in printing biomaterials and living cells: implications for islet cell transplantation. *Current Opinion in Organ Transplantation*, *21*(5), 467–475. https://doi.org/10.1097/MOT.0000000000000346

Yuqing Gu, Yiwei Zou, Yuxuan Huang, Renjie Liang, Yicong Wu, Yifan Hu, Yi Hong, Xianzhu Zhang, Yi-Chin Toh, Hongwei Ouyang, & Shufang Zhang. (2023). 3D-printed biomimetic scaffolds with precisely controlled and tunable structures guide cell migration and promote regeneration of osteochondral defect. *Biofabrication*, *16*(1), 015003. https://doi.org/10.1088/1758-5090/AD0071

Zein, I., Hutmacher, D. W., Tan, K. C., & Teoh, S. H. (2002). Fused deposition modeling of novel scaffold architectures for tissue engineering applications. *Biomaterials*, *23*(4), 1169–1185. https://doi.org/10.1016/S0142-9612(01)00232-0

Zeinali, R., Del Valle, L. J., Torras, J., & Puiggalí, J. (2021). Recent progress on biodegradable tissue engineering scaffolds prepared by thermally-induced phase separation (Tips). In *International Journal of Molecular Sciences* (Vol. 22, Issue 7, p. 3504). MDPI AG. https://doi.org/10.3390/ijms22073504

Zhai, C., Fei, H., Hu, J., Wang, Z., Xu, S., Zuo, Q., Li, Z., Wang, Z., Liang, W., & Fan, W. (2018). Repair of Articular Osteochondral Defects Using an Integrated and Biomimetic Trilayered Scaffold. *Tissue Engineering Part A*, *24*(21–22), 1680–1692. https://doi.org/10.1089/ten.tea.2018.0086

Zhang, B., Gao, L., Ma, L., Luo, Y., Yang, H., & Cui, Z. (2019). 3D Bioprinting: A Novel Avenue for Manufacturing Tissues and Organs. *Engineering*, *5*(4), 777–794. https://doi.org/10.1016/j.eng.2019.03.009

Zhang, B., Guo, L., Chen, H., Ventikos, Y., Narayan, R. J., & Huang, J. (2020). Finite element evaluations of the mechanical properties of polycaprolactone/hydroxyapatite scaffolds by direct ink writing: Effects of pore

geometry. *Journal of the Mechanical Behavior of Biomedical Materials*, *104*(November 2019). https://doi.org/10.1016/j.jmbbm.2020.103665

Zhang, B., Huang, J., & Narayan, R. J. (2020). Gradient scaffolds for osteochondral tissue engineering and regeneration. *Journal of Materials Chemistry B*, *8*(36), 8149–8170. https://doi.org/10.1039/D0TB00688B

Zhang, B., Huang, J., Narayan, R. J., Mater, J., Chem, B., Zhang, B., Huang, J., & Narayan, R. J. (2020). Gradient scaffolds for osteochondral tissue engineering and regeneration. *Journal of Materials Chemistry B*, *8*(36), 8149–8170. https://doi.org/10.1039/d0tb00688b

Zhang, K., Liu, B., Yang, Y., -, al, Miao, S., Cui, H., Nowicki, M., Wang, Z., Abdulla, R., Parker, B., Samanipour, R., Ghosh, S., & Kim, K. (2015). A simple and high-resolution stereolithography-based 3D bioprinting system using visible light crosslinkable bioinks. *Biofabrication*, *7*(4), 045009. https://doi.org/10.1088/1758-5090/7/4/045009

Zhang, P., Gao, Z., Zhang, Q., Khattab, A., & Li, G. (2018). *Fracture Behavior Characterisation of Arcan Polycaprolactone Based Polymer Composites Prepared by Polymerization Induced Phases Separation*. https://doi.org/10.1002/pc.24831

Zhang, S., Huang, Y., Yang, X., Mei, F., Ma, Q., Chen, G., Ryu, S., & Deng, X. (2009). Gelatin nanofibrous membrane fabricated by electrospinning of aqueous gelatin solution for guided tissue regeneration. *Journal of Biomedical Materials Research. Part A*, *90*(3), 671–679. https://doi.org/10.1002/jbm.a.32136

Zhang, T., Zhang, H., Zhang, L., Jia, S., Liu, J., Xiong, Z., & Sun, W. (2017a). Biomimetic design and fabrication of multilayered osteochondral scaffolds by low-temperature deposition manufacturing and thermal-induced phase-separation techniques. *Biofabrication*, *9*(2). https://doi.org/10.1088/1758-5090/aa7078

Zhang, Y., & Jordan, J. M. (2010). Epidemiology of osteoarthritis. In *Clinics in Geriatric Medicine* (Vol. 26, Issue 3, pp. 355–369). NIH Public Access. https://doi.org/10.1016/j.cger.2010.03.001

Zhang, Y. Z., Su, B., Ramakrishna, S., & Lim, C. T. (2008). Chitosan nanofibers from an easily electrospinnable UHMWPEO-doped chitosan solution system. *Biomacromolecules*, *9*(1), 136–141. https://doi.org/10.1021/bm701130e

Zhou, H., Chen, R., Wang, J., Lu, J., Yu, T., Wu, X., Xu, S., Li, Z., Jie, C., Cao, R., Yang, Y., Li, Y., & Meng, D. (2020a). Biphasic fish collagen scaffold for osteochondral regeneration. *Materials and Design*, *195*, 1–12. https://doi.org/10.1016/j.matdes.2020.108947

Zhou, X., Esworthy, T., Lee, S. J., Miao, S., Cui, H., Plesiniak, M., Fenniri, H., Webster, T., Rao, R. D., & Zhang, L. G. (2019). 3D Printed scaffolds with hierarchical biomimetic structure for osteochondral regeneration. *Nanomedicine: Nanotechnology, Biology and Medicine*, *19*, 58–70. https://doi.org/10.1016/J.NANO.2019.04.002

Appendix A. Cell Culture Solutions

A.1. – Cell Culture

A.1.1. Culture medium.

- 10 % Fetal bovine serum (FBS).
- 1% Antibiotic/Antimycotic (AA)
- 1% L-glutamine (LG).

A.1.2. Presto Blue

- 1:10 ratio.

A.1.3. Biochemical analysis.

A.1.4. LIVE/DEAD solution.

- Phosphate-buffered saline (PBS) 10 ml.
- Calcein AM (Component A) 5 µL.
- Ethidium homodimer-1 (Component B)- 20 µL.

A.1.5. Cell Distribution analysis.

- Toloudin Blue O 0.1g.
- Distilled water 100 ml

A.1.6. DNA

- Quant-iT^{TM} dsDNA HS buffer.
- Quant-iT^{TM} dsDNA HS reagent(200X).
- λdsDNA HS standard 0, 0.5, 1.0, 2.0, 4.0, 6.0, 8.0, 10.0 ng/µl.
- Trizma® hydrochloride solution.
- Triton TM X100

Appendix B. Standard Curves

B.1. Presto Blue standard curve

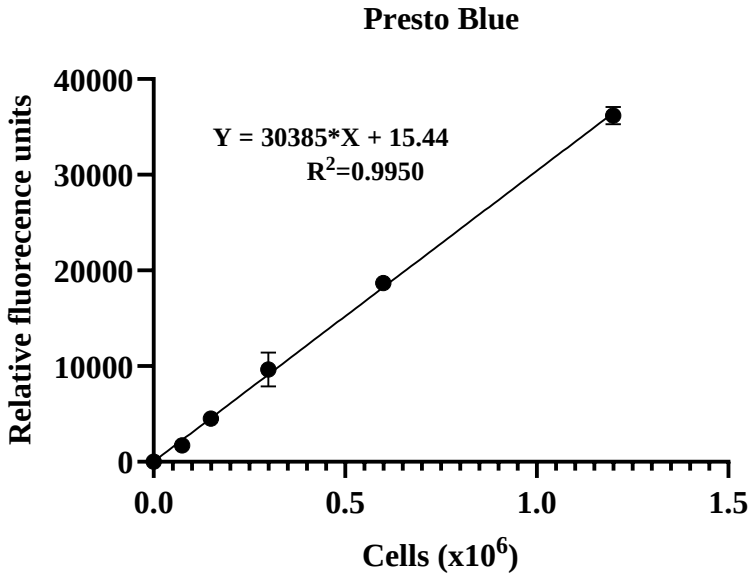


Figure B 1 **S**tandard curve profile of increasing cell populations using PrestoBlue assay. A viable cell concentration standard curve was created of 0, 0.075x10^6, 0.15x10^6, 0.3 x10^6, 0.6 x10^6 , and 1.2 x10^6 cells. Each cell concentration was transferred to 3 wells on a 96 well microplate. 200 µL of the Presto Blue® dye at 1:10 ratio (in culture media) was added to each well and the plate was incubated for 30 minutes at 37°C, away from light. Presto blue data is denote mean± S.D. (n=3, N=3)., each with three technical repeats.

B.2. dsDNA standard Curve

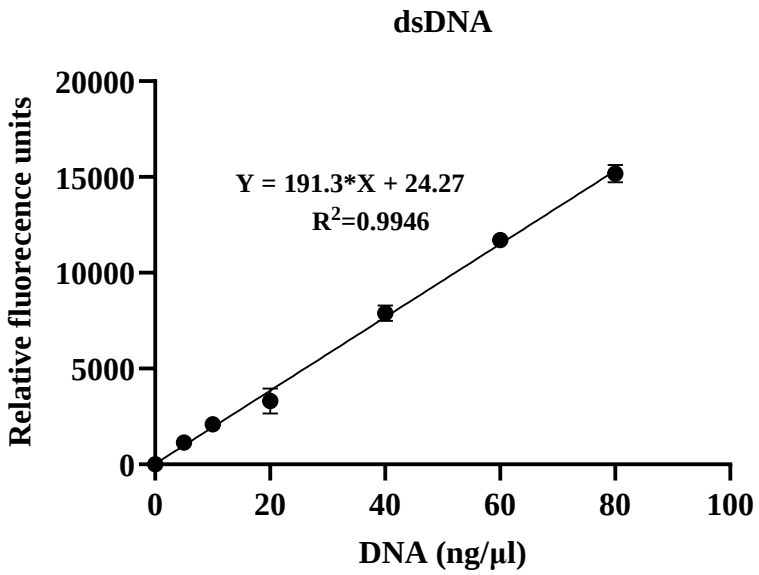


Figure B 2- **S**tandard curve profile of increasing cell populations using Quant-iT™ dsDNA assay. **S**tandard curve profile of increasing cell populations. A viable cell concentration standard curve was created from the lysates of known cell number of 0, 5, 10,20,40,60,80 and 100 ng/µl. Each cell concentration was transferred to 3 wells on a 96 well microplate. 20 µl of each lysates known cells and 180 µL of the buffer and reagent of Quant-iT dsDNA was added to each well. dsDNA data is denote mean± S.D. (n=2, N=2)., each with three technical repeats.